Fast Multi-parametric Acquisition Methods for Quantitative Brain MRI

Laura Núñez González

Fast Multi-parametric Acquisition Methods for Quantitative Brain MRI

Acknowledgements:
This research was partly funded by General electric Healthcare.

For financial support for the publication of this thesis the following organisations are gratefully acknowledged: Erasmus University and the department of Radiology and Nuclear Medicine of Erasmus MC.

Cover ideation: Laura Núñez González
Cover design: Wendy Schoneveld
Printing: Proefschriftmaken

Fast Multi-parametric Acquisition Methods For Quantitative Brain MRI

Snelle multiparametrische acquisitiemethoden voor kwantitatieve hersen-MRI

Thesis

to obtain the degree of Doctor from the

Erasmus University Rotterdam

by command of the

rector magnificus

Prof. dr. A.L. Bredenoord

and in accordance with the decision of the Doctorate Board.

The public defence shall be held on

Tuesday 12th April 2022 at 13:00 hrs

by

Laura Núñez González

born in Leganés (Madrid), Spain.

Erasmus University Rotterdam

Promotor:

Prof. dr. J.A. Hernández Tamames

Other members:

Dr. E.H.G. Oei
Prof. dr. W.J. Niessen
Prof. dr. M.I. Menzel

Copromotors:

Dr. D.H.J. Poot
Dr. G. Kotek

FAST MULTI-PARAMETRIC ACQUISITION METHODS FOR QUANTITATIVE BRAIN MRI

Thesis, Erasmus MC, University Medical Center, Rotterdam, The Netherlands

The research described in this thesis was performed at the Department of Radiology and Nuclear Medicine, Erasmus Medical Center, Rotterdam, The Netherlands.

To my nieces and nephews, the ones who are and the ones who may come.
May the steps I'm taking make me a better auntie.

A mis sobrinos, a los que están y a los que vengan.
Que los pasos que voy dando me hagan ser mejor tía.

CONTENTS

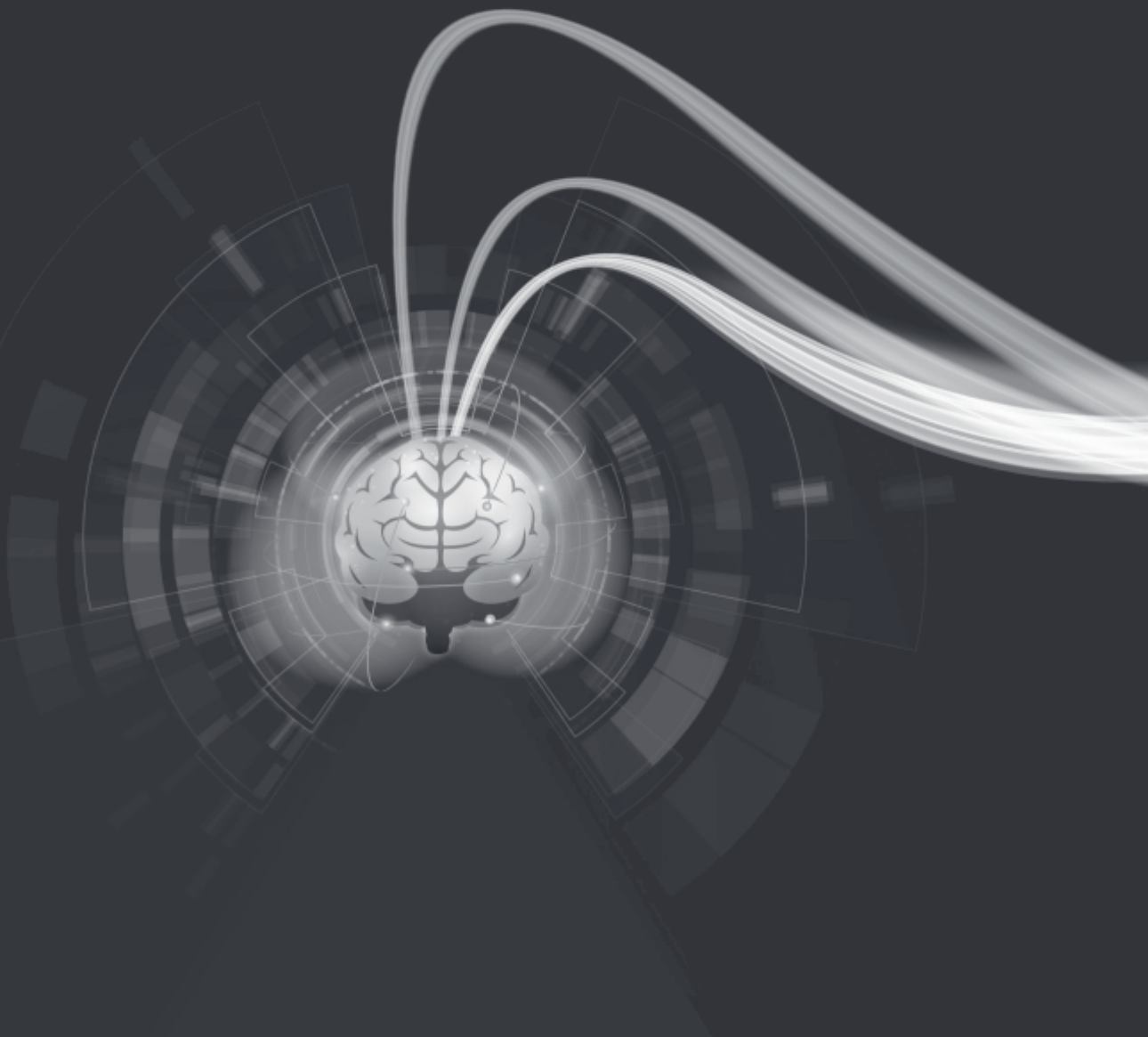

SUMMARY

Magnetic Resonance (MR) technology is in continuous development. Part of the ongoing research is focused on quantitative measurements of the tissue intrinsic parameters: proton density (PD), T1, and T2. Quantitative measurements could overcome inter-session and inter-system variability and facilitate longitudinal studies. However, until the recent development of fast multi-parametric sequences, such as MR Fingerprinting (MRF) or QRAPMASTER, the applicability of quantitative measurements was limited due to the long acquisition time needed.

The aim of this thesis is to gain insight into quantitative MR techniques and bring them closer to the clinical routine. As an initial step, we evaluated the **accuracy and the repeatability of QRAPMASTER and MRF-vFA**. This is explored in **chapter 2** using one phantom and 5 volunteers. These techniques showed good repeatability in phantom and in-vivo experiments, but QRAPMASTER was more accurate than MRF-vFA. However, an advantage of MRF-vFA is the rapid acquisition time (70s, 4.77 times faster than QRAPMASTER). More investigation is needed to reduce the bias of MRF-vFA and improve resolution but its rapid acquisition time could position MRF-vFA as a good candidate at least as a pre-exploration sequence.

The positive results obtained in phantom and healthy volunteers, positioned us for the next step: to evaluate these techniques in patients. The goal of this second step is to identify differences in the quantitative values between healthy and tumoral tissue. For this purpose, we focused on patients with brain tumors, acquiring images using a customized version of QRAPMASTER (MAGiC - **chapter 3**) and 3DQTI (**"Accelerated 3D whole-brain T1, T2, and proton density mapping: feasibility for clinical glioma MR imaging"** in Appendix-Publications) during the clinical protocol before injecting any contrast-agent.

In clinical routine, contrast media are administered to probe specific tissue properties, such as brain blood barrier leakage. In **chapter 3**, we evaluated if T1 and T2 values acquired prior to contrast admission could predict the regions that would enhance with contrast agent. Through receiver operating characteristic (ROC) and t-test analysis we showed that it is possible to differentiate the pre-contrast T1 and T2 values between tumoral tissue without T1-enhancement, tumoral tissue with T1-enhancement, and normal white matter. The accuracy of the classification should be improved, but these results encourage further exploration that could lead to

substituting some of the conventional sequences to shorten total acquisition time or even the possibility of avoiding contrast-agent injection. The possibility of avoiding contrast-agent injections in MRI could be very relevant, not only because of the elimination of the burden and possible risk for the patients, but also in developing countries where the contrast-agent is not always available.

Although more research is needed with larger cohorts and different pathologies than those used in this thesis, these fast quantitative MR techniques showed good repeatability and sensitivity to disease.

Furthermore, in this thesis, we showed two technical innovations. First, in **chapter 4** we showed the feasibility and repeatability of a multi-component analysis in highly undersampled MRF in-vivo data. We successfully obtained white matter, gray matter, CSF, and myelin water fraction maps. Further investigation on the accuracy of the in-vivo segmentation is needed, but the results of the Sparsity Promoting Iterative Joint Non-negative least squares algorithm applied to MRF data (SPIJN-MRF) were promising regarding parameter estimation and tissue-fraction maps segmentation.

The second innovation, presented in **chapter 5**, was a completely new approach and sequence for fast multi-parametric quantitative MR. We called this new sequence "Multiphase balance non Steady State Free Precession" (MP-b-nSSFP). We described analytically the transient-response of a repetitive sequence and used this to obtain intrinsic (PD, T1, T2) and extrinsic (B0, B1+) parameters with one acquisition. An optimized block of 4 pulses (30^o, 175^o, 30^o, 175^o) with phases 0^o, 90^o, 90^o and 0^o was repeatedly applied to complete a total of 100 pulses. The signal acquired during this train of pulses was used to estimate the intrinsic and extrinsic parameters. The results were accurate in phantom but it showed substantial underestimation of the T1 values for the in-vivo experiment. This could be due to different effects, such as magnetization transfer. To further validate this sequence, more experiments assessing the accuracy and the reproducibility should be carried out. Also, the sequence is still under investigation and the next steps are towards accelerated 3D acquisition.

In conclusion, the development of fast multi-parametric quantitative techniques improved the practical applicability of quantitative measurements, and with further investigation, they could be an improved tool over the conventional weighted MR images used in clinical imaging. This improvement in clinical routine could be the reduction of acquisition time of some standard scanning sessions by replacing several sequences with just one fast multi-parametric quantitative sequence, the possibility of depicting more substructures, or the amelioration of postprocessing pipelines, for example, avoiding registration (since all the images could be acquired with one single sequence).

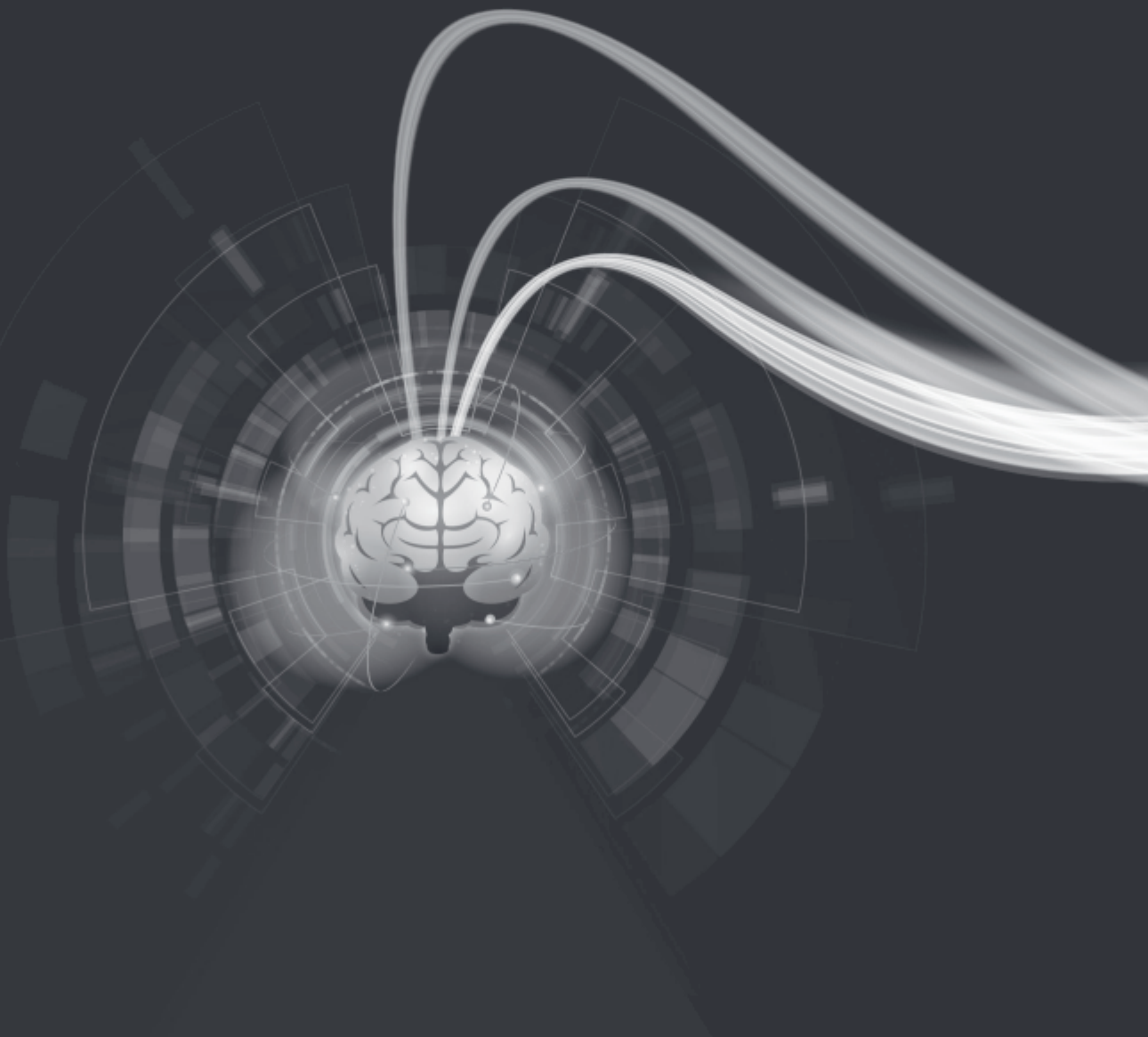

SAMENVATTING

Magnetic Resonance (MR) technologie is continu in ontwikkeling. Een deel van het huidige onderzoek richt zich op kwantitatieve metingen van intrinsieke weefsel eigenschappen, namelijk proton density (PD), T1 en T2. Kwantitatieve metingen zouden inter-sessie en inter-systeem variabiliteit kunnen verminderen en longitudinaal onderzoek kunnen vereenvoudigen. Echter was, tot de recente ontwikkeling van snelle multi-parametrische sequenties zoals MR Fingerprinting (MRF) of QRAPMASTER, de toepasbaarheid van kwantitatieve metingen beperkt vanwege de lange acquisitie tijd die nodig was.

Het doel van dit proefschrift is om inzicht te verkrijgen in kwantitatieve MR technieken en ze dichterbij de klinische praktijk te brengen. Als eerste stap, evalueerden we de nauwkeurigheid en herhaalbaarheid van QRAPMASTER en MRF-vFA. Dit wordt verkend in **hoofdstuk 2** met één fantoom en 5 vrijwilligers. Deze technieken toonden een goede herhaalbaarheid in zowel fantoom als in-vivo experimenten, maar QRAPMASTER bleek nauwkeuriger dan MRF-vFA. Echter, MRF-vFA heeft als voordeel dat het een snellere acquisitie heeft: 70s, wat 4.77 keer sneller is dan QRAPMASTER. Meer onderzoek is nodig om de bias van MRF-vFA te verminderen en resolutie te verbeteren, maar de snellere acquisitie positioneert MRF-vGA als goede kandidaat maken voor, ten minste, een exploratieve sequentie.

De positieve resultaten behaald in fantoom en gezonde vrijwilligers, bereidde ons voor op de volgende stap: het evalueren van deze technieken in patiënten. Het doel van deze tweede stap was om verschillen in de kwantitatieve waarden tussen gezond en tumor weefsel te identificeren. Voor dit doel, richten we ons op patiënten met hersentumoren die gescand werden met een aangepaste versie van QRAPMASTER (MAGiC **hoofdstuk 3**) and 3DQTI (**"Accelerated 3D whole-brain T1, T2, and proton density mapping: feasibility for clinical glioma MR imaging"** in Appendix-Publications)tijdens het klinisch protocol. Beide acquisities werden uitgevoerd voordat contrastmiddel werd toegediend aan de patiënten.

In de klinische praktijk wordt contrastmiddel toegediend om bepaalde weefsel eigenschappen te bestuderen, zoals bijvoorbeeld beschadiging van de hersen-bloed barrière. In **hoofdstuk 3** evalueerden we of T1 en T2 waarden, gemeten voordat contrast werd toegediend, konden voorspellen in welke gebieden contrastmiddel kon doordringen zodat deze oplichtten. Met de receiver operating characterisitc (ROC) en

t-test analyses toonden we aan dat het mogelijk was om onderscheid te maken tussen de T1 en T2 waarden van tumorweefsel zonder contrast-oplichting, tumorweefsel dat wel oplicht en normale witte stof. De nauwkeurigheid van de classificatie zou verbeterd moeten worden. Echter, deze resultaten motiveren verder onderzoek dat zou kunnen leiden tot het vervangen van sommige conventionele sequenties, om de totale acquisitie tijd te verminderen, of zelfs het vermijden van contrast-middel. Het vermijden van contrast-middel in MRI is relevant, niet alleen ter reductie van de last en risico voor patiënten, maar ook voor ontwikkelingslanden waar contrast-middel niet altijd beschikbaar is.

Hoewel er meer onderzoek nodig is met grotere cohorten en andere pathologieën dan die gebruikt in dit proefschrift, vertoonden deze snelle kwantitatieve MR-technieken een goede herhaalbaarheid en gevoeligheid voor ziekten.

Daarnaast toonden we twee technische innovaties in dit proefschrift. Ten eerste, in **hoofdstuk 4** hebben we de in-vivo haalbaarheid en herhaalbaarheid van multi-component analyse in sterk onderbemonsterde MRF acquisities laten zien. We hebben succesvol witte stof, grijze stof, CSF en myeline water fractie in kaart gebracht. Verder onderzoek naar de nauwkeurigheid van de in-vivo segmentatie is nodig, maar de resultaten van de Sparsity Promoting Iterative Joint Non-negative least squares algorithm toegepast op MRF data (SPIJN-MRF) waren veelbelovend met betrekking tot parameter schatting en de segmentatie van weefsel-fractie beelden.

De tweede innovatie, gepresenteerd in **hoofdstuk 5**, was een volledig nieuwe aanpak en sequentie voor snelle multi-parametrische kwantitatieve MR. We hebben deze nieuwe sequentie Multiphase balance non Steady State Free Precession (MP-b-nSSFP) genoemd. We hebben de opstartfase van een repetitieve sequentie analytisch beschreven en dit gebruikt om intrinsieke (PD, T1, T2) en extrinsieke (B0, B1+) parameters te verkrijgen met één sequentie. Een geoptimaliseerd blok van vier radiofrequente pulsen (30^o, 175^o, 30^o,175^o) met fases 0^o, 90^o, 90^o and 0^o werd herhaaldelijk toegepast tot een totaal van 100 pulsen. Het signaal dat tijdens deze trein van pulsen verkregen werd, werd gebruikt om de intrinsieke en extrinsieke parameters te schatten. De resultaten waren nauwkeurig in een fantoom, maar toonden substantiële onderschatting van de T1 waarden in-vivo. Dit zou het gevolg kunnen zijn van verschillende effecten, zoals de overdracht van magnetisatie. Om deze sequentie verder te valideren moeten meer experimenten gedaan worden waarmee de nauwkeurigheid en reproduceerbaarheid van de sequentie beoordeeld kan worden. De sequentie wordt op dit moment nog verder onderzocht en ontwikkeld, o.a. wordt er gewerkt aan vervolgstappen in de richting van versnelde 3D acquisitie.

Concluderend kunnen we zeggen dat het ontwikkelen van snelle multi-parametrische kwantitatieve technieken de praktische toepasbaarheid van

kwantitatieve metingen heeft verbeterd. Hoewel nog verder onderzoek nodig is zouden deze technieken beter kunnen zijn dan de conventionele gewogen MR beelden die momenteel gebruikt worden binnen de klinische beeldvorming. Deze verbetering kan bestaan uit het reduceren van de acquisitie tijd van een standaard scan sessie door het vervangen van meerdere sequenties door één snelle multi-parametrische kwantitatieve sequentie, of uit het weergeven van meer substructuren, of het verbeteren van post-processing pijplijnen door, bijvoorbeeld, registratie overbodig te maken aangezien alle beelden met één enkele sequentie opgenomen zijn.

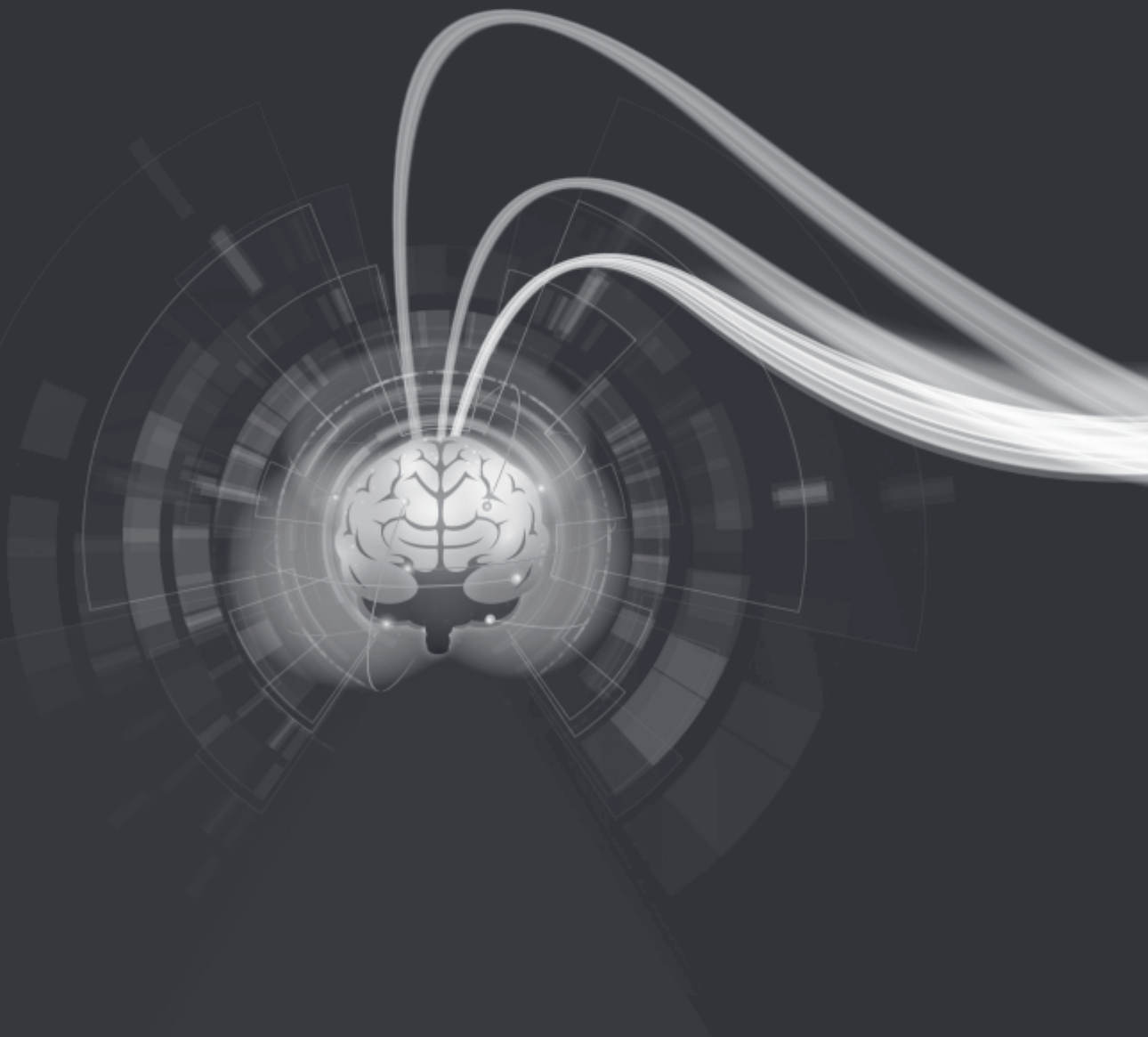

SUMARIO

La Resonancia Magnética es una tecnología que está en continuo desarrollo. Actualmente, un área en auge es la cuantificación de los parámetros intrínsecos a los tejidos, como la densidad protónica (PD), el T1 y el T2. Sustituir las imágenes ponderadas por imágenes con información cuantitativa de los tejidos eliminiraría la variabilidad entre sesiones y sistemas. Esto facilitaría, por ejemplo, los estudios longitudinales y grupales. Sin embargo, hasta la fecha, los largos tiempos de adquisición necesarios han dificultado la inclusión de imágenes cuantitativas, tanto en investigación como en clínica. Para solucionarlo, se han desarrollado técnicas rápidas multiparamétricas.

El objetivo de esta tesis es explorar estas técnicas cuantitativas y acercarlas a la rutina clínica. El primer paso consiste en evaluar la exactitud y precisión de técnicas que ya existen, QRAPMASTER y MRF-vFA. Esta evaluación es llevada a cabo en el **capítulo 2**, usando fantomas y 5 voluntarios. Aunque con QRAPMASTER se obtuvieron resultados más exactos, ambas técnicas demonstraron buena repetibilidad. A pesar de la necesidad de reducir el sesgo y mejorar la resolución de la imagen, MRF-vFA es una buena candidata para aplicarse en rutina clínica, al menos como secuencia para la pre-exploración, debido al escaso tiempo de acquisición necesario (70s, 4.77 veces más rápido que QRAPMASTER).

El siguiente paso, la evaluación de éstas técnicas en pacientes, está promovido por los buenos resultados obtenidos tanto en fantomas como en voluntarios sanos. El objetivo de esta fase de investigación es identificar diferencias en los valores cuantitativos obtenidos de tejido sano frente a los obtenidos en tejidos tumorales. Para ello, nos centramos en pacientes con tumores cerebrales y adquirimos imágnes usando una versión de QRAPMASTER adaptada a nuestros escáneres (MAGiC - **capítulo 3**) y 3D-QTI (**"Accelerated 3D whole-brain T1, T2, and proton density mapping: feasibility for clinical glioma MR imaging"** en Appendix-Publications). Estas adquisiciones fueron llevadas a cabo antes de la injección de contraste durante el protocolo clínico.

En rutina clínica, los medios de contraste son administrados para estudiar algunas propepiedades específicas de los tejidos, como rupturas en la barrera hematoencefálica. En el **capítulo 3**, investigamos si los valores cuantitativos de T1 y T2 acquiridos antes de la administración del contraste pueden predecir qué regiones se realzarían usando el contraste. Usando curvas características operativas del receptor

(ROC) y t-test análisis, se demuestra que es posible diferenciar los valores T1 y T2 (adquiridos antes de administrar contraste) de los tejidos sanos de materia blanca, los tejidos tumorales sensibles a la aplicación de contraste y los tejidos tumorales que no muestran realce tras la injección de contraste. Aunque los resultados de la clasificación usando el umbral de corte óptimo estimado deben ser mejorados, los resultados obtenidos incetivan a seguir investigando en torno a la differenciación de tejidos usando valores cuantitativos sin aplicar contraste. Futuras investigaciones podrían resultar en la redución del tiempo de adquisición necesario, sustituyendo algunas de las secuencias convencionales por MAGiC o, incluso, la posibilidad de evitar administrar medios de contraste. Esto último tendría un gran impacto, no sólo elminando las molestias y los posibles riesgos de los pacientes, sino también en países en vías de desarrollo dónde estas sustancias no están siempre disponibles.

Los resultados presentados en esta tesis muestran que estas técnicas rápidas de imágen cuantitativa son precisas y sensibles a los tejidos afectados por tumores. Sin embargo, para confirmar los resultados obtenidos, sería necesario ampliar esta investigación a un mayor número de pacientes y pacientes otras patologías.

Durante el desarrollo de este proyecto, además de investigar técnicas existentes, introducimos dos novedades técnicas. La primera, en el **capítulo 4**, demonstramos la viabilidad de extraer múltiples componentes en cada vóxel usando los datos acquiridos con MRF. Con este métodos obtuvimos segmentaciones de materia blanca, materia gris, líquido encefaloraquídeo y mielina. Aunque es necesario confirmar nuestros hallazgos con estudios más exhaustivos, los resultados usando el algoritmo 'Sparsity Promoting Iterative Joint Non-negative least squares' aplicado a datos de MRF (SPIJN-MRF) son muy prometedores en cuanto a la estimación de parámetros y segmentación de tejidos se refiere.

La segunda innovación introducida en esta tesis se reporta en el **capítulo 5**. En este caso, presentamos una secuencia nueva para obetner mapas cuantitativos multiparamétricos a la que denominamos Multiphase balance non Steady State Free Precession (MP-b-nSSFP). A través de la descripción analítica del estado transitorio de una secuencia repetitiva de pulsos obtenemos los parámetros intrínsecos (PD, T1, T2) y experimentales (B0, B1+) con una única adquisición. Utilizamos para ello un bloque de 4 pulsos (30^o, 175^o, 30^o, 175^o) con fases 0^o, 90^o, 90^o y 0^o que repetimos hasta completar 100 pulsos. La señal acquirida durante este tren de pulsos se usa para obtener los parámetros intrínsecos y experimentales. Los resultados fueron buenos en fantomas pero los valores de T1 fueron subestimados en los experimentos in-vivo. Esto podría ser consecuencia de differentes efectos, como transferencia de magnetización. Para validar esta secuencia, es necesario llevar a cabo más experimentos evaluando la exactitud y precisión de los valores cuantitativos obtenidos frente a otros métodos de referencia.

Además, seguimos desarrollando esta secuencia para implementar una adquisición en 3D acelerada.

En conclusión, el desarrollo de nuevas técnicas para adquirir imágenes cuantitativas rápidamente favorece su inclusión en investigación y en rutina clínica. Esto podría ser una mejora frente a las imágenes ponderadas, ya que una sóla acquisición podría sustituir varias de las secuencias estandar en los protocolos clínicos, se podrían caracterizar subestructuras dentro de un vóxel o mejorar el post-procesado (por ejemplo, evitando registrar imágenes al adquirirlas con una única secuencia).

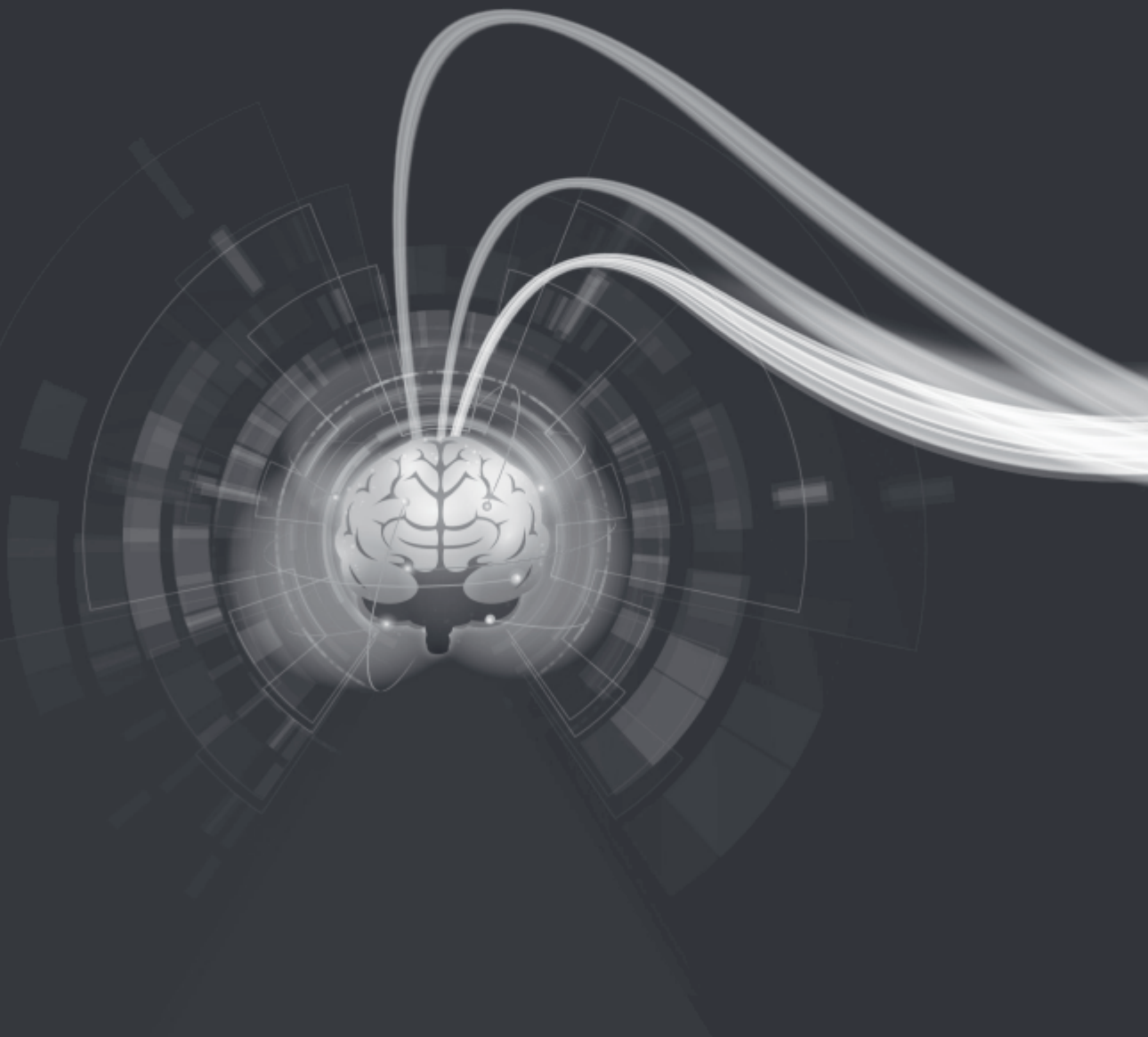

1

INTRODUCTION

1

Nuclear magnetic resonance (NMR) technology has been developed for more than 80 years [1]. The famous Bloch equation describing Nuclear Induction in 1946 [2], the reconstruction from projections using a rotating gradient published by Paul Lauterbur [3] and the reconstruction from Fourier by Mansfield and Granell [4] in 1973 are the foundations for the current Magnetic Resonance Imaging (MRI) techniques. However, its application in clinical diagnosis was considered only after Damadian showed in 1971 that cancer tumors and healthy tissue behave differently in an MR system [5]. In 1977, Damadian performed the first full body MRI-scan of a human being to diagnose cancer. Since then, MRI has experienced an impressive development and expansion, with the development of several sequences with different imaging purposes, the amelioration of the image quality, and becoming an essential tool in clinical imaging.

Nowadays, MRI is commonly used in clinical routine to detect and evaluate a wide range of diseases. The current protocols include several advanced techniques which provide weighted images of the tissues scanned. The signal intensity in each voxel image depends on the sequence of radio frequency (RF) pulses and the gradients of magnetic field that are played out and other intrinsic and external factors to the scanned object. We name 'intrinsic factors' to those related to the intrinsic properties of the tissues such as proton density (PD), the spin-lattice or longitudinal relaxation (T1), and the spin-spin or transverse relaxation (T2). The external factors would be related to the system, such as the strength of the main static magnetic field (B0) and its inhomogeneities, gradients, and system imperfections such as B1 inaccuracies. These external factors are an important source of variability in signal intensity across systems and sessions. This variability could hamper longitudinal and multi-site studies. In contrast, quantitative MR relaxometry (qMR) measures the actual intrinsic parameters of the tissue (T1, T2, and PD), and therefore qMR mitigates the influence of external factors on the final images. The capability of quantitative maps to distinguish and evaluate diseases such as multiple sclerosis, epilepsy, and dementia has been already shown [6].

The state of the art regarding qMR refers to inversion recovery [7], Carr-Purcell-Meiboom-Gill (CPGM) [8] and spin-echo [9] sequences as the gold standard for quantifying T1 and T2 values [10, 11]. However, to accurately retrieve T1 and T2 values using these sequences, long acquisition times are needed (> 30 minutes for the whole brain). Based on these sequences, DESPOT1 and DESPOT2 were proposed as an alternative for high-resolution T1 and T2 maps of the whole brain (voxel size 0.98 x 0.98 x 1.10 mm) within 16 min and 48 s [12].

The long acquisitions times prevented the extensive use of qMR in research and clinical environments. Some of the reasons for these long acquisition times are the waiting times between pulses or the waiting time until getting the steady-state to

acquire the images and the slow spatial encoding. The advantages of using the steady-state are the possibility of easily characterizing it mathematically and allowing several readouts with the same magnetization state for the spatial encoding. One readout consists in acquiring (reading) the transversal signal coming from the spins. These readouts are registered into a frequency-space, the so-called k-space, which is the Fourier Transform of the actual image [13]. The entire k-space is completed in several steps. In contrast, during the transient-response, the signal is oscillatory and complex because it is the evolution of the magnetization from the initial period of a sequence until the signal reaches the steady-state. These features hamper the image acquisition as well as the mathematical description. However, the transient-response would have the advantage of shortening acquisition times, since there is no need to wait until the steady-state is reached. Also, during the transient-response, the signal intensity can be higher as it decays towards the steady-state. Since the expected noise introduced by the system is similar than for the steady-state, the signal-to-noise ratio (SNR) would be higher.

In the past years, several new fast multi-parametric qMR techniques emerged avoiding the long acquisition times by either efficiently using the waiting times between pulses, as Quantification of Relaxation Times and Proton Density by Multi-Echo acquisition of a saturation-recovery using Turbo spin-Echo Readout[14] (QRAPMASTER), or by exploiting the advantages of the transient-response as MR Fingerprinting [15] (MRF). With these novel techniques, it is possible to obtain PD, T1, and T2 maps simultaneously of a whole brain in less than 6 minutes (2D acquisitions).

Quantification of Relaxation Times and Proton Density by Multi-Echo acquisition of a saturation-recovery using Turbo spin-Echo Readout - QRAPMASTER

QRAPMASTER retrieves the PD, T1, and T2 values of the tissue from the steady-state of the signal from a multi-echo acquisition of a saturation-recovery sequence with Turbo Spin-Echo (TSE) Readout [14]. The saturation pulse is applied prior to the acquisition to invert (partially) the magnetization across the longitudinal axis and to vanish the magnetization in the transversal plane by producing the maximal phase dispersion. When the acquisition sequence begins, the spins are relaxing from the inverted magnetization in the longitudinal axis and move towards the initial equilibrium (longitudinal magnetization).

After a saturation pulse, a variable delay (waiting time) is applied before the acquisition phase starts. The acquisition phase begins with an excitation 90 degrees pulse which is followed by multiple refocusing pulses of 180 obtaining a multi

1

spin-echo acquisition. To speed up the acquisition, QRAPMASTER acquires interleaved multi-slice. From the saturation pulse until the excitation pulse there is some 'death time' necessary only for the spins to relax towards the equilibrium, and this time-window is used to acquire (phase 2 in figure 1.1) another slice. Figure 1.1 shows a single block of the QRAPMASTER sequence and the readout gradients (measurements - Gm). Further acceleration is achieved by incorporating an echo-planar imaging (EPI) readout scheme where several k-space lines are acquired per each spin-echo (gradient spin-echo: GraSE).

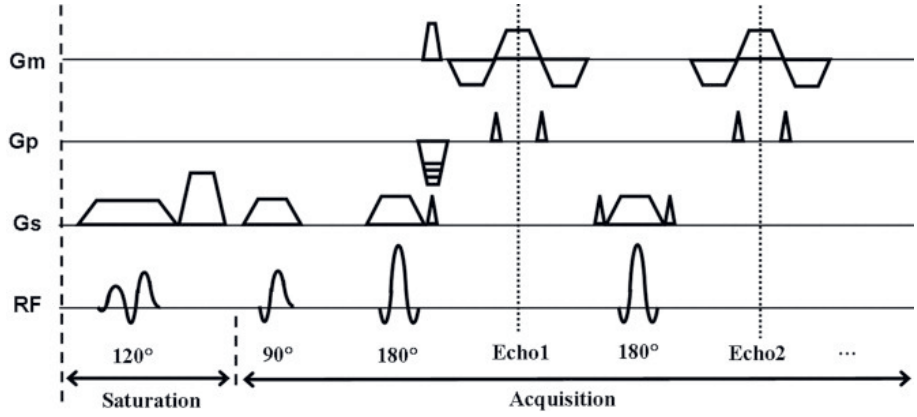

Figure 1.1: Schematic representation of a single block of the QRAPMASTER quantification sequence. Shown are the measurement (Gm), phase-encoding (Gp), and slice-selection (Gs) gradients and the RF pulse amplitude over time. There are two phases in each block. In phase 1 (saturation), the 120ř saturation pulse and subsequent spoiling acts on a slice m. In phase 2 (acquisition), the TSE acquisition is performed on slice n, using the 90ř excitation pulse and multiple 180ř refocusing pulses. The spin-echo acquisition is accelerated with an EPI readout scheme (GRaSE). Figure and caption from [14]. The x-axis represents the time. The dashed lines between the two phases indicate variable time between them.

T1 values are obtained by repeating for each slice the same procedure with different delay times after the saturation pulse. T2 values are obtained from the TSE readout. The T1 and T2 values are used to estimate the signal intensity at echo time zero and, hence, obtain the PD.

Once the quantitative values of the intrinsic parameters are calculated, the conventional contrast weighted images can be simulated (creating synthetic images) for any specified echo time (TE), repetition time (TR), and flip angle (FA) using the mathematical relations of the image intensity as a function of the quantitative PD, T1, and T2 values.

In this thesis, QRAPMASTER was used embedded in the commercial product Magnetic Resonance Image Compilation (MAGiC) marketed by General Electric

(General Electric Medical Systems, Waukesha, WI), which is a customized version of the package SyMRI IMAGE [16].

MAGNETIC RESONANCE FINGERPRINTING - MRF

MRF was published in 2013 [15] as a revolutionary concept in MRI. In contrast to previous existing sequences, MRF focuses on the transient response of the signal and avoids the stationary-state by randomizing the TRs and flip angles of a long sequence of pulses (1000 excitation pulses). After each excitation pulse, only one arm of the spiral readout is acquired and each of these readouts is considered a time-point of the entire signal evolution during the pulse sequence. At each time point, a rotated version of the same spiral arm is acquired. All this together provides 1000 images that have strong aliasing artifacts (due to the under-sampling) and together contain the signal evolution across the sequence. Figure 1.2 shows the sequence, the TRs, FAs, and readout trajectory.

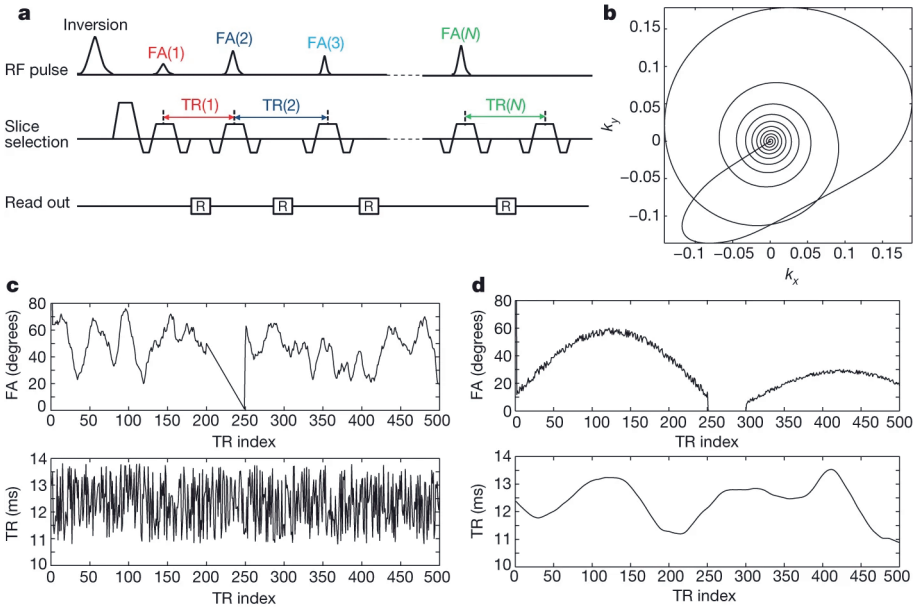

Figure 1.2: **a**, Acquisition sequence diagram. In each subsequent acquisition block, identified by a repetition time index (TR index; TR(1)...TR(N)), various sequence components are varied in a pseudorandom pattern. FA, flip angle. **b**, Here, one variable density spiral trajectory was used per repetition time. The Fourier coefficients sampled by the variable density spiral trajectory (given by the coordinates kx and ky) are rotated from one repetition time to the next. **c,d** Examples of the first 500 points of flip angle and repetition time patterns that were used in this study. Figure and caption from [15]

This signal evolution is different for every combination of T1 and T2 values which allows recovering the relaxation parameters by matching the signal evolution to a pre-computed dictionary using the extended phase graph formalism (EPG)[17].

MRF VARIABLE FLIP ANGLE

MRF variable flip angle only (MRF-vFA) follows the same principles of dictionary matching of MRF, but the sequence of excitation pulses is optimized and the randomization of the TRs and flip angles is not needed. Instead, MRF-vFA uses the same TR during all the acquisition and only varies the flip angle increasing from a very low FA (5 degrees) to a high FA (70 degrees) [18]. Aliasing-artefact-free images are obtained from each time point by applying compressed sensing to reconstruct the acquired k-space. This allows to obtain cleaner signals and more accurate matching to the dictionary entries than in the original MRF.

This scheme was investigated further and implemented in 3D resulting in quantitative transient-state imaging (3D-QTI) which also allows visualizing flow[19].

FAST QMRI EVALUATION AND CLINICAL PROSPECTIVE

Although qMRI has huge advantages in terms of acquisition time and information obtained, its accuracy and precision should be carefully evaluated [20, 21]. Previous studies have been studied the accuracy and precision of QRAPMASTER [22, 23] and MRF [24, 25] with promising results. In this thesis, we aimed to contribute to the validation of QRAPMASTER marketed as MAGiC and to assess the bias and repeatability of MRF-vFA. This is done for both techniques in **chapter 2**. In our opinion, these two techniques are the most interesting since QRAPMASTER is an efficient steady-state dictionary-free technique already accessible in clinical environments. And MRF-vFA, although it is newer, the possibility of acquiring the whole brain in 70 s, instead of the almost 6 minutes needed for QRAPMASTER or MRF, is a very attractive feature.

However, these techniques could be only considered for their inclusion in clinical routine after a thorough evaluation of their performance in patients. Some successful results are already reported using QRAPMASTER in children [23, 26, 27], patients with multiple sclerosis [28, 29], and patients with a brain tumor [30, 31]. Also, promising results in detecting pathology using QRAPMASTER were published in 2017 [32]. We intend to extend the existing knowledge by analyzing the quantitative values inside gliomas using QRAPMASTER in **chapter 3**.

MRF has been evaluated in clinical environments with limited results in distinguishing types of tumor [33], encouraging further investigation. This demonstrates that transient-state-based techniques could have clinical applicability,

which inspirited us to investigate another transient-state technique, 3D-QTI, in glioma patients. These results are published in Neuroradiology [34].

NEW DEVELOPMENTS

MULTICOMPONENT ANALYSIS

One of the limitations of the introduced techniques is the assumption of a single species in each voxel. However, rarely is the case that the tissue in one voxel has only one single species. One of the consequences of the multiple species within a voxel is the partial volume effect between tissue interfaces observed in weighted images. The partial volume effect is a well-known challenge for segmentation algorithms [35] that could hamper their reliability in applications that relate the volume of white and/or gray matter to disease stages[36–39]. Also, obtaining information about the mixture of components within the tissue, such as myelin water fraction of the white matter tissue [40–43], has been proven clinically relevant for white matter diseases such as Sturge-Weber syndrome [44] or Multiple Sclerosis [45]. Although MRF was used to depict multiple components within a voxel by Bayesian estimation for MRF [46], or by a reweighted-L1-norm regularized algorithm [47], they are limited by long computation times or the number of pre-defined tissues possible. Another solution for this problem is the Sparsity Promoting Iterative Joint NNLS (SPIJN) algorithm[48], which calculates component fraction maps in a few minutes without forcing them to a specific number of components. In **chapter 4** we apply this multi-component analysis to in-vivo data acquired with the MRF scheme [49] and assess the accuracy and repeatability of the method.

NEW TRANSIENT-STATE APPROACH

Most of the techniques and pulse sequences used in MRI study and analyze the steady-state signal. This implies the necessity of expending long acquisition times. Also, these techniques ignore the transient-state signal, which has high signal levels and plenty of information about the tissues and the system. Innovatively, MRF techniques have explored the transient state by using a dictionary to analyze the signal obtained. However, dictionary matching methods results are limited to the specific and discrete entries, and the computation complexity and the time required to estimate parameters increase with the number of entries and the number of parameters to estimate.

In **chapter 5** we exploit the transient-state without using a dictionary by mathematically describing the signal evolution. We propose a sequence composed of repetitive blocks whose signal evolution can be described by a discrete mathematical framework. This mathematical approach to Bloch equations was partially explored before [50–54] but without estimating any parameter quantitatively. Besides the

dictionary-free estimation of the parameters, this algebraic description allows a comprehensive understanding of the problem and an efficient design of the sequence. This new sequence, multi-phase balanced non-steady state free precession (MP-b-nSSFP), is capable of simultaneously obtaining intrinsic parameters such as T1, T2, and PD and experimental conditions such as the B0 and B1 fields.

AIM AND THESIS OUTLINE

This thesis aims to evaluate fast simultaneous multi-parametric quantitative MR imaging techniques and their application in brain tumor patients. This goal is pursued through different projects focusing on separate aspects. In this introduction chapter, the context of the thesis and background information was given.

In **chapter 2**, two fast quantitative MR techniques, QRAPMASTER and MRF-vFA, are assessed in phantom and healthy volunteers. Bias and repeatability are evaluated from data acquired the same week-day during 8 consecutive weeks. For this study, data was acquired from one phantom and five healthy volunteers.

In **chapter 3**, the quantitative values obtained with MAGiC in glioma are analyzed and compared to the quantitative values obtained in healthy tissue. By one single acquisition prior to the contrast-agent injection, we evaluate the capability to differentiate healthy tissue from tumoral tissue and to predict T1-enhancement.

In **chapter 4**, multi-component analysis is applied to MRF data to obtain fraction-tissue maps and its repeatability is evaluated in the MRF data obtained during the same scan sessions performed for **chapter 2**. The results are compared with two commonly used segmented software, FSL[55] and SPM[56].

In **chapter 5**, a new technique, called multi-phase balanced non-steady-state free precession (MP-b-nSSFP), for fast quantitative MR imaging is described. It is based on the transient-response (as MRF) but it relies on a mathematical framework to give more insight into the nature of the signal and to avoid the limitations of the dictionary-matching methods. This is a novel technique and it is patented under the number WO 2021/221501 [57] (See Appendix).

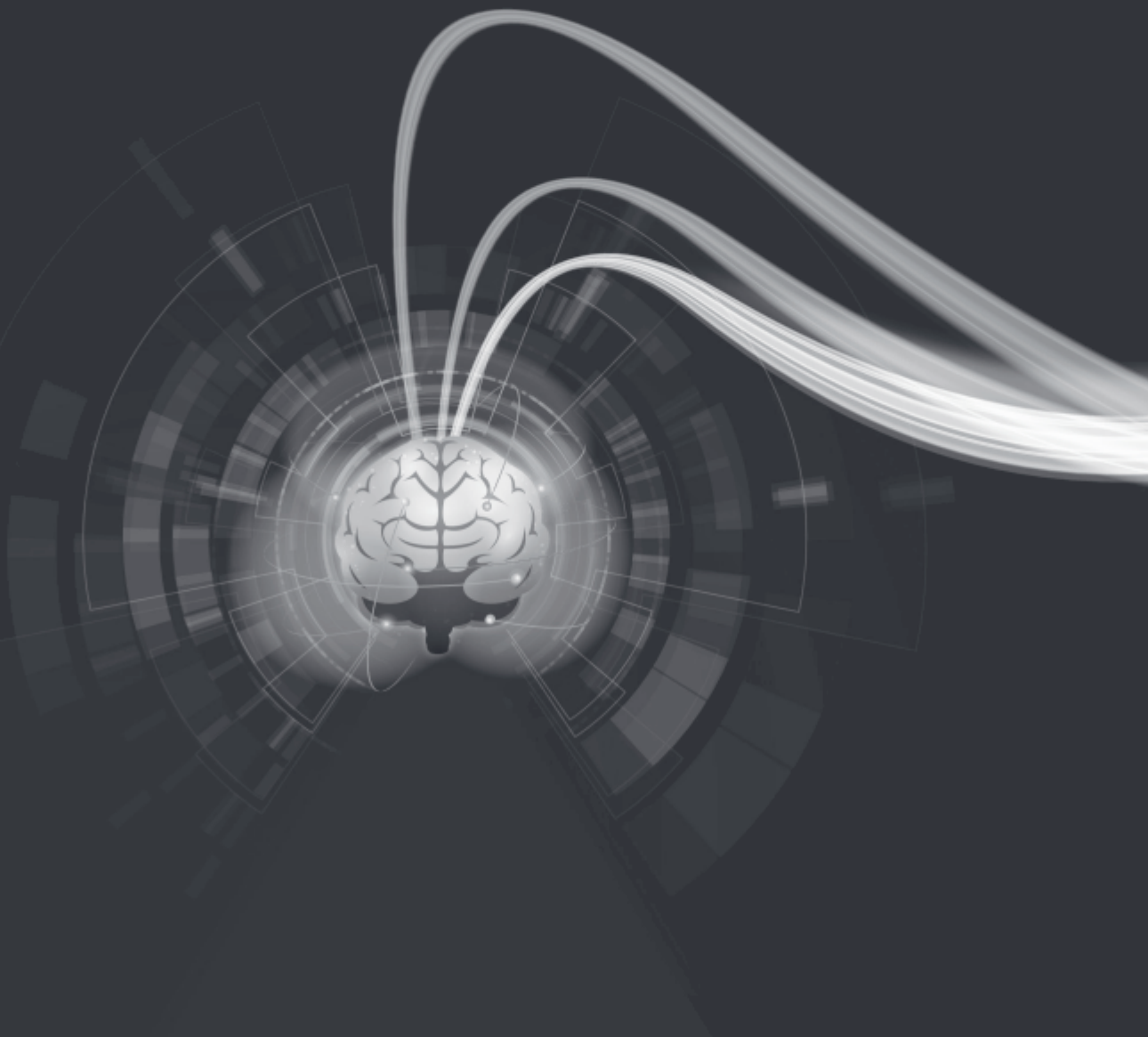

2

ACCURACY AND REPEATABILITY OF QRAPMASTER AND MRF-VFA

Laura NUÑEZ GONZALEZ[1], Gyula KOTEK[1], Pedro A. GÓMEZ[2], Guido BUONINCONTRI[3], Mika VOGEL[4],Gabriel P. KRESTIN[1], Dirk H.J. POOT[1], Juan A. HERNANDEZ-TAMAMES[1]

1 Department of Radiology and Nuclear Medicine, Erasmus Medical Center, Rotterdam, the Netherlands

2 Technische Universitĺat München, Computer Science, Munich, Germany

3 IMAGO7 Foundation, Pisa, Italy

4 General Electric, GE Healthcare, Hoevelaken, the Netherlands

This chapter has been published in Magnetic Resonance Imaging (2021);83:196207. https://doi.org/10.1016/j.mri.2021.09.004.

Abstract

Our purpose is to evaluate bias and repeatability of the quantitative MRI sequences QRAPMASTER, based on steady-state imaging, and variable Flip Angle MRF (MRF-VFA), based on the transient response.

Both techniques are assessed with a standardized phantom and five volunteers on 1.5 T and 3 T clinical scanners. All scans were repeated eight times in consecutive weeks.

In the phantom, the mean bias±95% confidence interval for T1 values with QRAPMASTER was 10±10% on 1.5T and 4±13% on 3.0T. The mean bias for T1 values with MRF-vFA was 21±17% on 1.5T and 9±9% on 3.0T. For T2 values the mean bias with QRAPMASTER was 12±3% on 1.5T and 23±1% on 3.0T. For T2 values the mean bias with MRF-vFA was 17±1% on 1.5T and 19±2% on 3.0T. QRAPMASTER estimated lower T1 and T2 values than MRF-vFA. Repeatability was good with low coefficients of variation (CoV). Mean CoV±95% confidence interval for T1 were 3.2±0.4% on 1.5T and 4.5±0.8% on 3.0T with QRAPMASTER and 2.7±0.2% on 1.5T and 2.5±0.2% on 3.0T with MRF-vFA. For T2 were 3.3±1.9% on 1.5T and 3.2±0.6% on 3.0T with QRAPMASTER and 2.0±0.4% on 1.5T and 5.7±1.0% on 3.0T with MRF-vFA.

The in-vivo T1 and T2 are in the range of values previously reported by other authors.

The in-vivo mean CoV±95% confidence interval in gray matter were for T1 1.7±0.2% using QRAPMASTER and 0.7±0.5% using MRF-vFA and for T2 were 0.9±0.4% using QRAPMASTER and 2.4±0.5% using MRF-vFA. In white matter were for T1 0.9±0.3% using QRAPMASTER and 1.3±1.1% using MRF-vFA and for T2 were 0.7±0.4% using QRAPMASTER and 2.4±0.4% using MRF-vFA. A GLM analysis showed that the variations in T1 and T2 mainly depend on the field strength and the subject, but not on the follow-up repetition in different days. This confirms the high repeatability of QRAPMASTER and MRF-vFA.

In summary, QRAPMASTER and MRF-vFA on both systems were highly repeatable with moderate accuracy, providing results comparable to standard references. While repeatability was similar for both methods, QRAPMASTER was more accurate. QRAPMASTER is a tested commercial product but MRF-vFA is 4.77 times faster, which would ease the inclusion of quantitative relaxometry.

Keywords: Quantitative MRI, MR Fingerprinting, MRF-vFA, QRAPMASTER, Repeatability, Accuracy

2.1. INTRODUCTION

Magnetic resonance imaging is widely used in clinical practice to detect and evaluate diseases. The signal level of each voxel depends not only on the nature of the tissue and the particular pulse sequence, but also on factors such as the strength of the main static magnetic field (B0) and its inhomogeneities, gradients and system imperfections such as B1 inaccuracies. All of these confounding factors could contribute to a potential high variability of the weighted images that traditionally are acquired in follow-up and multi-site studies. In contrast to weighted images, quantitative MR relaxometry tries to minimize such variability by measuring actual relaxometry parameters. Several clinical studies have shown the relationship between quantitative maps and diseases such as multiple sclerosis, epilepsy, and dementia [6, 33].

Despite of the advantages of quantitative MR relaxometry techniques and their potential capability to detect diseases, they are not yet routinely applied in clinical practice. There are two main reasons for this: long scanning time and concerns about the accuracy and repeatability of the quantifications. In fact, the long scan time has a negative impact on the clinical workflow. It hinders the incorporation of quantitative MRI into the clinical routine as well as adequate validation with fast conventional weighted imaging, such as SPGR, FIESTA, TSE/FSE, etc. To reduce the scan time, new fast quantitative multi-parametric imaging methods have been developed. Some of them based on steady-state pulse sequences, such as Quantification of Relaxation Times and Proton Density by Multi-Echo acquisition of a saturation-recovery using Turbo spin-Echo Readout (QRAPMASTER) [14] or PLANET [58]. Some others have been recently developed based on the transient response such as Magnetic Resonance Fingerprinting (MRF)[59], and MRF variable flip angle (MRF-vFA) [18]. Unlike other quantitative imaging methods that are commonly accepted such as DESPOT1 and DESPOT2 [12], those techniques obtain several quantitative maps within a single scan.

Despite the clear potential of these new techniques, to be used in research or clinical practice they have to demonstrate good accuracy and precision. The appropriate evaluation of the consistency of quantitative values is itself a challenge that requires evaluation of the bias and the repeatability [21]. Consistently with the metrology methods described in [21], clinically acceptable in-vivo bias and repeatability have been measured using QRAPMASTER [22, 23, 29, 32, 44, 60, 61]. Also, the bias and repeatability of the T1 and T2 quantification have been studied with other methods relying on the steady-state [12, 22, 62] and MRF [24, 25]. However, to our knowledge there are no studies extensively assessing the accuracy and precision of MRF-vFA.

The faster acquisition enabled by MRF-vFA (at least 3-fold faster) can make it a good

choice with minimum impact on the clinical workflow. However, MRF-vFA use can only be justified if its bias and repeatability are similar to those achieved by more standard techniques, like QRAPMASTER. In this work we compare bias and repeatability of MRF-vFA and QRAPMASTER with a test-retest study using a standardized phantom and healthy volunteers. To study the applicability for clinical workflow, both 1.5T and 3.0T clinical scanners are used.

2.2. METHODS

In this work we evaluated the accuracy and repeatability of two techniques using Bland-Altman plots [63], coefficients of variation (CoV)[24] and a General Linear Model (GLM) analysis [64]. Both techniques, QRAPMASTER and MRF-vFA, were provided by the systems vendor, General Electric Medical Systems. QRAPMASTER as a final product and MRF-vFA as research sequence.

2.2.1. DESCRIPTION OF THE TECHNIQUES

QRAPMASTER uses a multi-echo acquisition of a saturation-recovery sequence with Turbo Spin-Echo (TSE) Readout to obtain quantitative maps of T1, T2, and Proton Density (PD)[14]. For each slice a saturation pulse is applied and after some delay a series of excitation pulses of 90 degrees and refocusing pulses of 180 are played to obtain a multi spin-echo acquisition. This multi spin-echo acquisition allows quantifying the T2 values. By repeating the same sequence for the same slice with different delays the T1 values can be calculated. Finally, with the information of T1 and T2, the PD is calculated from the intensity at echo time zero. Once the quantitative maps have been obtained, T1 and T2 weighted images are synthesized from these maps. This sequence was acquired using Magnetic Resonance Image Compilation (MAGiC), which is a customized version of the package SyMRI IMAGE [16].

In contrast to QRAPMASTER, conventional MRF and MRF-vFA use a single rapid acquisition to retrieve a signal evolution that is sensitive to T1 and T2 during the transient response[59], not relying on steady-state models for parameter inference. Along the acquisition, the readout trajectory and some acquisition parameters such as repetition time (TR), echo time (TE) and pulse phase can be varied. Subsequently, the relaxation parameters are recovered by matching the signal evolution to a dictionary that, for many combinations of T1 and T2, can be pre-computed using the extended phase graph formalism (EPG) [18, 65].

In contrast to conventional MRF, MRF-vFA uses a constant TR and the flip angles are linearly increasing along the acquisition. Therefore, in the case of the MRF-vFA for each slice, first an inversion pulse is played out as in MRF. Then a series of excitation pulses

is applied with constant TR and TE. Additionally, the flip angle linearly increases from low flip angles (5 degrees) to high flip angles (70 degrees). After each excitation pulse, one arm from the spiral trajectory is acquired being rotated by a golden angle after each excitation pulse. Small flip angles after the inversion pulse allow capturing the recovery of the longitudinal magnetization for T1 estimation and the increase in the flip angle procure differentiation of the signal evolution for different T2 values. Furthermore, in order to improve estimations with a low number of TRs, MRF-vFA applies a compressed sensing reconstruction [18] to obtain unaliased images before parameter inference. The main advantage of using the MRF-vFA acquisition scheme [18] is that it allows at least 3 times reduction of the acquisition time compared to a zero-filled MRF reconstruction with the original MRF scheme [18].

2.2.2. ACQUISITION

The acquisitions for the Institutional Review Board-approved study were performed on two systems, a 1.5T GE MR450 and a 3.0T GE MR750 (General Electric Medical Systems, Waukesha, WI). In both systems, a 16 channel Head, Neck and Spine array coil was used.

For QRAPMASTER the acquisition parameters are given in table 2.1. The scan time to acquire 27 slices was 5 minutes and 34 seconds. MRF-vFA used 260 TRs with constant TR=10ms (Table 2.1). The flip angle was increased continually from 5 to 70 degrees as described in [18]. The scan time for 27 slices was 1 minute and 10 seconds.

Axial images from the NIST/ISMRM System Phantom [66] were acquired. To minimize temperature induced variations the phantom was kept in the scanner room of the 3.0T system. The temperature inside the 3.0T scanner room was measured to be between 22.6^{o}C and 22.9^{o}C. The temperature inside the 1.5T system room was measured to be between 22.5^{o}C and 23^{o}C.

A sampled size of 5 was calculated using G*Power [67] with a specificity of 95%, sensitivity of 90% and a correlation of 90% among repeated measurements, obtaining an statistical power of 0.92. This study design was approved by the Institutional Review Board. After providing informed consent, five healthy volunteers (3 females and 2 males, between 18-25 years) participated in the repeatability study. The READYBrain sequence [68] was used to align each quantitative MRI acquisition to the AC-PC plane. READYBrain automatically detects the AC-PC plane for each subject, facilitating the registration and the segmentation.

To assess the repeatability of QRAPMASTER and MRF-vFA the five volunteers and the phantom were scanned with the protocol mentioned above in both systems on the same week-day for 8 consecutive weeks.

Table 2.1: Acquisition parameters for QRAPMASTER and MRF-vFA for the phantom and the in-vivo (phantom/in-vivo when the parameter differs).

Technique	QRAPMASTER	MRF-vFA
Sequence type	2D Turbo Spin Echo	2D Spoiled Gradient Echo
Preparation	Saturation pulse	Inversion pulse
K-space trajectory	Cartesian, full k-space	Spiral, undersampled k-space
Orientation	Axial/AC-PC	Axial/AC-PC
FOV (cm)	31	31
Voxel size (mm Œ mm Œ mm)	1.2 Œ 1.2 Œ 5.0	1.2 Œ 1.2 Œ 5.0
Echo Train Length / # TRs	12	260
Flip Angle (degrees)	90	570
TR (ms)	4700/4400	10
Acquisition time (27 slices)	5 min 34 s	1 min 10 s

2.2.3. RECONSTRUCTION AND PARAMETER ESTIMATION

The data acquired with MRF-vFA were reconstructed using the non-uniform Fast Fourier algorithm [69] and temporal subspace reconstruction. The used solver is the alternating direction method of multipliers (ADMM) with 10 basis coefficients and regularized with local low rank regularization on spatiotemporal patches of dimension [8 x 8 x 10] [70].

For MRF-vFA, slice-profile imperfections were included in the dictionary generated with the extended phase graph formalism [65, 71]. We calculated a specific slice profile for each field strength. Therefore, separate dictionaries were created for the 1.5T and 3.0T systems. For both dictionaries, the range of T1 values was from 100 ms to 3000 ms with steps of 10 ms and the range of T2 values was from 10 ms to 1000 ms with steps of 5 ms. The selected T1 and T2 ranges were typical for brain tissue [10–12]. After the images were reconstructed, the signal evolution for each voxel was matched to the dictionary and the best match, i.e. the atom with the highest correlation, provided the estimate for the PD, T1 and T2 values.

In the case of QRAPMASTER, only synthetic T1-weighted, T2-weighted and FLAIR images provided by MAGiC could be exported with any repetition time (TR), echo time

(TE) and inversion time (TI). Images with different TR and TE where exported and used to obtain the PD, T1 and T2 maps.

The study of the PD, with T1 and T2, was performed only for in-vivo experiments and it was excluded from the phantom analysis.

2.2.4. DATA PREPARATION

Before the analysis, all the images were converted from DICOM (Digital Imaging and Communication On Medicine [72]) to NIfTI using the Statistic Parametric Mapping (SPM12) toolbox for MATLAB (Mathworks, Natick MA) [56].

For the phantom, a 2D plane through the center of the T2 contrast spheres was selected. We chose those spheres within the range supported by QRAPMASTER (T1 ≥ 300 ms and T2 ≤ 250 ms). A region of interest (ROI) was drawn for each one (Figure 2.1) and the average inside the ROIs was calculated. Perfect spatial alignment was assumed between maps acquired with different techniques in the same scan session. The T1-weighted image created with QRAPMASTER images from separate sessions were all rigidly co-registered [73] to the first scan session using SPM12 [56] allowing us to use the same ROIs for all the images.

For the in-vivo data, the pipeline was slightly different. First, co-registration within the same scan-session was needed to correct motion-induced misalignment of the images for both MRF-vFA and QRAPMASTER. For each session, all images were rigidly co-registered to a synthetic T1-weighted image created with QRAPMASTER. This T1-weighted image was also used to segment gray matter and white matter with SPM12 [56, 74]. Once the segmentation was completed, the results were applied to compute the mean values inside the gray and white matter of the quantitative maps within the same subject and scan-session. The mean values of all the subjects for gray matter and white matter were calculated for each technique, system, and scan-session (computed-tissue-values).

The last procedure applied to the in-vivo data was the creation of global maps using all the brain acquisitions. A T1-weighted template registered to the MNI (Montreal Neurological Institute) space [75], which defines a standard brain by using a large series of MRI scans on normal controls, was created using Diffeomorphic Anatomical Registration through Exponentiated Lie algebra (DARTEL) algorithm [76] with SPM12, including all the T1-weighted images created with QRAPMASTER in both scanners. The template generated was used to normalize the acquisitions to MNI space. It has been shown that diffeomorphic registration processing could bias the results [77–79] obtained in longitudinal studies because of the asymmetries of the non-linear interpolations applied. To reduce the impact of it, all the acquisitions were treated equally by creating a template with all the acquisitions (forward) and then aligning the

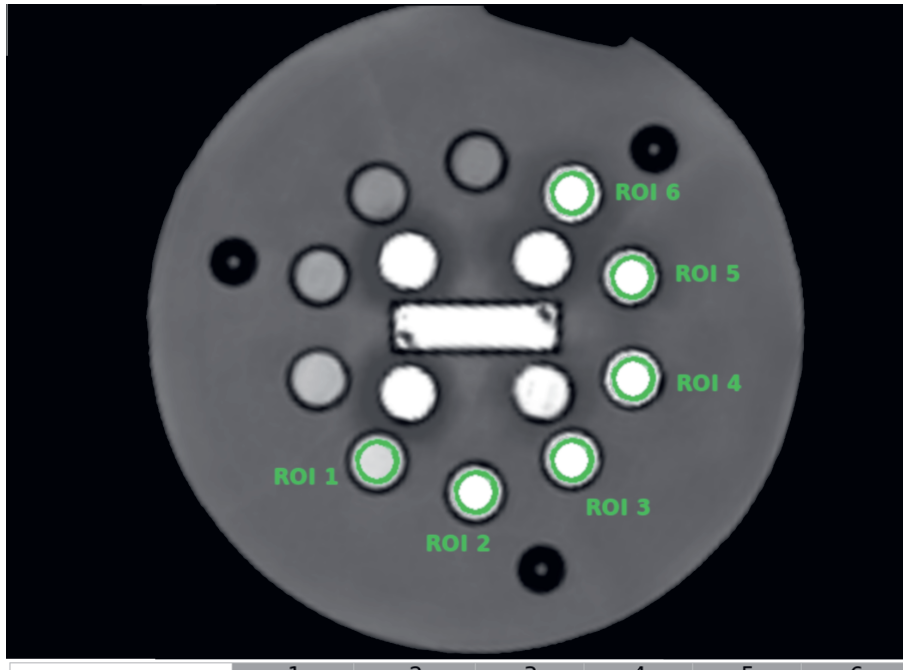

		1	2	3	4	5	6
1.5 T	T1 (ms)	1237.00 (0.40)	1030.00 (1.70)	752.20 (1.12)	550.20 (0.18)	413.40 (0.29)	292.90 (0.15)
	T2 (ms)	184.90 (0.110)	140.60 (0.050)	91.76 (0.029)	64.84 (0.029)	45.28 (0.029)	30.62 (0.014)
3.0 T	T1 (ms)	1332.00 (0.80)	1044.00 (3.20)	801.70 (1.70)	608.60 (1.03)	458.40 (0.33)	336.50 (0.18)
	T2 (ms)	133.27 (0.073)	96.89 (0.049)	64.07 (0.034)	46.42 (0.014)	31.97 (0.083)	22.56 (0.012)

Figure 2.1: Synthetic T1-weighted image of plate 4 of the NIST phantom. The ROIs are outlined in green and the nominal values for these ROIs are shown in the table. The standard deviation is reported in brackets.

acquisitions to this template (backward) [78]. The normalized acquisitions were used both to study the voxel-wise repeatability and as the input of for a GLM analysis as shown in the supplementary figure 2.9.

The relative proton density maps were self-normalized (nPD) to the average inside the brain mask in each case as in [25], in order to avoid variations due to coil sensitivity and scaling.

2.2.5. DATA ANALYSIS

PHANTOM

Accuracy of phantom acquisitions was assessed by comparing the ROI means to the nominal values as reported in the specifications manual [66]. The variation of the measurements reported by the manufacturer is negligible since they are in the order of 1ms or less except for the T1 value of the second ROI on 3.0T (standard deviation is 3.2 ms). The agreement between the ROI mean of each session and the nominal values was assessed through Bland-Altman plots [63]

To assess systematic differences in the estimated values using MRF-vFA and QRAPMASTER, we performed linear regression between their estimated ROI mean T1 and T2 values of the phantom. The linear regression was performed with Total Least Squares [80]. It provided the proportionality (slope) between the estimated values of MRF-vFA and QRAPMASTER as well as the offset (intercept). Additionally Pearsons coefficient of correlation (R-value) between the ROI mean T1 and T2 values of MRF-vFA and QRAPMASTER was calculated.

The repeatability was quantified with the coefficient of variation [24]:

$$CoV = \sigma / \mu \tag{2.1}$$

where is the standard deviation and μ is the mean of the averaged values within the ROIs over the 8 scan sessions and its 95% confidence interval of the CoV was calculated [81].

IN-VIVO

The accuracy was evaluated by comparison to the values reported by previous studies [11, 12, 16, 32, 82, 83]. The relative bias for each technique, was calculated using the median of the reported values using the inversion-recovery (T1) and CPGM (T2) standard relaxometry methods.

For each volunteer the in-vivo repeatability was assessed similarly as for the phantom, using the per session gray and white matter segmentation as the ROIs to evaluate. For each subject, the CoVs of gray and white matter were obtained from the average values over the segmented tissues. These CoVs were averaged over all the

subjects (averaged-tissue-CoVs). Separately, voxel-wise CoV maps were obtained in MNI space for each subject. These individual CoV maps were averaged over the volunteers into mean-CoV maps to study the dependence of the variability with the anatomy.

Besides the CoVs, a GLM analysis [64] was used to assess the repeatability of the quantitative maps nPD, T1 and T2 as in [25] using the implementation provided by SPM12 [56]. In our case, we modeled as binary covariates (bj) the subjects (1 to 5), the field strength (1.5T and 3.0T), and the week of acquisition (1 to 8). Supplementary figure 2.9 shows the design matrix that is used separately for each method and for each voxel of the nPD, T1 and T2 maps, normalized to MNI space.

The estimated bj maps from the GLM quantify the influence of the corresponding covariate on the nPD, T1 and T2 maps. To analyze how the covariates influence the variability among the quantitative maps, we calculated the average of the bj maps over tissue maps (normalize to the MNI space), while to take into account possible regional effects of variability; we extracted the bj maps for a representative slice.

2.3. RESULTS

2.3.1. PHANTOM

Figure 2.1 shows the selected slice of the phantom as well as the ROIs and their nominal T1 and T2 values with the standard deviation in brackets.

Figure 2.2 shows that the estimated T1 and T2 values for both techniques were within the limits of agreement respect to the reference values according to the Bland-Altman analysis. Table 2.2 shows the mean bias from the Bland-Altman analysis and the 95% limits of agreement. The bias was positive in all cases, including the null value only for T2 estimations on the 1.5T system and T1 estimations on the 3.0T system using QRAPMASTER, and T2 estimations on the 1.5T system using MRF-vFA. This means that the techniques are overestimating the values, as it can be seen in figure 2.2. Also, it can be appreciated that the mean bias with MRF-vFA was double than with QRAPMASTER for T1 values. However, for T2 values, the mean bias was high and similar for QRAPMASTER and MRF-vFA. In general, the spread for different days was similar across the values, except in the case of T2 values estimated on the 1.5T system, where lower T2 values had less dispersion. However, they had a higher bias than longer T2 values, which means a constant bias in milliseconds penalizing more the relative bias for smaller T2 values.

Table 2.2 and figure 2.3 show the results of the total least squares regression between the average ROI mean T1 and T2 values obtained by MRF-vFA and QRAPMASTER. The methods are strongly correlated (R-values > 0.99). The slopes for the T1 and T2 estimated

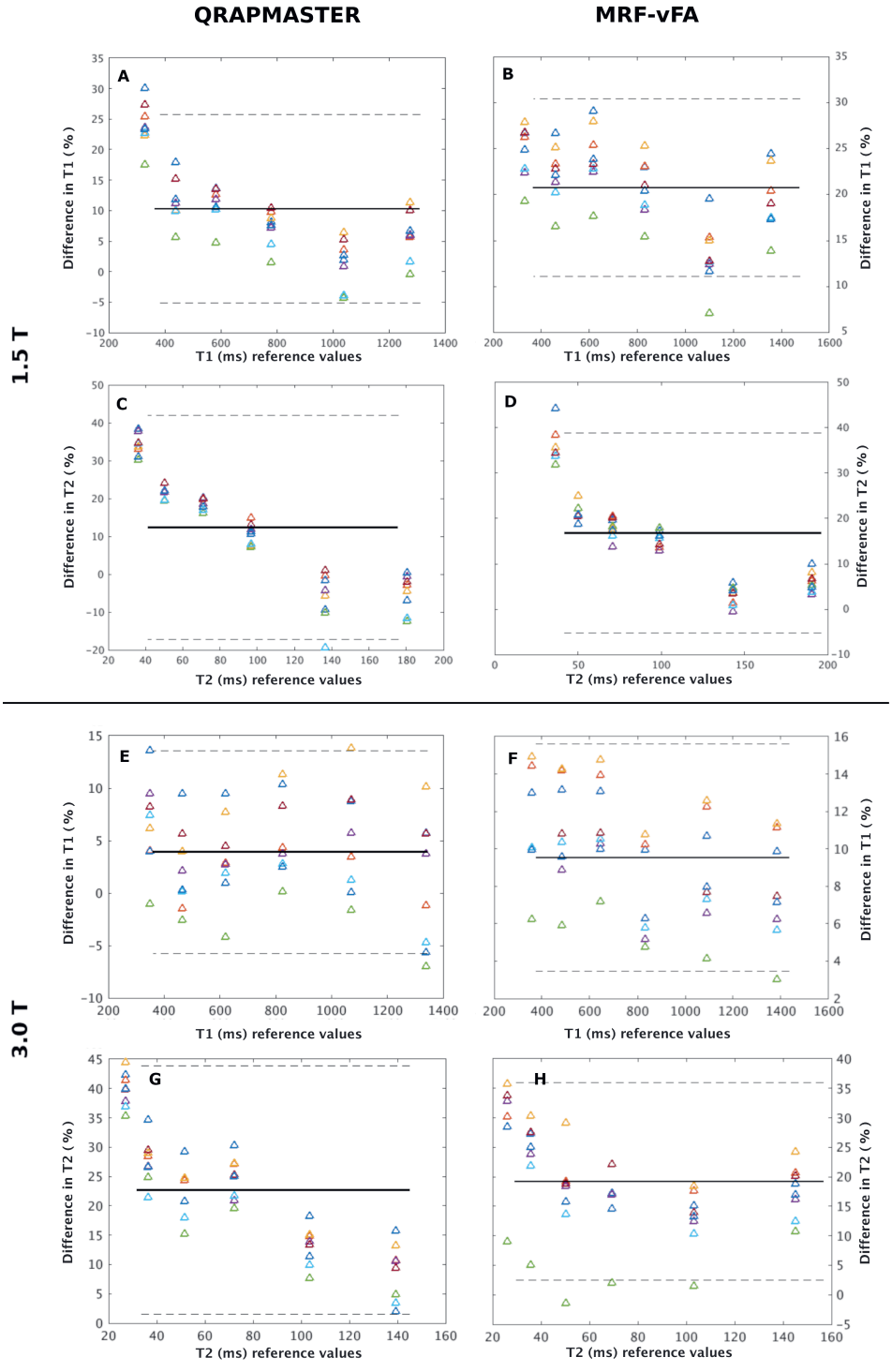

Figure 2.2: Bland-Altman plots showing the % difference between the estimated T1 (A, B, E, F) and T2 (C, D, G, H) values obtained on the 1.5T system (A, B, C, D) and the 3.0T (E, F, G, H) and the reference values from the NIST phantom by QRAPMASTER (A, C, E, G) and by MRF-vFA (B, D, F, H). The results are represented using different colors for each session. The black solid line marks the mean of the difference and the black dotted lines mark the mean ± 1.96* standard deviation of the difference.

Table 2.2: In the first two columns, the mean biases and the 95% limits of agreement (LOA) from the Bland-Altman analysis are reported for QRAPMASTER and MRF-vFA. Between brackets the 95% confidence interval of the bias and the LOA. In the following columns, the results of the linear regression between the estimated values with MRF-vFA and the values estimated with QRAPMASTER. The values of the slopes, intercept and correlation (R-value) resulted from the linear regression between both techniques are shown. The 95% confidence interval for the slope and the intercept is presented in brackets.

Field strength	Relaxation Parameter	Mean Bias (%) QRAPMASTER (95% CI) [95% LOA] (95% CI)	Mean Bias (%) MRF-vFA (95% CI) [95% LOA] (95% CI)	Slope TLS (95% CI)	Intercept (ms) TLS (95% CI)	R-value
1.5 T	T1	10.3 (±9.65) [-5.1, 25.7] (±3.9)	20.8 (±17.22) [11.1, 30.5] (±2.5)	1.157 (1.151, 1.164)	-36.298 (-41.749, -30.846)	0.999
	T2	12.4 (±3.09) [-17.2, 41.9] (±7.5)	16.8 (±1.11) [-5.3, 38.9] (±5.6)	1.164 (1.154, 1.173)	-9.529 (-10.554, -8.504)	0.999
3.0 T	T1	3.9 (±13.33) [-5.5, 13.6] (±2.4)	9.5 (±9.26) [3.5, 15.6] (±1.5)	1.051 (1.040, 1.062)	1.091 (-8.452, 10.634)	0.999
	T2	22.7 (±1.15) [1.5, 43.9] (±5.4)	19.2 (±2.04) [2.5, 35.9] (±4.2)	1.108 (1.090, 1.126)	-8.417 (-9.989, -6.846)	0.993

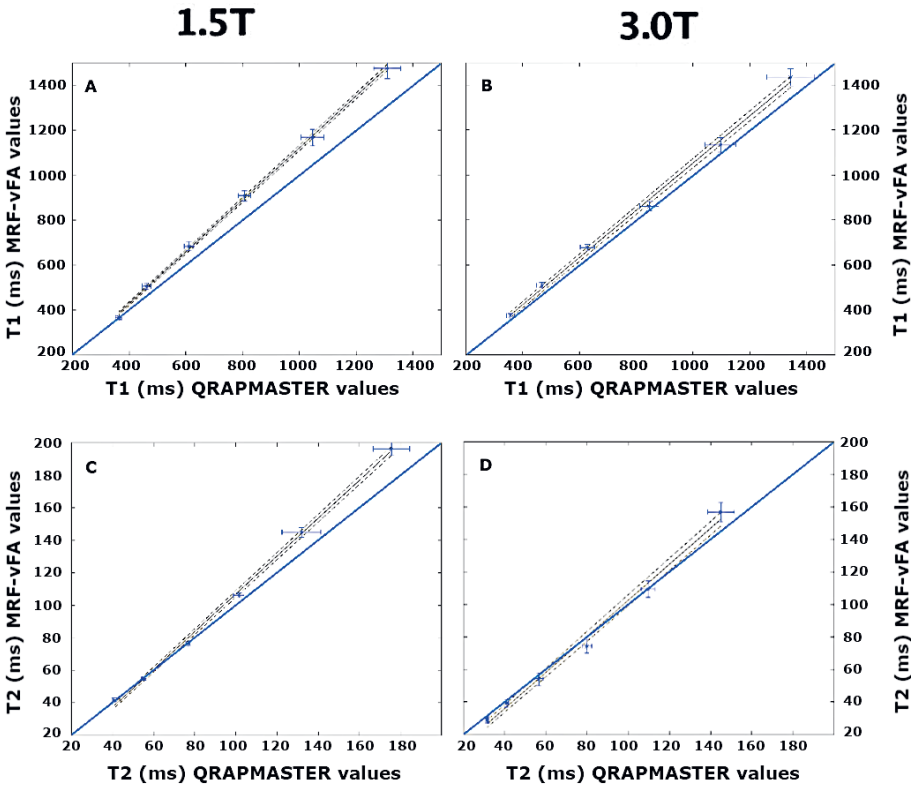

Figure 2.3: The estimated T1 (A, B) and T2 (C, D) values obtained from the NIST phantom by MRF-vFA against the values obtained by QRAPMASTER on the 1.5T system (A, C) and the 3.0T system (B, D). Vertical and horizontal lines mark the standard deviation for MRF-vFA and QRAPMASTER, respectively. A solid black line marks the fitted line. The dashed black lines mark the 95% confidence interval boundaries. The blue line is the identity line.

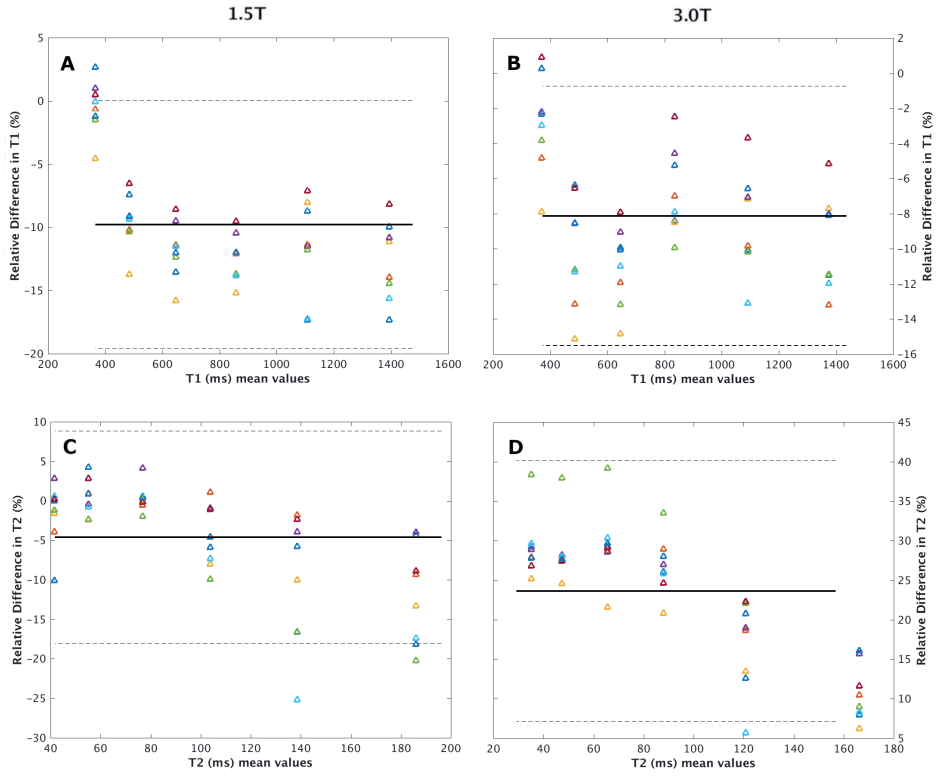

Figure 2.4: Bland-Altman plots showing the difference between the estimated values from the NIST phantom obtained by MRF-vFA and the values obtained by QRAPMASTER for T1(A, B) and T2 (C, D) over the 8 days on the 1.5T system (A, C) and the 3.0T system (B, D). The results are represented using different colors for each session. The black solid line marks the mean of the difference and the black dotted lines mark the mean ± 1.96* standard deviation of the difference.

values on the for both 1.5T system and on the 3.0T system were larger than one. This means that for MRF-vFA the spread in T1 and T2 values over the ROIs is larger than for QRAPMASTER. Consequently, the intercept is negative, except for the estimate T1 values on the 3.0T system where an intercept of zero is included within the 95% CI.

Figure 2.4 shows the Bland-Altman plots between MRF-vFA and QRAPMASTER. In general, the estimated values with MRF-vFA are within the limits of agreement comparing to QRAPMASTER. Only few sessions were outliers in which the estimated values of T1 were outside the limits of agreement on the 1.5T system and on the 3.0T system. In the case of the T2 values, only on the 1.5T system some values estimated with MRF-vFA fell outside the limits of agreement.

Figure 2.5 assesses the repeatability by showing the CoV of the ROI means. In all the

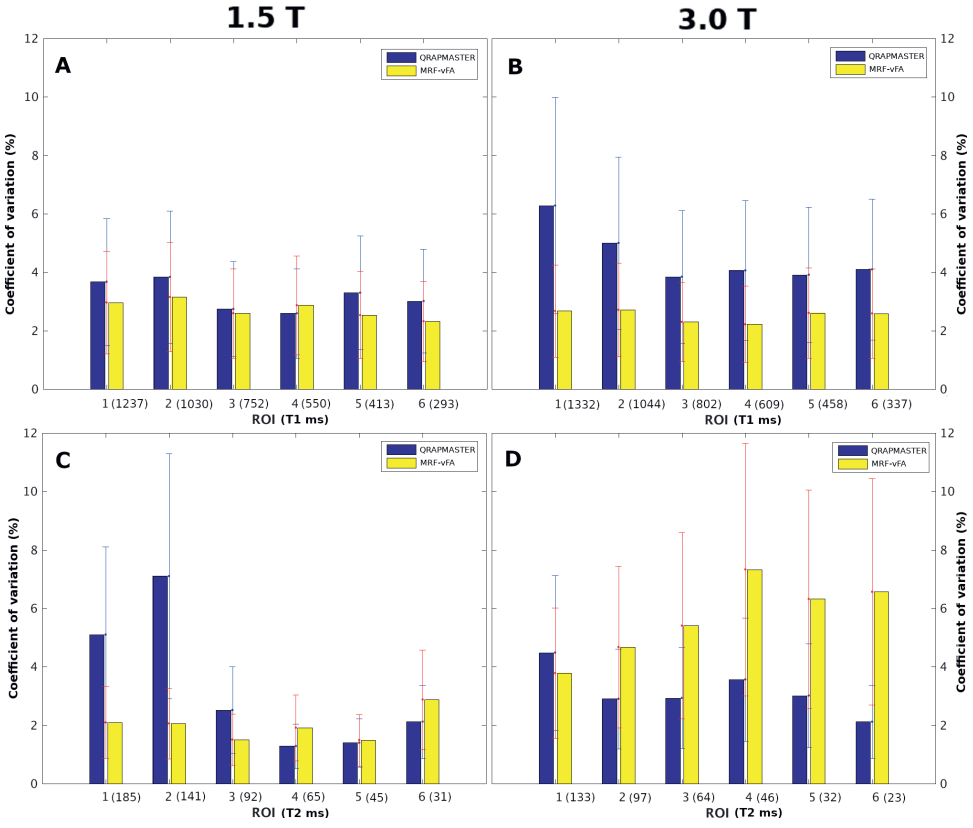

Figure 2.5: The coefficient of variation of T1 (top) and T2 (bottom) on a 1.5T system (left) and on a 3.0T system (right) from the NIST phantom using QRAPMASTER (blue) and MRF-vFA (yellow). Vertical lines show the 95% confidence intervals in blue (QRAPMASTER) and red (MRF-vFA). The ROIs are shown in figure 1. Horizontal axis labels show ROI numbers and corresponding T1 values (A, B) and T2 values (B, D) are in brackets.

Table 2.3: Estimated relaxation parameters from in-vivo data. Averaged computed-tissue-values over 8 sessions and its standard deviation in brackets.

	Relaxation	1.5 T		3.0 T	
Tissue	**Parameter**	**QRAPMASTER**	**MRF-vFA**	**QRAPMASTER**	**MRF-vFA**
Gray Matter	T1 (ms)	1057 (± 28)	964 (± 17)	1279 (± 31)	1156 (± 18)
	T2 (ms)	96 (± 2)	80 (± 2)	89 (± 2)	88 (± 3)
	nPD (au)	1.07 (± 0.011)	0.99 (± 0.012)	1.08 (± 0.014)	0.97 (± 0.014)
White Matter	T1 (ms)	501 (± 15)	699 (± 25)	621 (± 27)	798 (± 25)
	T2 (ms)	83 (± 2)	61 (± 2)	77 (± 2)	59 (± 2)
	nPD (au)	0.83 (± 0.016)	0.97 (± 0.016)	0.81 (± 0.013)	0.97 (± 0.016)

cases, the CoV was less than 8%. Note that the CoV is smaller than the bias, especially for T2 values on the 3.0T system, which present high bias but had low CoVs. Also, both techniques showed higher CoVs on the 3.0T system than on the 1.5T system. However, the performance of QRAPMASTER and MRF-vFA was different depending on the relaxation parameter (T1 or T2) and the system.

On the 3.0T system QRAPMASTER was more variable for T1 while MRF-vFA was more variable for T2 (the CoVs were 1% to 4% higher for the same ROIs).

On 1.5T, QRAPMASTER showed CoVs 1% higher for longer T1s (T1 > 1000 ms) and CoVs 2 to 3 times higher in the case of long T2 values (T2 > 100 ms). In contrast to the results on 3.0T, the CoVs for the estimated T1 and T2 values using MRF-vFA were similar.

On both systems, the variability of QRAPMASTER was more dependent on the T1s and T2s in the phantom than MRF-vFA, since the CoV was higher for longer T1 and T2 values (T1 > 1000 ms and T2 > 100 ms, ROI 1 and 2).

2.3.2. IN-VIVO

The quantitative T1 and T2 maps provided by both techniques showed a good contrast (Figure 2.6). However, QRAPMASTER showed T1 maps with higher contrast between gray and white matter than MRF-vFA, while MRF-vFA showed T2 maps with higher contrast than QRAPMASTER. This can be observed in multiple slices of the supplementary figures S4-S15. Also these differences in the contrast are present in the synthetic images created from the PD, T1 and T2 maps, as in the example showed in supplementary figures 2.24 and 2.25.

Table 2.3 shows the average value and the standard deviation of the computed-tissue-values of the gray and white matter over the 8 sessions. In all the cases, the estimated T1 and T2 values were in the range of the values reported in

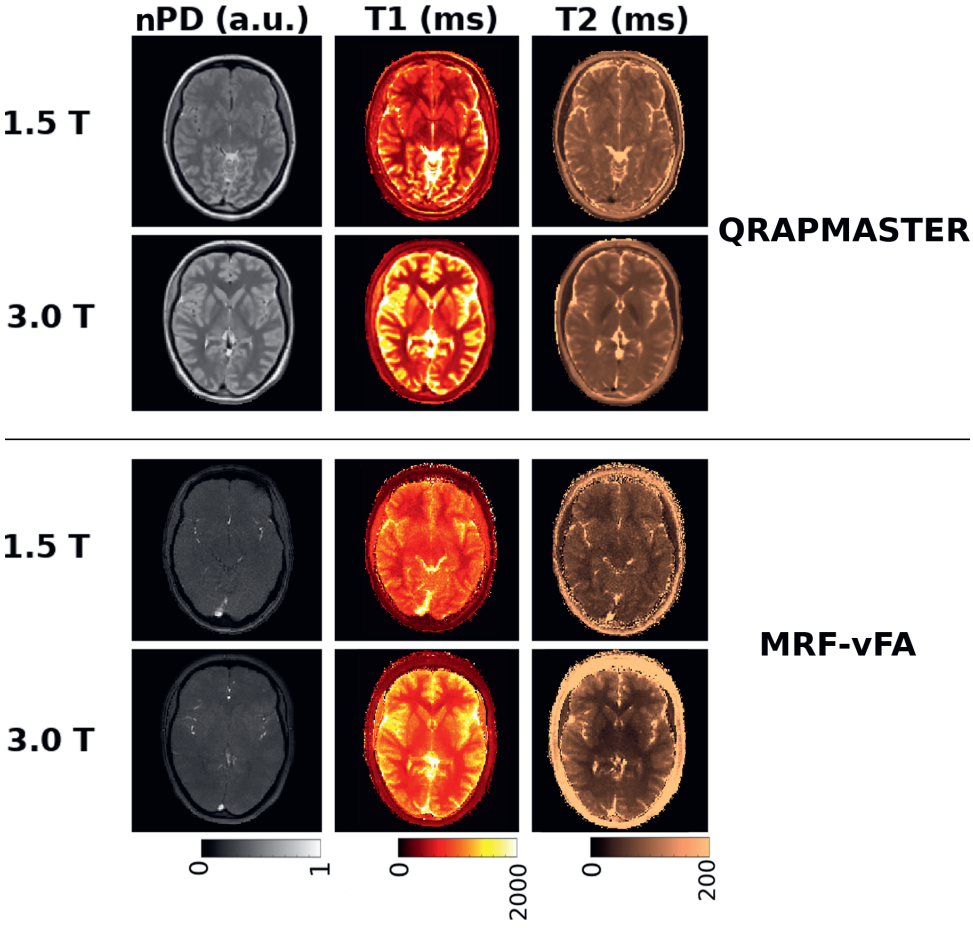

Figure 2.6: Quantitative PD (left), T1 (middle), and T2 (right) maps from a single subject obtained by QRAPMASTER (top) and MRF-vFA (bottom) on a 1.5 T system (odd rows) and on a 3.0 T system (even rows).

previous studies. The average T1 value in gray matter was lower for MRF-vFA than for QRAPMASTER, while in the case of white matter, QRAPMASTER produced lower T1 values than with MRF-vFA. In the case of T2, QRAPMASTER estimated larger values for gray and white matter than MRF-vFA. Regarding nPD, we saw that the ratio between gray and white matter is higher for QRAPMASTER than for MRF-vFA. While QRAPMASTER estimated around 30% higher nPD for gray matter than for white matter, for MRF-vFA the difference in estimated nPD for gray and white matter was smaller than 2%.

Table 2.4 reports the median values found in literature and the bias of the averaged values for QRAPMASTER and MRF-vFA to these values. In contrast to the phantom results, the bias was higher on the 3.0T system. Despite QRAPMASTER had lower bias than MRF-vFA in the phantom experiment, in gray matter the bias of QRAPMASTER was larger than that of MRF-vFA, except when estimating T1 values on the 3.0T system. Futhermore, the bias estimating T1 in white matter was higher using QRAPMASTER than MRF-vFA. Also, the T1 was underestimated in contrast to the positive bias found on the phantom, except for the gray matter using QRAPMASTER on the 1.5T system.

Figure 2.7 shows the averaged-tissue-CoVs (in percentage) on the 1.5T and the 3.0T system. All the CoVs were below 4%. On the 1.5T system (Figure 2.7-A), the CoV with QRAPMASTER were lower than with MRF-vFA, except for T1 estimated values in gray matter. On the 3.0T system (Figure 2.7-B), the CoVs for MRF-vFA were lower than for QRAPMASTER for T1 values, while for T2 values, QRAPMASTER had lower CoVs than MRF-vFA. Using QRAPMASTER, the CoVs were higher for T1 estimated values than for T2 estimated values, on both systems. In contrast, using MRF-vFA the CoVs were higher for T2 estimated values than for T1 estimated values.

We observed similar range dependence for the QRAPMASTER in the CoVs for the in-vivo data (Figure 2.7) than in the phantom. The estimated T1 values for gray matter were above 1000 ms (Table 2.3) and the CoVs for gray matter are higher than for white matter on both systems.

Figure 2.8 shows the mean-CoV maps (in percentage). The mean-CoVs were similar on both systems, but they differed between the techniques as well as among relaxation parameters. QRAPMASTER showed a lower mean CoV for the nPD and T2 values than MRF-vFA, while the estimation of T1 values with QRAPMASTER had higher mean-CoVs than with MRF-vFA. We observed higher mean-CoV for the CSF and the skull area than in gray and white matter. In the rest of the brain, the mean-CoV was low and similar between different areas.

In supplementary figures 2.26 and 2.27 the CoVs maps for all the volunteers are shown using QRAPMASTER and MRF-vFA respectively. They present low intra-subject

Table 2.4: Median of the T1 and T2 values (range) for gray matter found in literature for inversion recovery and CPGM sequences. For QRAPMASTER and MRF-vFA the average bias over all the subjects in percentage to the median literature value and the 95% confidence interval of the calculated bias are reported.

		1.5 T			3.0 T		
		Median [30] [range]	**Bias(%) QRAPMASTER (95% CI)**	**Bias (%) MRF-vFA (95% CI)**	**Median[29] [range]**	**Bias(%) QRAPMASTER (95 % CI)**	**Bias (%) MRF-vFA (95% CI)**
Gray Matter	**T1 (ms)**	1008 [940-1162]	4.9 (2.9, 6.7)	-4.4 (-5.5, -3.2)	1460 [1165-1615]	-12.4 (-13.9, -10.9)	-20.8 (-21.7, -19.9)
	T2 (ms)	78 [71-92]	23.1 (21.3, 24.8)	2.6 (0.0, 5.1)	83 [80-86]	7.2 (5.6, 8.9)	5.7 (3.5, 8,5)
White Matter	**T1 (ms)**	687 [657-735]	-27.1 (-28.9, -25.6)	-2.6 (-1.9, 5.4)	867 [728-954]	-28.4 (-30.5, -26.21)	-8.0 (-9.9, -5.9)
	T2 (ms)	75 [69-78]	10.7 (8.8, 12.5)	-18.7 (-21.3, 16.1)	75 [72-78]	2.7 (0.8, 4.5)	-21.3 (-23.2, -19.5)

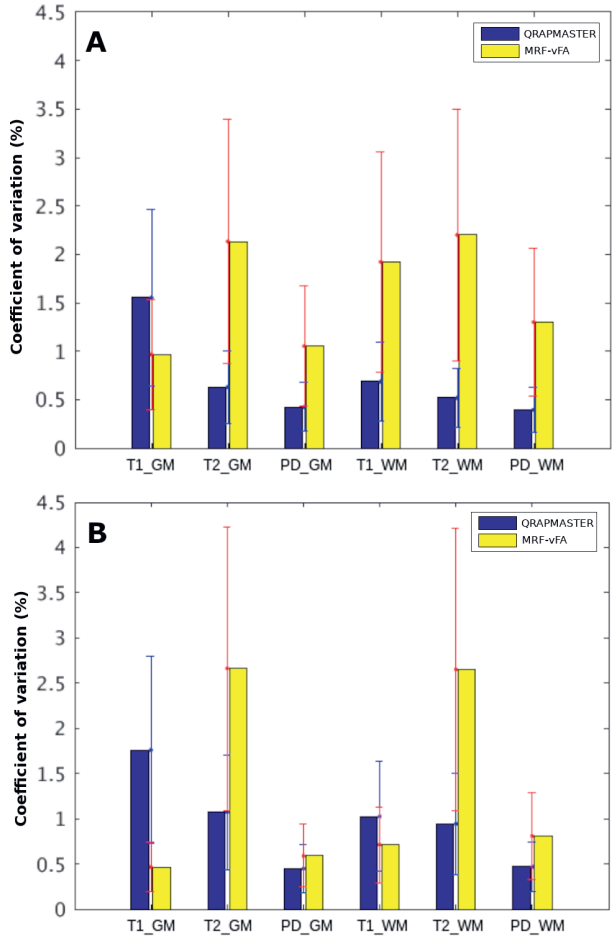

Figure 2.7: Graph showing the averaged-tissue-CoVs (in percentage) of the relaxation parameters in gray matter (T1_GM, T2_GM, PD_GM) and white matter (T1_WM, T2_WM, PD_WM) obtained by QRAPMASTER (blue) and MRF-vFA (yellow) on a 1.5 T system (A) and on a 3.0 T system (B) averaged over all subjects. Vertical lines show the 95% confidence intervals in blue (QRAPMASTER) and red (MRF-vFA).

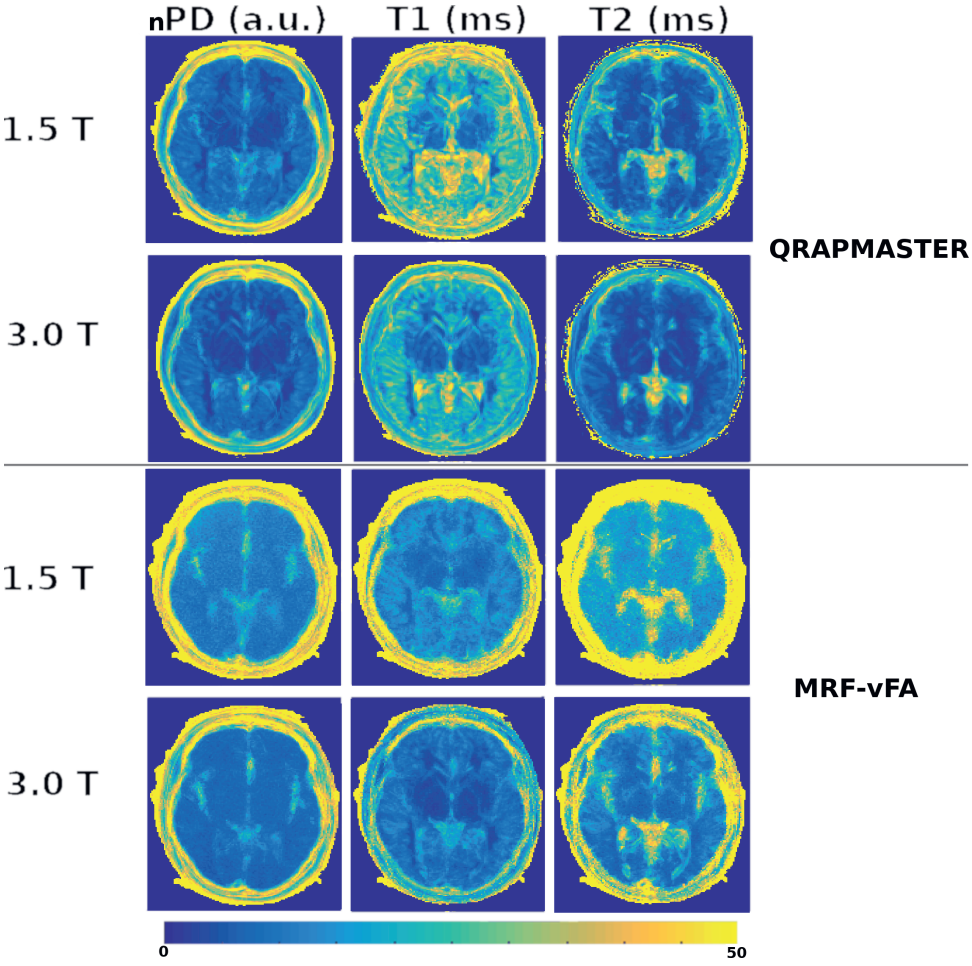

Figure 2.8: Maps of the coefficient of variation of nPD, T1, and T2 with QRAPMASTER and MRF-vFA on a 1.5T system and on a 3.0T system, averaged over all subjects.

variability in gray and white matter.

The results of the GLM analysis are shown in supplementary figures 2.10 and 2.11. Supplementary figure 2.10 shows the absolute value of the mean and the standard deviation of the estimated bj parameters over the gray matter, white matter and CSF for QRAPMASTER and MRF-vFA, respectively. In both cases, there was a deviation from the mean for T1 values in gray and white matter (> 10%) related to the field strength. T2 values were also influenced by the field strength but less (5%-10%). The nPD did not reflect the influence of the field strength. For the T1 and T2 estimated values, there was some variability between subjects (5%), especially for CSF. The different day of acquisition introduced very low variation (< 3%) for MRF-vFA and QRAPMASTER. Only Day1 and Day4 had higher bias for QRAPMASTER in CSF.

Supplementary figure 2.11 shows the bj maps associated with the covariance of the 1.5T system and 3.0T system. The GLM was designed with the parameters for the field strength being complementary (supplementary figure 2.9). We observed longer T1 values on the 3.0T system than in the 1.5T system. In the case of T2 values, MRF-vFA showed longer T2 estimated values on the 1.5T system than on the 3.0T system, while QRAPMASTER showed the longest T2 estimated values for the 3.0T system. The maps are quite uniform along all the brain using QRAPMASTER. Using MRF-vFA, we observed that only T1 map is uniform in all the brain. The nPD is more affected by the field strength from the left superior area to the center than in the rest of the brain. In the case of T2, the field strength seems to affect more the outer part of the brain than the inner part.

2.4. DISCUSSION

This work aimed to assess the accuracy and the repeatability of two novel techniques for fast quantitative imaging: QRAPMASTER and MRF-vFA. In this study, we used previously established methods [14, 18].

Both techniques showed accuracy and repeatability similar to results previously obtained with DESPOT1 and DESPOT2 [12]. However, QRAPMASTER and MRF-vFA are faster (3 and 14 times respectively) [14, 18].

Regarding accuracy, the Bland-Altman analysis on the phantom showed that all the estimated values were in good agreement. For QRAPMASTER the accuracy was assessed previously [16, 22, 32]. The total correlation analysis of the phantom, which assessed systematic differences between the methods, showed that the estimated T1 and T2 of the different ROIs differed more for MRF-vFA than QRAPMASTER. However, this should not limit the use of MRF-vFA since the Bland-Altman analysis showed good agreement between the estimated values of MRF-vFA and QRAPMASTER. Furthermore, bias could

be corrected either by adding a specific offset to the estimated quantitative values or by including related phenomena in the dictionary. For example, B1 could be included in the dictionary to reduce the T1 bias caused by B1 inhomogeneities [84]. In our work, we did not explore such possibilities to correct bias.

The repeatability in phantom is good for both methods. This allows reliable longitudinal measurements or population group comparisons since to detect changes along the time and/or differences between groups only low variability is needed, regardless of the bias.

The performance of the different techniques on the phantom demonstrated that QRAPMASTER is substantially more accurate since it had less bias. Regarding repeatability, there were some differences in the CoVs obtained with QRAPMASTER and with MRF-vFA depending on field strength and relaxation parameters. Similar to previous MRF (framework on which MRF-vFA is based) studies, MRF-vFA showed more variability for T2 values than for T1 values (in contrast to QRAPMASTER), likely because of its sensitivity to B0 inhomogeneities and intra-voxel incoherence [24, 85]. However, on average, we did not observe significant differences in repeatability between QRAPMASTER and MRF-VFA.

In the in-vivo data, no ground truth values are available. Although the phantom does notreflect all in-vivo phenomena, the performance in the phantom can give confidence in the in-vivo accuracy. This was the case for both techniques since the values for T1 and T2 values werein good concordance with other quantitative techniques [11, 12, 82]. Although there was some bias to the median literature values, a widespread in quantitative values, especially in T1, has been reported [84]. When looking in detail, the bias in the in-vivo data wassimilar to the bias in the phantom for the tubes with T1 and T2 values in the range of brain tissue. Quantitative T1 and T2 maps from both techniques hadgood contrast, allowing us to distinguish brain anatomy. The T2 estimated values for the brain with MRF-vFA compared to QRAPMASTER followed the trend expected from the phantom analysis, with a larger ratio between gray and white matter for MRF-vFA than QRAPMASTER. Consequently, MRF-vFAhadhigher contrast in the quantitative T2 maps. However, the estimated T1 values with MRF-vFA for gray matter weresmaller than the estimated for QRAPMASTER. From the linear regression, we would expect higher values than QRAPMASTER for gray matter. A plausible explanation could be the magnetization transfer effect [86, 87]. In a normal MRI experiment (on-resonance excitation of the free pool), the restricted pool is only partially excited and the protons are invisible to MRF due to the very short T2 (<0.1ms). The longitudinal relaxation (T1) is a consequence of the combination of the equilibrium between the two pools. However, if the restricted pool is saturated by off-resonance pulses, there is less longitudinal magnetization

available, and in consequence, this could cause an apparent T1 that is shorter than the T1 of the free water pool [49], especially when multiple inversion-recovery pulses are played out in multi-slice sequences [50]. In the case of MRF-vFA, each slice is acquired using an initial inversion recovery pulse which could induce a magnetization transfer effect in adjacent slices.

Another issue related to the variable flip-angle quantification methods are the deviations from the nominal B1 field [62, 84]. In QRAPMASTER B1 inhomogeneities are estimated and incorporated into the model to estimate T1, T2, and PD [14]. In MRF-vFA no B1 correction was applied and this could cause bias in the parameters. Including the B1 into the dictionary, as in [71] could potentially reduce this bias at the cost of increased dictionary size and compute times.

The repeatability obtained in the brain was high (CoVs< 4%) and within the same range as the CoVs reported in previous studies of quantitative imaging in-vivo [25, 83], with 9 and 10 subjects respectively. The low variability was present also voxel-wise and only CSF and skull area had high CoVs. Low variability in gray and white matter is very relevant since several studies focus on the relationship between disease and changes in gray and white matter relaxation parameters, as age-related changes in tissue [6, 27].

In addition to the CoVs, the GLM analysis showed that the variability in the estimated values was mainly due to the field strength, as we expected. Voxel-wise the field strength affected less homogeneously the estimations of MRF-vFA than the estimations of QRAPMASTER. MRF-vFA is based on gradient echoes instead of spin-echo as QRAPMASTER, therefore MRF-vFA is more sensitive to inhomogeneities in the magnetic field. Furthermore, MRF-vFA uses the transient response of the signal, instead of the steady-state as QRAPMASTER. This has the advantage of higher signal-to-noise but the disadvantage of being less stable and more sensitive to system imperfections [50, 51].

Our experience from this work suggests that accuracy is more challenging on the 1.5T system, while repeatability is more challenging on the 3.0T system. The reason could be that while accuracy benefits from higher SNR, higher field strength presents more inhomogeneities [83, 88]. It should be taken into account that, on the 1.5T system, the acquisition with MRF-vFA is more affected by noise, probably because of the highly undersampled data. The post-processing efficiency of these techniques was not evaluated in this study. QRAPMASTER was much faster (reconstruction online in about 1 minute for each acquisition) while MRF-vFA was reconstructed off-line and it took several hours per acquisition. The MRF-vFA reconstruction could be highly sped up by the use of GPUs instead of CPUs. Still, for many applications long post-processing times could be tolerated since the assessment of the images is done by a radiologist several hours or even days after the acquisition is performed.

One of the limitations of this study is that all the volunteers were healthy and in the same age range and may not be representative of aged or diseased tissue. Therefore, larger studies and studies for diseased groups should be carried out before reaching conclusions about the performance of QRAPMASTER and MRF-vFA in clinical environments.

Another limitation of this study is the use of systems of a single vendor which does not allow conclusions about reproducibility across vendors. The reproducibility and accuracy of the measurements can vary from one vendor to another due to different implementations [62, 66, 89].

2.5. CONCLUSIONS

Our work assessed the performance of two fast quantitative MR relaxometry acquisition techniques, QRAPMASTER and MRF-vFA, by evaluating accuracy and repeatability on two representative clinical systems at 1.5T and 3.0T. Our systematic study on a standardized phantom and on healthy brains showed that both techniques provide results comparable to previous studies. QRAPMASTER is already a tested commercial product but MRF-vFA is 4.77 times faster. MRF-vFA is accurate for the brain values range and repeatable enough to distinguish between tissues and appreciate changes on it. Therefore, it can be considered as a reliable alternative when acquisition duration is an important issue. Due to the good performance and short scan duration, MRF-vFA could enable the use of quantitative multi-parametric relaxometry mapping.

Future works should focus on the acquisition of patient data in order to evaluate the possible clinical impact of these techniques.

ACKNOWLEDGEMENTS

The authors gratefully acknowledge the support from Rolf F. Schulte providing and installing the pulse sequence.

This work was financed by a Research Grant from GE(B-GEHC-05).

AUTHORSHIP STATEMENT

All persons who meet authorship criteria are listed as authors, and all authors certify that they have participated sufficiently in the work to take public responsibility for the content, including participation in the concept, design, analysis, writing, or revision of the manuscript. Furthermore, each author certifies that this material or similar material has not been and will not be submitted to or published in any other publication before its appearance in the Magnetic Resonance Imaging Journal.

CONFLICTS OF INTEREST

The authors disclose that this project was partially funded by a Research Grant from GE (B-GEHC-05).

2.6. SUPPLEMENTARY MATERIAL

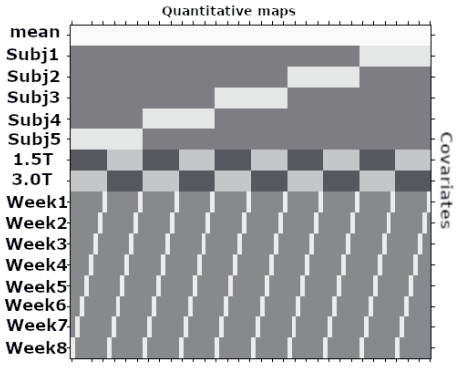

Figure 2.9: GLM design matrix. This design applies for each relaxation parameter map (PD, T1 and T2) and each technique separately. Each row represent a covariate and each column an specific single quantitative map.

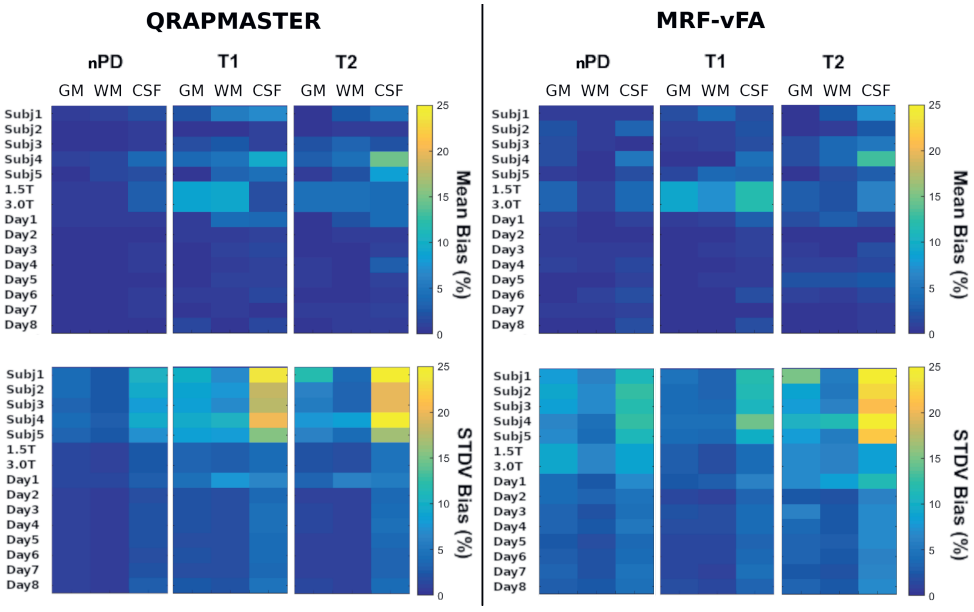

Figure 2.10: Result of the GLM analysis for QRAPMASTER and MRF-vFA and the relaxation parameters nPD, T1 and T2. The mean and the standard deviation of the estimated parameter is averaged over the segmented tissues (gray matter -GM-, white matter -WM- and cerebrospinal fluid -CSF-) and over the relaxation parameters (nPD, T1 and T2). The results are presented in percentage of the mean values estimated by the GLM.

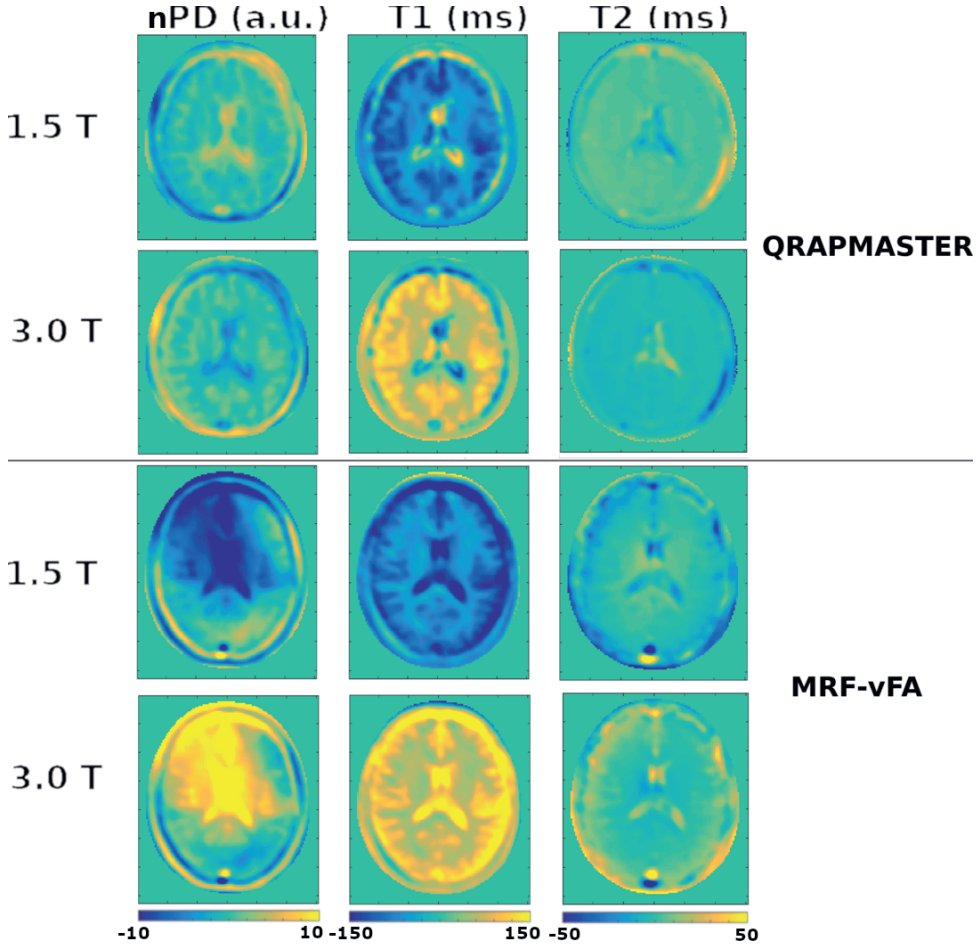

Figure 2.11: Maps of the estimated bias of the field strength resulted from the GLM analysis.

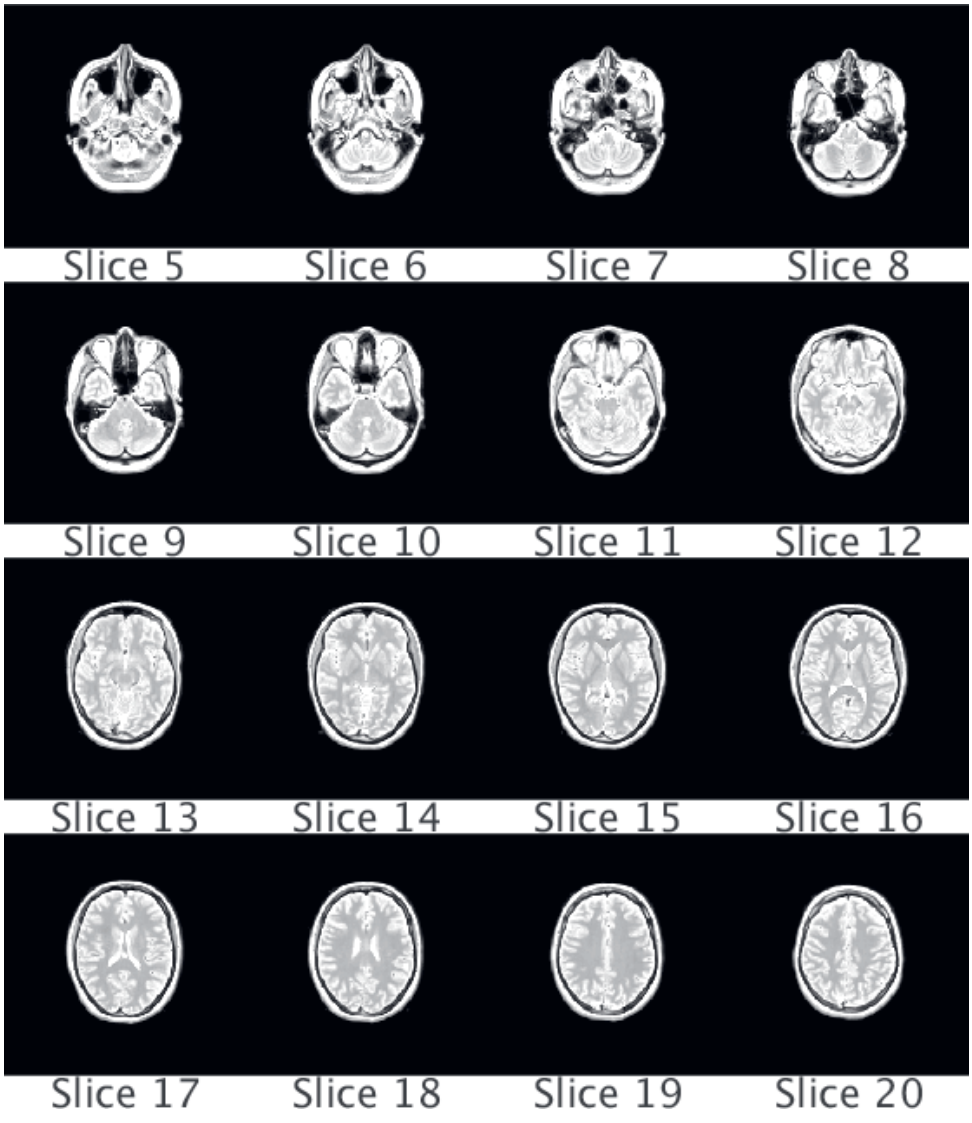

Figure 2.12: PD maps (a.u.) from a volunteer on the 1.5T system using QRAPMASTER.

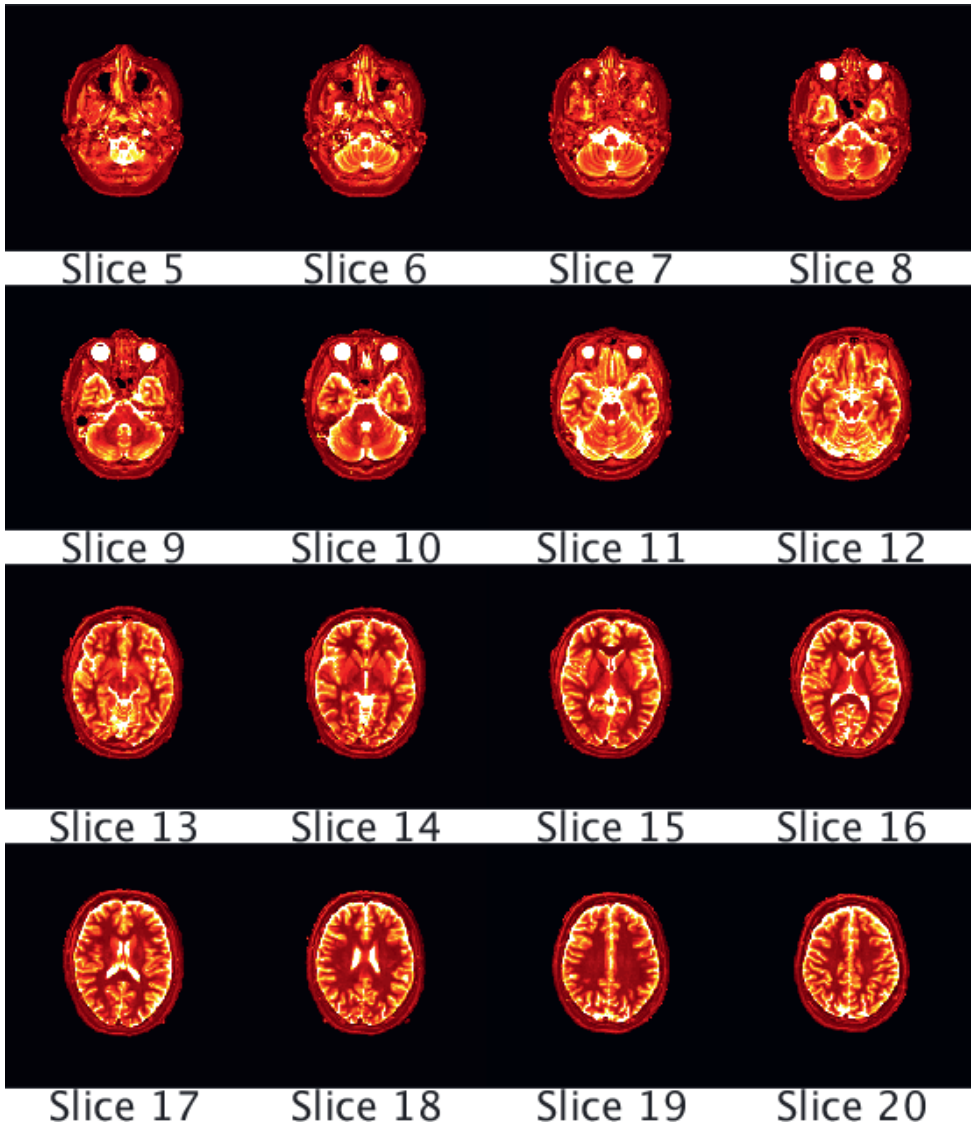

Figure 2.13: T1 maps (ms) from a volunteer on the 1.5T system using QRAPMASTER.

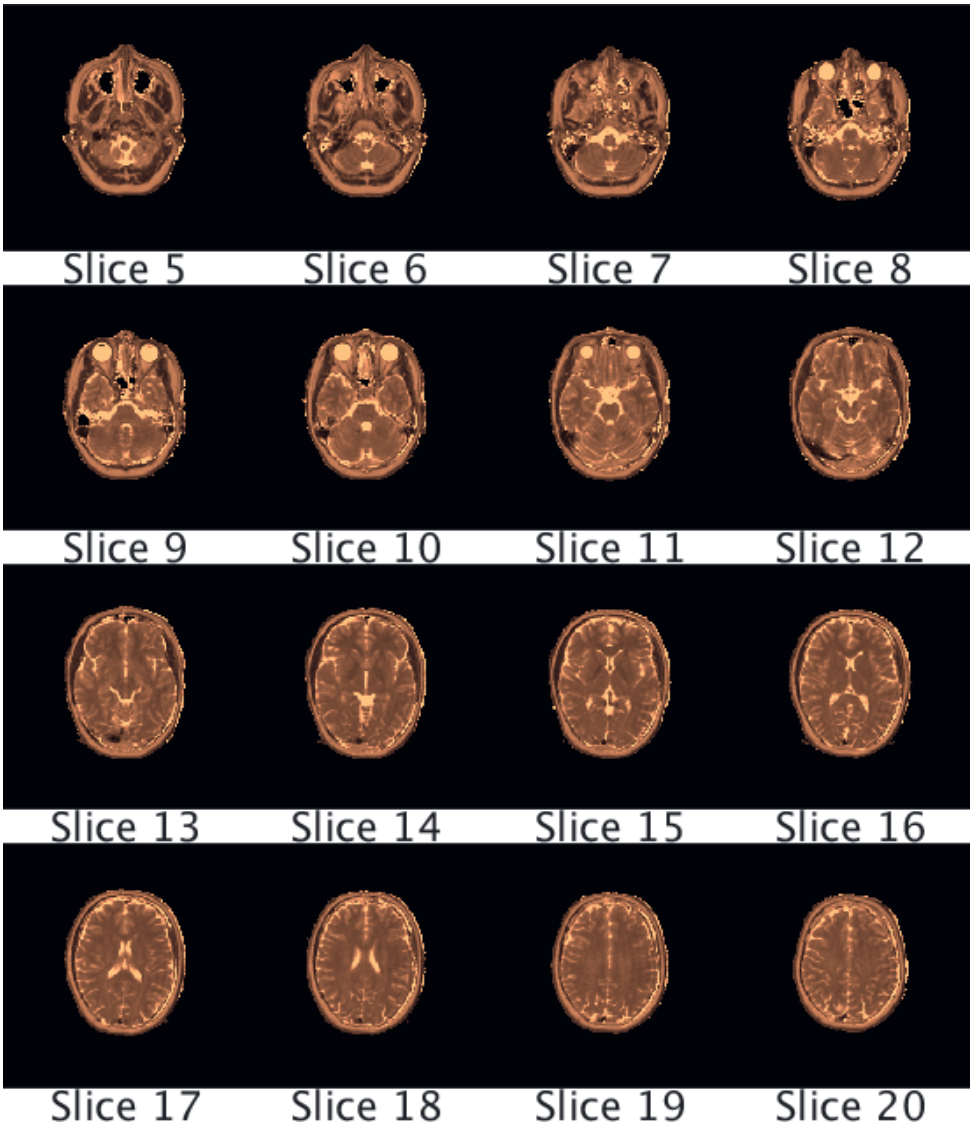

Figure 2.14: T2 maps (ms) from a volunteer on the 1.5T system using QRAPMASTER.

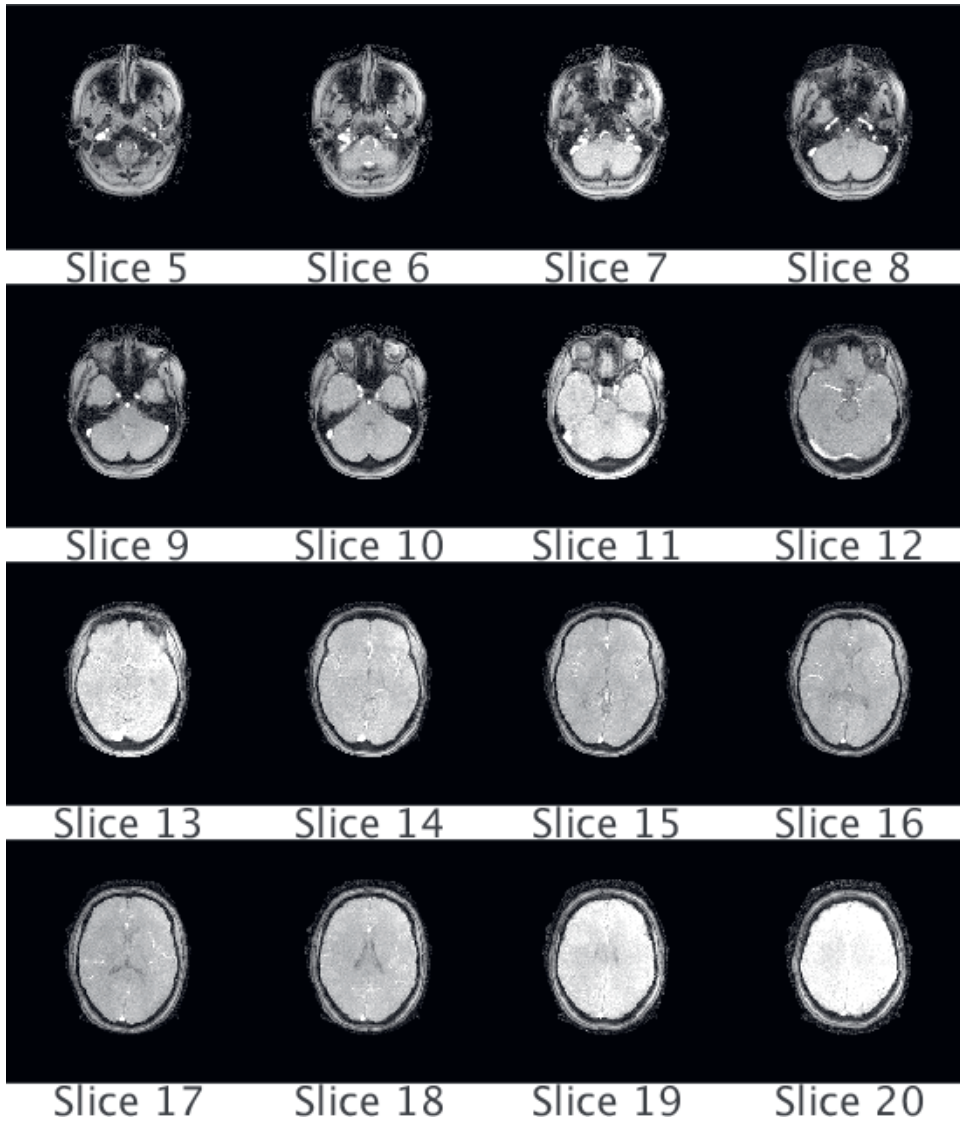

Figure 2.15: PD maps (a.u.) from a volunteer on the 1.5T system using MRF-vFA.

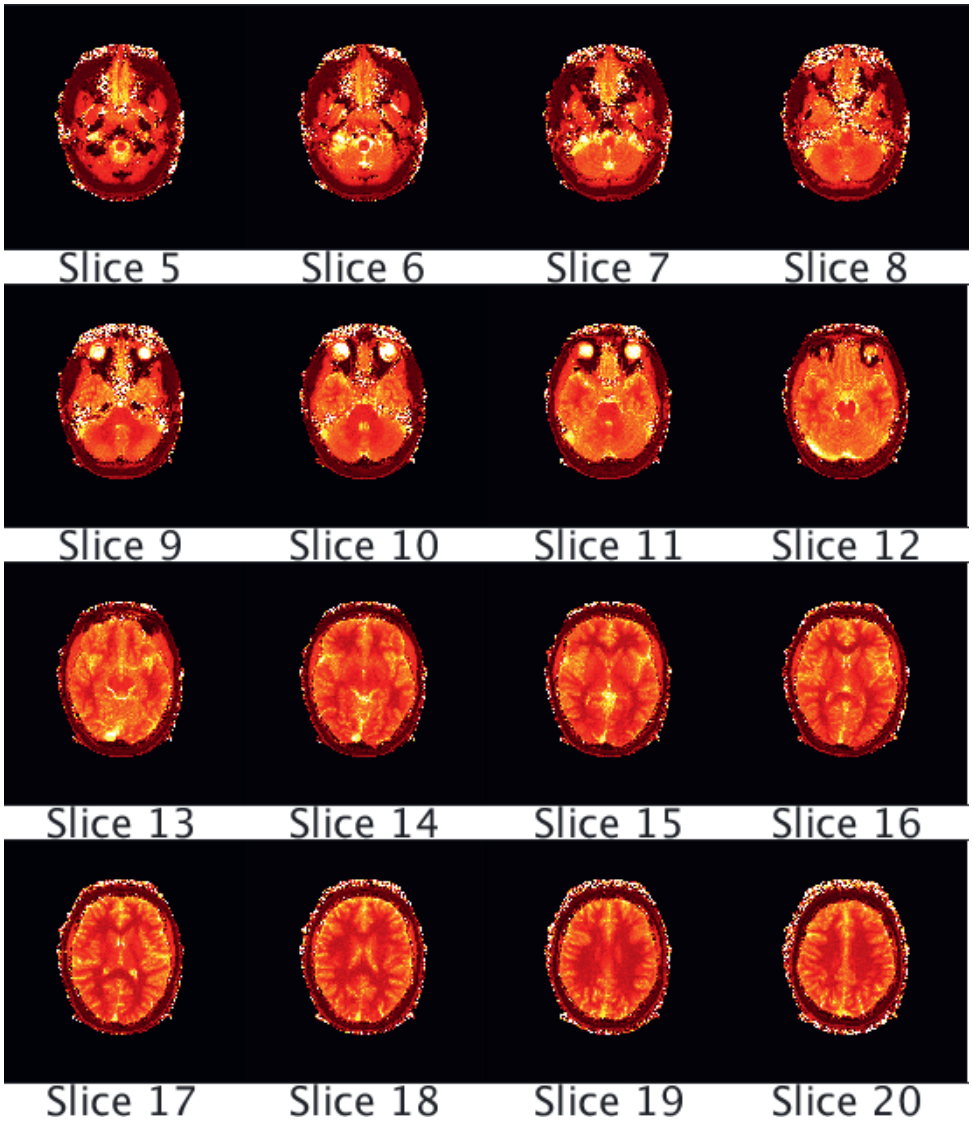

Figure 2.16: T1 maps (ms) from a volunteer on the 1.5T system using MRF-vFA.

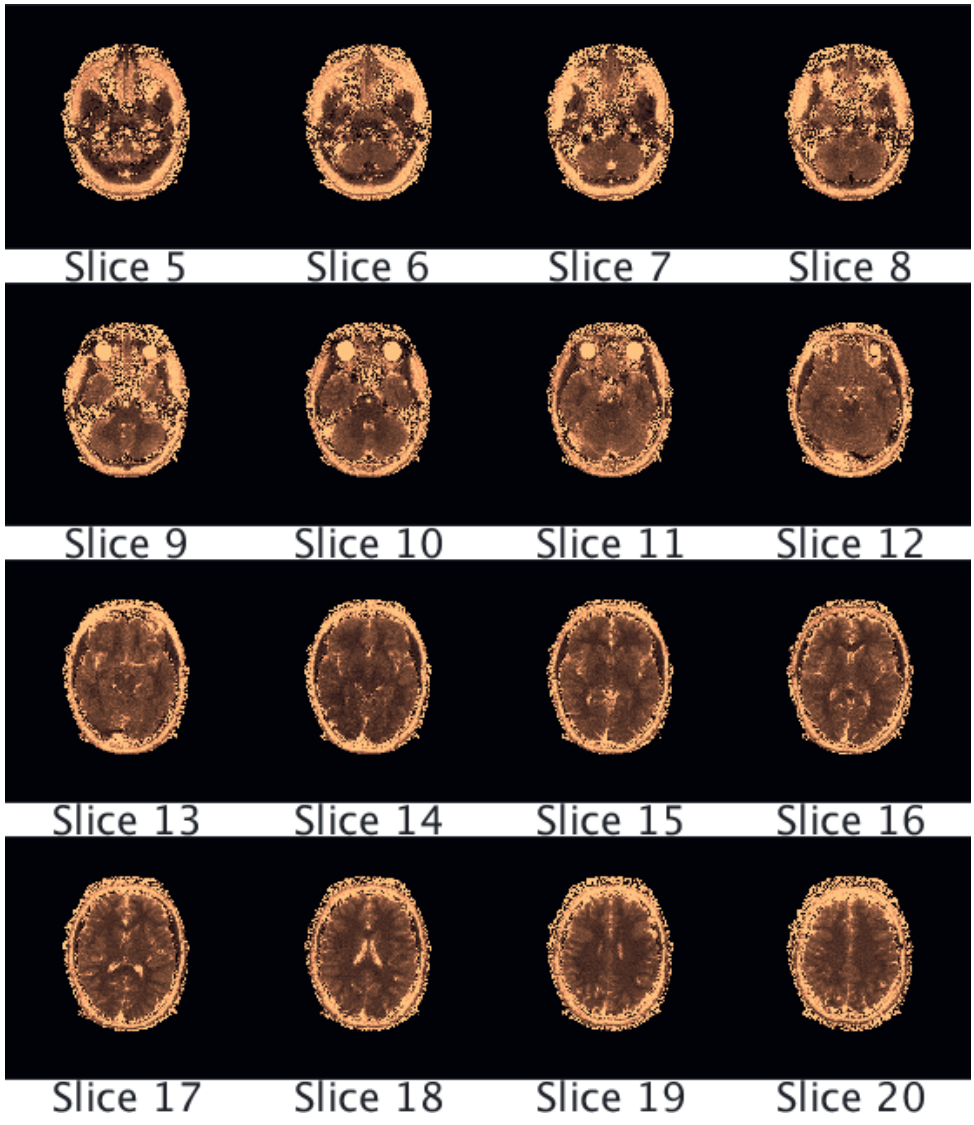

Figure 2.17: T2 maps (ms) from a volunteer on the 1.5T system using MRF-vFA.

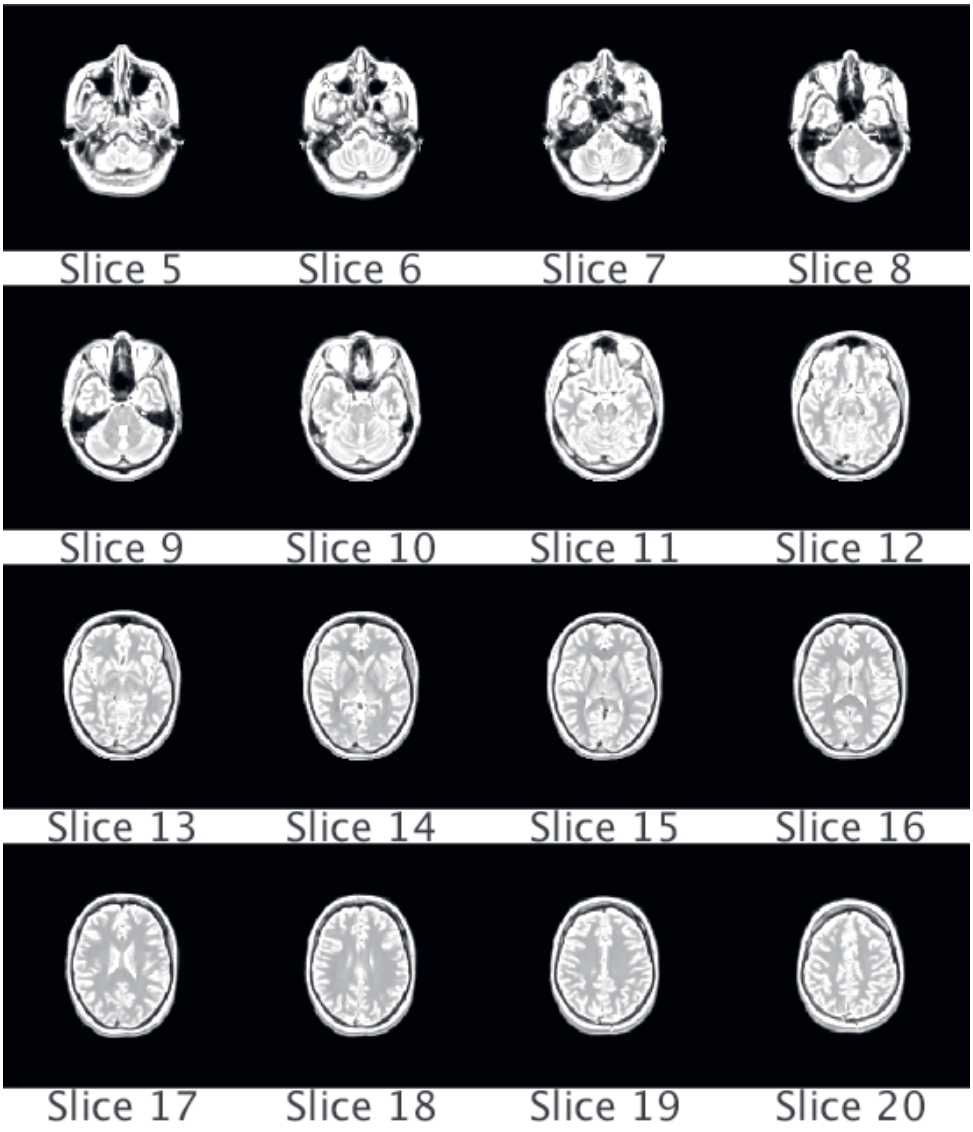

Figure 2.18: PD maps (a.u.) from a volunteer on the 3.0T system using QRAPMASTER.

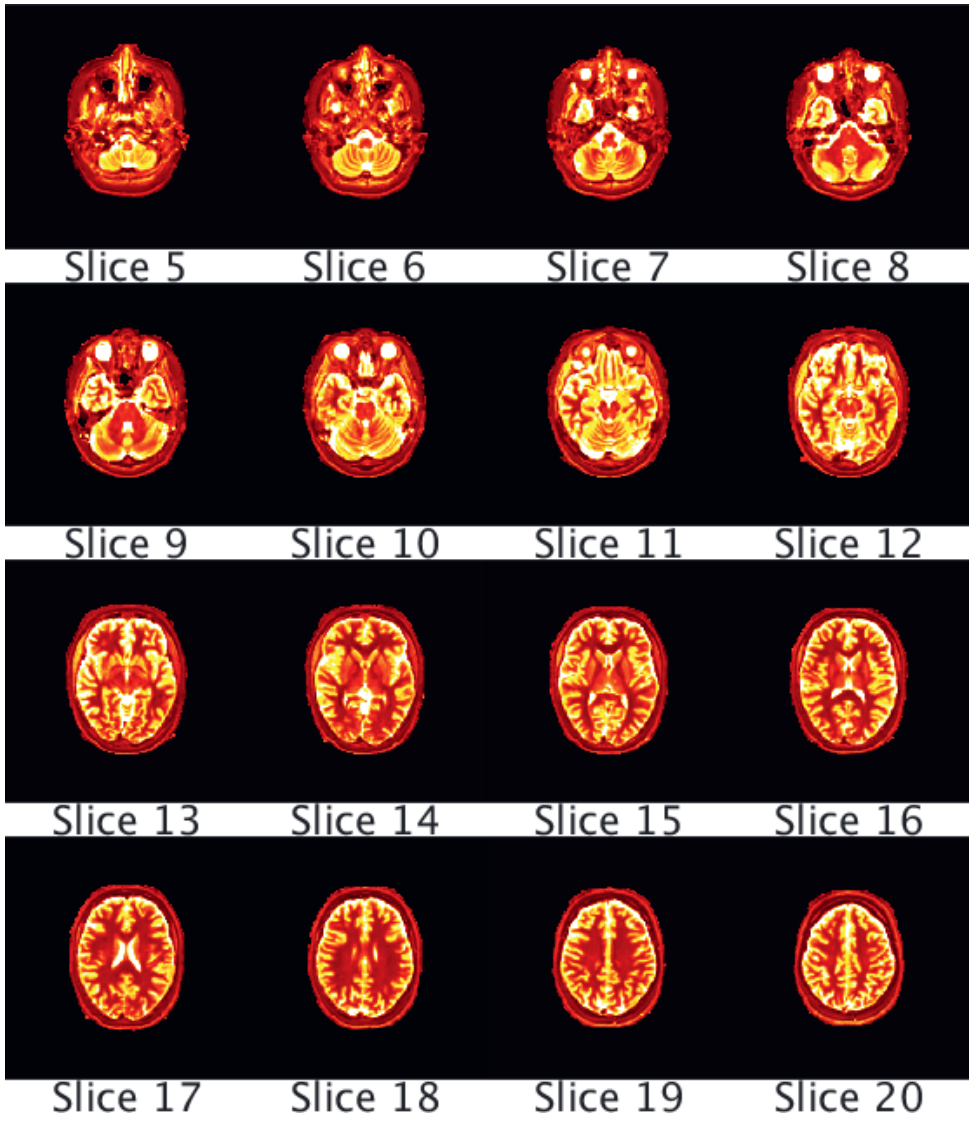

Figure 2.19: T1 maps (ms) from a volunteer on the 3.0T system using QRAPMASTER.

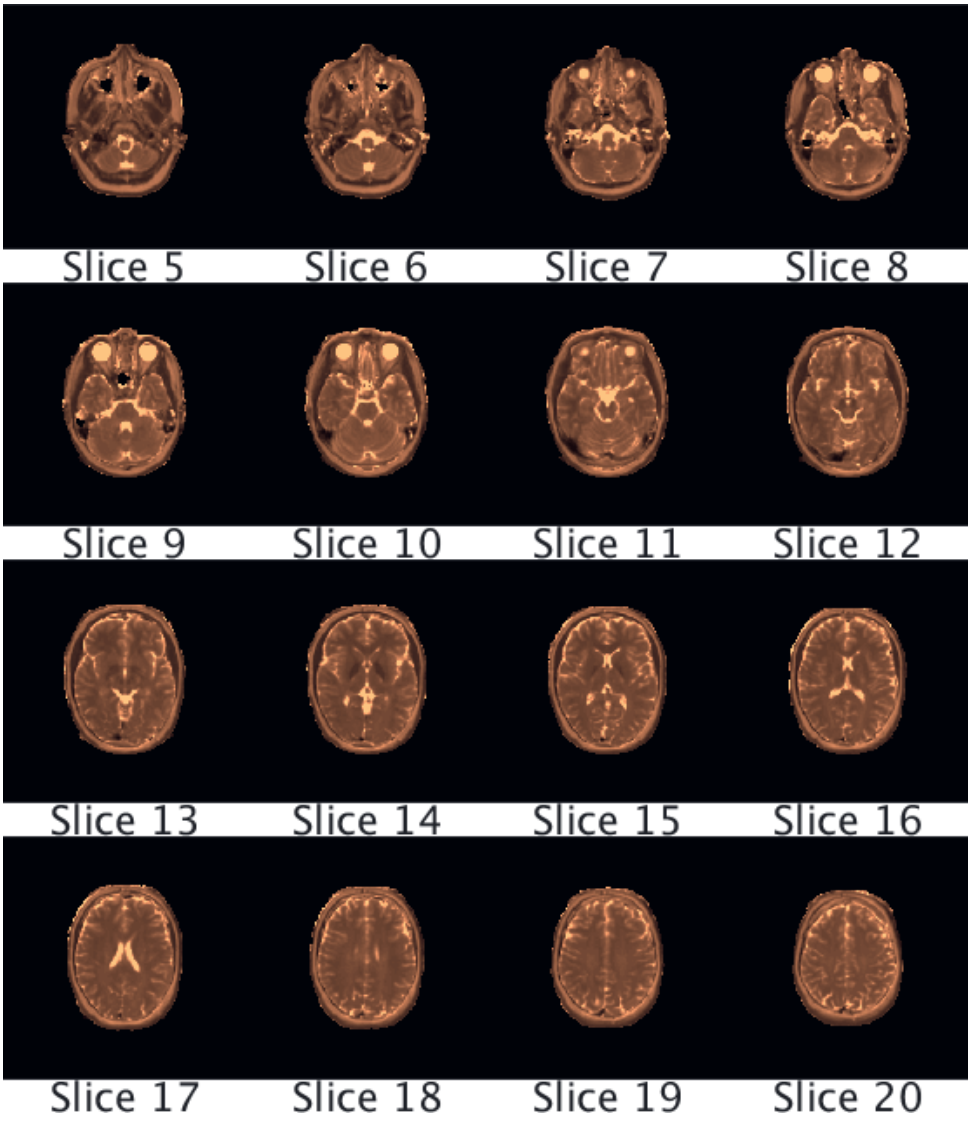

Figure 2.20: T2 maps (ms) from a volunteer on the 3.0T system using QRAPMASTER.

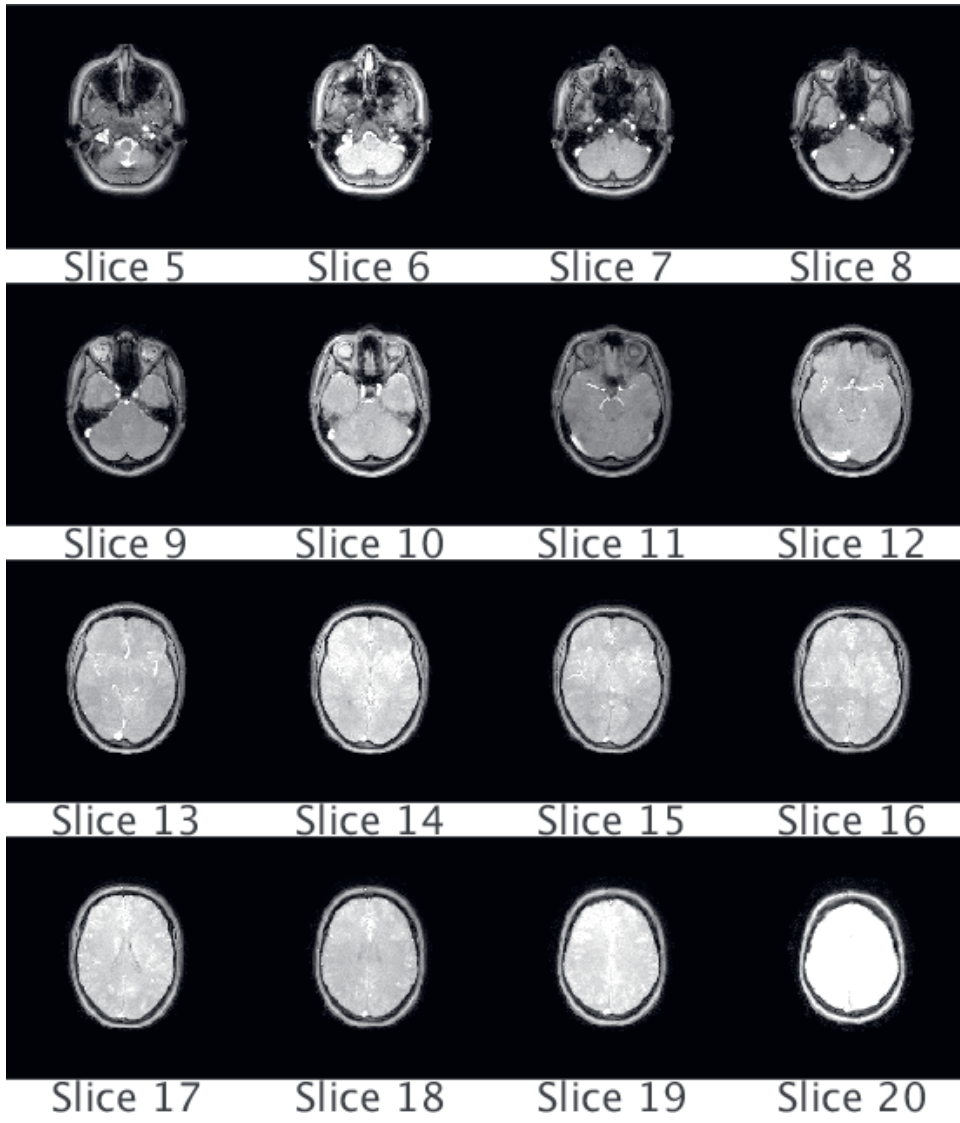

Figure 2.21: PD maps (a.u.) from a volunteer on the 3.0T system using MRF-vFA.

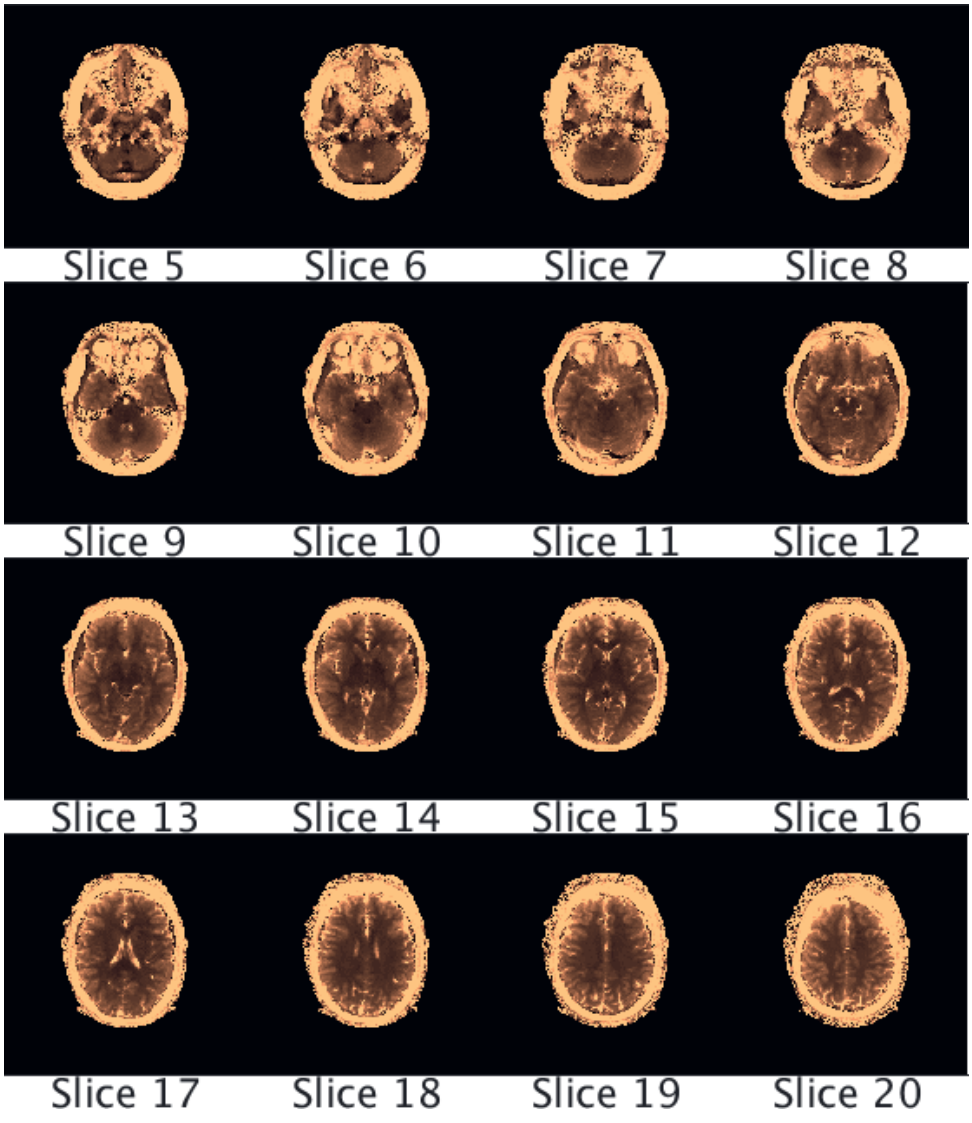

Figure 2.22: T1 maps (ms) from a volunteer on the 3.0T system using MRF-vFA.

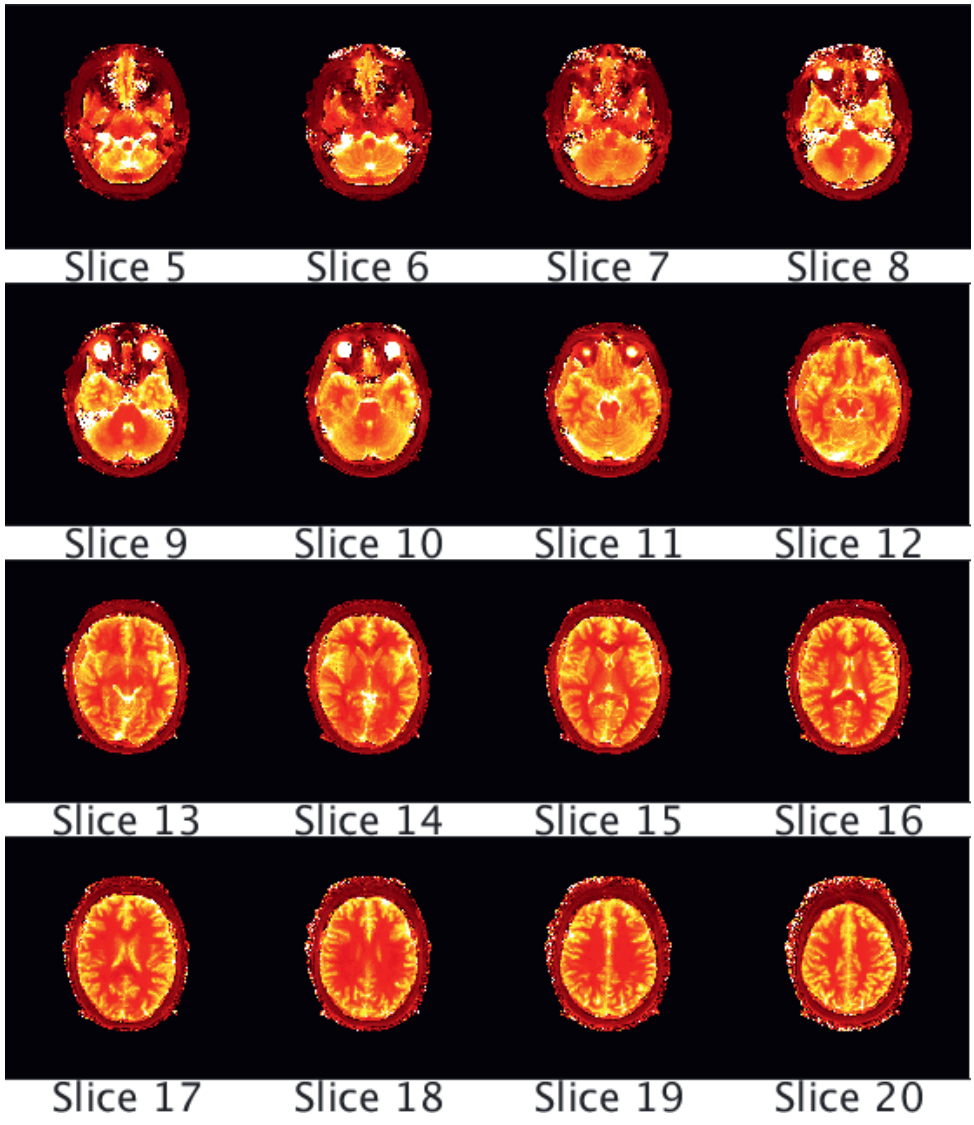

Figure 2.23: T2 maps (ms) from a volunteer on the 3.0T system using MRF-vFA.

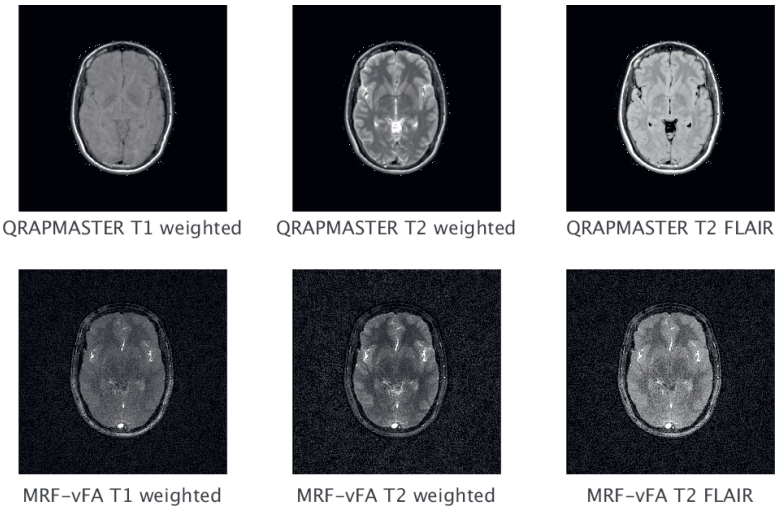

Figure 2.24: Synthetic T1 weighted (TR=550 ms, TE=15ms), T2 weighted (TR=4400 ms, TE=100 ms) and T2 Flair (TR=6000 ms, TE=120 ms, TI=2000 ms) on a 1.5T system with QRAPMASTER and MRF-vFA.

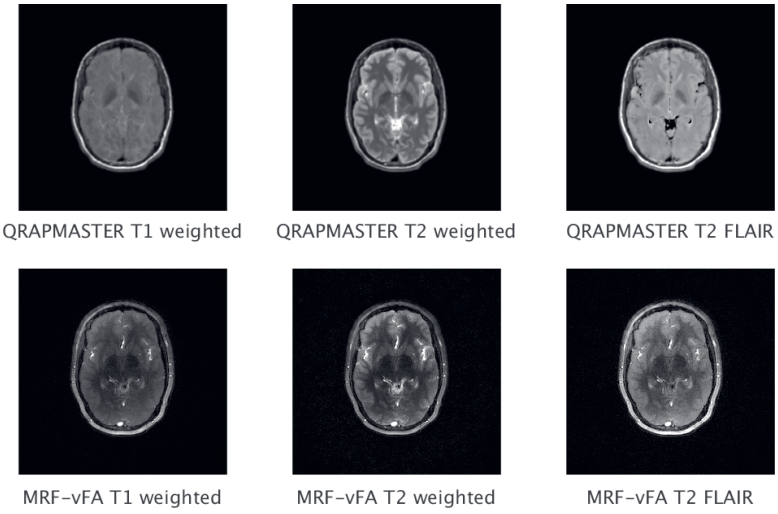

Figure 2.25: Synthetic T1 weighted (TR=550 ms, TE=15ms), T2 weighted (TR=4400 ms, TE=100 ms) and T2 Flair (TR=6000 ms, TE=120 ms, TI=2000 ms) on a 3.0T system with QRAPMASTER and MRF-vFA.

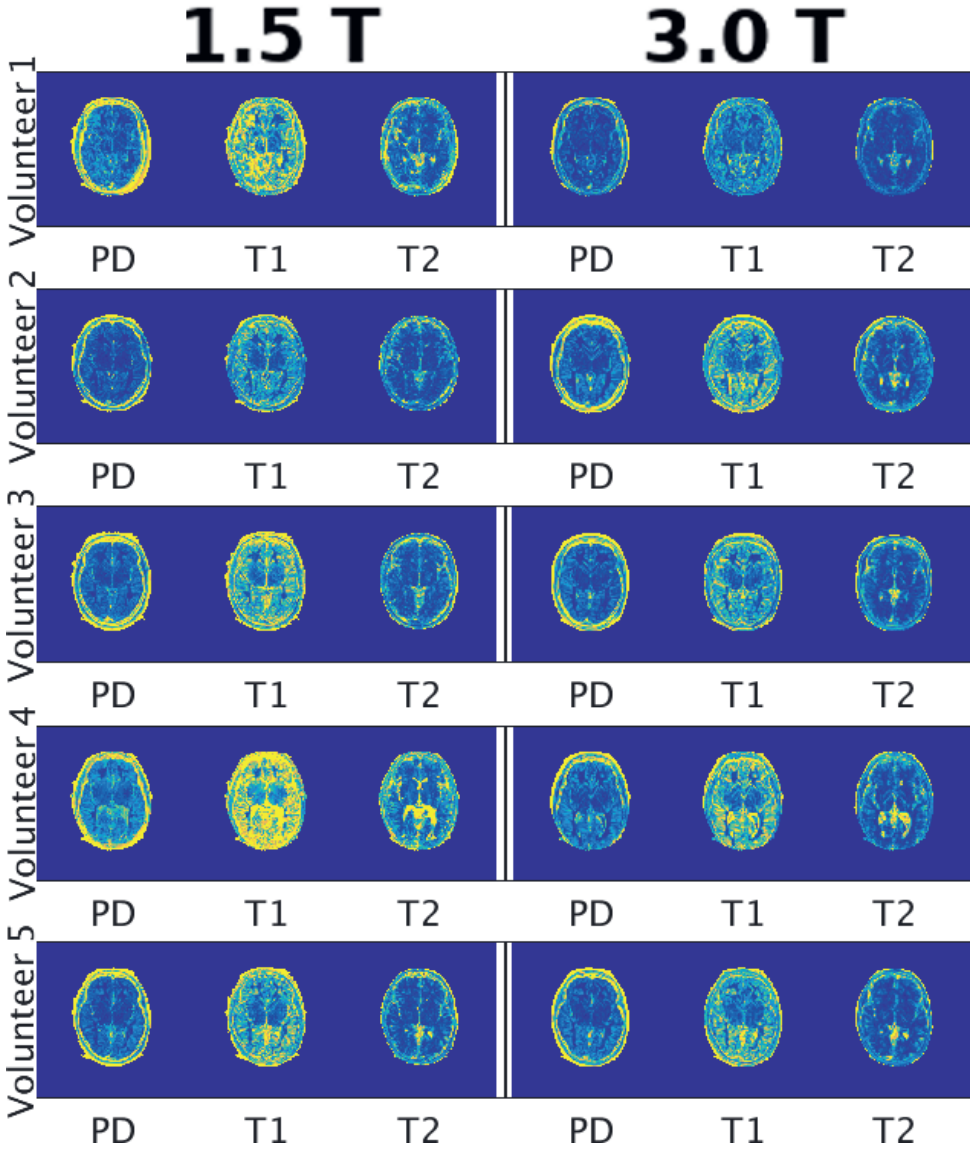

Figure 2.26: Maps of the coefficient of variation (%) of nPD, T1 and T2 with QRAPMASTER on a 1.5T system and on a 3.0T system for each volunteer.

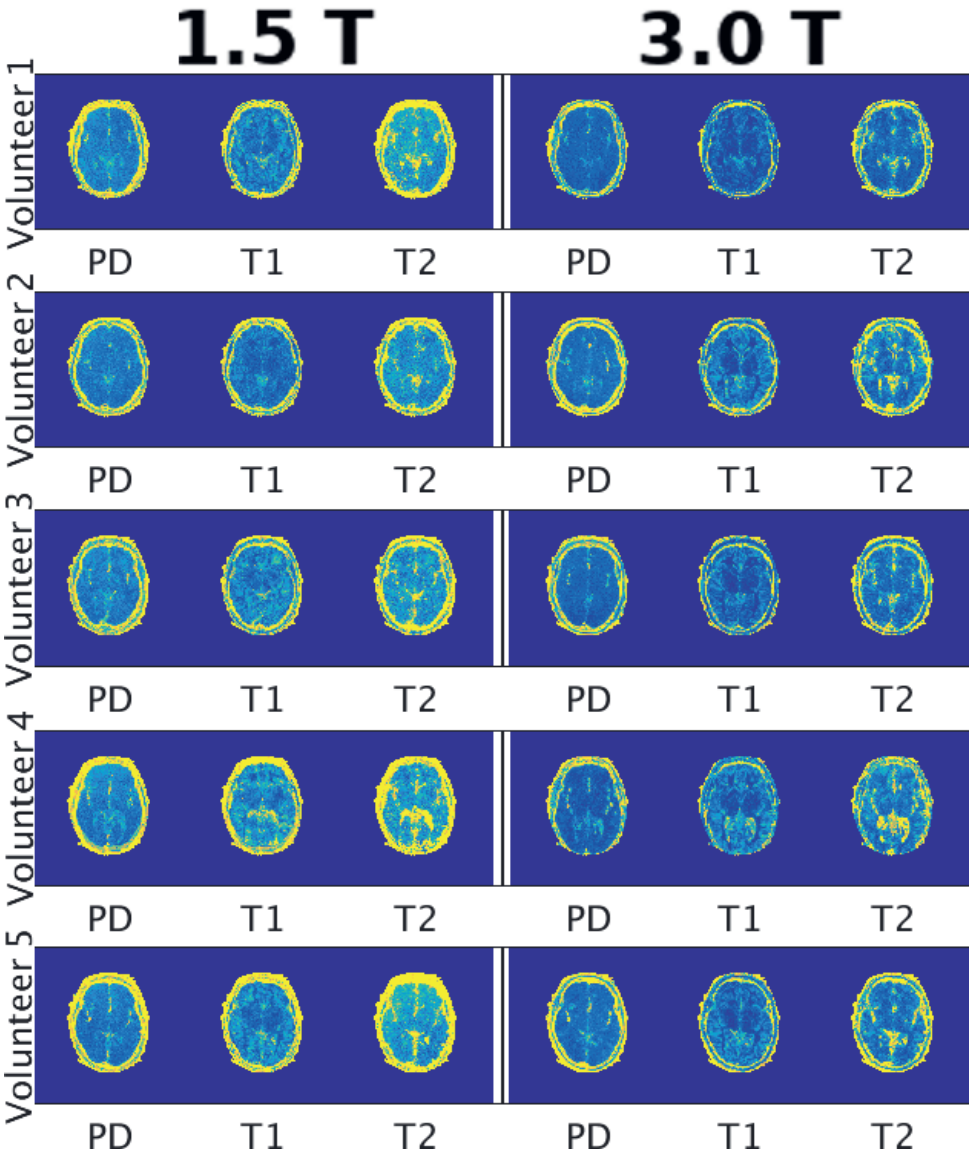

Figure 2.27: Maps of the coefficient of variation (%) of nPD, T1 and T2 with MRF-vFA on a 1.5T system and on a 3.0T system for each volunteer.

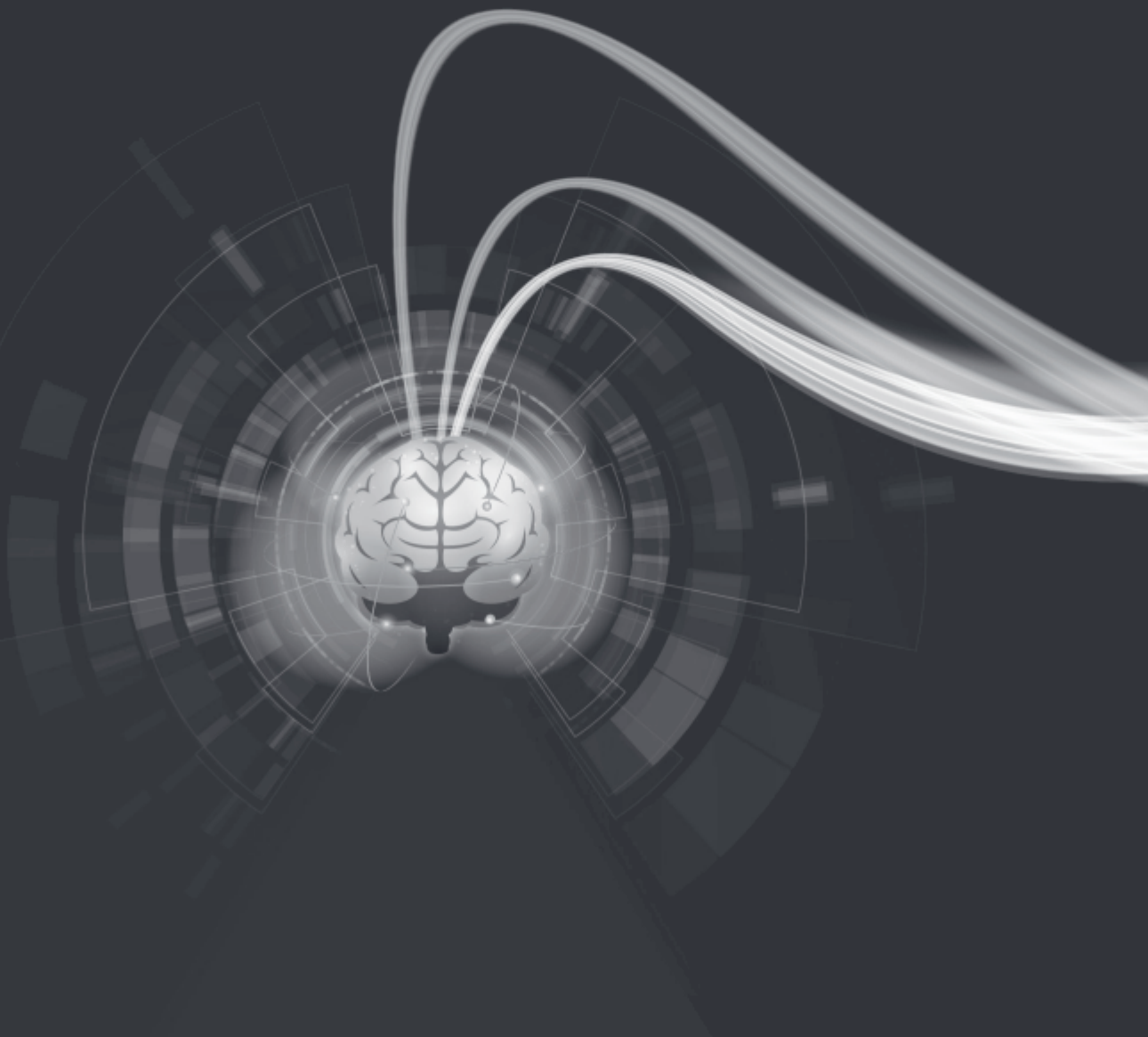

3

MAGiC pre-contrast in gliomas: Are quantitative MRI parameters different in tumors with versus without contrast-enhancement?

Laura Nunez-Gonzalez[1], Karin A. van Garderen[1,2], Marion Smits[1,2], Jaap Jaspers[3], Alejandra Méndez Romero[3], Dirk H.J. Poot[1], and Juan A. Hernandez-Tamames[1]

1 Department of Radiology and Nuclear Medicine, Erasmus Medical Center, Rotterdam, the Netherlands

2 Brain Tumor Center, Erasmus MC Cancer Institute, Rotterdam, the Netherlands

3 Department of Radiotherapy, Erasmus MC Cancer Institute, , Rotterdam, the Netherlands

Submitted

Abstract

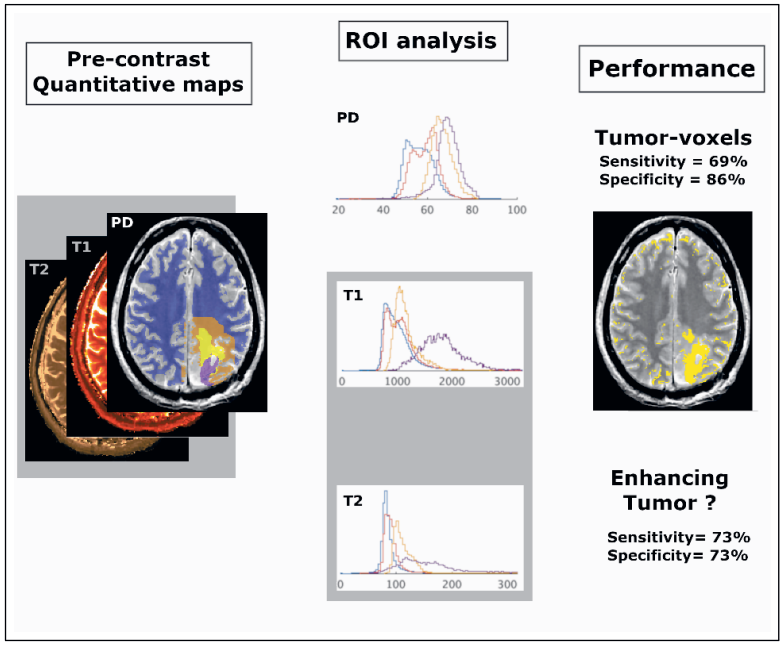

Graphical abstract

Quantitative MR imaging is increasing in popularity since new implementations have been developed. However, their applicability has to be thoroughly validated in order to be included in clinical practice. In our work, we acquired MAGiC in 14 glioma patients. Tumors were segmented based on conventional images (T1-weighted pre-contrast, T2-weighted, FLAIR and T1-weighted post-contrast) and using a deep learning segmentation technique (HD-GLIO) to define regions of interest (ROIs). The quantitative PD, T1 and T2 values inside ROIs were analyzed using the mean, the standard deviation, the Skewness and the Kurtosis and compared to the quantitative T1 and T2 values found in normal white matter. We found significant differences in T1 and T2 values in pre-contrast condition between tumoral region and healthy tissue, as well as between T1w-enhancing and non-enhancing regions. ROC analysis was used to evaluate the potential of quantitative T1 and T2 values for voxel-wise classification in tumor/non-tumor (AUC = 0.95) and T1w enhancement/non-enhancement (AUC =0.85). A cross-validated ROC analysis found high sensitivity (73%) and specificity (73%) with AUCs up to 0.68 on the a priori distinction between tumors with and without T1w-enhancement. These results suggest that normal tissue, tumor tissue, and tissue with T1w-enhancement are distinguishable by their pre-contrast quantitative values but further investigation is needed.

Keywords: MAGiC, Quantitative MR, Glioma, T1w-enhancement

3.1. INTRODUCTION

Characterization of gliomas of the brain has been approached by novel MRI techniques, such as perfusion, diffusion-tensor imaging, and diffusion-weighted imaging [90–92]. The standard assessment of diffuse gliomas includes images such as T1-weighted (before and after the application of contrast agent), T2w/T2w FLAIR and diffusion weighted images [93, 94]. Fast quantitative MR imaging has the potential of improving these protocols by reducing scan time and reducing variability due to system imperfections[6, 14, 95]. However, the sensitivity of quantitative values to changes in normal and disease-affected tissue must be validated. Some relationships between T1 and T2 values and glioma grade have been found in previous studies[96]. Papers characterizing tumor tissue and predicting enhancement using T1 and T2 maps have been published [34, 97–99], but these focus only on either quantitative T1 [97, 98] or quantitative T2 [34, 99]. The long scan time needed for the gold standard quantitative techniques [10, 11, 100] makes their inclusion in clinical protocols difficult.

Nowadays, several fast multi-parametric quantitative image techniques have been developed, such as Magnetic Resonance Fingerprinting (MRF)[15], Quantitative Transient-state Imaging (QTI)[95], and Magnetic Resonance Image Compilation (MAGiC) [14]. All of these are able of acquiring quantitative T1, T2, and proton density (PD) maps of the whole brain in less than 6 minutes, which facilitates their inclusion in clinical protocols and research studies.

MRF has been used to differentiate between common types of gliomas [33]. Depending on the glioma type, some deviation in T1 and T2 values has been found but the results were not conclusive so further investigation is needed.

To our knowledge, MAGiC is the only commercial product for multi parametric imaging that has been more extensively used in brain tumor patients recently. Several works compare the feasibility of using synthetic weighted images derived from the quantitative maps in tumors based on this technique [101–104]. Also, some studies have applied MAGiC to report quantitative relaxometry analysis of gliomas [30, 31], where the difference between pre and post contrast in R1 maps showed significant contrast enhancement in the peritumoral area unlike the conventional T1-weighted scans. For multiple sclerosis, an attempt was made to detect enhancing lesions with MAGiC maps without using contrast agent [105] but with negative results.

In this work, we extend previous attempts to characterize and differentiate healthy and tumoral tissue and tissue with and without T1w-enhancement using parametric maps with a single MAGiC acquisition before contrast injection. We also investigated the possibility of using multi-parametric maps with MAGiC for predicting T1 contrast enhancement in diffuse glioma.

3.2. MATERIALS AND METHODS

3.2.1. ACQUISTION

Acquisitions were performed in this Institutional Review Board approved study with a 3.0T GE MR750 system (General Electric Medical Systems, Waukesha, WI 53188 USA). A 16 channel Head and Neck array coil was used.

After giving written informed consent, 14 patients were scanned. See Table 3.1 for age, gender, diagnosis, WHO grade [106], treatment and time since last surgery. All patients had undergone surgery on the tumor before the scan.

For all patients the imaging protocol follows the recommendations from [93] consisting of: pre-contrast T1-weighted (T1W), T2-weighted (T2W), T2w FLAIR and post-contrast T1-weighted (T1c) scans. Additionally, a MAGiC acquisition was included before the contrast agent injection. This was acquired with TE of 92.24 ms, TR of 4000 ms, FOV of 224 mm, slice thickness of 4 mm and voxel size of 0.875 mm x 0.875 mm x 5 mm. The acquisition time for the whole brain with MAGiC was 5 minutes and 34 seconds.

3.2.2. DATA PREPARATION / ROIS DELIMITATIONS

The conventional sequences T1w, T1c, T2Wand T2 FLAIR were used to segment the gliomas in all patients using HD-GLIO brain tumor segmentation tool [107, 108]. This tool defines two regions of interest (ROIs), one for the non-enhancing T2-weighted hyperintensities (T2h) and other for regions with T1w-enhancement after injecting contrast agent (T1e).

Additionally, an ROI of 1 cm around the segmented tumor for the peritumoral area (PER), and a ROI for normal appearing white matter (nWM) were defined. For the nWM the segmentation was obtained from the T1-weighted image using the software for Statistical Parametric Mapping (SPM) [56, 74], after all the voxels belonging to either the tumor or the peritumoral area were removed. An additional ROI was defined for the whole tumor (TUM) that includes T2h and T1e.

For each patient, the quantitative maps obtained with MAGiC were coregistered to the T1-weighted images using FLIRT from FSL [55, 109, 110]. Subsequently, the quantitative T1 and T2 values were obtained per patient for all the voxels inside the TUM and reported using normalized histograms (probability density function -PDF-).

A white-matter-mask was created joining the segmented white matter and the TUM region.

Table 3.1: Patient demographics, diagnoses, WHO grade [26], treatment and months since surgery. *Treatment in course, not finished. **Treatment planned and not applied yet. S patient 9 had the first surgery 76 months before the scan and a second surgery 39 months before the scan.

Patient Id	Age (years)	Gender	Diagnosis	WHO Grade	Treatment	Months since surgery
1	69	Female	Glioblastoma	4	Chemotherapy, radiotherapy	52
2	63	Male	Astrocytoma	3	Chemotherapy, radiotherapy	49
3	49	Male	Glioblastoma	4	Chemotherapy, radiotherapy	5
4	69	Male	Glioblastoma	4	Chemotherapy*, radiotherapy	3
5	63	Male	Oligodendroglioma	2	Radiotherapy	122
6	52	Female	Oligodendroglioma	3	Chemotherapy*	5
7	50	Male	Astrocytoma	2	Radiotherapy, chemotherapy	34
8	58	Female	Oligodendroglioma	2	Radiotherapy, chemotherapy*	99
9	25	Female	Glioblastoma	4	Radiotherapy, chemotherapy	6s
10	24	Male	Oligodendroglioma	2	Radiotherapy**, chemotherapy**	1
11	50	Female	Astrocytoma	2	Radiotherapy**	1
12	37	Male	Astrocytoma	3	Radiotherapy**, chemotherapy**	1
13	56	Female	Oligodendroglioma	2	Radiotherapy**, chemotherapy**	72
14	44	Male	Astrocytoma	2	Radiotherapy**, chemotherapy**	1

3.2.3. DATA ANALYSIS

To study the distribution of the quantitative values for each patient, the following statistics were computed for each ROI: mean, standard deviation (STD), Skewness, and Kurtosis for PD, T1 and T2 in the nWM, T2h, T1e and PER.

Furthermore, for each ROI, the average and the 95% confidence interval (CI) of the statistical parameters (mean, standard deviation (STD), Skewness, and Kurtosis) across patients were computed and a signed-rank Wilcoxon test was used to detect significant differences between ROIs.

An analysis of the receiver operating characteristic curve (ROC) [111] was performed for three questions: to distinguish between TUM and nWM; to distinguish between T1e from the rest (joint nWM and T2h); and to distinguish between T1e from T2h (only inside TUM). The peritumoral area was excluded from the ROC analysis because it could contain tumoral tissue under the appearance of normal tissue [31]. Four possibilities were considered: ROC analysis only of T1 values, ROC analysis only of T2 values, ROC analysis of the Euclidian norm of the T1 and T2 values (normT1T2) and ROC analysis of the Euclidian norm of the logarithm of T1 and T2 values (normlog). Once an ROC curve was defined, the optimal operating point was calculated as the highest Youdens index[112] across the entire ROC curve. Similar ROC analysis was performed including PD values: the Euclidian norm of T1, T2 and PD values and the Euclidian norm of the logarithm of T1, T2 and PD values.

In a second step, the threshold obtained from the ROC analysis was applied to the quantitative maps inside the white-matter-mask to compare the selected regions with the initial segmentation. For the part of the analysis that considers predicting contrast enhancement, patients were divided in two groups based on the presence or absence of T1e within the TUM volume. The average and the 95% CI of the ROI statistics per patient were computed for each group and a signed-rank Wilcoxon test (using the ROI statistics previously calculated for each patient) was performed to study whether there were significant differences between the two groups or not. An ROC analysis was performed and its optimal operating point was calculated (the highest Youdens index) for each statistical parameter. To evaluate the validity of the ROC analysis, cross-validation was performed by a leaving-pair-out [113] for all possible combinations and an AUC was obtained for every set. The threshold associated to the optimal operating point was applied to classify the left-out-pair. The occurrence of being classified as tumor with T1-enhancement was calculated for each tumor. A unique AUC was calculated for each parameter as the average of all the AUCs obtained for each set separately.

3.3. RESULTS

3.3.1. GENERAL

Figures 3.1, 3.2 and 3.3 respectively shows the PDF of PD, T1 and T2 of every patient in each of the ROIs. Patients 2, 5, 7, 8, 9, 12 and 13 did not show T1-enhancement, which is typical for grade 2 diffuse glioma [106].

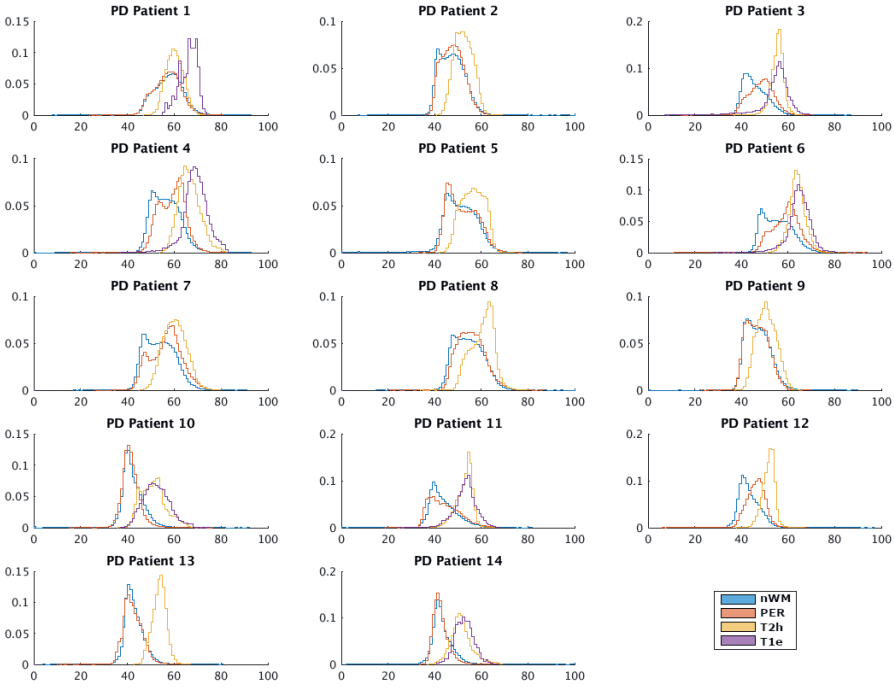

Figure 3.1: Probability density functions of the proton density (PD) (a.u.) of each patient for each region of interest (Blue-> normal white matter nWM-, Red-> peritumoral area PER-, Yellow-> T2 hyperintensity -T2h-, Purple -> T1w-enhancement -T1e-)

Tables 3.2, 3.3 and 3.4 report the average and 95% CI of the ROI statistics of PD, T1 and T2 across all patients as well as the P-values with regards to normal white matter, non-enhanced tumor tissue and T1-enhanced tissue. Table 3.2 reports similar mean values in PD for the T2h and T1e, although higher than for nWM or the peritumoral area (6 a.u. or more). We observed differences in the STD of the peritumoral area compared to nWM (p-value 0.02) or T2h (p-value 0.02) but not compared to T1e (p-value 0.94). The Skewness (zero value in the range mean±STD) and the Kurtosis (positive values) in all the ROIs reflected that the distribution of PD values is symmetric and more tailored than a normal distribution.

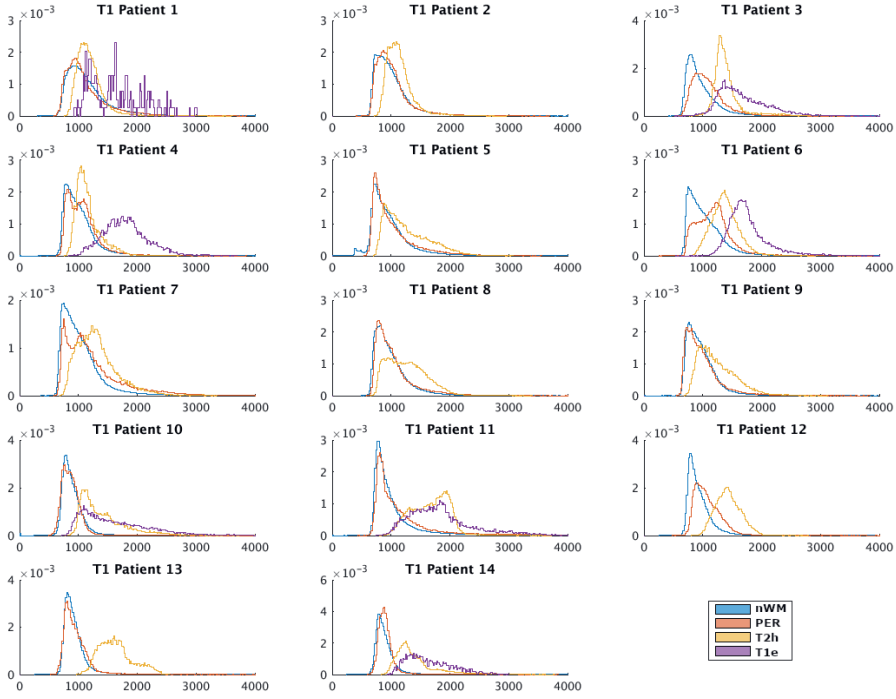

Figure 3.2: Probability density functions of the T1 values (ms) of each patient for each region of interest (Blue-> normal white matter nWM-, Red-> peritumoral area PER-, Yellow-> T2 hyperintensity -T2h-, Purple -> T1w-enhancement -T1e-)

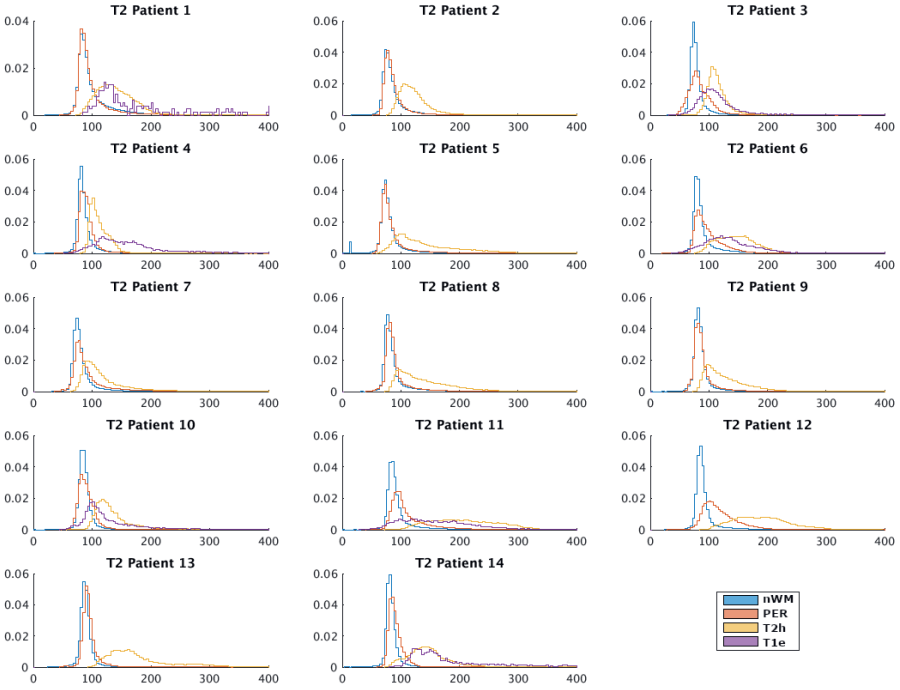

Figure 3.3: Probability density functions of the T2 values (ms) of each patient for each region of interest (Blue-> normal white matter nWM-, Red-> peritumoral area PER-, Yellow-> T2 hyperintensity -T2h-, Purple -> T1w-enhancement -T1e-)

Table 3.2: Table with the statistics of the proton density (PD) values from all the patients per region of interest (ROI). The ROIs correspond to normal white matter (nWM), T2-hyperintensity (T2h), T1w-enhancement (T1e) and peritumoral area (PER). Column 3: Mean over patients of the PD per ROI statistics. Column 4: 95% confidence interval (CI) of the mean over patients of the PD per ROI statistics. Column 5: P-values of the Wilcoxon signed-rank test with the nWM (P-val ROI vs nWM). Column 6: P-values of the Wilcoxon signed-rank test with the tumoral tissue without T1w-enhancement (P-val ROI vs T2h). Column 7: P-values of the Wilcoxon signed-rank test with the T1w-enhancement voxels (P-val ROI vs T1e). * indicates $p < 0.05$.

ROI	ROI statistic	Mean (a.u.)	95% CI (a.u.)	Pval(ROI vs nWM)	Pval (ROI vs T2h)	Pval (ROI vs T1e)
nWM	Mean	48.90	± 1.02	-	<0.01*	0.02*
	STD	5.57	± 3.27	-	<0.01*	0.47
	Skewness	0.23	± 0.60	-	0.27	0.10
	Kurtosis	5.57	± 0.36	-	0.02*	1.00
T2h	Mean	56.20	± 2.98	<0.01*	-	0.08
	STD	4.00	± 0.52	<0.01*	-	0.08
	Skewness	0.00	± 0.24	0.27	-	0.03*
	Kurtosis	3.18	± 0.52	0.02*	-	0.10
T1e	Mean	58.94	± 4.23	0.02*	0.08	-
	STD	5.08	± 0.62	0.47	0.08	-
	Skewness	-0.68	± 0.47	0.10	0.03*	-
	Kurtosis	5.15	± 1.48	1.00	0.10	-
PER	Mean	49.99	± 3.74	0.07	<0.01*	0.02*
	STD	5.15	± 0.60	0.02*	0.02*	0.94
	Skewness	0.33	± 0.30	0.86	0.04*	0.02*
	Kurtosis	3.82	± 1.02	0.04*	0.15	0.69

Table 3.3 shows that the T1e has the highest T1 followed by T2h, PER and nWM. Also the standard deviation was the highest in T1e followed by PER, and very similar for T2h and nWM. Skewness and Kurtosis were both positive in all the cases (mean Skewness ± 95% CI was nWM=2.64±0.98, T2h=1.23±0.68, T1e=1.00±0.34 and PER=2.27±0.94 and mean Kurtosis ± 95% CI was nWM=16.19±10.62, T2h=6.00±3.01, T1e=4.30±1.49 and PER=13.50±10.88), indicating that all the distributions were skewed to the left and had heavier tails than a normal distribution. These values were smaller for T1e than for T2h, PER and nWM had the highest values, which indicate that the distribution of T1 values were closer to a normal distribution for the voxels with T1-enhancement (ROI T1e). We can see this effect also in figure 3.1.

Using the Wilcoxon test, all T2h, T1e and PER ROI statistics were significantly different than normal white matter (Table 3.3, column 5), except the STD-T2h (p-value 0.95) and the STD-PER (p-value 0.24). The T1 values in the peritumoral area differed from the tumoral tissue in all the parameters except the STD (p-value 0.33) (this was consistent with the no rejection of the hypothesis for STD of nWM). The T1-enhanced voxels had higher mean than non-enhanced tumor tissue (Mean difference=359.52ms), but other ROI statistics were not significantly different (p-values 0.16 and 0.08 for Skewness and Kurtosis, respectively). Regarding T2 values, table 3.4 shows that T1e had the highest T2, followed by T2h, then PER and, finally, nWM. The standard deviation was also higher for T1e than for the rest. The Skewness and the Kurtosis followed the same trend than for T1, indicating distributions more skewed to the left and with higher tails for nWM than PER, T2h and, finally, T1e. Using the Wilcoxon test, the parameters of the distribution of T2 values for T2h, T1e and PER were significantly different (p-value <0.05) from nWM. Also the parameters for T2 values of PER were significantly different from T2h, except the STD (p-value 0.5). However, in contrast to the T1 values, the T2 values of T1e only significantly differed from T2h in STD.

3.3.2. VOXEL-WISE

To discriminate between TUM and nWM, normlog(Figure 3.4-A) was the metric with the highest AUC. The AUC was 0.95. The optimal point (Youdens index) of the ROC had a sensitivity of 92.03% and specificity of 86.88% at a threshold of 8.44.

For distinguishing T1-enhancement from the voxels without T1-enchancement (T2h + PER + nWM), the ROC with highest AUC was normT1T2, shown in Figure 3.4-B. The AUC was 0.85. Youdens point had a sensitivity of 81.79% and specificity of 71.99% at a threshold of 1344ms. Figure 3.4-C shows the ROC analysis distinguishing T1e from T2h within the TUM. In this case, the AUC over the normT1T2 was 0.76 with at Youdens point a sensitivity of 67.39 % and a specificity of 72.26% with a threshold at 1512ms. The ROC analysis including PD did not improve the AUC in any of the cases. To distinguish

Table 3.3: Table with the statistics of the T1 values from all the patients per region of interest (ROI). The ROIs correspond to normal white matter (nWM), T2-hyperintensity (T2h), T1w-enhancement (T1e) and peritumoral area (PER). Column 3: Mean over patients of the T1 ROI statistics. Column 4: 95% CI of the mean over patients of the T1 ROI statistics. Column 5: P-values of the Wilcoxon signed-rank test with the nWM (P-val ROI vs nWM). Column 6: P-values of the Wilcoxon signed-rank test with the tumoral tissue without T1w-enhancement (P-val ROI vs T2h). Column 7: P-values of the Wilcoxon signed-rank test with the T1w-enhancement voxels (P-val ROI vs T1e). * indicates $p < 0.05$.

ROI	ROI statistic	Mean (ms)	95% CI (ms)	Pval (ROI vs nWM)	Pval (ROI vs T2h)	Pval (ROI vs T1e)
nWM	Mean	993.16	± 38.20	-	<0.01*	0.02*
	STD	294.04	± 39.61	-	0.95	0.02*
	Skewness	2.64	± 0.57	-	<0.01*	0.02*
	Kurtosis	16.19	± 6.13	-	<0.01*	0.02*
T2h	Mean	1353.78	± 92.41	<0.01*	-	0.02*
	STD	294.68	± 39.78	0.95	-	0.02*
	Skewness	1.23	± 0.39	<0.01*	-	0.16
	Kurtosis	6	± 1.73	<0.01*	-	0.08
T1e	Mean	1713.3	± 53.19	0.02*	0.02*	-
	STD	448.03	± 51.00	0.02*	0.02*	-
	Skewness	1	± 0.19	0.02*	0.16	-
	Kurtosis	4.3	± 0.86	0.02*	0.08	-
PER	Mean	1056.78	± 60.48	0.01*	<0.01*	0.02*
	STD	315.16	± 65.47	0.24	0.33	0.03*
	Skewness	2.27	± 0.54	<0.01*	<0.01*	0.03*
	Kurtosis	13.5	± 6.28	<0.01*	0.01*	0.03*

Table 3.4: Table with the statistics of the T2 values from all the patients per region of interest (ROI). The ROIs correspond to normal white matter (nWM), T2-hyperintensity (T2h), T1w-enhancement (T1e) and peritumoral area (PER). Column 3: Mean over patients of the T2 ROI statistics. Column 4: 95% CI of the mean over patients of the T2 ROI statistics. Column 5: P-values of the Wilcoxon signed-rank test with the nWM (P-val ROI vs nWM). Column 6: P-values of the Wilcoxon signed-rank test with the tumoral tissue without T1w-enhancement (P-val ROI vs T2h). Column 7: P-values of the Wilcoxon signed-rank test with the T1w-enhancement voxels (P-val ROI vs T1e). * indicates $p < 0.05$.

ROI	ROI statistic	Mean (ms)	95% CI (ms)	Pval (ROI vs nWM)	Pval (ROI vs T2h)	Pval (ROI vs T1e)
nWM	Mean	92.33	± 4.43	-	<0.01*	0.02*
	STD	48.9	± 10.61	-	0.04*	0.02*
	Skewness	10.72	± 1.75	-	<0.01*	0.02*
	Kurtosis	184.88	± 57.84	-	<0.01*	0.02*
T2h	Mean	152.25	± 16.06	<0.01*	-	0.3
	STD	64.63	± 12.34	0.04*	-	0.02*
	Skewness	4.62	± 1.13	<0.01*	-	0.08
	Kurtosis	42.38	± 13.60	<0.01*	-	0.08
T1e	Mean	180.05	± 22.52	0.02*	0.3	-
	STD	130.81	± 45.67	0.02*	0.02*	-
	Skewness	3.57	± 0.95	0.02*	0.08	-
	Kurtosis	24.92	± 11.51	0.02*	0.08	-
PER	Mean	103.82	± 9.75	<0.01*	<0.01*	0.02*
	STD	63.56	± 24.05	0.01*	0.5	0.16
	Skewness	8.1	± 1.99	<0.01*	<0.01*	0.03*
	Kurtosis	111.55	± 54.74	<0.01*	<0.01*	0.03*

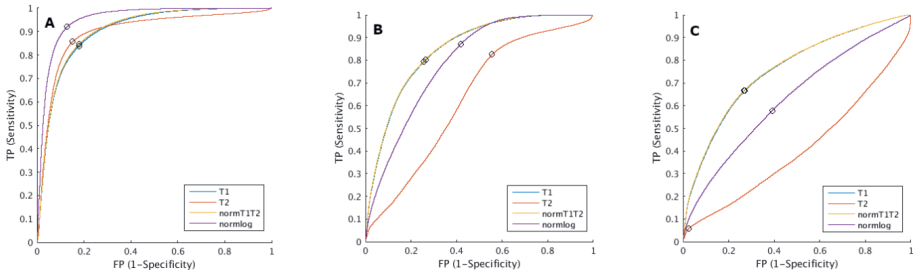

Figure 3.4: Receiver operating characteristic (ROC) curves using only T1 (blue), only T2 (red), the Euclidian norm of T1 and T2 normT1T2- (yellow) and the Euclidian norm of the logarithm of T1 and T2 normlog- (purple). A) ROC curves between the tumor (TUM) and normal white matter (nWM), (B) ROC curves between the T1w-enhanced region (T1e) and the rest of the voxels (T2 hyperintensity region -T2h- + peritumoral area -PER- + nWM), and (C) ROC curves between T1e and T2h. The point with the highest Youdens index is marked with a black circle.

tumor from healthy tissue (TUM vs nWM), the highest AUC obtained was 0.95 using the Euclidian norm of the logarithm of T1, T2 and PD. To distinguish T1-enhancement (T1e), the highest AUCs were using the Euclidian norm of T1, T2 and PD, with an AUC of 0.85 when applying over all ROIs (T2h+PER+nWM) and an AUC of 0.76 when applying vs T2h only inside the tumor (TUM). The lack of improvement in distinguishing tumor and T1-enhancement motivated the exclusion of PD values in the rest of the analysis. Figures 3.5 shows the segmentations for one representative patient (patient 3) within the white-matter-mask from HD-GLIO and the obtained by applying the thresholds from the ROC analysis to the patients T1 and T2 maps. Using the threshold values obtained in the ROC analysis, voxels with normlog> 8.44 were classified as tumor (TUM*), and the voxels with normT1T2>1344ms were classified as T1-enhancement (T1e*). The segmentations from the rest of the patients are shown in supplementary figures 3.7 to 3.19.

For T1e*, although it captured most of the actual T1-enhacement in all the patients, it designated regions within the tumor that are not enhanced as if they were. Even in patients with no T1-enhacement, T1e* defined big regions inside the tumor that could be mistaken as T1-enhancement. In table 3.5, the sensitivity over all the voxels in T1e and TUM, and the specificity and the accuracy over all the voxels in the white-matter-mask after applying the threshold for T1e* and TUM* is reported. In general the sensitivity was high (> 60%), except in three cases where the sensitivity for TUM* was 55, 59 and 49 for patients 2, 3 and 4 and one case where the sensitivity for T1e* was 59 for patient 10. Mean (95% CI) sensitivity across all the patients was 77 (±7.5) for T1e* and 69 (±9.1) for TUM*. The specificity was very high (>= 80%), except in patient 1 with specificity of 78% for T1e* and 68% for TUM*. Mean (95% CI) specificity across all the patients was 89 (±2.8) for T1e* and 86 (±4.0) for TUM*. The accuracy was very high (>= 80%), except

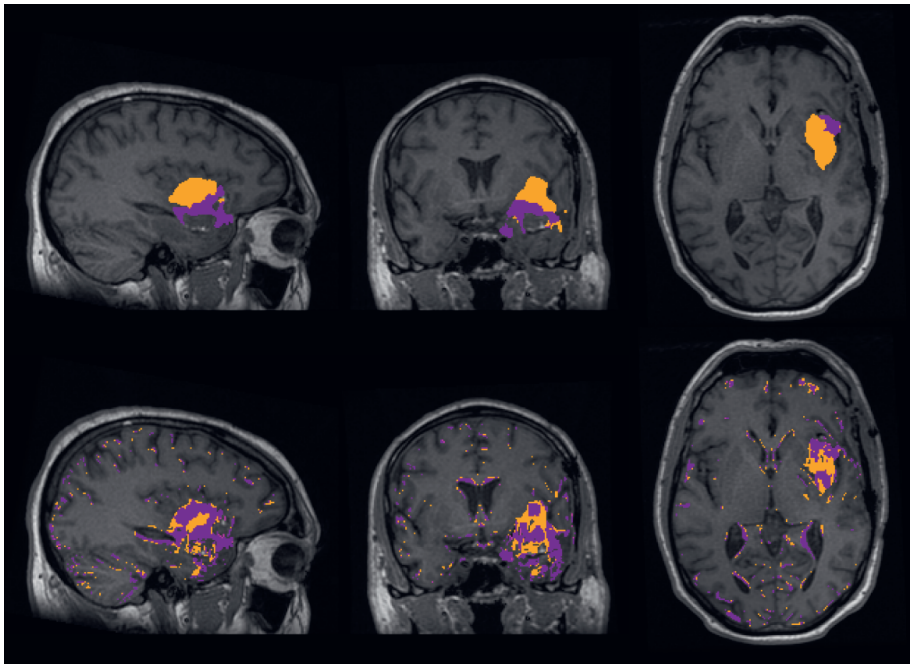

Figure 3.5: Patient 3. Sagittal, coronal and axial planes of the segmentations overlaid on the T1w scan from. Top: segmentation from HD-GLIO, T2-hyperintensity (T2h) in orange and T1-enhancement (T1e) in purple. Bottom: using thresholding, voxels classified as tumor (TUM*) in orange and voxels classified as T1w-enhanced (T1e*) in purple. The purple T1e* region is overlapped with the orange TUM*.

Table 3.5: Sensitivity, specificity and accuracy of the voxel-wise classification as T1w-enhancement (T1e*) and tumor (TUM*) for each patient in percentage.

	T1-enhancement			**Tumor**		
	Sensitivity	**Specificity**	**Accuracy**	**Sensitivity**	**Specificity**	**Accuracy**
Patient 1	65	78	78	73	68	69
Patient 2	-	89	89	55	84	82
Patient 3	79	91	91	59	90	90
Patient 4	90	91	91	49	86	85
Patient 5	-	89	89	61	86	85
Patient 6	95	86	86	71	81	82
Patient 7	-	86	86	64	84	83
Patient 8	-	88	88	65	88	85
Patient 9	-	92	92	60	88	87
Patient 10	59	96	96	62	94	93
Patient 11	84	84	84	85	80	81
Patient 12	-	93	93	99	91	91
Patient 13	-	95	95	99	93	93
Patient 14	75	95	95	85	95	94
Mean (95% CI)	**77 (±7.5)**	**89 (±2.8)**	**89 (±2.8)**	**69 (±9.1)**	**86 (±4.0)**	**85 (±3.8)**

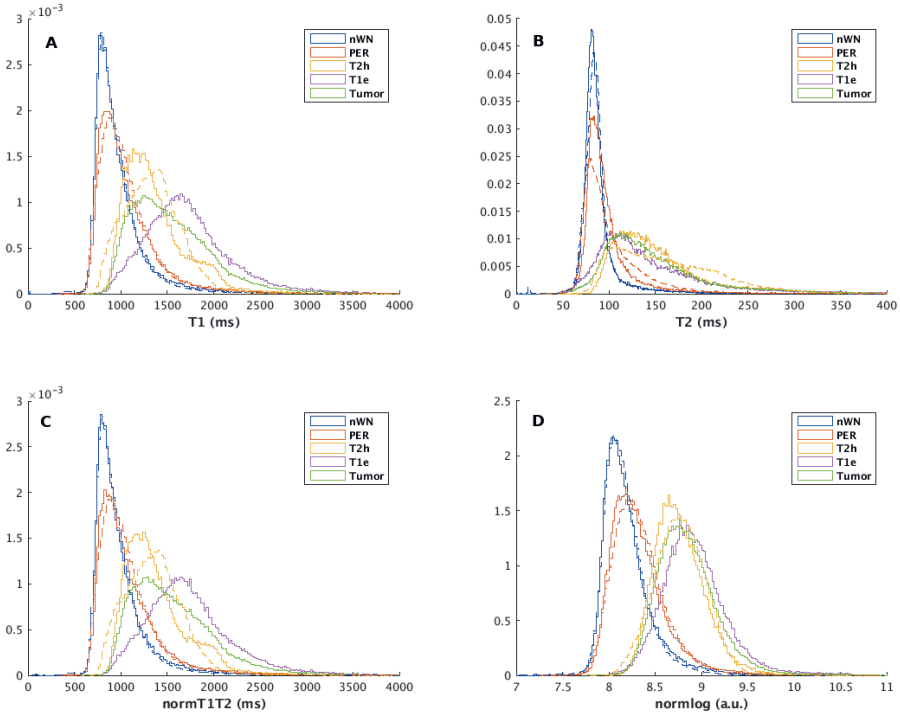

Figure 3.6: Probability density functions of the T1 values (A), T2 values (B), the norm of T1 and T2 values normT1T2- (C), and the norm of the logarithm of T1 and T2 values normlog- (D) for all the patients showing T1w-enhancement (solid line) and for all the patients without T1w-enhancement (dashed line) for each region of interest (ROI) (Blue->normal white matter -nWM-, Red-> peritumoral area PER-, Yellow-> T2 hyperintensity -T2h-, Purple -> T1w-enhancement -T1e-, Green -> T2h + T1e -TUMOR-)

in patient 1 with accuracy of 78% for T1e* and 69% for TUM*. Mean (95% CI) accuracy across all the patients was 89 (±2.8) for T1e* and 85 (±3.8) for TUM*.

3.3.3. T1-ENHANCEMENT

The PDF of the T1 values, T2 values, Euclidian norm of T1 and T2 values, and Euclidian norm of the logarithm of T1 and T2 values, are plotted using the values obtained from all the patients with T1-enhancement and without T1-enhancement (Figure 3.6) for each ROI .

The mean and standard deviation of the statistics (mean, STD, Skewness, and Kurtosis) of T1 and T2 values inside the TUM for each group are reported in Table 3.6. Also the P-values of the signed-rank Wilcoxon test between patients with T1-enhancement and without T1-enhancement are reported. We observed that

Table 3.6: Mean and its 95% confidence interval (CI) over subjects in the respective group (T1w-enhanced or no T1w-enhanced glioma) of the region of interest (ROI) statistics of the tumor for T1 values, T2 values, the Euclidian norm of the T1 and T2 values (normT1T2) and the Euclidian norm of the logarithm of the T1 and T2 values (normlog). The last column gives the P-values of the Wil-coxon signed-rank test between the patient groups. * indicates $p < 0.05$.

	Param	Mean No T1-enhancement	95% CI No T1-enhancement	Mean T1-enhancement	95% CI T1-enhancement	P-val
T1	Mean	1330.20	± 143.34	1457.06	± 139.30	0.08
	STD	299.50	± 58.42	366.34	± 69.23	0.16
	Skewness	0.95	± 0.44	1.51	± 0.35	0.03*
	Kurtosis	4.45	± 1.89	7.02	± 2.46	0.03*
T2	Mean	150.95	± 22.24	157.22	± 25.72	0.47
	STD	61.27	± 7.64	85.71	± 42.36	0.47
	Skewness	3.76	± 1.90	5.05	± 1.19	0.16
	Kurtosis	31.98	± 20.06	45.54	± 20.01	0.22
normT1T2	Mean	1339.20	± 144.45	1467.13	± 140.11	0.08
	STD	303.98	± 58.70	372.50	± 75.53	0.16
	Skewness	0.99	± 1.93	1.56	± 1.22	0.03*
	Kurtosis	4.69	± 19.93	7.39	± 20.09	0.03*
normlog	Mean	8.71	± 0.16	8.79	± 0.15	0.22
	STD	0.34	± 0.24	0.35	± 0.36	1.00
	Skewness	0.80	± 0.37	1.20	± 0.27	0.08
	Kurtosis	4.24	± 0.99	6.01	± 0.53	0.05*

Table 3.7: First row indicates if the tumor showed T1w-enhancement (Y) or not (N). The following rows report the number of times that subject was classified as having T1-enhanced tumor during the leave-pair-out cross-validation, which makes 7 predictions per patient. Patients with T1w-enhancement are marked using columns in green. Numbers in red indicates that the tumor was misclassified the majority of the times. The validation was done using only the T1 values, only the T2 values, the Euclidian norm of the T1 and T2 values (normT1T2) and the Euclidian norm of the logarithm of the T1 and T2 values (normlog).

	Param	Pat 1	Pat 2	Pat 3	Pat 4	Pat 5	Pat 6	Pat 7	Pat 8	Pat 9	Pat 10	Pat 11	Pat 12	Pat 13	Pat 14
T1-enhan	-	Y	N	Y	Y	N	Y	N	N	N	Y	Y	N	N	Y
T1	Mean	0	0	7	0	0	7	0	0	0	7	7	7	7	1
	STD	0	0	0	7	7	0	0	0	0	7	1	0	0	7
	Skewness	7	7	7	0	0	1	6	0	0	7	0	0	0	7
	Kurtosis	7	7	1	0	0	7	6	0	0	7	7	0	0	7
T2	Mean	0	0	0	0	6	3	0	4	4	5	7	7	7	5
	STD	0	0	0	0	0	0	0	0	0	7	0	0	0	6
	Skewness	7	7	7	0	0	3	7	7	7	7	3	0	0	3
	Kurtosis	7	7	7	0	5	6	7	7	6	6	6	0	0	0
normT1T2	Mean	0	0	7	0	0	7	0	0	0	7	7	7	7	1
	STD	0	0	0	7	7	0	0	0	0	7	1	0	0	7
	Skewness	7	7	7	0	0	2	6	0	5	7	0	0	0	7
	Kurtosis	7	7	1	0	0	7	6	0	0	7	7	0	0	7
normlog	Mean	0	0	7	0	0	7	0	0	0	7	7	7	7	7
	STD	0	0	7	7	7	1	7	7	7	7	7	0	6	7
	Skewness	7	7	7	0	0	0	0	0	0	7	0	0	0	7
	Kurtosis	7	7	7	0	0	2	6	0	5	7	0	0	0	7

Table 3.8: Averaged area under the curve (AUC) of the receiver operating characteristic (ROC) analysis on distinguishing between tumors with and without T1w-enhancement and its standard deviation between brackets from all the leave-pair-out sets used for cross-validation for each statistical parameter. Last three columns report the sensitivity, specificity and accuracy taking into account all the sets and the results showed in Table 3.7.

	Param	**Mean AUC (STD)**	**Sensitivity**	**Specificity**	**Accuracy**
T1	Mean	0.62 (0.03)	59.00%	71.00%	65.00%
	STD	0.65 (0.03)	45.00%	86.00%	65.00%
	Skewness	0.65 (0.03)	59.00%	73.00%	66.00%
	Kurtosis	0.68 (0.03)	73.00%	73.00%	73.00%
T2	Mean	0.54 (0.04)	41.00%	43.00%	42.00%
	STD	0.58 (0.03)	29.00%	100.00%	64.00%
	Skewness	0.58 (0.03)	61.00%	43.00%	52.00%
	Kurtosis	0.56 (0.03)	65.00%	35.00%	50.00%
normT1T2	Mean	0.62 (0.03)	59.00%	71.00%	65.00%
	STD	0.65 (0.03)	45.00%	86.00%	65.00%
	Skewness	0.66 (0.03)	61.00%	63.00%	62.00%
	Kurtosis	0.68 (0.03)	73.00%	73.00%	73.00%
normlog	Mean	0.61 (0.03)	71.00%	71.00%	71.00%
	STD	0.52 (0.04)	73.00%	31.00%	52.00%
	Skewness	0.61 (0.03)	57.00%	86.00%	71.00%
	Kurtosis	0.66 (0.03)	61.00%	63.00%	62.00%

although all parameters were higher for the T1-enhanced tumors, only the Skewness and the Kurtosis of T1, and normT1T2 differed significantly.

Table 3.7 reports the occurrence of a patient being classified as patient with T1-enhancement in the tumor during the leave-pair-out cross-validation process and Table 3.8 reports the averaged AUC obtained [38] and the sensitivity, specificity and accuracy taking into account all the leave-pair-out sets (49 in total). In all the cases, patient 2 was misclassified as T1-enhanced tumor when using the Skewness and the Kurtosis as parameter. Using the Mean as discriminative parameter, patients 12 and 13 were always misclassified as T1-enhanced tumor.

As we can see in table 3.8, the highest AUC was obtained using T1 and the normT1T2 as parameter to apply a ROC analysis (0.68). In both cases, the occurrence was the same for all the patients, and the sensitivity, specificity, and accuracy were 73%, being the highest sensitivity and accuracy of the table. The specificity using the STD of T1 and normT1T2, and the Skewness of normlog was higher than 73% but at the cost of very low sensitivity. The statistic parameters from T2 values were the least accurate, with sensitivities between 29% and 65% and specificity < 50%, except for the STD which did not have false positive values.

3.4. DISCUSSION

The results show that the distributions of T1 and T2 values differentiates tumor from normal white matter.

While not perfect, it was also possible to distinguish voxels with and without T1-enhancement with normT1T2 with an AUC of 0.85, resulting in a mean sensitivity of 77% and a mean specificity of 89% when applying the threshold to each patient separately. Using PD did not increase AUC in any of the cases, hence it was excluded from the voxel-wise experiments and from the T1-enhancement analysis in tumors. However, we suggest that PD should be further investigated as PD showed significant differences between the regions.

Regarding the applicability of the voxel-wise thresholds, the voxels defined in the ROIs TUM* and T1e* are not matching voxel by voxel with the segmentation provided by the HD-GLIO tool. However, that is not expected as HD-GLIO is a segmentation tool that makes use of the T2-weighted FLAIR sequence and is trained to incorporate high-level features.

By visual inspection of the ROIs of TUM* (those voxels over the threshold defined for tumor detection), the strong similarity with the tumor segmented by HD-GLIO tool is obvious. Even if they are not perfectly matching, most of the inner tumor is above the threshold with sensitivity 50 in all. Furthermore, we dont observe clusters above

the threshold in normal white matter. The voxels over the threshold outside the tumor, belong either to the edge of the white matter or are in the peritumoral area. The latter is not surprising as the peritumoral area may contain tumoral cells or be affected by the tumor (like having a leaky blood brain barrier) [31, 114].

Regarding voxel-wise T1-enhancement, the voxels over the threshold defined a clear cluster in all the patients with T1-enhancement, although not fully aligned with the original T1e ROI. However, the amount of misclassified voxels without enhancement as T1e* makes the voxel-wise distinction of the T1-enhancement difficult, since it could easily lead to false positive detection of T1-enhancement. Although it is possible that it could reflect some leakage in the blood brain barrier not appreciable in conventional images [31, 104], also it could be that only applying a threshold to the pre-contrast quantitative images has moderate ability to detect T1-enhancement, as it was previously published for Multiple Sclerosis lesions [105]. Further investigation could depict more insights in this regard.

Furthermore, the analysis done on tumors showed that it is possible to discriminate between tumors with and without T1-enhancement with AUCs > 0.6 [115] in almost all the cases, and providing a sensitivity, specificity and accuracy up to 73%. It is challenging due to the similarities of the quantitative T1 and T2 values of the tumor tissue with and without T1-enhancement. Still, it seems that the process of contrast leakage is correlated with the structural information obtained in the pre-contrast scans. The exact mechanisms should be investigated further, but these findings suggest the possibility of detecting blood barrier damage using quantitative images without contrast-agent injection. This study is limited because of the small number of patients and the use of ROI statistics. Hence, the results encourage further investigation using quantitative imaging to predict T1-enhancement. Also, intentionally this study excluded the analysis in the same fashion of weighted images, since we consider the rapid acquisition of MAGiC as a big advance in MRI.

Avoiding contrast agent could mean an improvement for brain tumor patients who need to undergo repeated MRI acquisitions. Some work was previously done using fast quantitative imaging to detect T1-enhancement. Although successful, in these cases contrast-agent injection was needed [31]. Equally relevant is the reduced scan time (less than 6 minutes for the whole brain) compared to the 20 to 30 minutes for a conventional protocol [93, 94].

To validate these findings more patients should be analyzed. Furthermore, the finding that pre-contrast quantitative imaging is predictive for the T1-enhancing region is applicable only to gliomas and it may be not the case for other diseases, as other authors showed negative results in detecting T1-enhancement in patients with Multiple Sclerosis lesions without injecting contrast-agent using quantitative imaging [105].

Classification of voxels in nWM, T1e and T2h could probably be improved, e.g. by taking into account neighboring voxels or more advanced deep learning based classification techniques as also used in the HD-GLIO tool. Also, the possibility of accurately determining the enhancement status of some tumors could prevent the use of contrast-agent in those. Additionally, such probabilistic prediction could be useful in cases where contrast agent is not available or cannot be administered.

In this work we aimed to identify the information present in the individual voxels as ultimately that forms the basis for any such more advanced technique.

3.5. CONCLUSIONS

The data analyzed in this work shows there are clear differences in the T1 and T2 quantitative values for the tumoral tissue and healthy tissue. Also, in glioma the pre-contrast Euclidian norm of the quantitative T1 and T2 values is predictive for the post-contrast enhancing tumor. PD was not relevant in this study but it presents different characteristics than the T1 and T2 values, suggesting that more complex analysis could benefit from the quantitative PD values. This work encourages further exploration of quantitative imaging in brain gliomas with the possibility of reducing scan-time and avoiding contrast-agent administration.

FUNDING

This research was funded by General Electric Healthcare, grant number B-GEHC-5 GE for the project MR Physiological Signature and The APC was funded by Erasmus Medical Center. Part of the study was funded by HollandPTC-Varian consortium-confined call 2018, grant number 2018013, for the project "Improving toxicity modelling, patient selection and clinical out-come of proton therapy in low grade glioma.

INSTITUTIONAL REVIEW BOARD STATEMENT

The study was conducted according to the guidelines of the Declaration of Helsinki, and approved by the Institutional Review Board of Erasmus Medical Center (protocol code:NL64907.078.18, Date of approval:18-09-2019).

AUTHOR CONTRIBUTIONS

Conceptualization, L.N.G., D.H.J.P and J.A.H.T; methodology, L.N.G., D.H.J.P and J.A.H.T; software, L.N.G. and K.A.G.; validation, L.N.G., M.S., D.H.J.P. and J.A.H.T.; formal analysis, L.N.G, D.H.J.P. and J.A.H.T.; investigation L.N.G, D.H.J.P. and J.A.H.T.;

resources, L.N.G., K.A.G, M.S., J.J, A.M.R, D.H.J.P and J.A.H.T.; data curation, L.N.G., M.S and J.A.H.T.; writingoriginal draft preparation, L.N.G; writingreview and editing, L.N.G, K.A.G, M.S., J.J, A.M.R., D.H.J.P and J.A.H.T.; supervision, D.H.J.P. and J.A.H.T.; project administration, J.A.H.T.; funding acquisition, A.M.R. and J.A.H.T. All authors have read and agreed to the published version of the manuscript.

CONFLICTS OF INTEREST

The authors declare no conflict of interest.

3.6. SUPPLEMENTARY MATERIAL

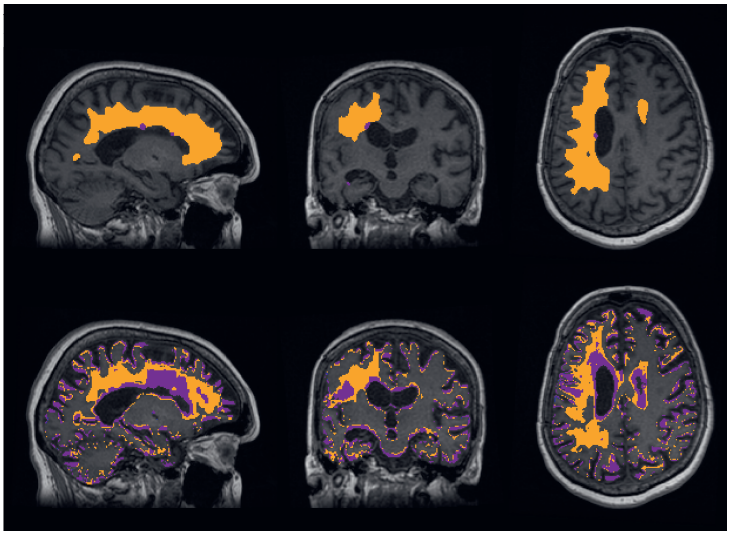

Figure 3.7: Patient 1. Sagittal, coronal and axial planes of the segmentations overlaid on the T1w scan. Top: segmentation from HD-GLIO, T2h in orange and T1e in purple. Bottom: TUM* in orange and T1e* in purple. The purple T1e* region is overlapped with the orange TUM*.

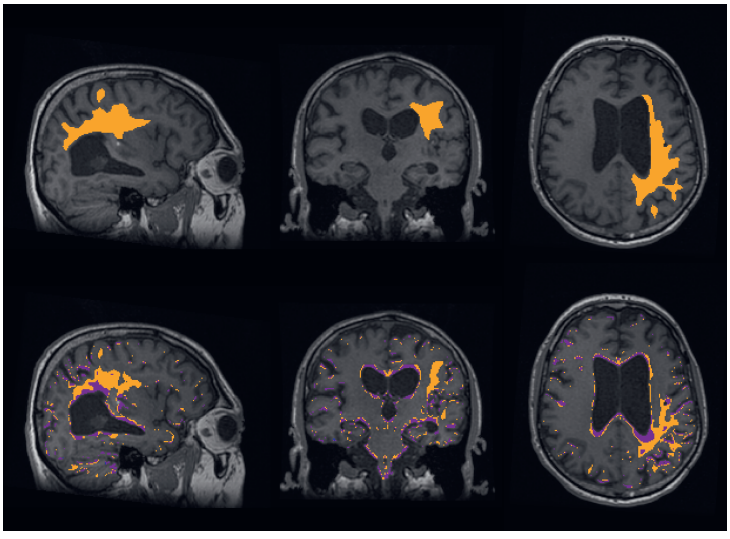

Figure 3.8: Patient 2. Sagittal, coronal and axial planes of the segmentations overlaid on the T1w scan. Top: segmentation from HD-GLIO, T2h in orange and T1e in purple. Bottom: TUM* in orange and T1e* in purple. The purple T1e* region is overlapped with the orange TUM*.

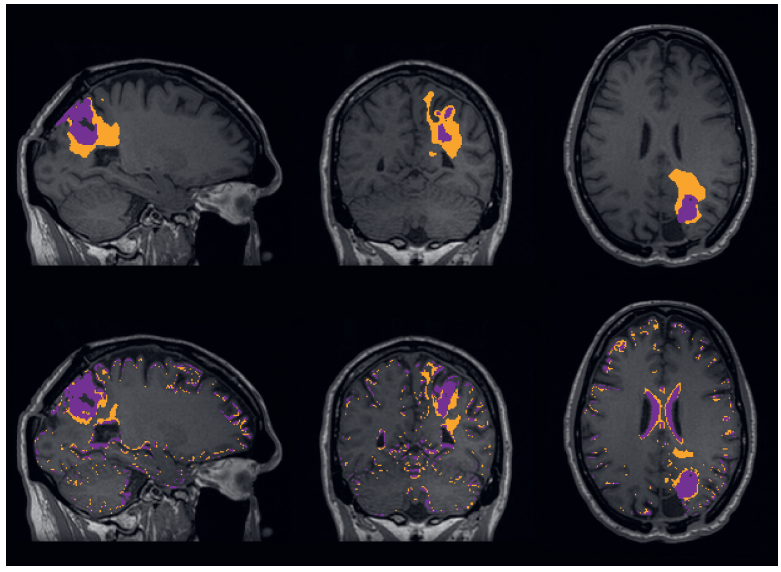

Figure 3.9: Patient 4. Sagittal, coronal and axial planes of the segmentations overlaid on the T1w scan. Top: segmentation from HD-GLIO, T2h in orange and T1e in purple. Bottom: TUM* in orange and T1e* in purple. The purple T1e* region is overlapped with the orange TUM*.

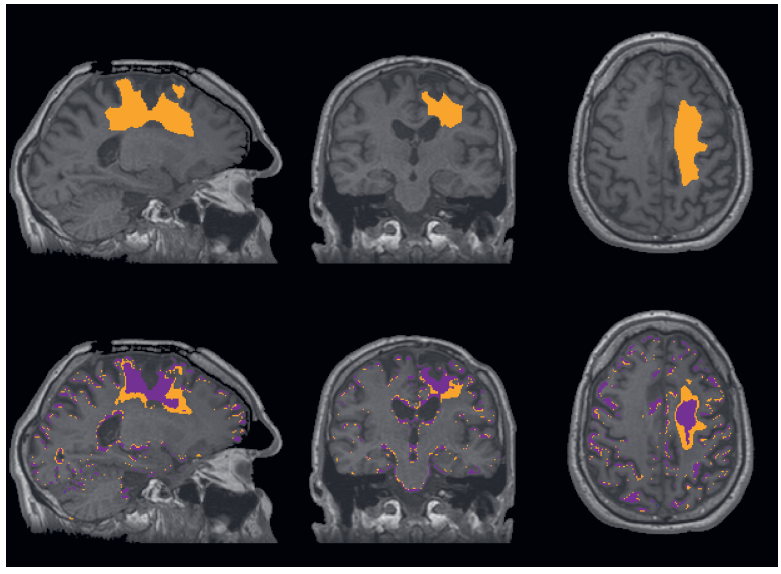

Figure 3.10: Patient 5. Sagittal, coronal and axial planes of the segmentations overlaid on the T1w scan. Top: segmentation from HD-GLIO, T2h in orange and T1e in purple. Bottom: TUM* in orange and T1e* in purple. The purple T1e* region is overlapped with the orange TUM*.

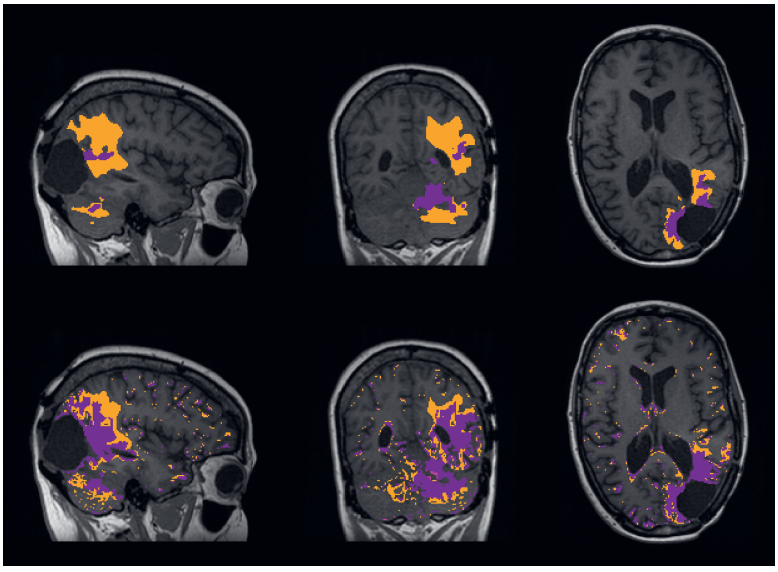

Figure 3.11: Patient 6. Sagittal, coronal and axial planes of the segmentations overlaid on the T1w scan. Top: segmentation from HD-GLIO, T2h in orange and T1e in purple. Bottom: TUM* in orange and T1e* in purple. The purple T1e* region is overlapped with the orange TUM*.

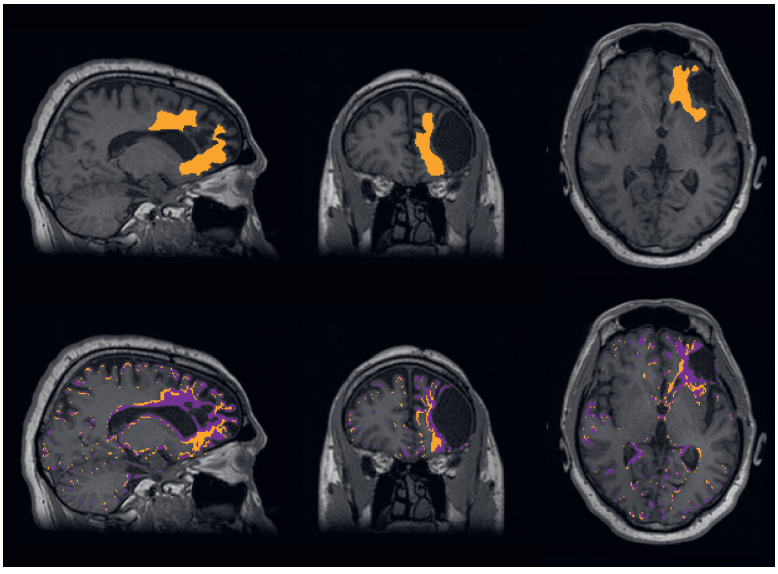

Figure 3.12: Patient 7. Sagittal, coronal and axial planes of the segmentations overlaid on the T1w scan. Top: segmentation from HD-GLIO, T2h in orange and T1e in purple. Bottom: TUM* in orange and T1e* in purple. The purple T1e* region is overlapped with the orange TUM*.

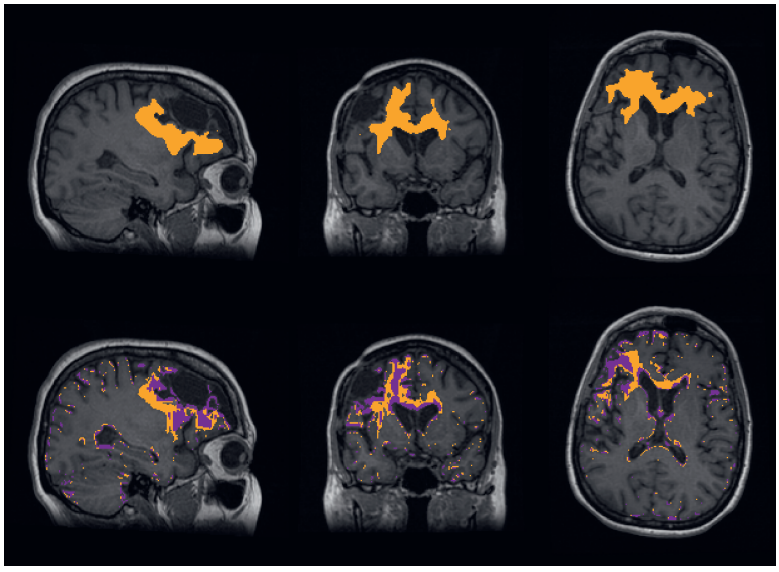

Figure 3.13: Patient 8. Sagittal, coronal and axial planes of the segmentations overlaid on the T1w scan. Top: segmentation from HD-GLIO, T2h in orange and T1e in purple. Bottom: TUM* in orange and T1e* in purple. The purple T1e* region is overlapped with the orange TUM*.

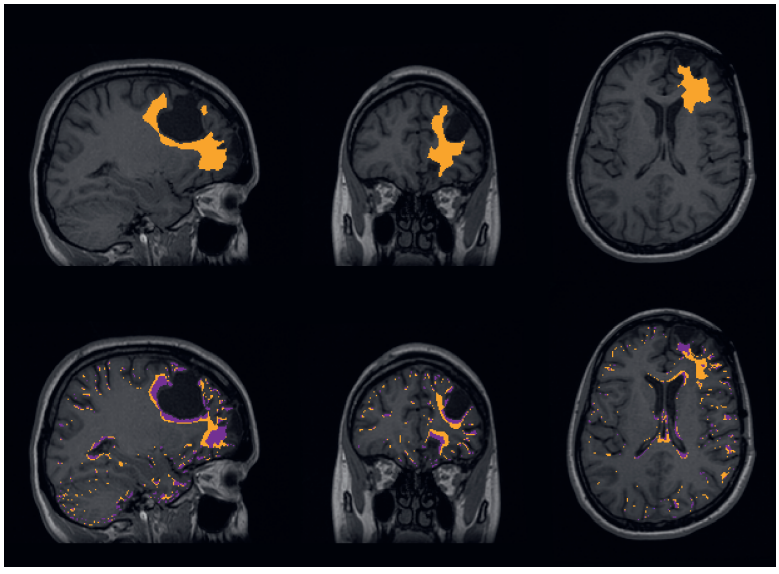

Figure 3.14: Patient 9. Sagittal, coronal and axial planes of the segmentations overlaid on the T1w scan. Top: segmentation from HD-GLIO, T2h in orange and T1e in purple. Bottom: TUM* in orange and T1e* in purple. The purple T1e* region is overlapped with the orange TUM*.

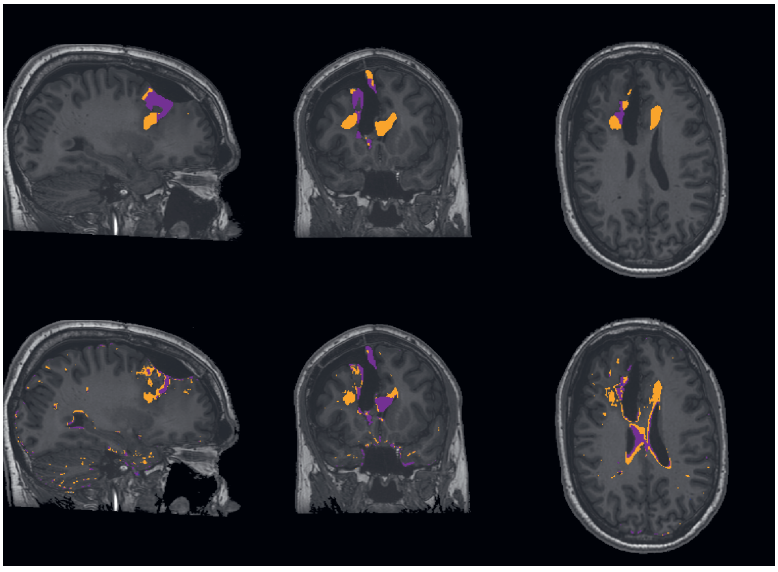

Figure 3.15: Patient 10. Sagittal, coronal and axial planes of the segmentations overlaid on the T1w scan. Top: segmentation from HD-GLIO, T2h in orange and T1e in purple. Bottom: TUM* in orange and T1e* in purple. The purple T1e* region is overlapped with the orange TUM*.

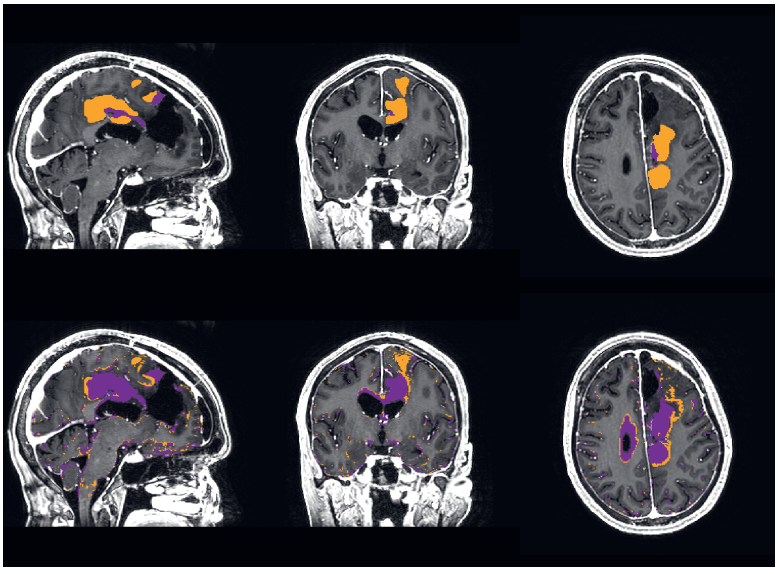

Figure 3.16: Patient 11. Sagittal, coronal and axial planes of the segmentations overlaid on the T1w scan. Top: segmentation from HD-GLIO, T2h in orange and T1e in purple. Bottom: TUM* in orange and T1e* in purple. The purple T1e* region is overlapped with the orange TUM*.

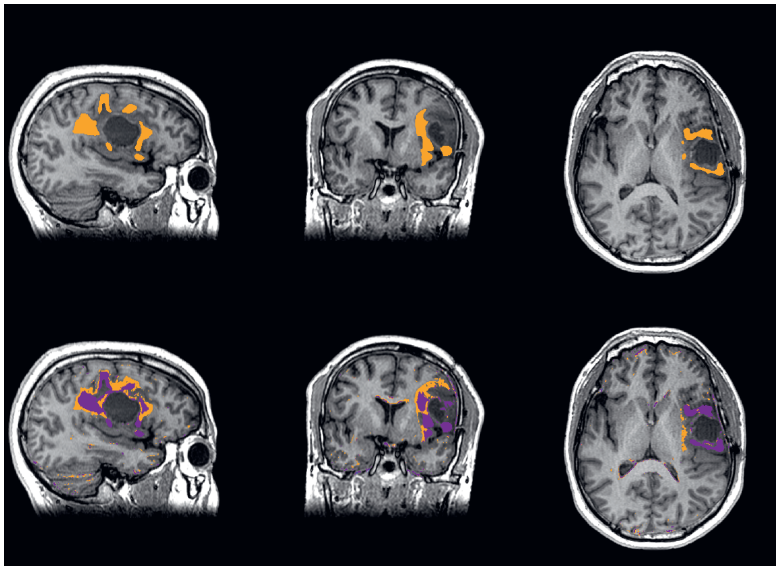

Figure 3.17: Patient 12. Sagittal, coronal and axial planes of the segmentations overlaid on the T1w scan. Top: segmentation from HD-GLIO, T2h in orange and T1e in purple. Bottom: TUM* in orange and T1e* in purple. The purple T1e* region is overlapped with the orange TUM*.

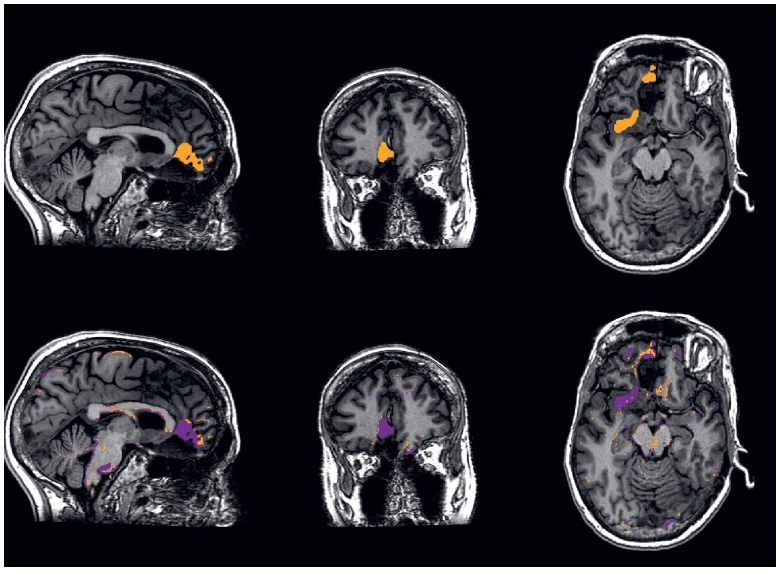

Figure 3.18: Patient 13. Sagittal, coronal and axial planes of the segmentations overlaid on the T1w scan. Top: segmentation from HD-GLIO, T2h in orange and T1e in purple. Bottom: TUM* in orange and T1e* in purple. The purple T1e* region is overlapped with the orange TUM*.

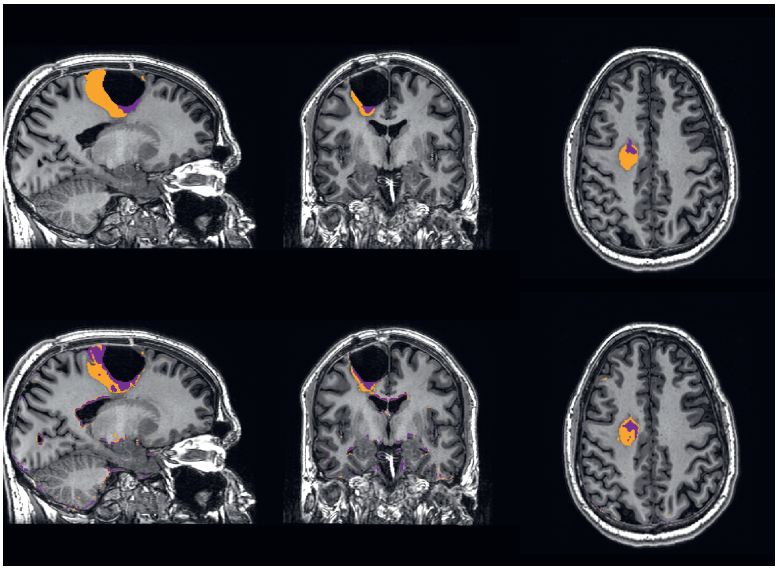

Figure 3.19: Patient 14. Sagittal, coronal and axial planes of the segmentations overlaid on the T1w scan. Top: segmentation from HD-GLIO, T2h in orange and T1e in purple. Bottom: TUM* in orange and T1e* in purple. The purple T1e* region is overlapped with the orange TUM*.

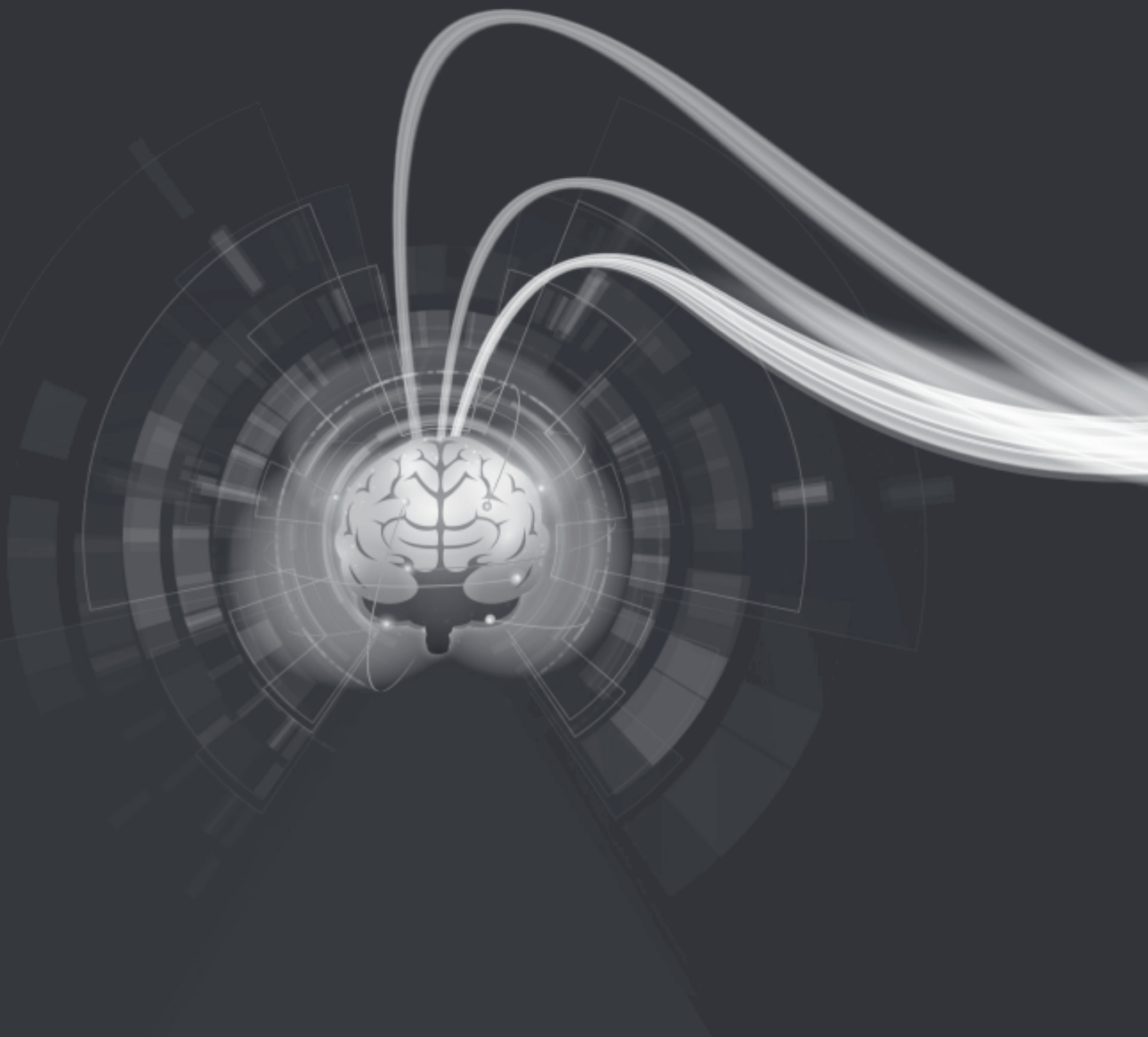

4

ACCURACY AND REPEATABILITY OF JOINT SPARSITY MULTI-COMPONENT ESTIMATION IN MR FINGERPRINTING

Laura NUNEZ-GONZALEZ[1,*], Martijn NAGTEGAAL[2,*], Dirk POOT[1], Jeroen DE BRESSER[3], Matthias VAN OSCH[4], Juan HERNANDEZ-TAMAMES[1,2], Frans VOS[1,2]

1 *Department of Radiology and Nuclear Medicine, Erasmus Medical Center, Rotterdam, the Netherlands*

2 *Department of Imaging Physics, Delft University of Technology, Delft, the Netherlands*

3 *Department of Radiology, Leiden University Medical Center, Leiden, the NetherlandsIMAGO7 Foundation, Pisa, Italy*

4 *C.J. Gorter Center for High Field MRI, Radiology Department, Leiden University Medical Center, Leiden, the Netherlands*

* *These authors contributed equally*

Submitted

Abstract

MR fingerprinting (MRF) is a promising method for quantitative characterization of tissues. Traditionally, voxel-wise measurements are made, assuming a single tissue-type per voxel. Alternatively, the Sparsity Promoting Iterative Joint Non-negative least squares Multi-Component MRF method (SPIJN-MRF) facilitates tissue parameter estimation for identified components as well as partial volume segmentations.

The aim of this paper was to evaluate the accuracy and repeatability of the SPIJN-MRF parameter estimations and partial volume segmentations. This was done (1) through numerical simulations based on the BrainWeb phantoms and (2) using in-vivo acquired MRF data from 5 subjects that were scanned on the same week-day for 8 consecutive weeks. The partial volume segmentations of the SPIJN-MRF method were compared to those obtained by two conventional methods: SPM12 and FSL.

SPIJN-MRF showed higher accuracy in simulations in comparison to FSL- and SPM12-based segmentations: Fuzzy Tanimoto Coefficients (FTC) comparing these segmentations and Brainweb references were higher than 0.95 for SPIJN-MRF in all the tissues and between 0.6 and 0.7 for SPM12 and FSL in white and gray matter and between 0.5 and 0.6 in CSF. For the in-vivo MRF data, the estimated relaxation times were in line with literature and minimal variation was observed. Furthermore, the coefficient of variation (CoV) for estimated tissue volumes with SPIJN-MRF were 10.5% for the myelin water, 6.0% for the white matter, 5.6% for the gray matter, 4.6% for the CSF and 1.1% for the total brain volume. CoVs for CSF and total brain volume measured on the scanned data for SPIJN-MRF were in line with those obtained with SPM12 and FSL. The CoVs for white and gray matter volumes were distinctively higher for SPIJN-MRF than those measured with SPM12 and FSL.

In conclusion, the use of SPIJN-MRF provides accurate and precise tissue relaxation parameter estimations taking into account intrinsic partial volume effects. It facilitates obtaining tissue fraction maps of prevalent tissues including myelin water which can be relevant for evaluating diseases affecting the white matter.

Keywords: Repeatability, accuracy, multi-component MR Fingerprinting, segmentation, brain, quantitative MRI

4.1. INTRODUCTION

Quantitative magnetic resonance imaging is getting increasingly more attention since several fast, multiparametric quantitative methods have emerged, e.g. MR-Fingerprinting (MRF) [15] and QRAPMASTER [14]. The reduced scan-time of these acquisitions has facilitated their usefulness in research and clinical protocols [33, 34, 102, 116, 117]. While these approaches can have a rich sensitivity to a wide range of tissue properties, the measurements are traditionally made voxel-wise, assuming a single tissue-type per voxel. However, partial volume effects are known to hinder this so-called single component approach [36–39]. Several methods were proposed facilitating multi-parameter estimates for a range of tissue components in a voxel. Examples of such multi-component techniques for MRF are modelling the signal with 3 a priori defined tissues [15], a Bayesian approach [46] and a reweighted-L1-norm regularized algorithm [47]. However these methods are limited by long computation times and a restricted number of pre-defined tissues within a voxel.

Another recently published method for coping with different tissue types within a voxel is the Sparsity Promoting Iterative Joint Non-negative least squares algorithm that was applied to MRF data [48] (SPIJN-MRF). This approach asserted joint sparsity of the number of tissue components in a region of interest, i.e. in a voxel as well as spatially. A priori no assumptions are made about the number of tissues and relaxation times while the method still proved faster than previously proposed techniques. As such it yields tissue parameters for each identified tissue component as well as tissue volume fraction maps. The SPIJN-MRF algorithm estimated brain tissue fraction maps from fully sampled MRF data with promising accuracy and precision [48]. These maps particularly showed components representing myelin water, white matter (WM), gray matter (GM) and cerebrospinal fluid (CSF) components.

Although the initial results with the SPIJN-MRF method were encouraging, an extensive study into the accuracy and precision of the method has not yet been performed. Additionally, it is unknown how the obtained brain tissue fraction maps relate to existing methods for tissue segmentations.

The aim of this work is to evaluate the accuracy and repeatability of the SPIJN-MRF parameter estimations from highly undersampled MRF acquisitions. The accuracy of the method will be assessed through estimation of the relaxation times and tissue fractions on simulated data from the BrainWeb numerical phantom environment, including a comparison to conventional techniques: the Functional Magnetic Resonance Imaging of the Brain Software Library (FSL) and the Statistical Parametric Mapping Software (SPM12). Furthermore, the repeatability will be assessed through the parameter estimates in eight weekly repeated scan sessions in 5 healthy volunteers. As

in the simulations, tissue fraction maps will be compared to the SPM12 and FSL segmentations.

4.2. METHODS

4.2.1. SIMULATIONS

Numerical simulations using the 20 BrainWeb phantoms [118] were performed to test the accuracy and precision of the segmentations obtained with SPIJN-MRF and T1 weighted based methods (FSL,SPM12). Simulations were performed with resolution 1x1x5mm^3. T2 values were as defined in the BrainWeb database, but for white and gray matter T1=930 ms and 1300ms were used instead of 500 ms and 830 ms as these are more realistic relaxation times for 3T [25, 83].

The MRF data was created by simulating a gradient-spoiled MRF sequence with a train of 1000 radiofrequency pulses as in [49]. This was done by performing extended phase graph signal generation [17, 119] for each tissue after which a weighted combination of the signals based on the BrainWeb partial volume fractions yielded the MRF images. Subsequently, independent random complex Gaussian noise with standard deviation $\sigma = max(abs(X))/100$ was added to each MRF image Xi, to yield the same noise level for all voxels and time points. No undersampling was performed in these simulations to remain comparable to previous studies and out of practicality since undersampling would require a realistic multi-coil model e.g. including transmit phase effects and noise correlations.

The T1 weighted images were also simulated by the BrainWeb simulator after which Rician noise was added with noise level parameter $\sigma = max(abs(signal))/100$. The input tissue parameters and partial volume segmentations from the BrainWeb database served as ground truth values.

4.2.2. IN VIVO DATA ACQUISITION

In vivo acquisitions were performed on a 3.0T GE MR750 MRI scanner (General Electric, Milwaukee, WI, USA). A Head, Neck and Spine array coil was used from which the 12 channels dedicated to the head were used for imaging.

Five healthy volunteers (3 females and 2 males, between 18-25 years) participated in this Institutional Review Board-approved study. All volunteers gave written informed consent to usage of their data prior to the first scan session.

MRF imaging was performed on the same day of the week for 8 consecutive weeks. As such the same gradient-spoiled MRF sequence as in the simulations was applied, varying the flip angle and the TR along a train of 1000 radiofrequency pulses [49]. The acquisition was performed with a FOV of 31 cm and slice thickness of 5 mm and slice

gap of 1 mm (voxel size 1.2 mm x 1.2 mm x 5 mm). Total number of slices was 27, consisting of 256 x 256 voxels. The total scan time was 5 minutes and 54 seconds.

In each session, a READYBrain sequence [68] was applied to align the MRF acquisitions to the AC-PC plane. READYBrain automatically detects the AC-PC plane for each subject and exploits this to plan the MRF with comparable imaging orientation across time and subjects.

Slices showing motion artefacts (known to affect 2D-MRF data [120–123]) were visually identified and excluded from the analysis, unless explicitly stated otherwise.

4.2.3. IMAGE RECONSTRUCTION

The acquired MRF data was reconstructed using an in-house implemented low-rank (LR) reconstruction algorithm in which the LR images were obtained while a compression matrix was iteratively updated. The spatial L1 norm of the L2 norm across the component images was applied for regularization purposes. A complete description of the used method can be found in Appendix 4.6.

4.2.4. SINGLE AND MULTI-COMPONENT PARAMETER ESTIMATION

A dictionary was precomputed with the extended phase graph algorithm [17, 119]. This dictionary was created for T1 values ranging from 100 ms to 3042 ms and T2 values from 10 ms to 1030 ms, sampled with increasing step sizes by 5% (chosen as a compromise between dictionary size and resolution). Synthetic T1 weighted images were calculated based on the T1, T2 and M0 maps estimated by single-component dictionary matching. Applied settings were: TE = 25 ms, TR = 300 ms, FA = 90 degree. We chose to generate synthetic T1 weighted images from the same data to have perfect spatial correspondence of the MRF and T1 weighted data. As such differences in imaged volume were avoided. Based on the synthetic T1 weighted images a brain mask was created using FSL-BET [55].

Subsequently, the SPIJN-MRF algorithm [48] was applied to the MRF data, to obtain multi-component estimations for the tissues present in the brain mask region. The SPIJN-MRF algorithm is based on the following optimization function:

$$\hat{C} = \underset{C \in \mathbb{R}_{\geq 0} N_A x J}{\arg\min} ||X - DC||_F^2 + \lambda \sum_i^N ||C_i||_0 \tag{4.1}$$

Where X are the (compressed) MRF images with J voxels per time frame, D is the (compressed) dictionary with N_A atoms and C consists of N_A tissue fraction maps Ci of J voxels. The regularization parameter balances the data fidelity and joint sparsity regularization terms. Multi-component estimations were performed for all slices simultaneously. This yielded tissue parameters and magnetization fractions per voxel.

Note that the number of tissues is not fixed a priori, but controlled through a sparseness constraint. A regularization value of 0.03 was used in the multi-component analysis. This regularization level was manually determined for one in-vivo dataset and kept constant with all subsequent numerical and in vivo analyses.

4.2.5. SPM12 AND FSL SEGMENTATIONS

The conventional methods were applied to the synthetic T1 weighted images (created as described above). FSL-FAST [55, 124] was applied after brain extraction (through FSL-BET) to obtain tissue segmentations while using default settings. SPM12 segmentation [56, 74] was also used with default settings, but the sampling distance was set to 1 instead of 3 to produce the most accurate segmentations (at the cost of consuming more time and memory resources). Tissue volumes in a voxel were calculated by multiplying obtained tissue probabilities in a voxel from SPM12 and FSL with the voxel size.

4.2.6. ATLAS REGISTRATION

To facilitate assessment of particular brain regions, all imaging data was aligned to the ICBM 152 Nonlinear atlases version 2009 [125, 126]. This alignment was based on the synthetic T1-weighted images using the Diffeomorphic Anatomical Registration through Exponentiated Lie algebra (DARTEL) algorithm [76] as implemented in SPM12 [56]. Subsequently, the obtained deformations were applied to all SPIJN-MRF, SPM12 and FSL partial volume segmentations to achieve voxel-wise alignment to the atlas. All subsequent analyses focused on a common brain region, specifically: the region for which the mean intracranial volume fraction per voxel (WM+GM+CSF) was at least 75% with all segmentation methods.

4.2.7. ANALYSIS

TISSUE DISCRIMINATION

From the SPIJN-MRF parameter estimations, different components were identified based on the relaxation times, see Table 4.1 [11, 25, 41, 43, 83]: myelin water, white matter (excluding myelin water), gray matter, CSF and veins and arteries. CSF was partitioned into a short and long T2 component after inspection of first results, as was observed in [48]. Simultaneously, components with T1 and T2 relaxation times around 1s were identified, which we associated with veins and arteries. Total tissue volumes were calculated by summing the tissue fraction estimates multiplied by the voxel size (using an effective slice thickness of 6 mm to correct for slice gap).

Table 4.1: Ranges used to categorize SPIJN-MRF tissue/material components [11, 25, 41, 43, 83]

Name	T1 range [ms]	T2 range [ms]
White matter (without myelin water)	800 - 1050	50 - 100
Gray matter	1050 - 1500	50 - 100
CSF short T2	2000 - 4000	9 - 300
CSF long T2	2000 - 4000	300 - 2000
Myelin water	99 - 500	9 - 20
Veins and arteries	500 - 2000	200 - 1200

ANALYSIS OF ACCURACY

The accuracy, i.e. systematic error, of the obtained SPIJN-MRF, and SPM12 and FSL segmentations was evaluated using the simulated data. The agreement between estimated total white matter (including myelin water), gray matter and CSF volumes and the reference volumes was evaluated through Bland-Altman style plots. These showed the deviation from the reference as a function of reference value. Furthermore, the voxel-wise similarity between estimated partial volume and reference was assessed using the Fuzzy Tanimoto Coefficient (FTC) [35], which expresses the similarity of paired data as

$$FTC(A,B) = \frac{\sum_{i \in \Omega_{ROI}} MIN(A_i, B_i)}{\sum_{i \in \Omega_{ROI}} MAX(A_i, B_i)} \tag{4.2}$$

where A,B is a pair of tissue fraction maps of a complete volume, specific region or slice; subscript i represents a spatial index of the concerned voxels. The FTC is an adaptation of the Jaccard index or Tanimoto coefficient for non-binary segmentations.

ANALYSIS OF REPEATABILITY

The repeatability of the SPIJN-MRF method was determined for the tissue parameter estimations and partial volume segmentations on the in vivo imaging data. First, the mean and standard deviation of the SPIJN-MRF relaxation times were calculated per subject and tissue over the eight different time points. Subsequently, the repeatability was evaluated based on the range of standard deviations across the subjects per tissue. Second, the repeatability of tissue volume estimation of the SPIJN-MRF and conventional methods over the time points was evaluated voxel-wise, in different brain regions and for the entire brain per tissue. In each case the mean value and corresponding standard deviation was determined per subject across the time points. The repeatability was quantified using the Coefficients of Variation ($CoV = \frac{\sigma}{\mu}$, where σ

is the standard deviation and μ is the mean of the tissue volume over the 8 scan sessions) and the Combined Fuzzy Tanimoto Coefficient (CFTC) [35] for each subject and tissue

$$CFTC(A) = \frac{\sum_{k=1}^{\#days-1} \sum_{j=k+1}^{\#days} \sum_{i \in \Omega_{ROI}} MIN(A_{ki}, B_{ji})}{\sum_{k=1}^{\#days-1} \sum_{j=k+1}^{\#days} \sum_{i \in \Omega_{ROI}} MAX(A_{ki}, B_{ji})} \tag{4.3}$$

where A_{ki} denotes the volume fraction of voxel i at day k for a subject and tissue of interest.

COMPARISON WITH CONVENTIONAL METHODS

Initially, comparison of the methods was performed by visual assessment of the segmentation maps. Subsequently, estimated total tissue volumes for the entire brain and per region were compared across the methods. While doing so, the volume fractions obtained with SPIJN-MRF for white matter and myelin water were summed into a single white matter tissue. Similarly, the SPIJN-MRF CSF fractions of long and short T2 times were summed to yield the total CSF partial volumes. CoVs and CFTCs for total brain tissue volumes were calculated including and excluding the slices with motion artefacts to evaluate the effect of these artifacts on the repeatability.

4.3. RESULTS

4.3.1. SIMULATIONS

SPIJN-MRF yielded exact estimates of underlying T1 and T2 tissue parameters in all 20 datasets. Figure 4.1 shows representative partial volume segmentations obtained with SPIJN-MRF, SPM12 and FSL. Observe that the SPIJN-MRF images closely resemble the ground truth with soft transitions between tissue and background, while these transitions are sharper in the SPM12 and FSL segmentations.

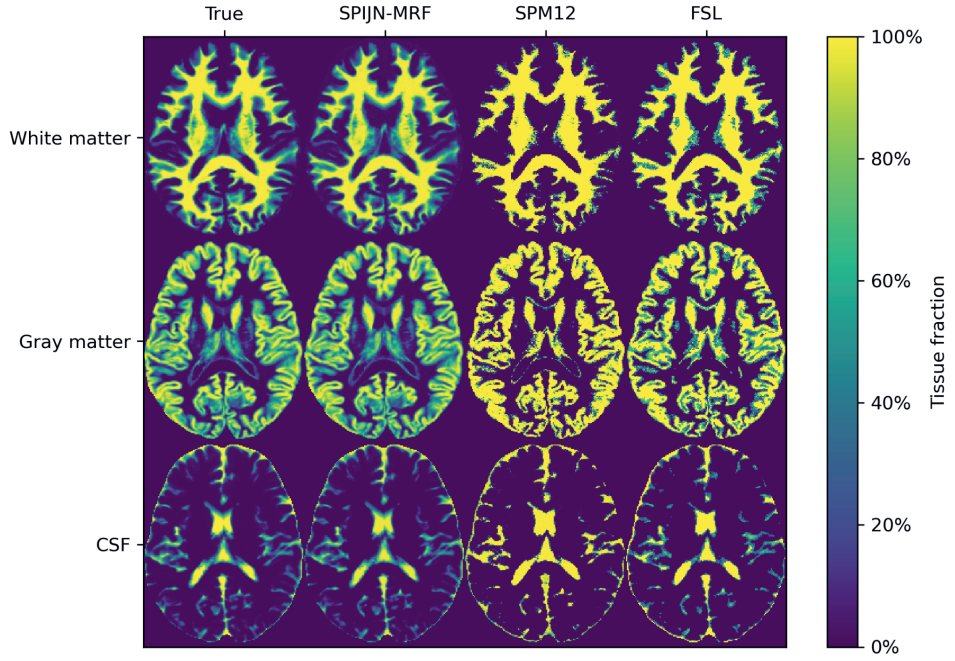

Figure 4.1: Representative example of partial volume segmentations obtained with multi-component MRF, SPM12 and FSL in simulations based on a BrainWeb phantom (first column) for a central slice.

Figure 4.2 shows Bland-Altman style plots, for each subject, method and the three tissues of interest, with the deviation from the true total tissue volume (vertically) as a function of the true value (horizontally).The mean deviations from the true value are indicated by solid lines. Limits of agreement are delineated by the light blue regions. It can be observed that SPIJN-MRF and FSL showed little bias (defined as only a small deviation from the true value), whereas marked bias was found with SPM12. All three methods had the lowest bias in gray matter compared to the other tissues (max 3.3 cm^3 for SPM12). SPM12 had the largest bias for white matter (mean deviation -78.4 cm^3). The limits of agreements between the estimated volumes and the reference values were smaller for SPIJN-MRF than for SPM12 and FSL, indicating that the differences between SPIJN-MRF estimations and the true values vary less than for SPM12 and FSL. SPM12 had the largest spread in the limits of agreements, which indicates a lower precision.

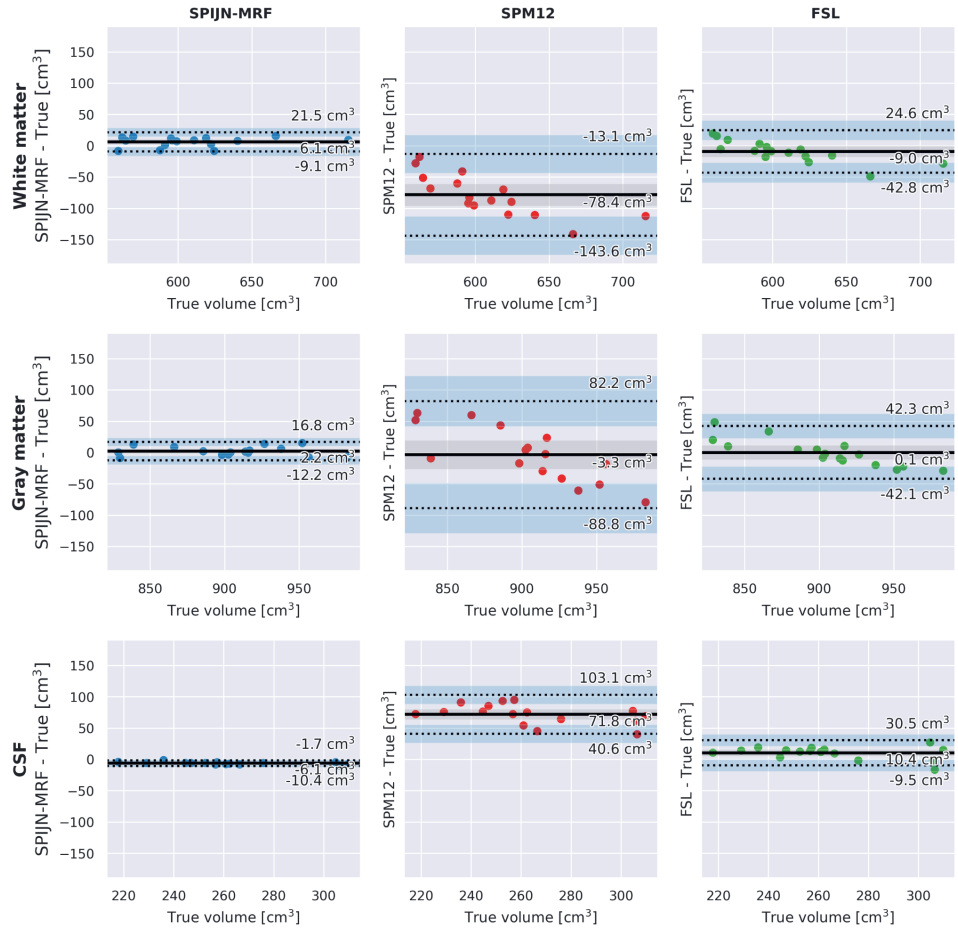

Figure 4.2: Bland-Altman style plots showing the deviation (vertically) from the true volume in the 20 BrainWeb phantom volumes obtained with the SPIJN-MRF (left), SPM12 (middle), and FSL (right) methods. The solid lines indicate the mean deviation in each plot (i.e. the bias), the exact value of which is indicated next to each line. Dotted lines reflect the limits of agreement (1.96 times the standard deviation of the bias). Shadowed areas in gray and blue delineate the 95% confidence interval of the mean and the limits of agreement respectively.

Figure 4.3 shows the distribution of FTCs obtained with SPIJN-MRF, SPM12 and FSL. In all the tissues, the segmentations performed by SPIJN-MRF were the most similar to the true segmentations, with FTCs around 0.97. SPM12 and FSL had lower FTCs: between 0.6 and 0.7 for white and gray matter and between 0.5 and 0.6 for CSF, respectively. Segmentations made with FSL had slightly higher FTCs than segmentations with SPM12. FTCs varied across slices, following a similar trend as the total amount of tissue per slice (see Supplementary Figure 4.1). A fixed SNR level (100)

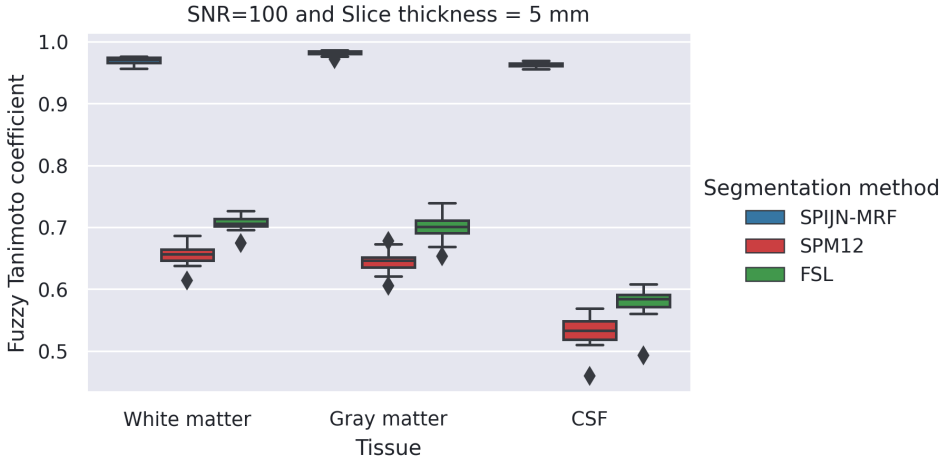

Figure 4.3: Box plots showing distributions of the Fuzzy Tanimoto Coefficient (FTC) for white matter (left), gray matter (middle), and CSF (right) comparing the 20 BrainWeb phantoms and the tissue segmentations using SPIJN-MRF(blue), SPM12 (red), and FSL (green).

was used in the shown results, in additional experiments different noise levels led to similar findings (data not shown).

4.3.2. IN VIVO DATA ANALYSES

A total of 10 MRF acquisitions (out of 40) were affected by motion artefact in one or more slices. It concerned 3% of the total number of slices.

TISSUE DISCRIMINATION

Figure 4.4 shows all components resulting from the MRF data of a single acquisition across several slices from one representative subject. The leftmost column shows the T1 and T2 values for each of 9 identified components while the images depict corresponding estimated tissue fractions.

In figure 4.5, the main component maps obtained after grouping as per Table 4.1 for a central slice from the same subject are depicted for each acquisition day (prior to registration). Observe that there are minimal differences over time. Global intensity variations can be observed in the myelin water map (in particular concerning scans 5 and 6 seem to yield higher tissue fractions).

Table 4.2 collates the means and standard deviations of T1 and T2 relaxation times across all subjects and scans per tissue as well as the mean intra-subject standard deviations per tissue. On average 8.3 components were identified over all acquisitions (26 times 8 components, 13 times 9 and 1 time 10). The mean intrasubject standard

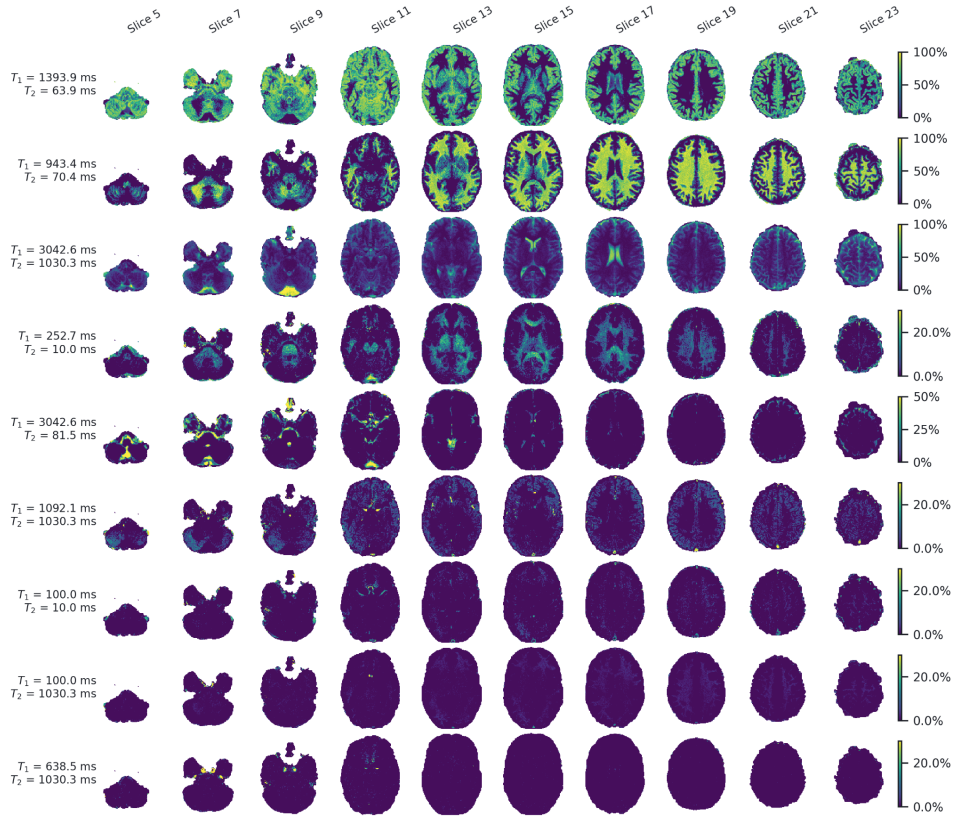

Figure 4.4: Multi-component tissue fraction maps for one MRF dataset of a single subject. Obtained T1 and T2 relaxation times are shown in the left column. All non-zero component maps are shown. Note that the component maps are only estimated inside the brain mask. For illustration purposes only the ten central odd slices are shown instead of the total 28 slices.

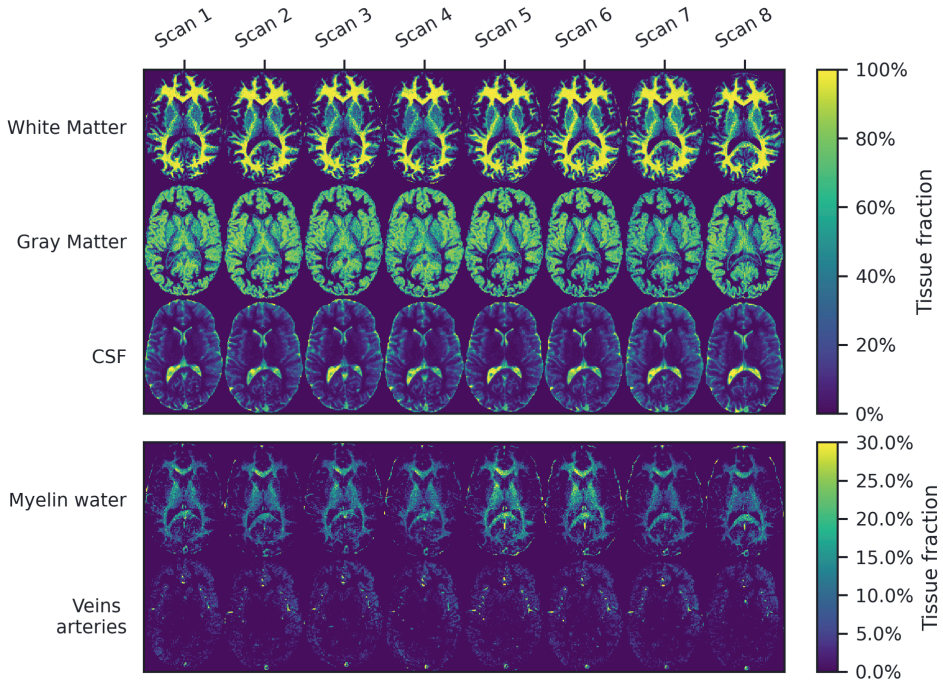

Figure 4.5: SPIJN-MRF maps across days and tissue types are for a central slice for one subject after grouping based on relaxation time and before registration. Note that the lower two rows use a different color range for illustration purposes.

deviations of myelin water and veins and arteries for T1 estimation and of short CSF for T2 estimation was larger than 10% percent of the reported mean value. For all other tissues the intrasubject standard deviations of T1 and T2 relaxation times showed small variation.

After changing the dictionary ranges the observed clipping to the dictionary boundaries appeared persistent and visually did not appear to affect the estimated partial volume maps. Supplementary figure 4.11 shows scatter plots of the estimated T1 and T2 values across subjects and scans.

REPEATABILITY

Table 4.3 presents the CoVs of the total volume estimates of myelin water, white matter (including myelin water), gray matter, CSF and the total brain volume (WM + GM) across subjects. Total brain volume showed minor variation (mean CoV = 1.1 %); the volume estimates of CSF, GM and WM (including MW) were slightly more variable, with mean CoV of 4.6%, 5.6% and 6.0%, respectively, while MW by itself had higher mean CoV (10.5%).

COMPARISON WITH BRAIN VOLUME MEASUREMENT METHODS

Figure 4.6 illustrates that the SPIJN-MRF tissue maps from the in vivo data contained more gradual transitions between brain tissues than the conventional methods, similar to simulated data. For instance, the SPIJN-MRF CSF map shows small details not observed in the other maps (green circle) whereas parts are more confined in the SPM12 and FSL segmentations (red circle). Furthermore, the GM SPIJN-MRF component was almost always identified as a mixture of GM and CSF or WM components (maximal GM fraction around 90%). This highlights the ability of SPIJN-MRF to approximate brain tissue content of partial volume voxels.

The distributions of total volumes for each subject with SPIJN-MRF, SPM12 and FSL are collated in figure 4.7. It can be observed that SPM12 estimates are lower in white matter than FSL estimates, and consequently, the opposite is noticeable for gray matter and CSF as the sum of tissue percentages is 100% by definition. In general, the estimated volumes with SPIJN-MRF appear between the estimated volumes of SPM12 and FSL. Furthermore, the SPIJN-MRF volume distributions show a larger spread than those of SPM12 and FSL.

In figure 4.8, the estimated relative volumes per anatomical region for each tissue, method and subject are summarized (see supplementary figure 4.12 for absolute volumes per region). In general, the three methods had relatively similar relative volumes per region. However, for the cerebellum and for the deep gray matter FSL gave higher white matter volume than SPIJN-MRF and SPM12 in all subjects. As a consequence, FSL yielded lower gray matter volumes.

Table 4.2: Means and corresponding standard deviations of estimated T1 and T2 relaxation times across all 5 subjects and 8 repeated scans per tissue as well as the means of 5 intrasubject standard deviations per tissue. *T1 or T2 values are the minimum/maximum value represented in the dictionary, which also occured with extended boundaries.**White matter excluding myelin water.

Tissue	T1 (ms)		T2 (ms)	
	Mean ± Std across all subjects and scans	Mean intra-subject standard deviation	Mean ± Std across all subjects and scans	Mean intra-subject standard deviation
White matter**	943.4 ± 0.0	0.0	69.2 ± 1.2	2.5
Gray matter	1383.9 ± 10.8	17.7	62.3 ± 1.2	1.7
CSF longer T2	3042.6 ± 0.0*	0.0	1030.3 ± 0.0*	0.0
CSF shorter T2	3042.6 ± 0.0*	0.0	149.3 ± 9.4	18.3
Myelin water	230.7 ± 20.1	34.0	10.0 ± 0.0*	0.0
Veins and arteries	876.2 ± 93.9	106.7	1030.3 ± 0.0*	0.0

Table 4.3: CoVs of the estimated total myelin water volume, white matter volume (including myelin water), gray matter volume, CSF volume and total brain volume. The last column reports the mean of the CoVs over all subjects.

Tissue	Subject					Mean
	A	B	C	D	E	
Myelin water (MW)	13.7%	13.3%	4.4%	13.3%	7.6%	10.5%
White matter (including MW)	3.8%	6.4%	7.0%	4.7%	8.2%	6.0%
Gray matter	3.4%	5.5%	8.7%	3.7%	6.6%	5.6%
CSF	6.4%	6.5%	6.4%	2.1%	1.7%	4.6%
Brain volume	1.0%	1.7%	1.8%	0.5%	0.7%	1.1%

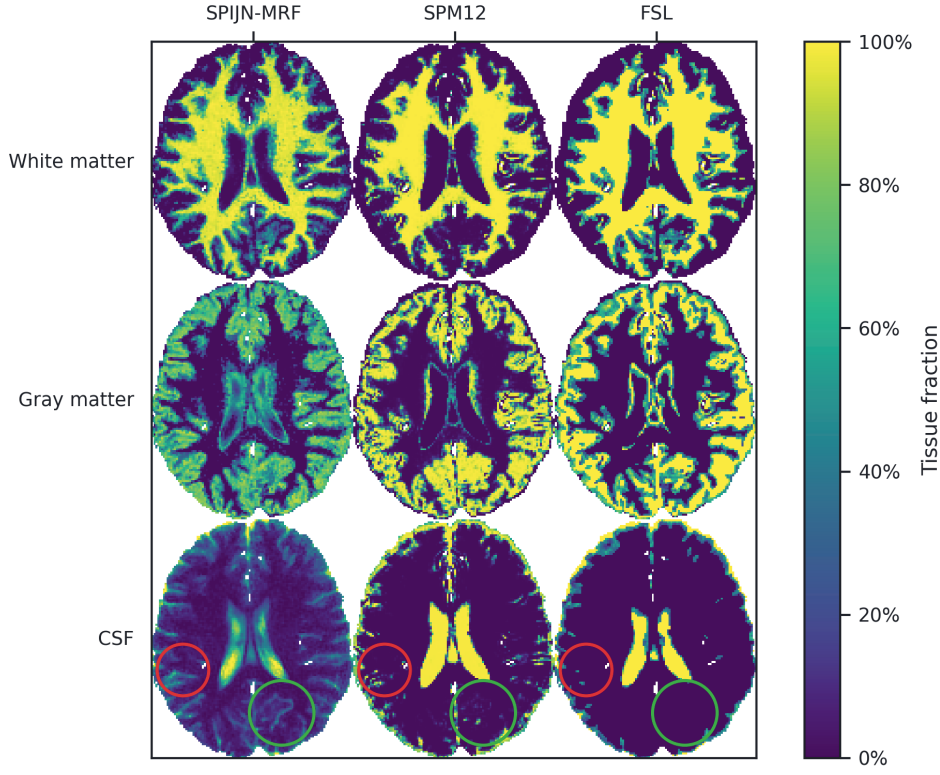

Figure 4.6: A representative slice showing the white matter (top), gray matter (middle) and CSF (bottom) fraction maps obtained using SPIJN-MRF (left), SPM12 (middle), and FSL (right) for one single acquisition of one subject (subject B, day 5). Red and green circles point out notable differences in CSF between methods.

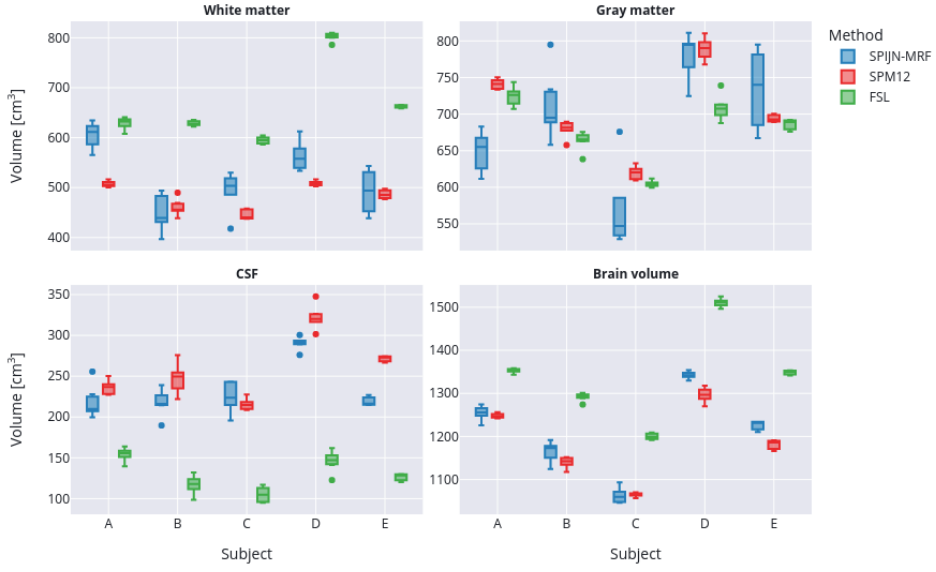

Figure 4.7: Box plots showing for each subject the total volume of the white matter (top-left), the gray matter (top-right), the CSF (bottom-left), and the total brain (bottom-right) estimated using SPIJN-MRF (blue), SPM12 (red) and FSL (green).

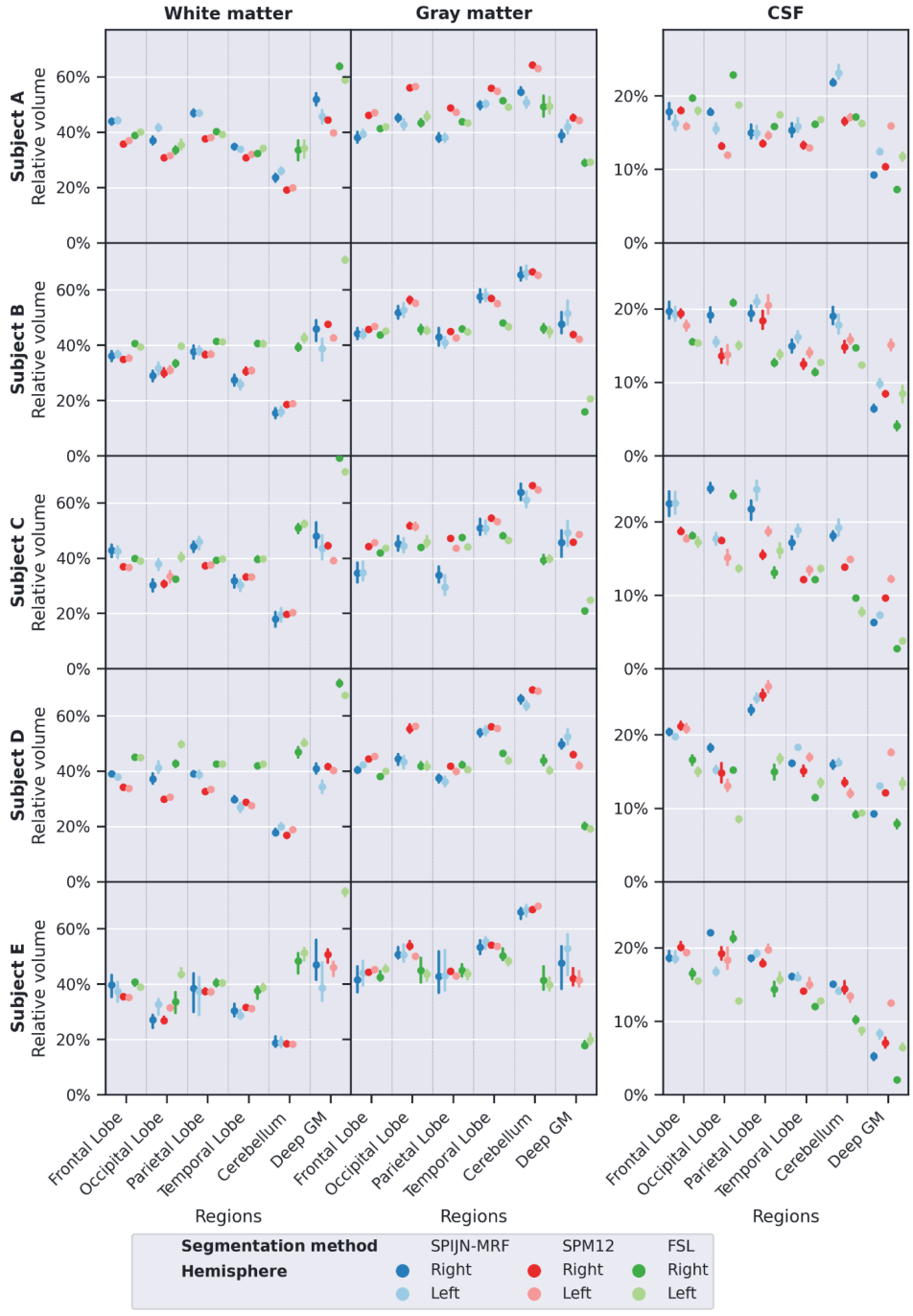

Figure 4.8: Mean relative volume for each subject over time (dots) and associated standard deviation (vertical lines) for different anatomical regions of the white matter (left), the gray matter (middle), the CSF (right) estimated using SPIJN-MRF (blue), SPM12 (red) and FSL (green).

Figure 4.9 shows CFTCs (upper row) and CoVs (lower row) for the motion-artefact-free data and the full dataset across the subjects and the tissues. The SPM12 yielded slightly higher CFTC than SPIJN-MRF in white and gray matter in all subjects. SPIJN-MRF gave higher CFTCs compared to both SPM12 and FSL in CSF, which was observed consistently across slices (see supplementary figure 4.13). Also, the CoVs of SPM12 and FSL were distinctly lower than those of SPIJN-MRF for white and gray matter, whereas differences were smaller for CSF and total brain volume. The CoVs for SPIJN-MRF were lower using the data without motion artefacts than with all data in all tissues but one in subjects C and D, and E. The only exception was in subject E, in which the white matter score was barely affected. We did not observe a particular trend in the CFTCs nor in the CoVs of the motion-artefact-free data related to anatomical region nor any specific differences between left/right brain regions (see supplementary figure 4.14).

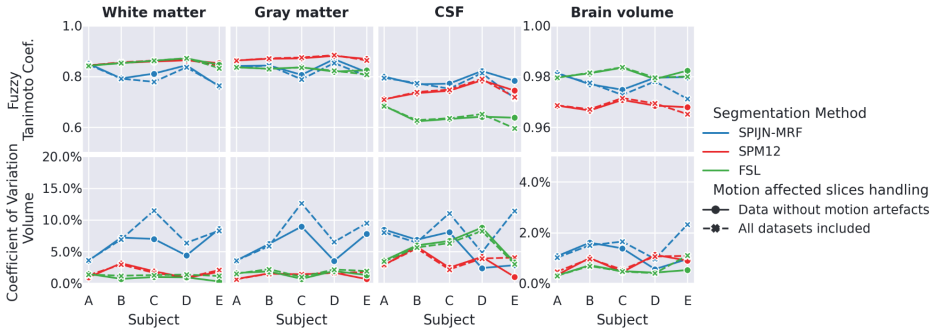

Figure 4.9: Combined Fuzzy Tanimoto Coefficient and CoV of estimated total volumes for each subject for white matter (including myelin), gray matter, CSF and total brain (white matter plus gray matter) obtained with SPIJN-MRF (blue), SPM12 (red), and FSL (green). Results from the data without motion artefacts are depicted using circles and solid lines, results obtained using all data are depicted with squares and dashed lines.

4.4. DISCUSSION

This paper aimed at evaluating the accuracy and repeatability of the joint sparsity based SPIJN-MRF estimations [13]. The results show that it yields accurate brain tissue voxel fraction estimation in simulated data (mean systematic errors between 2cm^3 and 6cm^3 and Fuzzy Tanimoto Coefficient above 0.95) and gives good repeatability in in-vivo data (Fuzzy Tanimoto Coefficient above 0.7 and mean (across subjects) CoVs between 5.7% and 6.1%).

The simulation results showed that the white matter, gray matter and CSF fraction maps obtained with SPIJN-MRF had smaller systematic errors than those obtained with SPM12 and FSL in both total volume estimation as voxel-wise similarity.

The T1 and T2 values obtained by SPIJN-MRF from the in-vivo data for each component were very stable for all the acquisitions and in the range of previous quantitative studies [11, 40, 43, 127, 128]. Unexpectedly, we found that the T2 value from the white matter component was slightly longer than the T2 value found for the gray matter. This might be partly due to the attribution of myelin water (having very short T2 time) to a separate component. In effect, this will lead to longer relaxation values for the (remaining) white matter component. Previously, a thorough study of the T2 distributions in the brain indeed demonstrated that T2 distributions are affected by properties of the spaces between myelin sheaths [129].

Furthermore, CSF was consistently represented by two different components, one with longer T2 (around 1 s) and one with shorter T2 (around 150 ms). This separation could be caused by the choroid plexus within the ventricles or by flow effects. The identification of the veins and arteries component as shown in Figure 4.5 was not observed before in multi-component relaxometry to our knowledge. This component had high T1 and T2 times (both around 1s) and consistently appeared in all subjects and scans. Further research into physiologically understanding this component would be an interesting direction of future work.

Estimated T1 relaxation times showed a very high repeatability, but for some components the maximum T1 value of the dictionary was selected. The use of a maximum T1 value of 6s instead of 3s did not affect this biasing effect (data not shown here) and was therefore not used any further. For better estimation of T1 relaxation times in CSF a different MRF sequence would probably be required to improve discrimination between long T1 components.

The consistent estimation of a separate myelin water fraction (MWF) map with the SPIJN-MRF approach is useful, e.g. for assessment of multiple sclerosis as well as other white matter diseases [43]. A comparison to other MWF estimation methods would be valuable in the future.

The study on repeatability of the SPIJN-MRF yielded CoVs < 10% for the total white matter volume (including myelin water), the gray matter volume and the CSF volume for all subjects. This variation of the estimated volumes with the SPIJN-MRF is similar to the variation found previously with commonly accepted methods, such as SPM12 and FSL [130, 131]. The estimation of the myelin water volume showed more variation (average CoV = 10%) than other tissues. The closer resemblance of the SPIJN-MRF maps to the reference in the simulations was reflected in higher FTC values with smaller standard deviations compared to the conventional methods. This suggests that SPIJN-MRF could be more accurate than the conventional methods. The small mean difference compared to the reference and associated standard deviation (see the Bland-Altman plots) confirm this, although the mean difference was on par with the

FSL outcome. Especially in the CSF maps (both in simulation and in-vivo), more details of the anatomy were visible with the SPIJN-MRF method than with SPM12 and FSL. These results could indicate that SPIJN-MRF in particular improves measuring partial volume properties of smaller brain structures. SPM12 uses a probability atlas with anatomical information to segment the brain tissues, which could enhance the repeatability of results but potentially also introduces a bias. FSL uses a hidden Markov random field model and an expectation-maximization algorithm to obtain robust results with improved denoising, but this might lead to removing small brain structures. Instead, the joint sparsity multi-component MRF model does not incorporate explicit spatial regularization or anatomical a priori knowledge.

Differences in estimated brain tissue volumes between SPM12 and FSL were already previously reported [130]. Our estimated volumes for FSL are higher in white and gray matter and lower in CSF compared to SPM12 with the simulated data just as in [131]. Contrary to the simulated data, the estimated total brain volumes for the in-vivo data by SPIJN-MRF are closer to the estimated volumes from SPM12 than those from FSL. Also, the relative volume per region calculated by SPIJN-MRF is closer to the relative volume calculated by SPM12 than FSL for the in-vivo data. This could be caused by intrinsic differences between the T1 weighted brainweb images (used in the simulations) and the MRF based T1 weighted images (used in the in-vivo experiments). The differences in the contrast could result in slightly different classification of the voxels and affect the local partial volume estimates. In contrast to the simulations, the CoVs of SPIJN-MRF for in-vivo data reflected higher variability than those of SPM12 and FSL for almost all subjects and tissues. The low variability of SPM12 and FSL, also in comparison with previous studies [130, 131], could be due to the use of synthetic images. This is because the quantitative parameters (M0, T1 and T2) from MRF were highly repeatable, differing only between 0 and 2% amongst all the acquisitions. As a consequence the resulting synthetic T1-weighted images are also highly similar. This likely biases the repeatability of the SPM12 and FSL segmentations. We chose to create synthetic T1 images in order to have perfect spatial correspondence of the data. As such differences in imaged volume were avoided.

SPM12 and FSL demonstrated to be slightly more robust against motion artefacts than SPIJN-MRF, resulting in minimal differences in CoV and FTC when using data without and with motion artefacts. Although motion effects were observed in a relatively small number of slices, it did affect the volume estimates. Simultaneously, however, estimated T1 and T2 relaxation times were not affected by motion affected slices. Nevertheless, our results show that efforts to minimize the impact of subject-motion in the MRF data may enhance in particular the repeatability, e.g. by applying motion-correction [122] or 3D-acquisitions with possible use of navigators

[132] or self-navigations[123]. A limitation of this work could be that the evaluation of accuracy was done only on simulated data. Further validation could be done by acquiring myelin water fraction maps using any of the accepted methods [40] or by expert neuroradiologists who could visually assess the obtained segmentations. Future work could also take into account other potentially relevant aspects in the simulations, such as: reconstructions from undersampled data, modeling of B0 or B1+ inhomogeneities, representation of the presence of myelin water or inclusion of other biological phenomena such as magnetization transfer or flow.

Another limitation could be that we did not include B1+ field inhomogeneity as a parameter in our SPIJN-MRF estimation. Although B1+ inhomogeneity might affect the SPIJN-MRF parameter estimation and especially MWF estimation, we did not observe specific spatial variations in obtained fraction maps that could be explained by B1+ inhomogeneities. Furthermore, optimizing the MRF sequence for SPIJN-MRF [133] could improve the obtained tissue fraction maps. However, we consider such optimization beyond the scope of our current paper.

4.5. CONCLUSION

We studied the accuracy and repeatability of the SPIJN-MRF method in simulations and in-vivo brain MRI scans. SPIJN-MRF showed more accuracy and higher repeatability in simulated data than conventional methods (SPM12 and FSL). In the in-vivo data, SPIJN-MRF consistently identified the same brain tissue components and gave highly repeatable relaxation times related to these tissues. SPIJN-MRF partial volume maps showed more small details especially in CSF compared to SPM12 and FSL. Only the repeatability of the estimated brain tissue volumes of SPIJN-MRF was somewhat lower compared to SPM12 and FSL. A further advantage of using SPIJN-MRF is the additional simultaneous estimation of MWF maps, which is not obtainable with single compartment based conventional methods.

ACKNOWLEDGEMENTS

This research was partly funded by the Medical Delta consortium, a collaboration between the Delft University of Technology, Leiden University, Erasmus University Rotterdam, Leiden University Medical Center and Erasmus Medical Centre. This work was partially financed by a Research Grant from GE(B-GEHC-05)

DATA AND CODE AVAILABILITY STATEMENT

In-vivo reconstructed data is publicly available at https://doi.org/10.5281/zenodo.5576039 . The code for the SPIJN-MRF algorithm was previously published (https://doi.org/10.1002/mrm.27947) and available at https://github.com/MNagtegaal/SPIJN .

AUTHOR CONTRIBUTIONS

Conceptualization: M.A.N., L.N.G., D.H.J.P, J.B., M.J.P.v.O., J.A.H.T. and F.M.V.; Data curation: L.N.G., M.A.N. and D.H.J.P; Formal analysis: M.A.N. and L.N.G.; Funding acquisition: J.B., J.A.H.T. and F.M.V.; Investigation: L.N.G. and M.A.N.; Methodology: M.A.N., L.N.G., D.H.J.P, J..B., J.A.H.T. and F.M.V.; Project administration: L.N.G., M.A.N., J.A.H.T. and F.M.V.; Resources: J.A.H.T.; Software: M.A.N., L.N.G. and D.H.J.P; Supervision: D.H.J.P, J.B., M.J.P.v.O., J.A.H.T. and F.M.V.; Validation: L.N.G. and M.A.N.; Visualization: M.A.N. and L.N.G.; Writing original draft: L.N.G. and M.A.N.; Writing - review & editing: M.A.N., L.N.G., D.H.J.P, J.B., M.J.P.v.O., J.A.H.T. and F.M.V.;

CONFLICTS OF INTEREST

The authors declare no conflict of interest.

4.6. APPENDIX I

The acquired MRF data was reconstructed using an in-house created low-rank reconstruction algorithm, solving

$$P,U = \arg\min P,U \sum_{c,j} |S_{j,c} - F_j C_c P U_j|_2^2 + R(P) \tag{4.4}$$

where $P \in \mathbb{C}^{|\omega_X| \times N}$ is a matrix containing the N low-rank component images of spatial dimension $|\omega_X|$, which is the compressed representation of the MRF series; $U \in \mathbb{C}^{N \times 1000}$ contains the N time components based on which the MRF signal is compressed, i.e. the time-compression matrix, and $U \in \mathbb{C}^N$ is a particular column from this matrix for contrast weighting j (thus, $x = PU_j$ is the reconstructed contrast image j from the MRF series); $S_{j,c} \in \mathbb{C}^{|\omega_j|}$ is the acquired undersampled data of MRF contrast weighting j of coil c; $C_c \in \mathbb{C}^{|\omega_X| \times |\omega_X|}$ is a diagonal matrix specifying the sensitivity of coil c; $F_j \in \mathbb{C}^{|\omega_j| \times |\omega_X|}$ represents the non-uniform Fast Fourier transform [69] for contrast weighting j. Furthermore, $R(P) = \sum_x \sqrt{\sum_i P_{x,i}^2}$, i.e. the spatial L1 norm of the L2 norm across the component images, is applied for regularization purposes. The equation was solved by three iterations of a block coordinate descent optimization, alternating the optimization between U and P. The initial time compression matrix U was constructed from the first 6 singular vectors obtained through SVD of a dictionary precomputed as described in Methods in the subsection Single and multi-component parameter estimation. After this, initial-images were created by subsequently applying to S_j: a density compensation, an adjoint non-uniform Fourier transformation, and a projection to the subspace with the initial U. Then, using the first subspace component derived from the initial-images, the cross-correlation matrix among the 12 acquired channels was computed for each voxel. The output was a matrix of 12 by 12 images which were filtered using a box blur filter of size 5, resulting in a modified correlation-among-channels matrix for each voxel. Each voxel of the coil sensitivity maps (C_c) was created from the first singular vector of its modified correlation-among-channels matrix. The initial P was created by the projection of the initial-images on C_c. In subsequent iterations the explicit least squares solution for Uj was computed followed by ortho-normalization. Subsequently, the subproblem for P was solved by the conjugate gradient algorithm, where $R(P)$ was approximated by its tight quadratic overbound [134].

4.7. SUPPLEMENTARY MATERIAL

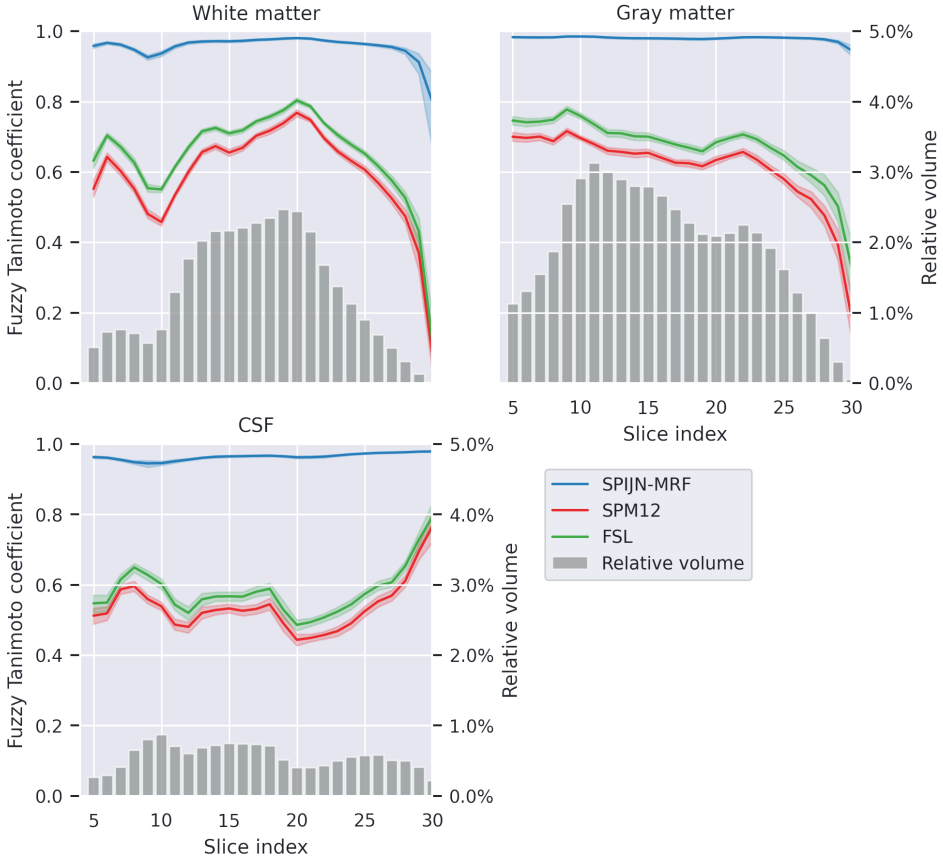

Figure 4.10: Line plots showing the averaged Fuzzy Tanimoto Coefficient (and the 95% confidence interval as the shaded region) over the 20 BrainWeb phantoms between tissue fraction maps estimated with SPIJN-MRF (blue), SPM12 (orange), and FSL (green) and the Brainweb partial volume maps across all the slices. Gray bars indicate the relative tissue volume compared to the total brain volume for each slice.

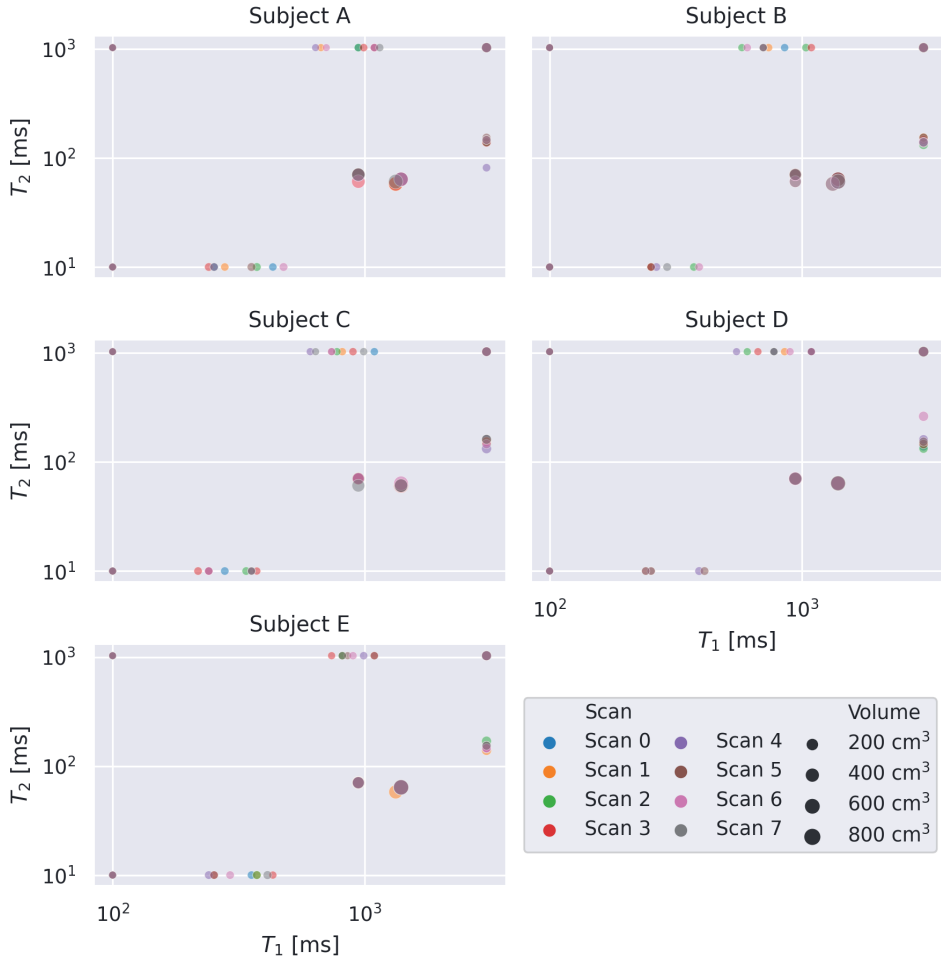

Figure 4.11: Estimated T1 and T2 relaxation times for the different acquisitions (represented with different color). The estimated volume of each component is reflected in the size of the spheres. We refer to an online interactive figure for further exploration of these data.

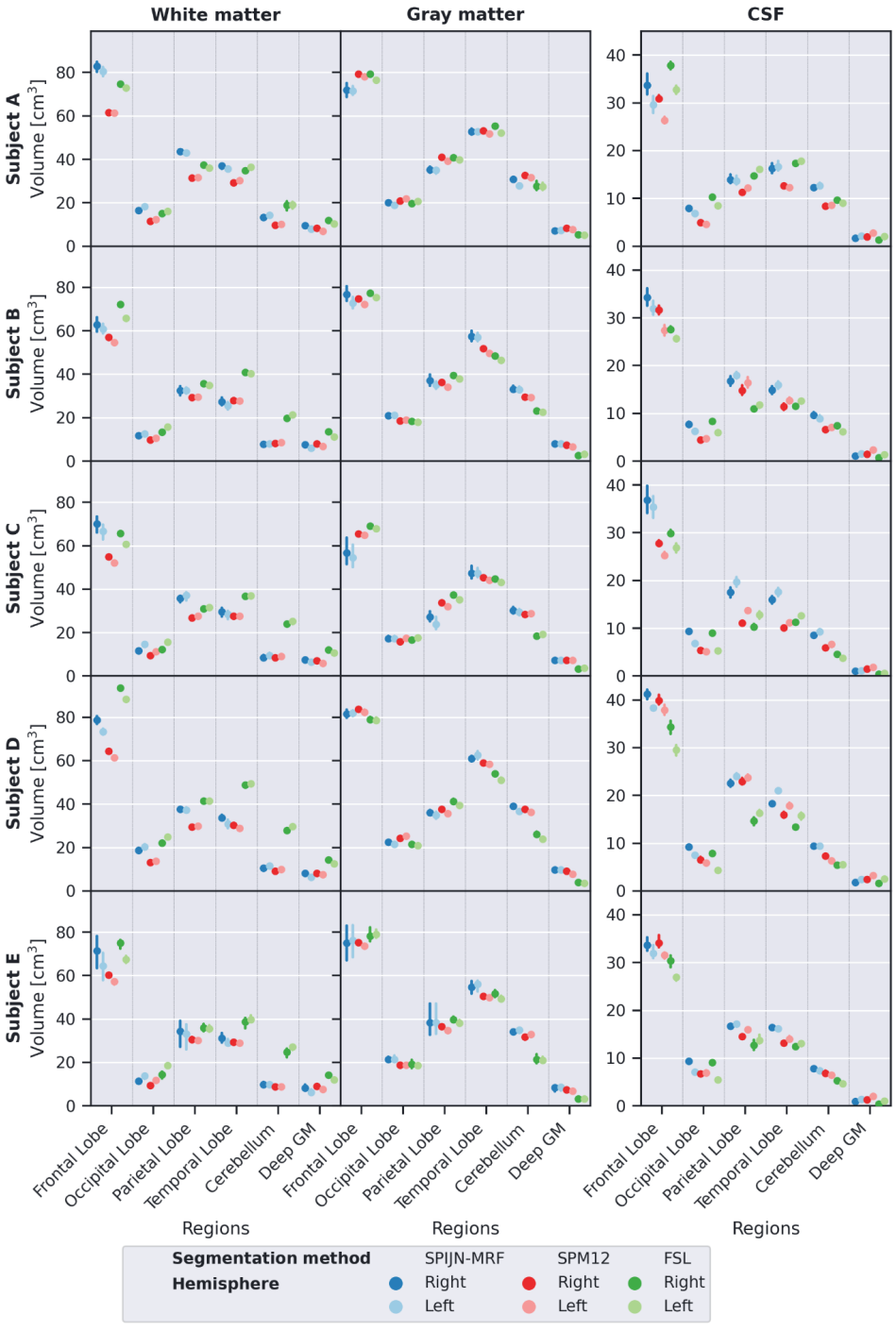

Figure 4.12: Mean absolute volumes for each subject over time (dots) and associated standard deviation (vertical lines) for different anatomical regions of the white matter (left), the gray matter (middle), the CSF (right) estimated using SPIJN-MRF (blue), SPM12 (red) and FSL (green).

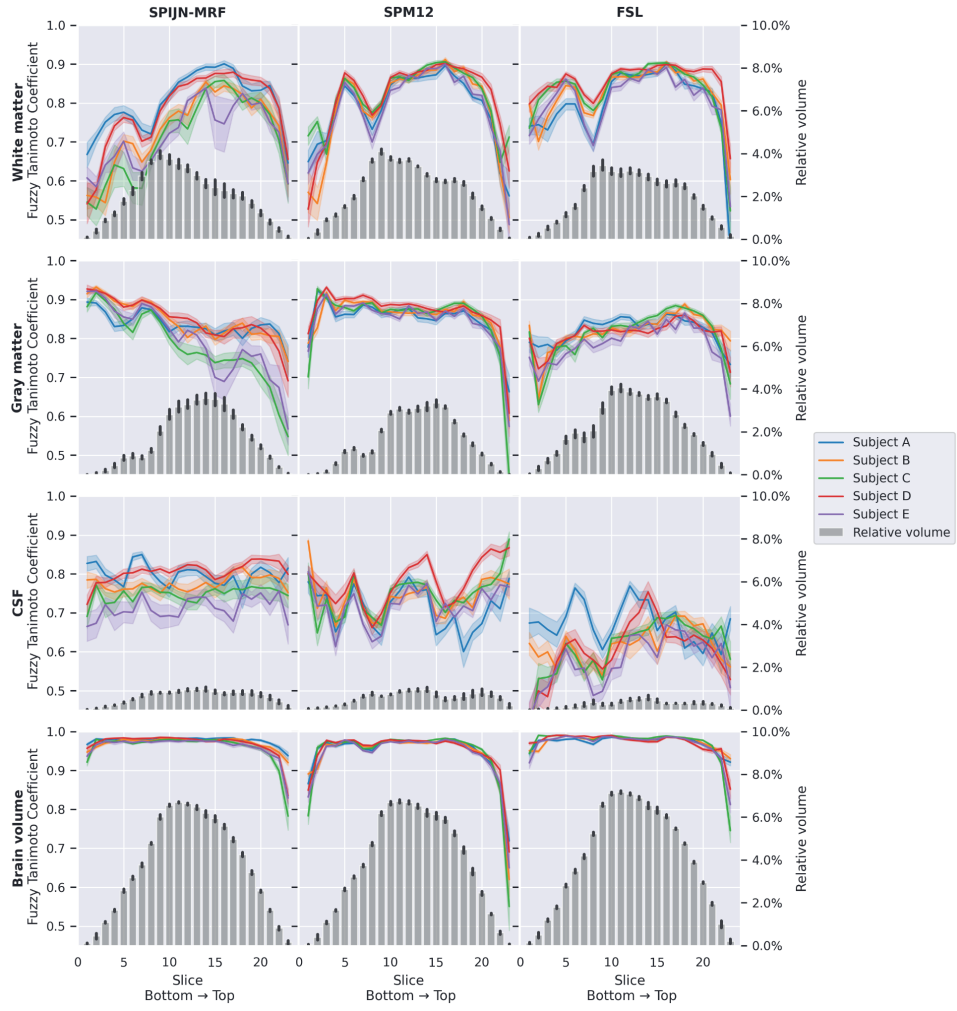

Figure 4.13: Line plots showing averaged pair-wise Fuzzy Tanimoto Coefficient (and the 95% confidence interval shadowed) for each subject with SPIJN-MRF , SPM12, and FSL for each slice. Gray bars indicate the averaged across the subjects relative tissue volume compared to the total brain volume for each slice. Vertical line on top of the bars indicates the standard deviation.

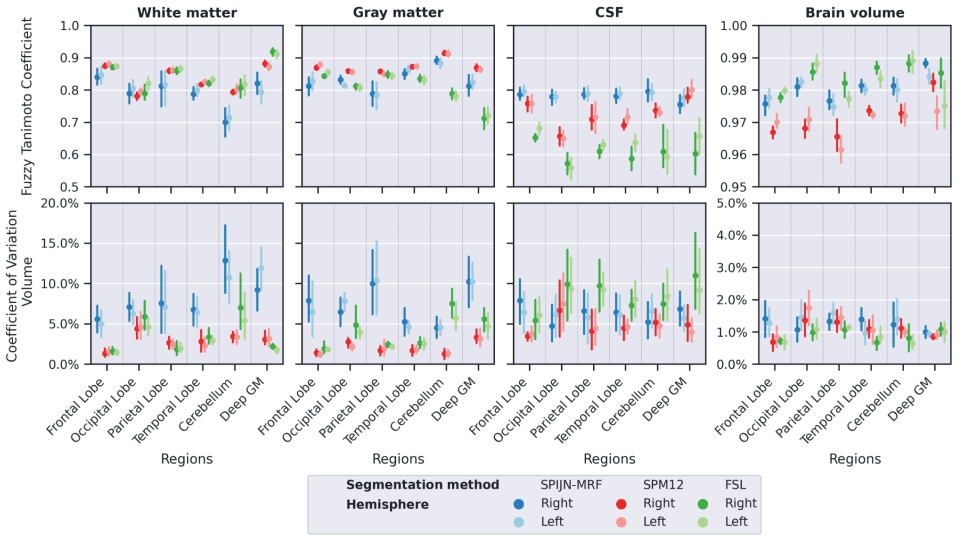

Figure 4.14: Mean Combined Fuzzy Tanimoto Coefficient and CoV in different brain regions for white matter (including myelin), gray matter, CSF and total brain volumes (white matter, gray matter plus CSF) obtained with SPIJN-MRF (blue), SPM12 (red), and FSL (green). Darker colors represent values for the right side of the brain, lighter colors reflect values for the left side of the brain.

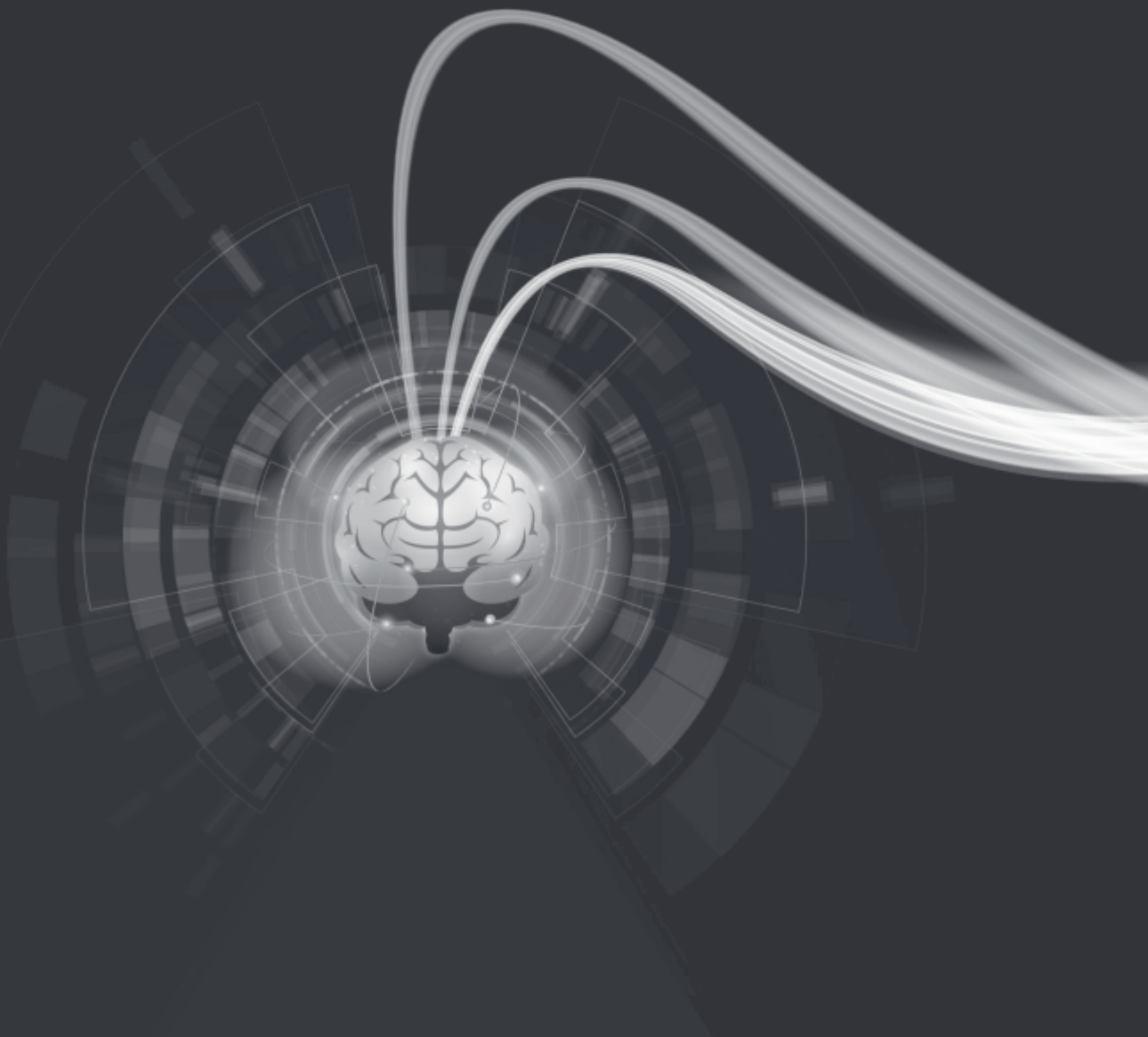

5

FROM SIGNAL-BASED TO COMPREHENSIVE MAGNETIC RESONANCE IMAGING

Gyula KOTEK[1,*], Laura NUÑEZ GONZALEZ[1], Mika VOGEL[2], Gabriel P. KRESTIN[1], Dirk H.J. POOT.[1], Juan A. HERNANDEZ-TAMAMES[1,*]

1 Department of Radiology and Nuclear Medicine, Erasmus Medical Center, Rotterdam, the Netherlands

2 General Electric, GE Healthcare, Hoevelaken, the Netherlands

** These authors contributed equally*

This chapter has been published in Nature Scientific Reports (2021);11:17216. https://doi.org/10.1038/s41598-021-96791-w.

Abstract

We present and evaluate a new insight into magnetic resonance imaging (MRI). It is based on the algebraic description of the magnetization during the transient responseincluding intrinsic magnetic resonance parameters such as longitudinal and transverse relaxation times (T1, T2) and proton density (PD) and experimental conditions such as radiofrequency field (B1) and constant/homogeneous magnetic field (B0) from associated scanners. We exploit the correspondence among three different elements: the signal evolution as a result of a repetitive sequence of blocks of radiofrequency excitation pulses and encoding gradients, the continuous Bloch equations and the mathematical description of a sequence as a linear system. This approach simultaneously provides, in a single measurement, all quantitative parameters of interest as well as associated system imperfections. Finally, we demonstrate the in-vivo applicability of the new concept on a clinical MRI scanner.

Keywords: Quantitative MRI, MR Fingerprinting, MRF-vFA, QRAPMASTER, Repeatability, Accuracy

5.1. INTRODUCTION

MRI is extensively used in medicine and biology. It provides meaningful images of different organs and pathologies based on the magnetic properties of specific nuclei present in tissues.

Quantitative MR measures these properties and currently relies on the single species approximation of the nuclear magnetization evolution as described by Blochs equation[2]. However, accurate and precise absolute quantification of the properties requires long scan times and is challenging because of the high sensitivity to MR system imperfections such as magnetic field inhomogeneity and radiofrequency pulse inaccuracies[135]. These factors hamper the reproducibility across MR systems.

It is well known that there is no explicit closed-form solution to the Bloch equations for a general, time-dependent magnetic field. There is a solution thoughand it is abundantly exploited in MRI technologyfor a very simple case, where the magnetic field is constant as stated by Torrey in 1949[136]. We extend this solution from the continuous Bloch equation to a discrete description of an entire imaging sequence. This approach has been partially explored before by other authors [50–54, 137]. We take this initiative further and establish a novel application and framework in the domain of the impending field of parametric transient MR Imaging [19, 59].

For nearly 50 years, MR imaging mainly used steady state MR pulse sequences [9, 138]. Such sequences are designed to allow a model with a single magnetization vector per voxel and avoid the magnitude and phase changes that happen during the transient response as these could introduce undesirable modulations across the k-space. For this reason Hargreaves et al. proposed to reduce the duration of the transient response in refocused-SSFP sequences to reach the steady state faster [51].

In our opinion, insufficient attention has been focused on exploiting the transient response to simultaneously obtain multiple intrinsic MR relaxation times by taking advantage of more complicated signal evolutions than simple exponential recoveries. A patent was filed in 2001 for simultaneous multiparametric estimation from the transient response [139] and in 2003, Scheffler pointed out the possibility of extracting relaxation parameters from the transient response but without further development or implementation [52]. Assländer et al. [140], using a similar formalism that Hargreaves, propose to reduce the population of complex conjugate eigenvalues in order to reduce the sensitivity to system imperfections for obtaining only T1 and and T2 maps without performance comparison to other reference methods.

Recently, Magnetic Resonance Fingerprinting (MRF) has emerged as a new paradigm for quantitative, multi-parametric MR imaging [59]. It takes advantage of the transient response to generate maps of the intrinsic tissue properties such as T1, T2 and

PD. In the original MRF sequence the acquisition parameters are pseudorandomized, which the authors suggest to be essential for generating unique signal evolutions for each tissue. In MRF the signals are matched to an a priori dictionary to find the relaxation properties. This matching procedure avoids the fitting to an explicit signal model based on repeatedly solving the Bloch equations. It thereby essentially extends the successful compressed sensing principle [141] to the temporal direction.

Some improved alternatives have recently been published, such as Quantitative Transient Imaging (QTI)[19] that uses a fixed time of repetition and a linearly increasing variable flip angle (vFA) and Magnetic Resonance Field Mapping[142] which additionally provides B1 and B0 maps through including multiple B0 and B1.values in the dictionaries. Sbrizzi et al. recently proposed a brute force approach named MR-STAT providing all the relevant maps (T1, T2, PD, B1 and B0) that also avoids dictionary matching[143].

In this work, we propose a new MR method based on a mathematical closed-form description of the magnetization evolution of a single species along a sequence of repetitive blocks which contain RF pulses and readout gradients. This provides four important advantages. First, it enables a comprehensive simultaneous estimation of all intrinsic parameters and avoids confounding by experimental imperfections such as B0 inhomogeneities and B1 inaccuracies. Second, the analytical description of the sequence of blocks gives a new insight that facilitates the selection of pulse sequence design (TR, FA and phase) to increase sensitivity for all relevant parameters. Third, no dictionary is required to perform the estimation. Fourth, we also show that, the proposed design, based on the insight given by the algebraic mathematical model, avoids the banding artefact (a long-standing issue in the standard balanced Steady State Free Precession (bSSFP) MRI technique).

We propose that the use of the comprehensive MR method described in this work could contribute to standardized MR through the adoption of multiparametric methods in clinical protocols and to increased reproducibility in follow-up and multi-site or multi-vendor studies.

5.2. THEORETICAL FRAMEWORK —FROM LINEAR ALGEBRA TO DISSIPATIVE COUPLED HARMONIC OSCILLATORS

We provide an algebraic description of the signal evolution during the entire MR sequence. Our goal is to establish a theoretical framework for quantitative sequences that utilizes a single transient response and can yield quantitative maps for all relevant parameters, intrinsic (T1, T2, PD) and experimental (B0, B1) at once. First, we will consider an imaging voxel as homogeneous and represented by a single magnetization

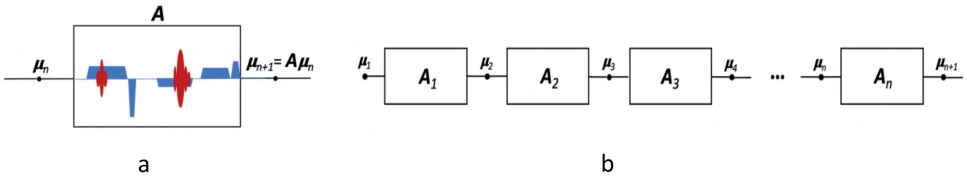

Figure 5.1: (a) Illustration of the propagator: a single block of events. μ is the inputoutput magnetization, in red the RF excitations and in blue the gradients. (b) A typical train of blocks in a MR pulse sequence. We will use identical blocks or operators $A = A1 = A2 = = An$.

vector, i.e. we use a single species model. In general, the assumption of the intra-voxel homogeneity is not valid. However, as we demonstrate, it can be maintained by a careful choice of the acquisition scheme.

5.2.1. DISCRETE ALGEBRAIC DESCRIPTION OF AN MR IMAGING SEQUENCE

MRI sequences consist of a train of acquisition blocks (Fig. 5.1). The acquisition blocks alter the magnetization vector. Each block consists of radiofrequency excitations (Fig. 5.1-a, in red), magnetic field gradients (Fig. 5.1-a, in blue) and wait times (Fig. 5.1-a, μ periods for free precession, absent of RF excitations or magnetic field gradients) each of which can be described as linear operator that acts on the magnetization vector [51]. Hence, the combined effect is also a linear operator called *propagator*.

We focus on a special case when the propagator, A, is identical along the train of acquisition blocks and has duration TR. As only the net effect of the propagator is equal, blocks differing in spatial coding k-space trajectories are possible. In this case the magnetization vector m evolves according to the recursive equation:

$$m_{n+1} = A \cdot m_n + (I - A) \cdot m_{ss} \tag{5.1}$$

where m_{ss} is the steady state magnetization and m_0 the initial state. We can focus on the homogeneous recursive Eqs. 5.5,5.9:

$$\mu_{n+1} = A \cdot \mu_n \tag{5.2}$$

with the solution:

$$\mu_n = A^n \cdot \mu_0 \tag{5.3}$$

where $\mu_n = m_n - m_{ss}$.

In comparison, for continuous modeling, the kinetics are described by the differential equation:

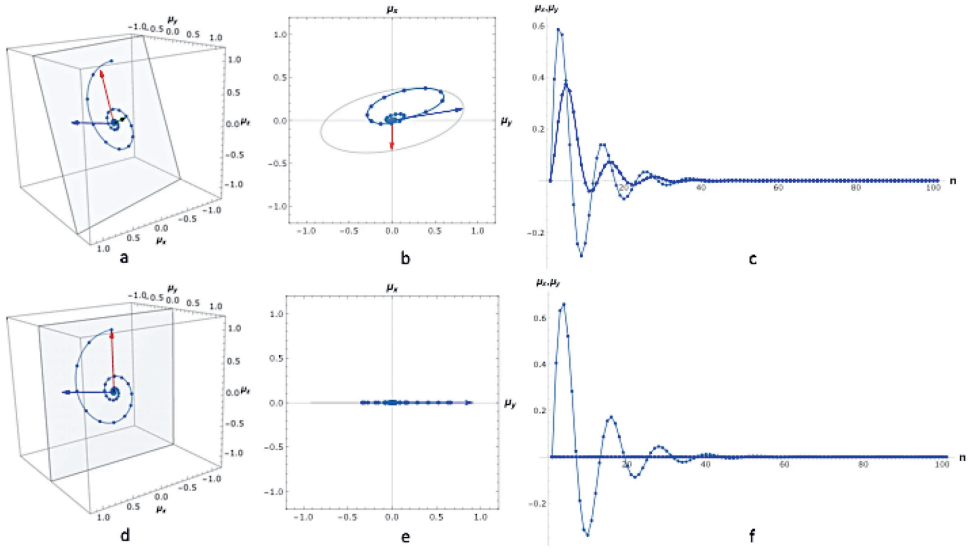

Figure 5.2: (**a**-**c**) The repeated block consists of an excitation with flip angle $\alpha = 30^o$, $\beta = 14^o$ (accumulated phase as a result of off-resonance during TR,TR =10 ms), relaxation times are T1= 878 ms, T2= 47.5 ms. n_1 and n_2 span the plane of oscillation. The magnetization vector always points to a point of this plane. Only the orientation of the plane is fixed throughout the evolution; it shifts parallel to n_3. Figure (**a**) 3D trajectory, (**b**) xy projection (transversal plane), (**c**) x and y component (signals measured in quadrature). Figures (**df**) similar to (**ac**) with on-resonance ($\beta = 0^o$). The plane spanned b. n_1 and n_2 is the xz plane throughout the entire evolution. The points represent the magnetization difference vector and its evolution along the sequence. The continuous line is the corresponding continuously parametrized $y(\tau) = A^{\tau/TR}\mu_0$. The quantity $y(\tau)$ satisfies the differential equation: $\frac{d}{dt}y(t) = B \cdot y(t)$ with $exp(B) = A^{1/TR}$. $y(\tau)$ is not the fully continuous trajectory of the magnetization μ. However, $y(\tau)$ and μ are equal at the discrete time points: $y(\tau = nTR) = \mu_n$.

$$\frac{d}{dt}y(t) = B \cdot y(t), with\ the\ solution: y(t) = A^{t/TR} \cdot y(0) \tag{5.4}$$

The constant matrix coefficients in the differential equation and the recursive equation are related as $e^B = A^{1/TR}$ [144] . Figure 5.2 depicts both the continuous and the discrete solutions.

In the case of an imaging sequence consisting of k consecutive excitations and free precession periods, **A** takes the following form:

$$A = \prod_{j=1}^{k} (E(\tau_j) \cdot R_z(\beta_j) \cdot R_y(\alpha_j) \cdot R_z(\gamma_j)) \tag{5.5}$$

with $R_s(\vartheta)$ specifying a rotation of angle ϑ around axis s (x, y or z in Eq. 5.5), where the α, β, γ are a function of the RF flip angle, phase and local off-resonance frequency,

and

$$E(\tau_j) = \begin{pmatrix} e^{-\tau_j/T2} & 0 & 0 \\ 0 & e^{-\tau_j/T2} & 0 \\ 0 & 0 & e^{-\tau_j/T2} \end{pmatrix} \tag{5.6}$$

represents the relaxation in the period τ_j , $\sum_j = TR$.

5.2.2. A REAL-VALUED EXPRESSION FOR THE SIGNAL IN AN MR SEQUENCE

In order to exploit the information content of the signal evolution, it is convenient to have a closed-form expression for μ_n in Eq. 5.3. This requires an expression for A^n, where A is a general, real-valued 3×3 matrix.

The usual method to derive an expression for A^n is to diagonalize A by its eigenvectors provides a simple expression with the eigenvalues λ_1, λ_2, λ_3 :

$$A^n = V^{-1} \cdot \begin{pmatrix} \lambda_1^n & 0 & 0 \\ 0 & \lambda_2^n & 0 \\ 0 & 0 & \lambda_3^n \end{pmatrix} \cdot V \tag{5.7}$$

where $V = [v_1, v_2, v_3]$ is the matrix formed by the eigenvectors of A [51, 52].

A sufficient and necessary condition of the diagonalization is $det(V) \neq 0$, i.e. the eigenvectors of A are linearly independent. This condition is met if the eigenvalues are distinct, however this is not a necessary condition (multiplicity of the eigenvalues of A alone does not preclude diagonalization).

We follow a different method for derivation of the expression of A^n. This method does not rely on the diagonalizability of A and it is also idependent of the multiplicity of the eigenvalues. The discrete Putzers algorithm [145, 146] relies on a consequence of the Cayley-Hamilton theorem: A^n can be expressed as an (d-1) order polynomial of $A \in \mathbb{R}^{d\times d}$, in our case with the identity matrix I, A and A^2. Applying the Putzers algorithm the resulting expression for 3×3 matrices with distinct eigenvalues is:

$$A^n = \lambda_1^n I + \frac{\lambda_1^n - \lambda_2^n}{\lambda_1 - \lambda_2}(A - \lambda_1 I) + \frac{\lambda_1^n(\lambda_2 - \lambda_3) + \lambda_2^n(\lambda_3 - \lambda_1) + \lambda_3^n(\lambda_1 - \lambda_2)}{(\lambda_1 - \lambda_2)(\lambda_1 - \lambda_3)(\lambda_2 - \lambda_3)}(A - \lambda_1 I)(A - \lambda_2 I) \tag{5.8}$$

The expression is also valid in its limit for multiple eigenvalues, may any of the eigenvalues as roots of the characteristic polynomial be identical: $\lambda_1 \to \lambda_2$, $\lambda_1 \to \lambda_3$, $\lambda_2 \to \lambda_3$. A is a product of rotation and dilation operations, represented by a non-singular, real valued matrix. The eigenvalues of A can always be expressed as $\lambda_1 = \rho e^{i\varphi}$, $\lambda_2 = \rho e^{-i\varphi}$, and $\lambda_3 = \eta$, where ρ and η are real valued, and φ is either real or

purely imaginary. A has one real- valued eigenvalue and its real eigenvector (λ_3 and v_3), but the other two eigenvalue and eigenvector pairs are usually complex conjugates. It is also relevant to realize that $\rho^2 \cdot \eta$ is the determinant of the propagator which depends on the intrinsic T1 and T2 and it is essentially the total dissipation during the entire propagator block. This amount can be voxel-wise obtained and it can be reconstructed as a map. This map is characteristic of the specific harmonic oscillator and we will refer to it as the HO (harmonic oscillator) map, or image, for the rest of the document.

Substituting the eigenvalues in Eq. 5.8, with a somewhat lengthy, but otherwise straightforward derivation we get:

$$A^n = \rho^n \cdot \sin(n\varphi) \cdot M_1 + \rho_n \cdot \cos(n\varphi) \cdot M_2 + \eta^n \cdot M_3, \tag{5.9}$$

The real-valued matrices M_j are:

$$\begin{aligned} M_1 &= \frac{1}{\rho \cdot \sin(\varphi)} \cdot A - \frac{\cos(\varphi)}{\sin(\varphi)} \cdot I + (-\frac{\eta}{\rho} + \cos(\varphi)) \cdot M_3 \\ M_2 &= I - M_3 \\ M_3 &= \frac{1}{\rho^2 + \eta^2 - 2\rho \cdot \eta \cos(\varphi)} (A^2 + \rho^2 I - 2\rho \cdot \cos(\varphi) \cdot A) \end{aligned} \tag{5.10}$$

The expression for the special cases when two or all three eigenvalues are identical can be derived in the limit, e.g. $\varphi \to 0$, $\rho \to \eta$.

So, the explicit discrete expression of the magnetization evolution as in Eq. 5.3 is :

$$\mu_n = \rho^n \cdot \sin(n\varphi) \cdot n_1 + \rho^n \cdot \cos(n\varphi) \cdot n_2 + \eta^n \cdot n_3 \tag{5.11}$$

where the real-valued normal mode[147] vectors $n_1 = M_1 \cdot \mu_0$, $n_2 = M_2 \cdot \mu_0$, and $n_3 = M_3 \cdot \mu_0$ depend on the initial state μ_0 .

At this point it is important to make two important remarks.

First, in order to clarify the terminology: these normal modes are not the eigenvectors (sometimes also called normal modes, especially if A is a symmetric matrix). They are always real valued and represent special directions in real 3D space, along which motion is defined in Eq. 5.11.

Second, it is important to point out that the matrix expressions in Eq. 5.10. include a projection matrix: $Re(A - \lambda_1 I) = (A - \rho \cos(\varphi) I)$. Based on this one, we can predict that the normal modes can also have zero length. This happens to be the case when μ_0 is in the null-space of a matrix M_1, M_1 or M_1. The normal modes n_1, n_2 and n_3 form a complete non-orthogonal basis in 3D if μ_0 is not in the nullspace of any of the matrices in Eq. 5.10.

It is clear from Eq. 5.11 that μ follows decaying oscillations in two directions n_1 and n_2 with locked phase and frequency. In the third n_3 direction it will follow an exponential decay towards zero.

The detectable signal is a projection of m_n on the plane of detection (xy-plane). It is a straightforward calculation to show from Eq. 5.11, by the usual quadrature detection with a complex expression:

$$s_n = a\rho^n e^{i(n\varphi+\delta)} + b\eta^n e^{i\xi} \tag{5.12}$$

where a, b, δ and ξ are real parameters determined by the initial value m_0 and the propagator. δ is the phase difference between transmit and receive. This equation resembles Torreys solution of the Bloch Eq. 5.3 but stretched to the repetitive pulse sequence.

The parameters in Eqs. 5.11 and 5.12 are uniquely determined by the T1, T2, and PD (intrinsic parameters) as well as the propagator (experimental parameters). Equation 5.12 highlights the decaying oscillation characteristics of the signal evolution, directly indicating the role of the propagator eigenvalues, parametrized by the intrinsic and experimental parameters.

The evolution of μ (the magnetization difference from the steady state) in three dimensions is illustrated in Fig. 5.2-a,d for a specific propagator and particular experimental conditions: the propagator consists of a single excitation with α flip angle, a phase evolution β accumulated during TR time during the repetition time (TR) due to off-resonance. The 2D projection over the detection plane is shown Fig. 5.2-b,e, and the detected signal resembling the free induction decay (FID)3 is shown in Fig. 5.2-c,f.

Figures a, b and c are in off-resonance condition [50] and figures d, e and f are in on-resonance condition[51, 52].

5.3. EXPERIMENTAL DESIGN

There are three conceptual aspects of our experimental design that render our technique viable in terms of the applicability of a single species model and the sensitivity to intrinsic parameters: (a) Information content of the signal, (b) Single species description, (c) Eigenvalues of the propagator.

(A) INFORMATION CONTENT OF SIGNAL-RESONANCE CONDITION

The description of the motion of μ allows the physical analogy of three independent, linear and damped oscillators, linked to each other only by the initial condition [53]. Although n_1, n_2 and n_3 span the space that holds the trajectory of the magnetization, they do not necessarily form a complete basis in 3D. In Fig. 5.2, the trajectories of μ are

depicted in the rotating frame of resonance, where the propagator consists of a single excitation. The case of off-resonance ($\beta \neq 0$) and on-resonance ($\beta \neq 0$) are shown, where β is the phase accumulated during a TR. In practice, $B0$ can not be fully controlled in an imaging volume, and β can take any value in $[0, 2\pi]$. In the on-resonance case, the last term in Eq. 5.11 vanishes because $n_3 \neq 0$, therefore the signal evolution carries no information about the real eigenvalue η. The information loss on-resonance can not be avoided with a block containing only one excitation. Hence, a special composite propagator is required.

(B) SINGLE SPECIES MODEL

Equation 5.11 describes the temporal evolution of the magnetization in a voxel under the assumption that it can be characterized as a single species. There are arguably two reasons why this assumption is not valid: (1) Related to limitations of the imaging technology: Multiple distinct tissue properties in one voxel due to the finite size of voxels or due to experimental imperfections in magnetic and RF fields ($B0$ and $B1$ inhomogeneities). (2) Related to the limitations of the Bloch equations, which are an approximation of the complex microscopic behavior of spin relaxation1, excluding multiple-pools for magnetization transfer, diffusion etc. In our experimental design we limit the $B1$ imperfections with an appropriate slice profile, and the imperfections in $B0$ homogeneity on a more conceptual level in the following section.

(C) EIGENVALUES OF THE PROPAGATOR

An important aspect of adopting an analytically described signal evolution is to estimate intrinsic and experimental parameters. As described in Eqs. 5.11 and 5.12, the theoretical description relies on the eigenvalues of the propagator.

The propagator can also be viewed as a mapping between the parameter space (T2,β) (Fig. 5.3-a) and the space of one of the complex eigenvalues (ρ, φ). As a minimal requirement, this mapping should preserve topology, i.e. it should maintain proximity between points and should be single valued. Otherwise, it would result in indistinguible signal behaviours for distinct (T2,β) species and, consequently, the MR experiment would loose sensitivity to some particular combinations of T2 and β.

5.3.1. DESIGN OF A PULSE SEQUENCE —COMPOSITE PROPAGATOR

The propagator that facilitates parametric mapping should fulfill the following requirements:

- The effect of variation of $B0$ on the eigenvalues is limited in order to allow the single species description

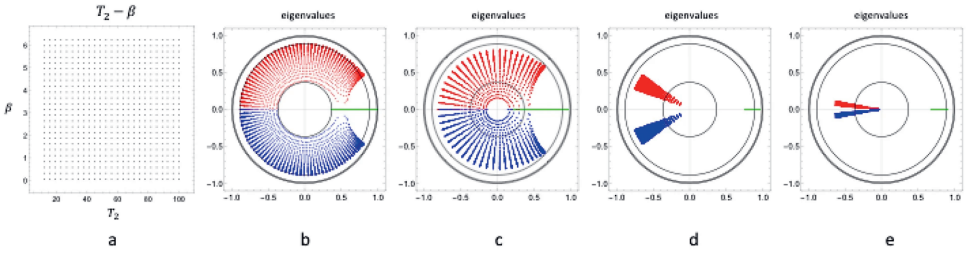

Figure 5.3: (**a**) T2β species: parameter space, (**b**-**e**) are the eigenvalue maps on the complex plane where three eigenvalues belong to each parameter species: red and blue are the complex eigenvalues, green represents the real eigenvalue. Eigenvalues of the repeated α_x propagator are shown in (**b**). The $\alpha_x\alpha_y$ propagator with excitation flip angle $\alpha = 30^o$ is shown in (**c**), and in (**d**) $\alpha_x\alpha_{x+\delta}$ scheme with $\alpha = 150^o$ and $\delta = 75^o$. The eigenvalue space for $\alpha_x - \gamma_y - \alpha_y - \gamma_x$ with $\alpha = 30^o$ and $\gamma = 175^o$ is shown in (**e**). For all maps T1=878 ms and TR=12 ms. In (**c**) one eigenvalue point belongs to the two β and $\beta + 180^o$ species.

- The 3D trajectory of μ is maintained at any value of B0 in order to avoid loss of information (none of the normal mode vectors vanish)
- The mapping between parameter space and eigenvalue space preserves topology in order to distinguish between species by their signal evolution

Figure 5.3 illustrates the problem of non-preserved topology and also demonstrates proper choices of the scheme, which we use for a set of propagators fulfilling the properties for a better estimation. Also, the inspection of the eigenvalue space provides immediate insight into the signal evolution: the radial distance from the origin determines the decay rate, and the angular position determines the oscillation frequency in the signal along the train of acquisition blocks. Figure 5.3-a shows the grid of (T2,β) pairs that are evaluated with fixed T1 and excitation flip angle. Figure 5.3-be show the resulting eigenvalue space in the complex plane for four different schemes. Figure 5.3-b shows the α_x scheme, in which a block consists of a single excitation with 30ř flip angle and readout. Figure 5.3-c shows the $\alpha_x\alpha_y$ scheme that consists of two equally spaced excitations along x and y axis with $\alpha = 30^o$. Figure 5.3-d shows the $\alpha_x - \alpha_{x+\delta}$ scheme consisting of two excitations along the x axis and $x + 75^o$ axis with flip angle $\alpha = 150^o$. Figure 5.3-e shows the $\alpha_x - \gamma_y - \alpha_y - \gamma_x$ scheme consisting of four equally spaced excitations with alternating x and y axis and $\alpha = 30^o$ and $\gamma = 175^o$.

Both the $\alpha_x\alpha_y$ scheme (with large flip angle) and the $\alpha_x - \gamma_y - \alpha_y - \gamma_x$ scheme preserve topology and also limit the effect of β.

Due to the alternating excitation axis, these composite propagators enforce a 3D trajectory of μ (see Eq. 5.11 for any β. In order to maintain the 3D trajectory for every possible β value, a minimum two RF excitations are necessary with different excitation

phases. The large excitation angle for the $\alpha_x\alpha_y$ scheme may not be practical due to high demand on RF peak power when a sharp slice profile is used. A split of flip angles into two excitations can be realized in the $\alpha_x - \gamma_y - \alpha_y - \gamma_x$ scheme: one of sharp slice profile, α, and one with no or very weak slice select gradients, γ.

5.3.2. NUMERICAL OPTIMIZATION —CHOICE OF PARAMETERS IN THE SELECTED SCHEME

The schemes were compared and the parameters of the schemes optimized with a Cramér-Rao lower bound (CRLB) analysis[140].

Specifically, we evaluated the CRLB for all ten unique $k = 4$ schemes differing in the axis around which the RF pulses are played out, using two alternating flip angles $\alpha \in [20^o, 180^o]$, $\gamma \in [10^o, 190^o]$, with steps of 5^o. The simulation used the actual RF profiles as played out on the MR scanner scaled to the nominal flip angle.

For all evaluated settings, the coefficient of variation (CV) of the T1 and T2 was evaluated as the division of the square root of the CRLB by the nominal T1 (800 and 1100 ms) or T2 (50 and 200 ms) values for $\beta \in [0, 2\pi]$. These T1 and T2 values approximately span most of the commonly quantified tissues [127].

It was observed that for the schemes with low CV, the CV depended only weakly on $B0$. However, for some schemes strong dependence on FA was observed close to the minimum CV. Avoiding those situations, overall the $\alpha_x - \gamma_y - \alpha_y - \gamma_x$ scheme with $\alpha = 30^o$ and $\gamma = 175^o$ was considered to provide the best compromise over the range of T1, T2, and $B0$.

Hence this scheme is the building block of the new sequence that we named Multi-Phase balanced, non-Steady State Free Precession (MP-b-nSSFP).

5.3.3. ACQUISITIONS

The IRB (ethics committee name: Medische Ethische Toetsings Commissie Erasmus MC, https://www.erasmusmc.nl/nl-nl/pages/metc) approved the in-vivo study (protocol 2014-096) and the acquisition was carried out after obtaining the informed consent from the volunteers. All experiments were performed in accordance with relevant guidelines and regulations. Only one representative volunteer is presented in this work to show the outcomes obtained. The acquisitions were performed on a 1.5 T clinical scanner (GE Optima MR450w, General Electric Medical Systems, Waukesha, WI) with a 16 channel head and neck coil.

The reference map were obtained with a multiparametric method that currently is a product for different vendors (MAGiCMagnetic Resonance Image Compilationfor GE scanners). It is based on QRAPMASTER [14] that uses a multi-echo acquisition of a

saturation-recovery sequence combined with a Fast Spin-Echo (FSE) as readout to obtain quantitative maps of T1, T2, and Proton Density (PD). Once the quantitative maps have been obtained, weighted images are synthesized from these maps. The acquisition was performed in axial orientation (AC-PC) with a TR of 4.7, FOV of 31 cm, and voxel-resolution of 1.2×1.2×5.0 mm. The total acquisition time of 20 slices covering all the brain was 5 min and 34 s. The phantom was scanned with the same protocol.

Additionally, reference B1 and B0 maps were obtained for the phantom, in order to compare them from those derived from the method poposed in this work. The B1 map is a two-dimensional gradient echo based pulse sequence as described in [148]. B0 map is based on 2D GRE pulse sequence repeated two times with different TE as described in [149, 150].

The images with our sequenceMP-b-nSSFPwere acquired with a Field of View 24 cm, reconstruction matrix 256×256, slice thickness 5 mm and 64 rewinded spiral out arms with 512 samples per arm for complete data collection. The images were reconstructed by density compensated non-uniform fast Fourier transform (FFT).

For the proposed MP-b-bSSFP, we acquired 25 repeats of the $\alpha_x - \gamma_y - \alpha_y - \gamma_x$ scheme (Fig. 5.3-e) $\alpha = 30^o$, $\gamma = 175^o$, four readouts per block and TR=120 ms per block with a delay of 3 s between blocks that acquire different spiral arms. The total acquisition time was 6 m and 40 s in this proof of concept study in which no acceleration was used. Due to radiofrequency specific absorption rate (SAR) and time restrictions, the pulses were not slice selective and instead surrounded by crushers to suppress out-of-slice signals.

The maps were obtained by for each voxel fitting

$$\theta = \underset{\theta}{\arg\min} |S - Bloch(\theta)|^2 \; with \; \theta = [Re(S0), Im(S0), E1, E2, \beta, B1]^T \tag{5.13}$$

where S is a vector with the complex valued signal of all 100 echoes, $Bloch(\theta)$ is a single species bloch simulation using hard RF pulses, $E1 = e^{-TR/T1}$, $E2 = e^{-TR/T2}$ model the longitudinal, respectively transversal magnetization decay, β the offresonance induced phase evolution, $B1$ a scaling factor for the RF pulses and $S0$ is proportional to proton density and contains the transmit-receive phase.

After fitting, the T1 and T2 were computed from E1 and E2.

The non-linear optimization was started from the best 5 out of 1000 candidate points, pseudo-randomly selected in the range $E1 \in [0.91]$, $E2 \in [0.31]$, $\beta \in [\pi, \pi]$, $B1 \in [0.51.5]$, with linear least squares solution for $S0$. The non-linear optimization was performed with a custom trust region quasi Newton method implemented in MATLAB and the final fit with the lowest cost was returned[151]. The entire fitting procedure took 0.56 s/voxel at our workstation (i7-8700 CPU).

An evaluation of the applicability of the model to the acquired data in the presence of intra-voxel B0 dispersion is presented in the supplementary material.

5.3.4. DEMONSTRATION OF THE SIGNAL EVOLUTION ON A CLINICAL SCANNER

Figure 5.4 shows the typical banding artifact present in balanced sequence and how the theoretical model (see Eq. 5.1) closely matches the data points despite the presence of external field ($B0$) inhomogeneities.

Figure 5.5 shows images and different time points of the signal evolution and the signal evolution for three different tissues using as propagator the $\alpha_x - \gamma_y - \alpha_y - \gamma_x$ scheme in a balanced pulse sequence. The banding artifact is gone and the signal evolution is also described by the same theoretical model (see Eq. 5.1).

5.3.5. STANDARDIZED PHANTOM AND PARAMETRIC MAPS

In order to evaluate the accuracy and precision, 12 vials from the Eurospin phantom (https://www.leedstestobjects.com/index.php/phantom/t1-t2-gels/) with known T1 and T2 values were scanned with both methods MAGiC and MP-b-nSSFP.

Next figure shows the T1 and T2 maps from the MP-b-nSSFP and MAGiC (Fig. 5.6).

Figure 5.7 shows a BlandAltman comparison between MAGiC and MP-b-nSSFP.

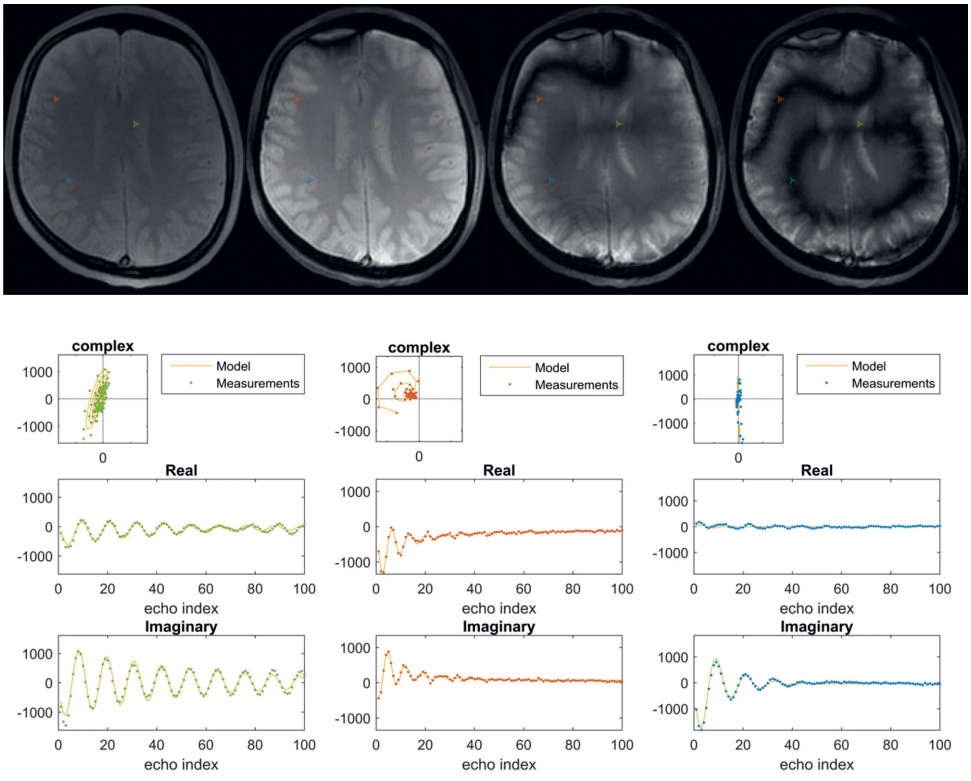

Figure 5.4: Images in the first row show the transient contrast at time points 1, 3, 5, 7 along the acquisition in a balanced pulse sequence in a α_x scheme. The second row shows for this sequence the signal as it evolves along the echo train for three voxels (depicted on the anatomical image). The left and right subfigures shows are from the blue and green voxels, where the spins are on-resonance. The middle subfigure (red voxel) shows a spiral in the complex signal plane. This clearly shows the regularity of the evolution. On the right subfigure middle and bottom the orthogonal real and imaginary components are depicted. The frequency of the oscillations is constant, the decay of the amplitudes is exponential. The steady state is not zero. The fitted curves show the fitted harmonic oscillator model.

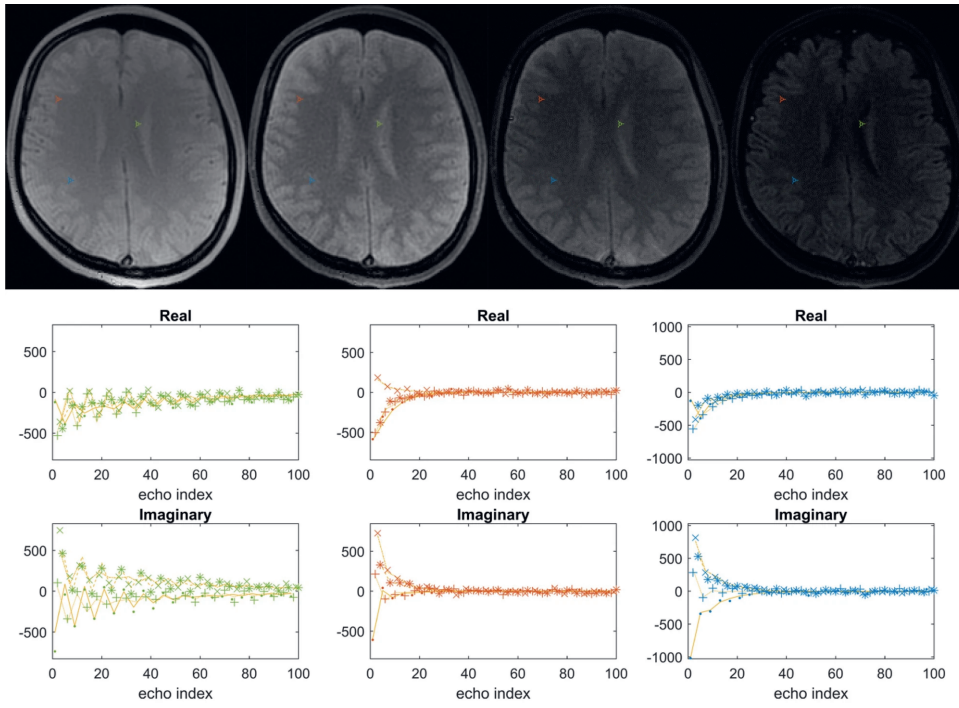

Figure 5.5: The first row shows the transient contrast at different time points along the acquisition in a balanced pulse sequence for the propagator as a composite of pulses according to the $\alpha_x - \gamma_y - \alpha_y - \gamma_x$ MP-b-nSSFP scheme. The second and third rows show the signal and fit for three highlighted voxels from three different tissues. The observations of the four different echoes in each block of the propagator is shown with different symbols (.,+, Œ,*).

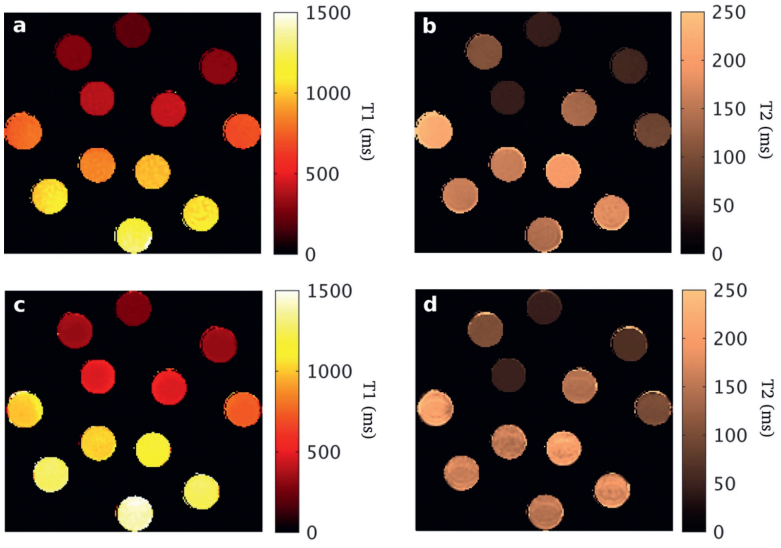

Figure 5.6: The first row shows the maps from the proposed balanced pulse sequence for the propagator as a composite of pulses according to the $\alpha_x - \gamma_y - \alpha_y - \gamma_x$ MP-b-nSSFP scheme ($\alpha = 30^o; \gamma = 175^o$). The second row show maps obtained using conventional MAGiC. (a,c) T1 maps. (b,d) T2 maps.

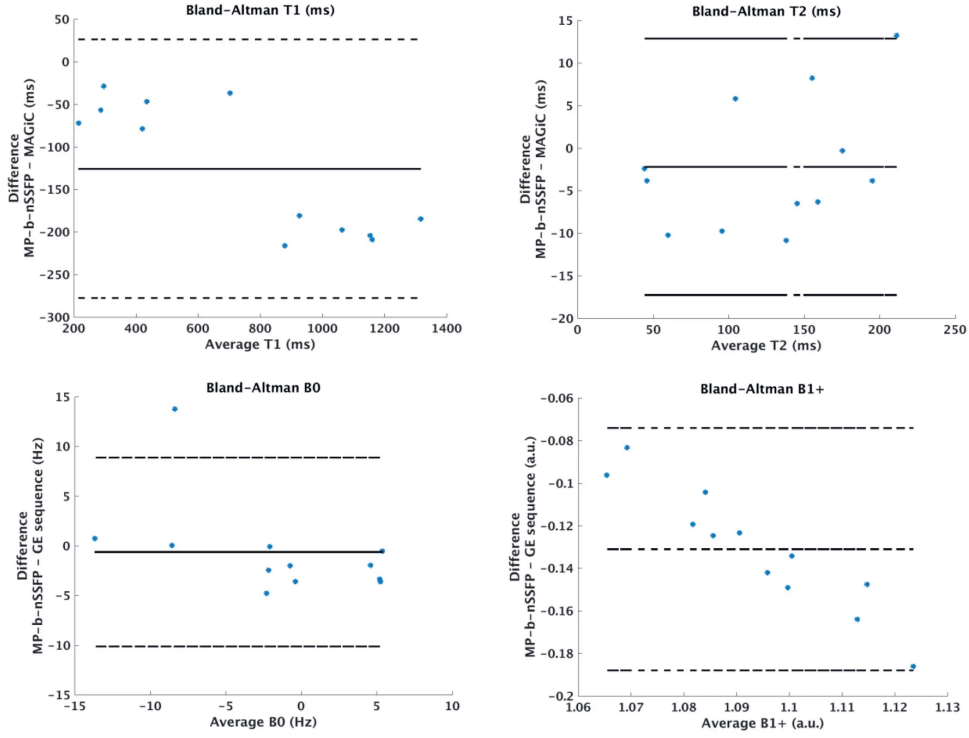

Figure 5.7: BlandAltman plots comparing ROI mean T1 and T2 values of the proposed MP-b-nSSFP sequence with the $\alpha_x - \gamma_y - \alpha_y - \gamma_x$ scheme ($\alpha = 30^o; \gamma = 175^o$) and MAGiC.

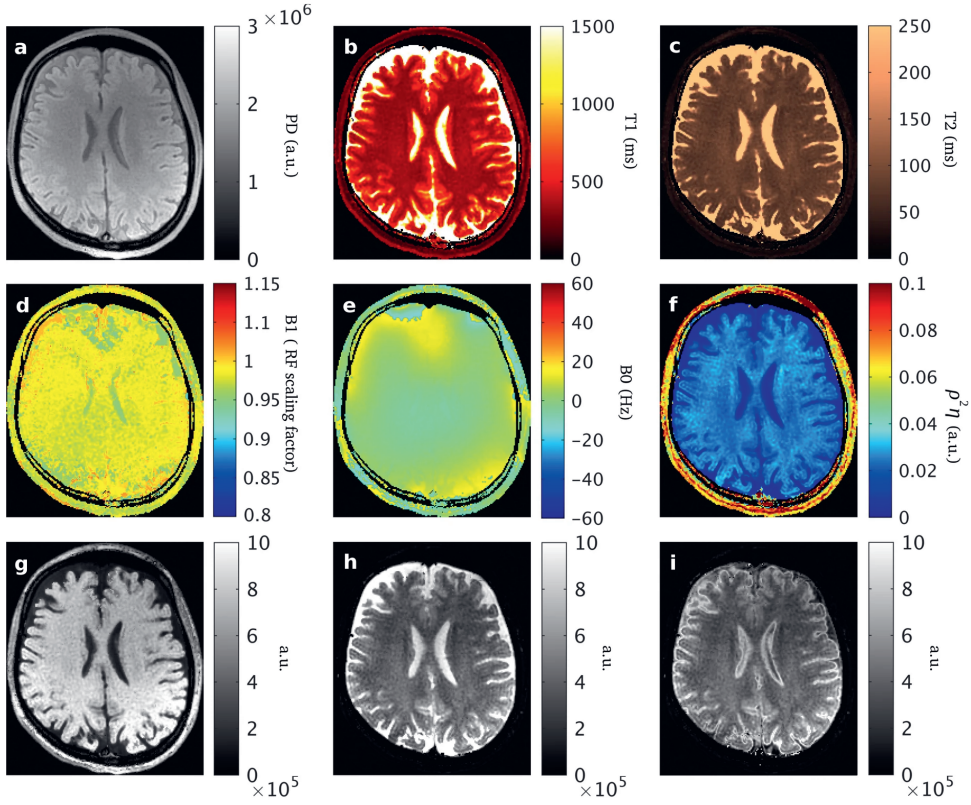

Figure 5.8: The parametric maps derived with the proposed model are shown estimated from the MP-b-nSSFP sequence with $\alpha = 30^o$, $\gamma = 175^o$, TR=30 ms. Top row shows: (**a**) PD (proton density, a.u.); (**b**) T1(ms); (**c**) T2 (ms); (**d**) B+1 (excitation RF field scaling factor); (**e**)B0 (deviation in static magnetic field; Hz); (**f**) $\rho 2\eta = det(A) = \epsilon_2^2\epsilon_1$ (HO harmonic oscillator), (**g**) synthetic T1-weighted; (h) synthetic T2-weighted; (i) synthetic T2-FLAIR.

5.3.6. IN-VIVO PARAMETRIC AND SYNTHETIC MAPS

Figure 5.8 shows the results from the MP-b-nSSFP in-vivo scan including the HO maps explained above. Additionally, figure 5.8 shows synthetic weighted images [14]. The T1-weighted image was simulated with TE=20 ms and TR=300 ms. The T2-weighted image was simulated with TE=120 ms and TR=4500 ms. The T2-FLAIR images were simulated with TE=120 ms, TR=15,000 ms and inversion time (TI) equal to 3000 ms. In order to provide a fair comparison we have used with the same protocol described above.

Table 5.1: T1 and T2 values estimated in gray and white matter from the prosposed method, MP-b-nSSFP and MAGIC. Standard deviations are expressed in parenthesis. Reference columns respectively are: (1) Deoni et al.[12], (2) Shcherbakova et al.[58] and (3) Warntjes et al.[14]

Param	Tissue	MP-b-nSSFP	MAGIC	Ref. 1	Ref. 2	Ref. 3
T1	GM	628 (115)	1082 (231)	1065 (51)	813 (54)	1048 (61)
	WM	339 (28)	602 (65)	608 (23)	496 (22)	561 (12)
T2	GM	98 (5)	93 (4)	98 (7)	85(5)	94 (6)
	WM	73 (4)	78 (5)	54 (4)	63(22)	63 (2)

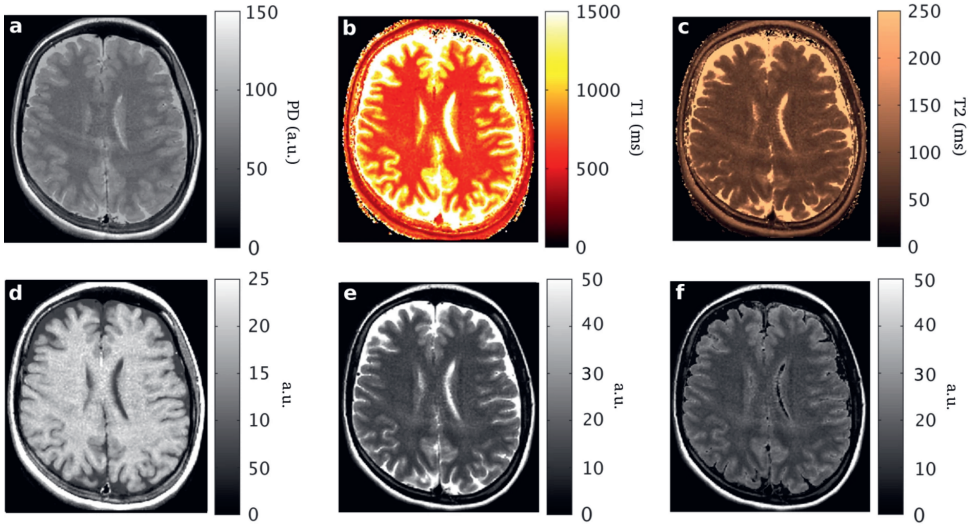

Figure 5.9: The parametric maps and synthetic images as obtained with MAGiC : (**a**) PD (proton density, a.u.); (**b**) T1(ms); (**c**) T2 (ms); (**d**) synthetic T1-weighted; (**e**) synthetic T2-weighted; (**f**) synthetic T2-FLAIR.

Figure 5.9 shows the maps as acquired with MAGiC.

Table 5.1 summarizes the estimated values of T1 and T2 in gray and white matter with MP-b-nSSFP and MAGiC and reference values from DESPOT1 and DESPOT2[12], PLANET [58] and QRAPMASTER [14] respectively.

5.4. DISCUSSION

In this work, we conceptually addressed several important aspects for enabling quantitative mapping from the fast transient response in a balanced pulse sequence.

With this we extend previous work in this domain [52, 139] to allow composite propagators. It deviates from MR fingerprinting approaches[19, 59] in which experimental parameters are varied along the transient evolution and relaxation parameters are estimated by dictionary matching. Instead, we provide an analytical description of the transient response of a balanced sequence with repetitive blocks. This comprehensively provides simultaneous mapping as well as maps of the experimental conditions.

We proposed a train of acquisition blocks without variations along the train and without suppression of any part of the signal. We showed that a simple and very compact description can be provided for such a sequence. To our knowledge, the resulting real-valued expression has not been previously published.

Additionally, there were two separate aspects that we challenged. One was the impracticality or even impossibility to describe the signal in an analytical form in the transient state, especially when no part of the signal is suppressed (e.g. spoiling). The second aspect was the unfeasibility of using a single species approximation of complex and heterogeneous voxels for the transient evolution of a balanced sequence.

Moreover, we simultaneously addressed a long-standing problem of the balanced Steady State Free Precession technique: banding artefacts. By virtue of the conceptual design of the sequence (i.e.: 3D trajectory maintained by the composite propagator) every point in the image plane bears the same signal evolution characteristics. Along the transient evolution the phase dispersion is limited (see Fig. 5.3-d,e) as the oscillation frequency (φ, Eqs. 5.11,5.12) is nearly the same for all off-resonance frequencies (β). Consequently no (propagating) banding waves in the image space will appear at any time point of the transient response (compare Fig. 5.4 vs Fig. 5.5), achieving the desired artefact-free images from balanced MR sequences. This could also be interpreted as a result of the pulse which acts as a refocusing pulse, however, the sequence is still sensitive to B0 inhomogeneities across the image because the model contains and estimates the intra-voxel phase accrual. To our knowledge, this is a novel achievement that is different from the typical phase cycling in different runs [152, 153].

The resulting signal evolution demonstrates the validity of the single species description despite experimental imperfections.

It can be observed in the results from a standardized phantom (Fig. 5.7) that most of the results for T2 are in good agreement with MAGiC. However, the results for T1 are underestimated. Possibly, this is due to slice profile imperfections [154–157] and finite echo train length as well.

In In-vivo experiments, T2 results are also in good agreement wih MAGiC. For T1, there is a substantial underestimation as well. There are some additional intra-voxel

physiological conditions that could be hindering the accuracy in T1: intrinsic intra-voxel assymetries [158–161] water molecules exchanges[162], diffusion[163] and magnetization transfer [58, 127, 164]. If validated and specific enough, such sensitivity to these other phenomena could be exploited for obtaining physiological information such as myelin content. The supplementary material demonstrates that in the current implementation intra-voxel B0 dispersion and off-resonance can bias the T1 and T2 estimation. However, still the effect of B0 dispersion is limited as the estimated T2 value is substantially above the T2* value that would be obtained in, for example, a gradient echo experiment. Addressing these T1 and T2 biases is a topic of further research.

Our method relies on the topological interpretation of an algebraic object (i.e. the propagator: a transformation between the parameter space and the eigenvalue space). With the proposed propagators preserving the topology, the analytical single species description remains valid and allows simultaneous multi-parametric mapping.

It allows the separation of conceptual details of the propagator design and the numerical optimization of the nominal experimental parameters. Regarding the propagator, our method allows single species description even on the presence of B0 inhomogeneities based on the range of the appropriate eigenvalues without excluding those complex (unlike Asslanders proposal[140]). Furthermore, the 3D trajectory of μ is maintained at any value of B0 in order to avoid loss of information (none of the normal mode vectors vanish). Moreover, the mapping between parameter space and eigenvalue space preserves topology in order to distinguish between species by their signal evolution. To demonstrate the feasibility on actual scanners, we have selected one of the propagators that fulfills these requirements. In addition to the analytical approach, a numerical optimization of parameters such as flip angles and phases is carried out for the best estimation of T1, T2, PD, B1, B0. So, our novel approach not only enables the estimation of intrinsic parameters, but from the same data and estimation process, one can derive the imperfections of the experimental setup. The macroscopic confounding factors (experimental imperfections such as B0 inhomogeneities and B1 inaccuracies) are not simply suppressed or excluded in our acquisition, rather they are included in the theoretical description as parameters to be determined (see results 'd' and 'e' in Fig. 5.6).

To our knowledge, no other parametric imaging methods provide estimation of this set of intrinsic and experimental parameters simultaneously based on an analytical solution describing the transient response of the magnetization with using dictionaries.The concurrent estimation of intrinsic and experimental imperfections based on the proposed comprehensive analytical model makes this new technique less affected by common system imperfections and could allow for the development of less demanding MR scanners. Based on the robustness of the synchronized estimation of

experimental imperfections and parametric maps, synthetic MR images for different clinically relevant contrasts can also be reconstructed without relevant artifacts (see results g, h and i in Fig. 5.8). As a consequence of these features, our method could contribute to the standardization of MR imaging based on simultaneous multi-parametric mapping and synthetic weighted MR.

5.5. CONCLUSIONS

Building on signal-based MR, we provide a complete and comprehensive analytical expression for the signal evolution of a balanced sequence. We extend this solution from the continuous Bloch equation to a discrete description of an entire imaging sequence. The analytical expression relies on a simple, single species model of an imaging voxel which is shown to be appropriate despite the heterogeneity of voxels in-vivo. We demonstrate the importance of an analytical approach in the design of the sequence propagator. This theoretical model could be fitted to experimental data without requiring a dictionary. We simultaneously derive parametric maps of the intrinsic properties (T1, T2, PD) as well as from imperfections of the experimental parameters (B0, B1). We demonstrate the feasibility of our method on clinical MRI scanners for in-vivo brain scans.

ACKNOWLEDGEMENTS

We thank Perry Frederik (GE Healthcare) for comments on the manuscript. This work was partially supported by GE Healthcare (WS B-GEHC-8-2018).

AUTHORSHIP STATEMENT

G.K.: conception, design of the work, acquisition, analysis, interpretation of data, creation of new software used in the work, drafting and substantively revision of the paper. L.N.: conception, design of the work, acquisition, analysis, interpretation of data and substantively revision of the paper. M.V.: conception, design of the work, acquisition, analysis, interpretation of data, creation of new software used in the work and substantively revision of the paper. G.P.K., Interpretation of data, drafting and substantively revision of the paper. D.P.: conception, design of the work, analysis, interpretation of data, creation of new software used in the work, drafting and substantively revision of the paper. J.A.H.-T.: conception, design of the work, acquisition, analysis, interpretation of data, drafting and substantively revision of the paper. G.K. and J.A.H.-T. are equally contributors.

CONFLICTS OF INTEREST

The authors declare no conflict of interest.

5.6. SUPPLEMENTARY MATERIAL

5.6.1. EVALUATION OF SLICE PROFILE AND INTRA-VOXEL B0 DISPERSION

To evaluate if the proposed model applies to the actual pulse sequence with imperfections in the slice profile and intra-voxel B0 dispersion the following simulation study is performed. Signals of a voxel are generated by an extensive Bloch simulation that includes the full slice/slab selective RF pulse shapes as well as slice selection gradients as they are played out on the scanner for the proposed 25 repeats of the scheme with $\alpha = 30^o$ and $\gamma = 175^o$ (it corresponds to the figure 5.3-e in the manuscript). Figure 5.10 shows 1 repeat of the pulse sequence for this scheme.The pulses have a sharp slice profile and the hard pulses are crushed.

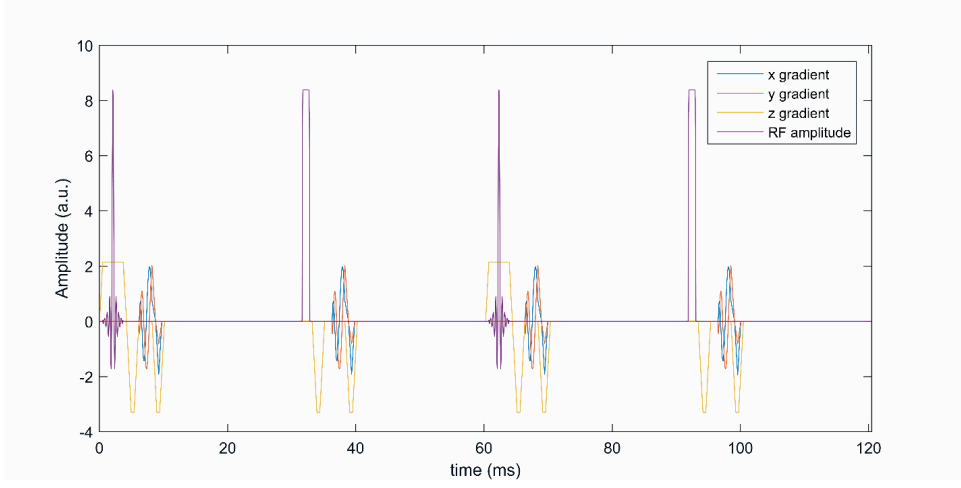

Figure 5.10: A single-block of the scheme , with $\alpha = 30^o$ and $\gamma = 175^o$ as played out on the scanner.

In the simulation, the balanced readout was not included as the simulated spins comprised a single voxel, and the signal was captured at the start of the center-out spiral readout. To simulate the slice profile 400 spins were distributed uniformly over an extend of 1.7 times the slice width of 5mm and the simulation was performed for 1001 values of B0 linearly spaced in [-500, 500] Hz. Other simulation parameters are PD = 1, T1 = 800 ms, T2=80 ms , and nominal scaling of the RF power.

As realistic model of intra-voxel B0 dispersion we constructed Cauchy weighted combinations of the simulated signals with the width corresponding to $T2' = [20, 40, 80, 160, 320, \text{inf}]\, ms$ with center frequency from -100Hz to 100Hz.

The thus generated signals include the slice profile as generated by the scanner as well as intra-voxel B0 dispersion. Subsequently these signals were fitted by the method

described in the main manuscript.

5.6.2. RESULTS

Figure 5.11 shows the fitted parameters as function of B0.

The results with long T2' indicate a low bias in the estimates obtained with the single species model. A relevant effect in the simulation of the current sequence as implemented on the scanner is the different gradient strength during the α and γ pulses. With off-resonance, the gamma pulse shifts slice position much more than the alpha pulse. Hence effectively for $|B0| > 25Hz$ the gamma pulse is lower inside the slice selected by the α pulse. This seems to primarily cause a bias towards lower values of T1. With 3D acquisitions or a different design of the RF pulses this could be remedied.

The results shows that intra-voxel dispersion is causing bias to the estimated parameters. For low |B0| the T1 seems to be positively biased when $T2' < 2TR$. T2 is underestimated when substantial intra-voxel B0 dispersion is present (i.e. low T2'). However, as aimed for in the design, the dispersion is limited and hence the estimated T2 value is substantially above the T2' value that would be obtained in, for example, a gradient echo experiment.

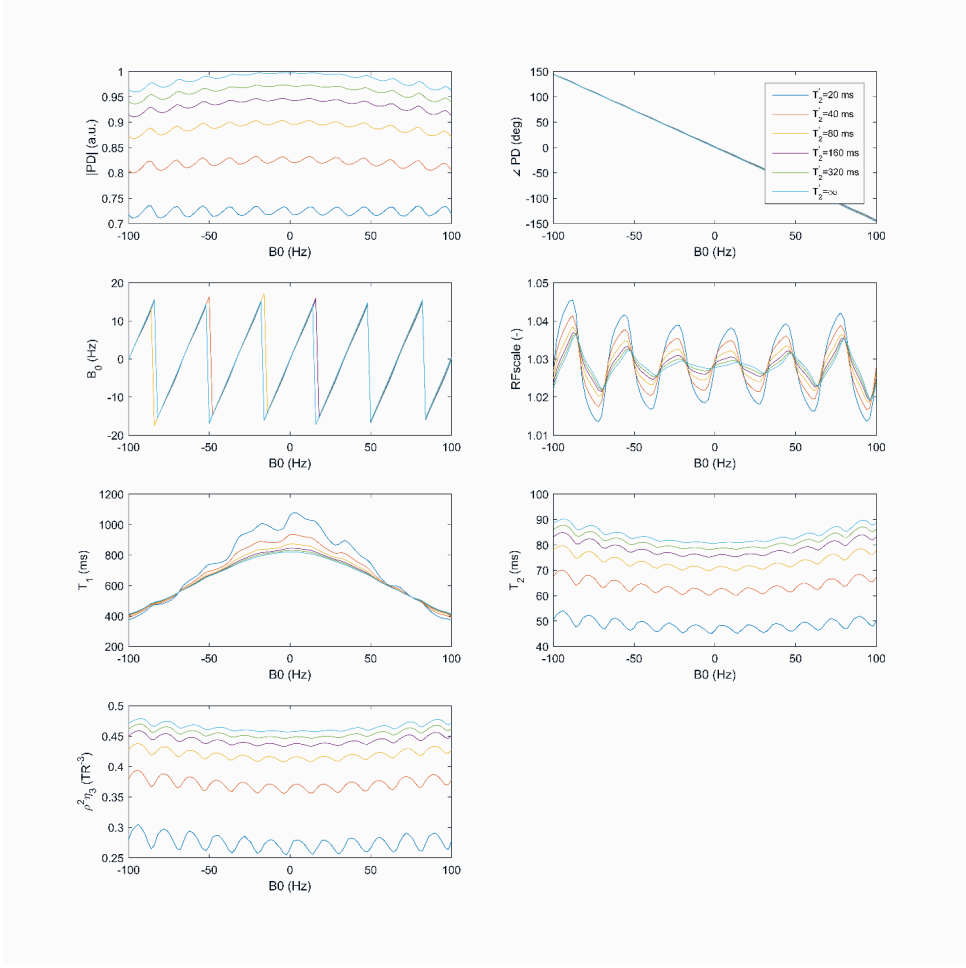

Figure 5.11: Parameters estimated from the data simulated including slice profile and for different T2' as function of B0.

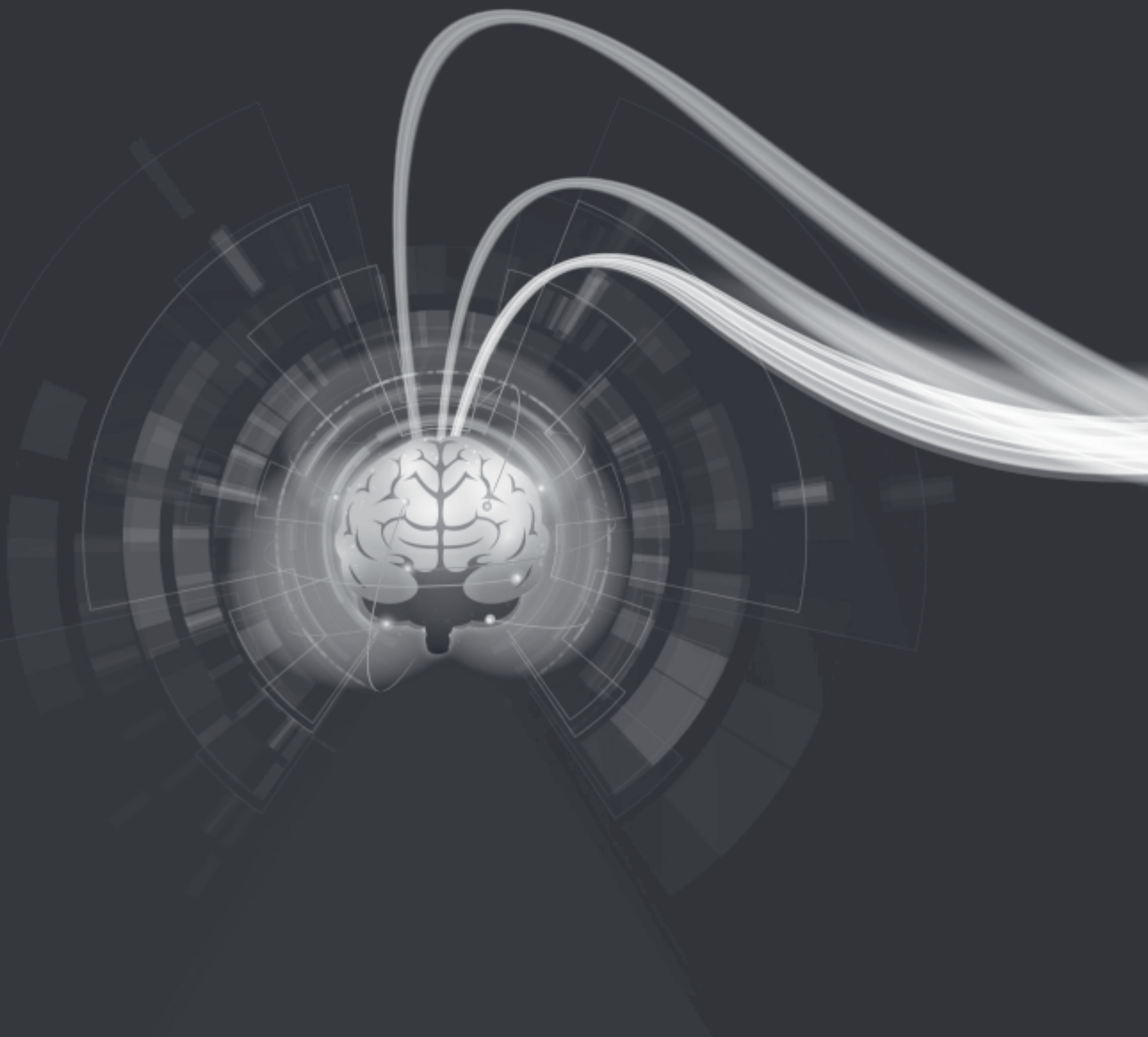

6

GENERAL DISCUSSION AND FUTURE WORK

In this thesis, we investigated and evaluated fast multi-parametric quantitative MR techniques, developed a new analysis method, and proposed a new quantitative MRI sequence. These techniques share the characteristic feature of acquiring several quantitative maps simultaneously in a short acquisition time (around 5-6 minutes for the whole brain).

First, in **chapter 2** we demonstrated good accuracy and repeatability (following standard metrics for bias and repeatability [20, 165]) of the already existing techniques QRAPMASTER [14] and MRF-vFA [18] in 5 volunteers and a phantom. Our results showed that although MRF-vFA had significantly more bias, both techniques are repeatable, and comparable to the repeatability of other techniques such as MRF [24, 25, 166], DESPOT1, and DESPOT2 [12]. Furthermore, the quantitative values obtained with QRAPMASTER and MRF-vFA were both in good concordance with widely accepted quantitative MR techniques, such as inversion-recovery for estimating T1 values and CPGM for estimating T2 values [10, 11]. The acquisition time of these techniques is especially relevant as they enable acquiring the whole brain within 5 minutes and 34 seconds using QRAPMASTER and 70 seconds using MRF-vFA.

After evaluating these techniques in a phantom and volunteers, we went one step further and assessed the results obtained with these techniques in glioma patients [34, 167]. There were three motivations to pursue this research. First, the existence of previous reports on the relationship between T1 and T2 quantitative values and diseases such as multiple sclerosis, epilepsy, and dementia [6]. Second, the findings encountered in glioma assessment by other authors using MRF [33] and QRAPMASTER [30, 31]. And finally, our positive results using QRAPMASTER and MRF-vFA regarding accuracy and repeatability.

In the case of QRAPMASTER, we acquired data from 14 glioma patients using the sequence MAGiC from GE. This is included in **chapter 3**, where two main important results are reported and discussed. The first is that the tumoral tissue and the healthy tissue could be differentiated by its quantitative relaxometry parameters prior to contrast injection. One significant aspect is that we found improved differentiation between tissue types when T1 and T2 were used jointly compared to each parameter individually. This could boost the importance of these new techniques, since their acquisition is multi-parametric, shortening the acquisition time needed and avoiding problems in postprocessing steps such as registration between different images.

The second important result of **chapter 3** is that pre-contrast-agent acquisition allowed the distinction (with sensitivity, specificity, and accuracy up to 73%) among tumors showing T1-enhancement after the injection of the contrast agent and those which did not show any T1-enhancement. This finding is especially relevant regarding patient well-being. Besides the discomfort, gadolinium-based contrast-agent injections

could have side effects (although not very common), such as nephrogenic systemic fibrosis in patients with reduced function of the kidneys or the liver[168], and the potential risk of immediate adverse reactions [169]. A technique that could predict the T1-enhancement without injecting contrast-agent could eliminate any risk and discomfort associated with the contrast injection and would reduce the resources needed. Furthermore, the deposition of gadolinium in the body after the contrast-agent injection has been proven[170], which could impact the subsequent future MR acquisitions [171, 172]. This could have a considerable impact on those patients who need several follow-up acquisitions[173].

As an MRF-based technique, we used 3D-QTI [19] (which is the 3D version of the so-called MRF-vFA). This sequence was acquired prior to contrast agent injection in 9 patients, which were also part of the group of patients in **chapter 3** and both acquisitions (3D-QTI and MAGiC) were performed during the same session. The acquisition of this 3D version was considerably longer than for the 2D version MRF-vFA (6min and 25s versus 70s). However, besides higher resolution, mainly in the slice direction, and isotropic voxels, it has the advantage of allowing motion correction as in [120, 123]. In [34] we showed how using neural networks to infer the quantitative PD, T1 and T2 parameters improves the estimation. Also, a gaussian mixture analysis was applied showing the capability of the quantitative values to distinguish different substructures, such as peritumoral edema, enhancing tumor and necrotic core. These results are in line with those discussed in **chapter 3**.

One limitation of QRAPMASTER/MAGiC and MRF-vFA/3DQTI is the assumption of single-species voxels. This is rarely the case for in-vivo acquisitions and it was previously reported as a source of problems when using weighted images to segment or depict different tissue types within the brain such as white matter, grey matter, and CSF [174–176]. This hampers the assessment of diseases based on volumetry and longitudinal studies since it blurs the boundaries between tissue types [36, 38]. Furthermore, it is well-known that complex tissues, such as white matter, contain several components, such as myelin[40, 43, 177]. Accurately measuring the myelin contain has been proven relevant in diseases affecting the white matter tissue of the brain[43–45]. To overcome this issue of multi-component tissues, previous attempts to depict different components within a voxel were reported by modelling MRF signals with 3 a priori defined tissues [142], by considering a Bayesian approach [46], or by applying a reweighted-L1-norm regularized algorithm [47]. In **chapter 4** of this thesis, we evaluated another technique to depict the components within a voxel, SPIJN-MRF [48]. This technique has the advantage of using relatively fast computation times (a few minutes per slice) without limiting the number of predefined tissues within a voxel. This multicomponent analysis produced highly repeatable results in synthetic fully

sampled data and in highly undersampled MRF data from 5 volunteers. In simulation experiments, SPIJN-MRF showed higher accuracy and precision than the commonly used SPM[56] and FSL[55] segmentation software. The obtained tissue-fraction maps with SPIJN-MRF from the in-vivo data were compared with the segmentations obtained by SPM and FSL using the synthetic data (instead of real T1-weighted acquisitions) produced from the estimated PD, T1, and T2 maps with single-specie dictionary matching. Visually, the three techniques were similar, although SPIJN-MRF showed a bit more substructures in the CSF map. The tissue maps obtained with SPM and FSL were more similar than the ones obtained with SPIJN-MRF. However, the estimated volumes were different for the three techniques. Similar differences were previously reported between SPM and FSL [130, 178]. These results suggest that SPIJN-MRF could be an accurate and repeatable technique for segmented tissue, with the added value of obtaining an estimation of the T1 and T2 values per tissue and more components than the usual white matter, gray matter, and CSF. For instance, a relevant component was found which could be associated with myelin water fraction. This advantage would be possible because SPIJN-MRF tries to tear apart signal contributions, instead of classifying the voxels by tissue type, as SPM or FSL. This is a relevant feature because a single tissue type might have multiple signal components, and this is not considered by SPM or FSL. Further investigation is needed to confirm our findings, by acquiring high-resolution T1-weighted images to be processed with SPM and FSL and by measuring the myelin water fraction using a well-established technique.

Another limitation of the introduced QRAPMASTER/MAGiC and MRF-vFA/3DQTI techniques is the lack of information on extrinsic parameters related to the system, such as B0 and B1 inhomogeneities. This information has been of interest to the MR community since accurate measurements of these parameters can be used to improve image quality, such as using B0 mapping for correcting geometric distortion [179] or using B1 mapping to improve quantitative measurements [71, 84]. In this thesis, we overcome this issue in **chapter 5** by proposing a completely new sequence under the acronym MP-b-nSSFP. We first described the evolution of the signal evolution during the transient response of a repetitive sequence under a comprehensive mathematical framework and then we optimized the sequence to obtain accurate quantitative intrinsic parameters (PD, T1, and T2) and accurate quantitative extrinsic parameters (B0 inhomogeneities and B1+). This new sequence has the advantage of not being limited by the dictionary since it uses a mathematical description as QRAPMASTER/MAGiC and the advantage of using the transient-response as MRF-type sequences. Moreover, the MP-b-nSSFP sequence is a breakthrough in the actual state of the art of multi-parametric quantitative MRI since it analytically describes the transient-response and uses it to estimate at once the intrinsic and extrinsic

parameters. To our knowledge, no other technique offers this complete set of information. The transient-response was explored before but for other purposes, such as reaching the steady-state earlier, compensating for the off-resonance effects, analytically calculating echo amplitude, or using the analytical solutions in composite laser-pulse spectroscopy. [50–54, 137].

In summary, although these fast multi-parametric quantitative techniques have some limitations, we demonstrated that they are accurate, repeatable, and sensitive to different types of tissues. Not to mention that their rapid acquisition times facilitate their inclusion in research and clinical environments, which favors new developments and applications. A good example of that is the new approach for the MRF data and the new multi-parametric sequence that we presented. These two novelties give deeper insight into the content of a voxel than existing quantitative imaging techniques and analysis.

FUTURE WORK

This thesis is devoted to the world of fast quantitative MRI, by reporting more data assessing existing techniques and proposing a new analysis and a new technique. The results obtained are promising regarding faster and richer MRI acquisitions, which encourage further research.

In this thesis, two already existing techniques (QRAPMASTER and MRF-vFA) were evaluated with positive results in accuracy and repeatability. However, the number of volunteers was limited and further validation is needed in larger groups of healthy volunteers of different ages and large cohorts of patients with other pathologies. Additionally, multi-system and multi-vendor repeatability and reproducibility studies should be conducted.

Regarding glioma patients, the work presented in this thesis is an initial approach, since the cohort of patients was small, the results were not quantitatively compared to other imaging techniques, and only relatively simple classification methods were applied. Using more complex algorithms for classification, such as using machine learning, could give more accurate results. However, the purpose of this work was to identify the information that is present in the T1 and T2 maps in an interpretable way, before investing algorithms that require more resources and (often) produce harder to interpret relations between the maps and the classification results. Also, the quantitative maps obtained can be used to obtain synthetic images with the same scan parameters as the conventional weighted images. Increasing the resolution, these synthetic images (instead of the acquired weighted images) could be used to feed the deep learning segmentation tool HD-GLIO, in order to compare the results obtained to

the segmentation obtained from the original weighted images. If synthetic images produce the same results as the conventional weighted images, the scan protocols could be sped up by substituting some of the conventional sequences with a single multi-parametric quantitative sequence. To be able to generalize the conclusions, data from larger cohorts of patients should be analyzed. As well as from patients with different diseases affecting the brain tissue to assess the capability of quantitative MR values of distinguishing between healthy and diseased tissue.

SPIJN-MRF is a very novel approach that estimates multiple components in each voxel but in-vivo measurement of the accuracy of the segmentation obtained should be addressed to ensure the truthfulness of those components. Acquiring in the same session MRF images and T1-weighted images with higher resolution would allow a rigorous comparison of the segmentation from SPIJN and the state of the art (either using specialized software or manual-expert-segmentation). Also, it would be important to compare the myelin water fraction maps from SPIJN-MRF with the myelin water fraction maps obtained with accepted techniques, such as measuring the spin-spin relaxation decay curves from a 32 echo imaging pulse sequence[43] or subsequent proposals using 3D Gradient and Spin-Echo, multigradient echo or mc DESPOT [40]. An evaluation from expert radiologists would provide more clear insights on the myelin water fraction maps and the quality of the myelin water fraction maps obtained with SPIJN-MRF.

Finally, the MP-b-nSSFP sequence is in a development phase and several aspects should be addressed. Currently, the sequence has a limited resolution and uses 2D acquisitions with long acquisition times. The latter is because, in the proof of concept, the full k-space is acquired without applying any acceleration technique. These limitations are being addressed in our group by developing a fast 3D MP-b-nSSFP sequence. The goal is to accelerate the acquisition enough to properly compare this sequence to the already existing ones. Once high-resolution images of the whole brain can be obtained in a reasonable time (5-10 minutes), an extensive assessment of its accuracy and precision should be performed in several volunteers and multiple systems.

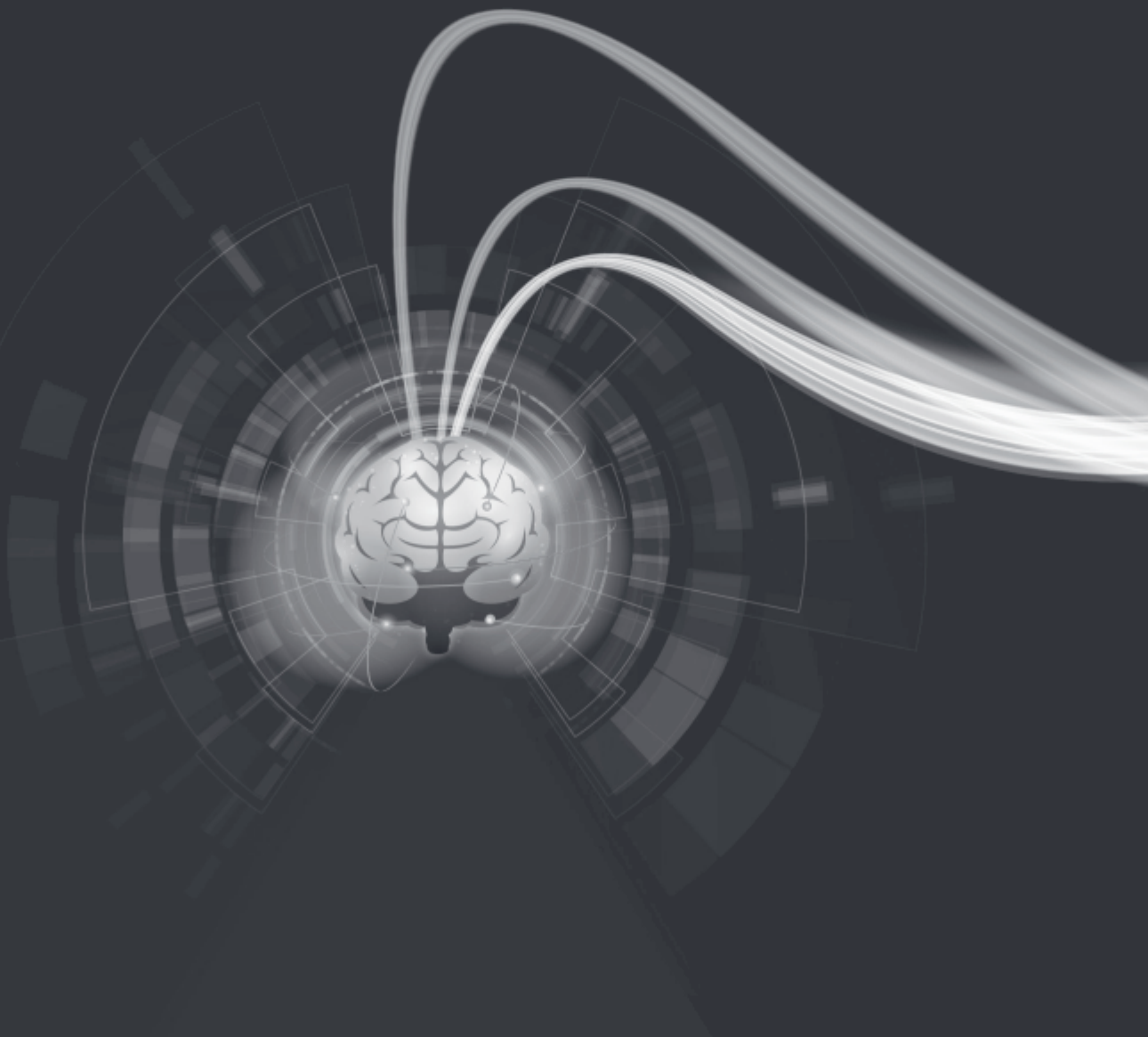

BIBLIOGRAPHY

[1] I. I. Rabi, J. R. Zacharias, S. Millman, and P. Kusch, *A New Method of Measuring Nuclear Magnetic Moment,* Physical Review **53**, 318 (1938).

[2] F. Bloch, *Nuclear Induction,* Physical Review **70**, 460 (1946).

[3] P. C. Lauterbur, *Image Formation by Induced Local Interactions: Examples Employing Nuclear Magnetic Resonance,* Nature **242**, 190 (1973).

[4] P. Mansfield and P. K. Grannell, *NMR 'diffraction' in solids?* Journal of Physics C: Solid State Physics **6**, L422 (1973).

[5] R. Damadian, *Tumor Detection by Nuclear Magnetic Resonance,* Science **171**, 1151 (1971).

[6] S. C. Deoni, *Quantitative Relaxometry of the Brain:,* Topics in Magnetic Resonance Imaging **21**, 101 (2010).

[7] G. M. Bydder and I. R. Young, *MR imaging: Clinical use of the inversion recovery sequence,* J Comput Assist Tomogr **9**, 659 (1985).

[8] H. Y. Carr and E. M. Purcell, *Effects of Diffusion on Free Precession in Nuclear Magnetic Resonance Experiments,* Physical Review **94**, 630 (1954).

[9] E. L. Hahn, *Spin Echoes,* Physical Review **80**, 580 (1950).

[10] R. K. Breger, A. A. Rimm, M. E. Fischer, R. A. Papke, and V. M. Haughton, *T1 and T2 measurements on a 1.5-T commercial MR imager.* Radiology **171**, 273 (1989).

[11] J. Z. Bojorquez, S. Bricq, C. Acquitter, F. Brunotte, P. M. Walker, and A. Lalande, *What are normal relaxation times of tissues at 3 T?* Magnetic Resonance Imaging **35**, 69 (2017).

[12] S. C. L. Deoni, T. M. Peters, and B. K. Rutt, *High-resolutionT1 andT2 mapping of the brain in a clinically acceptable time with DESPOT1 and DESPOT2,* Magnetic Resonance in Medicine **53**, 237 (2005).

[13] S. Ljunggren, *A simple graphical representation of fourier-based imaging methods,* Journal of Magnetic Resonance (1969) **54**, 338 (1983).

[14] J. Warntjes, O. D. Leinhard, J. West, and P. Lundberg, *Rapid magnetic resonance quantification on the brain: Optimization for clinical usage,* Magnetic Resonance in Medicine **60**, 320 (2008).

[15] D. Ma, V. Gulani, N. Seiberlich, K. Liu, J. L. Sunshine, J. L. Duerk, and M. A. Griswold, *Magnetic resonance fingerprinting,* Nature **495**, 187 (2013).

[16] A. Hagiwara, M. Warntjes, M. Hori, C. Andica, M. Nakazawa, K. K. Kumamaru, O. Abe, and S. Aoki, *SyMRI of the Brain: Rapid Quantification of Relaxation Rates and Proton Density, With Synthetic MRI, Automatic Brain Segmentation, and Myelin Measurement,* Investigative Radiology **52**, 647 (2017).

[17] M. Weigel, *Extended phase graphs: Dephasing, RF pulses, and echoes - pure and simple: Extended Phase Graphs,* Journal of Magnetic Resonance Imaging **41**, 266 (2015).

[18] P. A. Gomez, G. Bounincontri, M. Molina-Romero, J. I. Sperl, M. I. Menzel, and B. H. Menze, *Accelerated parameter mapping with compressed sensing: An alternative to MR fingerprinting,* in *ISMRM* (Honolulu, HI, USA, 2017) p. 6.

[19] P. A. Gómez, M. Molina-Romero, G. Buonincontri, M. I. Menzel, and B. H. Menze, *Designing contrasts for rapid, simultaneous parameter quantification and flow visualization with quantitative transient-state imaging,* Scientific Reports **9**, 8468 (2019).

[20] L. G. Kessler, H. X. Barnhart, A. J. Buckler, K. R. Choudhury, M. V. Kondratovich, A. Toledano, A. R. Guimaraes, R. Filice, Z. Zhang, D. C. Sullivan, and QIBA Terminology Working Group, *The emerging science of quantitative imaging biomarkers terminology and definitions for scientific studies and regulatory submissions,* Statistical Methods in Medical Research **24**, 9 (2015).

[21] D. C. Sullivan, N. A. Obuchowski, L. G. Kessler, D. L. Raunig, C. Gatsonis, E. P. Huang, M. Kondratovich, L. M. McShane, A. P. Reeves, D. P. Barboriak, A. R. Guimaraes, R. L. Wahl, and For the RSNA-QIBA Metrology Working Group, *Metrology Standards for Quantitative Imaging Biomarkers,* Radiology **277**, 813 (2015).

[22] A. Hagiwara, M. Hori, J. Cohen-Adad, M. Nakazawa, Y. Suzuki, A. Kasahara, M. Horita, T. Haruyama, C. Andica, T. Maekawa, K. Kamagata, K. K. Kumamaru, O. Abe, and S. Aoki, *Linearity, Bias, Intrascanner Repeatability, and Interscanner Reproducibility of Quantitative Multidynamic Multiecho Sequence for Rapid Simultaneous Relaxometry at 3 T: A Validation Study With a Standardized Phantom and Healthy Controls,* Investigative Radiology **54**, 39 (2019).

[23] A. M. Betts, J. L. Leach, B. V. Jones, B. Zhang, and S. Serai, *Brain imaging with synthetic MR in children: Clinical quality assessment,* Neuroradiology **58**, 1017 (2016).

[24] Y. Jiang, D. Ma, K. E. Keenan, K. F. Stupic, V. Gulani, and M. A. Griswold, *Repeatability of magnetic resonance fingerprinting T_1 and T_2 estimates assessed using the ISMRM/NIST MRI system phantom: Repeatability of MR Fingerprinting,* Magnetic Resonance in Medicine **78**, 1452 (2017).

[25] G. Buonincontri, L. Biagi, A. Retico, P. Cecchi, M. Cosottini, F. A. Gallagher, P. A. Gómez, M. J. Graves, M. A. McLean, F. Riemer, R. F. Schulte, M. Tosetti, F. Zaccagna, and J. D. Kaggie, *Multi-site repeatability and reproducibility of MR fingerprinting of the healthy brain at 1.5 and 3.0 T,* NeuroImage **195**, 362 (2019).

[26] S. M. Lee, Y. H. Choi, J.-E. Cheon, I.-O. Kim, S. H. Cho, W. H. Kim, H. J. Kim, H.-H. Cho, S.-K. You, S.-H. Park, and M. J. Hwang, *Image quality at synthetic brain magnetic resonance imaging in children,* Pediatric Radiology **47**, 1638 (2017).

[27] S. M. Lee, Y. H. Choi, S.-K. You, W. K. Lee, W. H. Kim, H. J. Kim, S. Y. Lee, and H. Cheon, *Age-Related Changes in Tissue Value Properties in Children: Simultaneous Quantification of Relaxation Times and Proton Density Using Synthetic Magnetic Resonance Imaging,* Investigative Radiology **53**, 236 (2018).

[28] W. Krauss, M. Gunnarsson, M. Nilsson, and P. Thunberg, *Conventional and synthetic MRI in multiple sclerosis: A comparative study,* European Radiology **28**, 1692 (2018).

[29] F. Di Giuliano, S. Minosse, E. Picchi, G. A. Marfia, V. Da Ros, M. Muto, M. Muto, C. A. Pistolese, A. Laghi, F. Garaci, and R. Floris, *Comparison between synthetic and conventional magnetic resonance imaging in patients with multiple sclerosis and controls,* Magnetic Resonance Materials in Physics, Biology and Medicine **33**, 549 (2020).

[30] I. Blystad, J. B. M. Warntjes, Ö. Smedby, P. Lundberg, E.-M. Larsson, and A. Tisell, *Quantitative MRI using relaxometry in malignant gliomas detects contrast enhancement in peritumoral oedema,* Scientific Reports **10** (2020), 10.1038/s41598-020-75105-6.

[31] I. Blystad, J. B. M. Warntjes, Ö. Smedby, P. Lundberg, E.-M. Larsson, and A. Tisell, *Quantitative MRI for analysis of peritumoral edema in malignant gliomas,* PLOS ONE **12**, e0177135 (2017).

[32] L. Tanenbaum, A. Tsiouris, A. Johnson, T. Naidich, M. DeLano, E. Melhem, P. Quarterman, S. Parameswaran, A. Shankaranarayanan, M. Goyen, and A. Field, *Synthetic MRI for Clinical Neuroimaging: Results of the Magnetic Resonance Image Compilation (MAGiC) Prospective, Multicenter, Multireader Trial,* American Journal of Neuroradiology **38**, 1103 (2017).

[33] C. Badve, A. Yu, S. Dastmalchian, M. Rogers, D. Ma, Y. Jiang, S. Margevicius, S. Pahwa, Z. Lu, M. Schluchter, J. Sunshine, M. Griswold, A. Sloan, and V. Gulani, *MR Fingerprinting of Adult Brain Tumors: Initial Experience,* American Journal of Neuroradiology **38**, 492 (2017).

[34] C. M. Pirkl, L. Nunez-Gonzalez, F. Kofler, S. Endt, L. Grundl, M. Golbabaee, P. A. Gómez, M. Cencini, G. Buonincontri, R. F. Schulte, M. Smits, B. Wiestler, B. H. Menze, M. I. Menzel, and J. A. Hernandez-Tamames, *Accelerated 3D whole-brain T1, T2, and proton density mapping: Feasibility for clinical glioma MR imaging,* Neuroradiology (2021), 10.1007/s00234-021-02703-0.

[35] W. Crum, O. Camara, and D. Hill, *Generalized Overlap Measures for Evaluation and Validation in Medical Image Analysis,* IEEE Transactions on Medical Imaging **25**, 1451 (2006).

[36] A. Giorgio and N. De Stefano, *Clinical use of brain volumetry,* Journal of Magnetic Resonance Imaging **37**, 1 (2013).

[37] D. E. Ross, *Review of longitudinal studies of MRI brain volumetry in patients with traumatic brain injury,* Brain Injury **25**, 1271 (2011).

[38] R. Heinen, W. H. Bouvy, A. M. Mendrik, M. A. Viergever, G. J. Biessels, and J. de Bresser, *Robustness of Automated Methods for Brain Volume Measurements across Different MRI Field Strengths,* PLOS ONE **11**, e0165719 (2016).

[39] J. de Bresser, M. P. Portegies, A. Leemans, G. J. Biessels, L. J. Kappelle, and M. A. Viergever, *A comparison of MR based segmentation methods for measuring brain atrophy progression,* NeuroImage **54**, 760 (2011).

[40] E. Alonso-Ortiz, I. R. Levesque, and G. B. Pike, *MRI-based myelin water imaging: A technical review: MRI-Based Myelin Water Imaging,* Magnetic Resonance in Medicine **73**, 70 (2015).

[41] A. V. Dvorak, T. Swift-LaPointe, I. M. Vavasour, L. E. Lee, S. Abel, B. Russell-Schulz, C. Graf, A. Wurl, H. Liu, C. Laule, D. K. B. Li, A. Traboulsee, R. Tam, L. A. Boyd, A. L. MacKay, and S. H. Kolind, *An atlas for human brain myelin content throughout the adult life span,* Scientific Reports **11**, 269 (2021).

[42] A. V. Dvorak, V. Wiggermann, G. Gilbert, I. M. Vavasour, E. L. MacMillan, L. Barlow, N. Wiley, P. Kozlowski, A. L. MacKay, A. Rauscher, and S. H. Kolind, *Multi-spin echo T_2 relaxation imaging with compressed sensing (METRICS) for rapid myelin water imaging,* Magnetic Resonance in Medicine **84**, 1264 (2020).

[43] A. Mackay, K. Whittall, J. Adler, D. Li, D. Paty, and D. Graeb, *In vivo visualization of myelin water in brain by magnetic resonance,* Magnetic Resonance in Medicine **31**, 673 (1994).

[44] A. Hagiwara, C. Andica, M. Hori, and S. Aoki, *Synthetic MRI showed increased myelin partial volume in the white matter of a patient with Sturge-Weber syndrome,* Neuroradiology **59**, 1065 (2017).

[45] C. Laule, P. Kozlowski, E. Leung, D. K. Li, A. L. MacKay, and G. W. Moore, *Myelin water imaging of multiple sclerosis at 7 T: Correlations with histopathology,* NeuroImage **40**, 1575 (2008).

[46] D. McGivney, A. Deshmane, Y. Jiang, D. Ma, C. Badve, A. Sloan, V. Gulani, and M. Griswold, *Bayesian estimation of multicomponent relaxation parameters in magnetic resonance fingerprinting: Bayesian MRF,* Magnetic Resonance in Medicine **80**, 159 (2018).

[47] S. Tang, C. Fernandez-Granda, S. Lannuzel, B. Bernstein, R. Lattanzi, M. Cloos, F. Knoll, and J. Assländer, *Multicompartment magnetic resonance fingerprinting,* Inverse Problems **34**, 094005 (2018).

[48] M. Nagtegaal, P. Koken, T. Amthor, and M. Doneva, *Fast multi-component analysis using a joint sparsity constraint for MR fingerprinting,* Magnetic Resonance in Medicine **83**, 521 (2020).

[49] Y. Jiang, D. Ma, N. Seiberlich, V. Gulani, and M. A. Griswold, *MR fingerprinting using fast imaging with steady state precession (FISP) with spiral readout: MR Fingerprinting with FISP,* Magnetic Resonance in Medicine **74**, 1621 (2015).

[50] C. Ganter, *Off-resonance effects in the transient response of SSFP sequences,* Magnetic Resonance in Medicine **52**, 368 (2004).

[51] B. A. Hargreaves, S. S. Vasanawala, J. M. Pauly, and D. G. Nishimura, *Characterization and reduction of the transient response in steady-state MR imaging,* Magnetic Resonance in Medicine **46**, 149 (2001).

[52] K. Scheffler, *On the transient phase of balanced SSFP sequences,* Magnetic Resonance in Medicine **49**, 781 (2003).

[53] T. E. Skinner, *Comprehensive solutions to the Bloch equations and dynamical models for open two-level systems,* Physical Review A **97**, 013815 (2018).

[54] N. Lukzen and A. Savelov, *Analytical derivation of multiple spin echo amplitudes with arbitrary refocusing angle,* Journal of Magnetic Resonance **185**, 71 (2007).

[55] M. Jenkinson, C. F. Beckmann, T. E. Behrens, M. W. Woolrich, and S. M. Smith, *FSL,* NeuroImage **62**, 782 (2012).

[56] *SPM12 - Statistical Parametric Mapping,* https://www.fil.ion.ucl.ac.uk/spm.

[57] H.-T. Juan A., K. Gyula, N. G. Laura, P. Dirk H.J., and V. Mika, *Balanced Phase Cycling non Stationary Free Precession Sequence; Banding Artifact Free Imaging For MR Multi-Parametric Estimation,* (2021).

[58] Y. Shcherbakova, C. A. van den Berg, C. T. Moonen, and L. W. Bartels, *PLANET: An ellipse fitting approach for simultaneous T_1 and T_2 mapping using phase-cycled balanced steady-state free precession: Ellipse Fitting Approach for T_1 and T_2 Mapping,* Magnetic Resonance in Medicine **79**, 711 (2018).

[59] D. Ma, V. Gulani, N. Seiberlich, K. Liu, J. L. Sunshine, J. L. Duerk, and M. A. Griswold, *Magnetic resonance fingerprinting – overview,* Nature **495**, 187 (2013).

[60] H. West, *Clinical validation of synthetic brain MRI in children: Initial experience,* , 8 (2017).

[61] C. Andica, A. Hagiwara, M. Nakazawa, K. Tsuruta, N. Takano, M. Hori, H. Suzuki, H. Sugano, H. Arai, and S. Aoki, *The Advantage of Synthetic MRI for the Visualization of Early White Matter Change in an Infant with Sturge-Weber Syndrome,* Magnetic Resonance in Medical Sciences **15**, 347 (2016).

[62] O. Bane, S. J. Hectors, M. Wagner, L. L. Arlinghaus, M. P. Aryal, Y. Cao, T. L. Chenevert, F. Fennessy, W. Huang, N. M. Hylton, J. Kalpathy-Cramer, K. E. Keenan, D. I. Malyarenko, R. V. Mulkern, D. C. Newitt, S. E. Russek, K. F. Stupic, A. Tudorica, L. J. Wilmes, T. E. Yankeelov, Y.-F. Yen, M. A. Boss, and B. Taouli, *Accuracy, repeatability, and interplatform reproducibility of T_1 quantification methods used*

for DCE-MRI: Results from a multicenter phantom study, Magnetic Resonance in Medicine **79**, 2564 (2018).

[63] J. M. Bland and D. G. Altman, *Measuring agreement in method comparison studies,* Statistical Methods in Medical Research **8**, 135 (1999).

[64] C. F. Beckmann, M. Jenkinson, and S. M. Smith, *General multilevel linear modeling for group analysis in FMRI,* NeuroImage **20**, 1052 (2003).

[65] M. Weigel, S. Schwenk, V. Kiselev, K. Scheffler, and J. Hennig, *Extended phase graphs with anisotropic diffusion,* Journal of Magnetic Resonance **205**, 276 (2010).

[66] K. Keenan, Kathryn E., K. Stupic, Karl F., M. A. Boss, S. E. Russek, T. L. Chenevert, P. V. Prasad, W. E. Reddick, J. Zheng, P. Hu, and E. F. Jackson, *Comparison of T1 measurement using ISMRM/NIST system phantom,* in *ISMRM* (Singapore, 2016).

[67] F. Faul, E. Erdfelder, A.-G. Lang, and A. Buchner, *G*Power 3: A flexible statistical power analysis program for the social, behavioral, and biomedical sciences,* Behavior Research Methods **39**, 175 (2007).

[68] K. McMillan, M. Uike, X. Tao, H. Okuda, and G. Healthcare, *MR Efficiency Becomes Critical as Healthcare Costs, Scanner Time Demand Increases,* , 4.

[69] J. Fessler and B. Sutton, *Nonuniform fast fourier transforms using min-max interpolation,* IEEE Transactions on Signal Processing **51**, 560 (2003).

[70] J. I. Tamir, M. Uecker, W. Chen, P. Lai, M. T. Alley, S. S. Vasanawala, and M. Lustig, T $_2$ *shuffling: Sharp, multicontrast, volumetric fast spin-echo imaging: T* $_2$ *Shuffling,* Magnetic Resonance in Medicine **77**, 180 (2017).

[71] G. Buonincontri and S. J. Sawiak, *MR fingerprinting with simultaneous B1 estimation: MRF with B1 Estimation,* Magnetic Resonance in Medicine **76**, 1127 (2016).

[72] P. Mildenberger, M. Eichelberg, and E. Martin, *Introduction to the DICOM standard,* European Radiology **12**, 920 (2002).

[73] A. Collignon, F. Maes, D. Delaere, D. Vandermeulen, P. Suetens, and G. Marchal, *AUTOMATED MULTI-MODALITY IMAGE REGISTRATION BASED ON INFORMATION THEORY,* , 12.

[74] J. Ashburner and K. J. Friston, *Unified segmentation,* NeuroImage **26**, 839 (2005).

[75] A. Evans, D. Collins, S. Mills, E. Brown, R. Kelly, and T. Peters, *3D statistical neuroanatomical models from 305 MRI volumes,* in *1993 IEEE Conference Record Nuclear Science Symposium and Medical Imaging Conference* (IEEE, San Francisco, CA, USA, 1993) pp. 1813–1817.

[76] J. Ashburner, *A fast diffeomorphic image registration algorithm,* NeuroImage **38**, 95 (2007).

[77] W. K. Thompson and D. Holland, *Bias in tensor based morphometry Stat-ROI measures may result in unrealistic power estimates,* NeuroImage **57**, 1 (2011).

[78] M. Reuter, N. J. Schmansky, H. D. Rosas, and B. Fischl, *Within-subject template estimation for unbiased longitudinal image analysis,* NeuroImage **61**, 1402 (2012).

[79] P. A. Yushkevich, B. B. Avants, S. R. Das, J. Pluta, M. Altinay, and C. Craige, *Bias in estimation of hippocampal atrophy using deformation-based morphometry arises from asymmetric global normalization: An illustration in ADNI 3 T MRI data,* NeuroImage **50**, 434 (2010).

[80] G. H. Golub and C. F. van Loan, *An Analysis of the Total Least Squares Problem,* SIAM Journal on Numerical Analysis **17**, 883 (1980).

[81] M. G. Vangel, *Confidence Intervals for a Normal Coefficient of Variation,* , 7 (1996).

[82] J. P. Wansapura, S. K. Holland, R. S. Dunn, and W. S. Ball, *NMR relaxation times in the human brain at 3.0 tesla,* Journal of Magnetic Resonance Imaging **9**, 531 (1999).

[83] G. Körzdörfer, R. Kirsch, K. Liu, J. Pfeuffer, B. Hensel, Y. Jiang, D. Ma, M. Gratz, P. Bär, W. Bogner, E. Springer, P. Lima Cardoso, L. Umutlu, S. Trattnig, M. Griswold, V. Gulani, and M. Nittka, *Reproducibility and Repeatability of MR Fingerprinting Relaxometry in the Human Brain,* Radiology **292**, 429 (2019).

[84] N. Stikov, M. Boudreau, I. R. Levesque, C. L. Tardif, J. K. Barral, and G. B. Pike, *On the accuracy of T_1 mapping: Searching for common ground: Accuracy of T_1 Mapping,* Magnetic Resonance in Medicine **73**, 514 (2015).

[85] J. Assländer, S. J. Glaser, and J. Hennig, *Pseudo Steady-State Free Precession for MR-Fingerprinting: pSSFP for MR-Fingerprinting,* Magnetic Resonance in Medicine **77**, 1151 (2017).

[86] R. M. Henkelman, G. J. Stanisz, and S. J. Graham, *Magnetization transfer in MRI: A review,* NMR in Biomedicine **14**, 57 (2001).

[87] J. G. Sled and G. Pike, *Quantitative Interpretation of Magnetization Transfer in Spoiled Gradient Echo MRI Sequences,* Journal of Magnetic Resonance **145**, 24 (2000).

[88] J. T. Vaughan, H. P. Hetherington, J. O. Otu, J. W. Pan, and G. M. Pohost, *High frequency volume coils for clinical NMR imaging and spectroscopy,* Magnetic Resonance in Medicine **32**, 206 (1994).

[89] T. L. Chenevert, D. I. Malyarenko, D. Newitt, X. Li, M. Jayatilake, A. Tudorica, A. Fedorov, R. Kikinis, T. T. Liu, M. Muzi, M. J. Oborski, C. M. Laymon, X. Li, Y. Thomas, K.-C. Jayashree, J. M. Mountz, P. E. Kinahan, D. L. Rubin, F. Fennessy, W. Huang, N. Hylton, and B. D. Ross, *Errors in Quantitative Image Analysis due to Platform-Dependent Image Scaling,* Translational Oncology **7**, 65 (2014).

[90] K. I. Olsen, P. Schroeder, R. Corby, I. Vucic, and D. M. Bardo, *Advanced magnetic resonance imaging techniques to evaluate CNS glioma,* Expert Review of Neurotherapeutics **5**, 3 (2005).

[91] H.-W. Kao, S.-W. Chiang, H.-W. Chung, F. Y. Tsai, and C.-Y. Chen, *Advanced MR Imaging of Gliomas: An Update,* BioMed Research International **2013**, 1 (2013).

[92] S. J. Fouke, T. Benzinger, D. Gibson, T. C. Ryken, S. N. Kalkanis, and J. J. Olson, *The role of imaging in the management of adults with diffuse low grade glioma: A systematic review and evidence-based clinical practice guideline,* Journal of Neuro-Oncology **125**, 457 (2015).

[93] B. M. Ellingson, M. Bendszus, J. Boxerman, D. Barboriak, B. J. Erickson, M. Smits, S. J. Nelson, E. Gerstner, B. Alexander, G. Goldmacher, W. Wick, M. Vogelbaum, M. Weller, E. Galanis, J. Kalpathy-Cramer, L. Shankar, P. Jacobs, W. B. Pope, D. Yang, C. Chung, M. V. Knopp, S. Cha, M. J. van den Bent, S. Chang, W. K. Al Yung, T. F. Cloughesy, P. Y. Wen, M. R. Gilbert, and J. B. T. D. D. C. I. S. S. Committee, *Consensus recommendations for a standardized Brain Tumor Imaging Protocol in clinical trials,* Neuro-Oncology (2015), 10.1093/neuonc/nov095.

[94] M. Weller, M. van den Bent, M. Preusser, E. Le Rhun, J. C. Tonn, G. Minniti, M. Bendszus, C. Balana, O. Chinot, L. Dirven, P. French, M. E. Hegi, A. S. Jakola, M. Platten, P. Roth, R. Rudà, S. Short, M. Smits, M. J. B. Taphoorn, A. von Deimling, M. Westphal, R. Soffietti, G. Reifenberger, and W. Wick, *EANO guidelines on the diagnosis and treatment of diffuse gliomas of adulthood,* Nature Reviews Clinical Oncology **18**, 170 (2021).

[95] P. A. Gómez, M. Cencini, M. Golbabaee, R. F. Schulte, C. Pirkl, I. Horvath, G. Fallo, L. Peretti, M. Tosetti, B. H. Menze, and G. Buonincontri, *Rapid three-dimensional multiparametric MRI with quantitative transient-state imaging,* arXiv:2001.07173 [physics] (2020), comment: 43 pages, 12 Figures, 5 Tables, arXiv:2001.07173 [physics] .

[96] S. Newman, V. Haughton, Z. Yetkin, R. Breger, L. Czervionke, A. Williams, K. Ho, R. Papke, A. Rimm, M. Fischer, G. Meyer, and R. Asleson, *T1, T2 and proton density measurements in the grading of cerebral gliomas,* European Radiology **3** (1993), 10.1007/BF00173524.

[97] E. Hattingen, A. Müller, A. Jurcoane, B. Mädler, P. Ditter, H. Schild, U. Herrlinger, M. Glas, and S. Kebir, *Value of quantitative magnetic resonance imaging T1-relaxometry in predicting contrast-enhancement in glioblastoma patients,* Oncotarget **8**, 53542 (2017).

[98] J. Kleesiek, J. N. Morshuis, F. Isensee, K. Deike-Hofmann, D. Paech, P. Kickingereder, U. Köthe, C. Rother, M. Forsting, W. Wick, M. Bendszus, H.-P. Schlemmer, and A. Radbruch, *Can Virtual Contrast Enhancement in Brain MRI Replace Gadolinium?: A Feasibility Study,* Investigative Radiology **54**, 653 (2019).

[99] C. Laule, T. A. Bjarnason, I. M. Vavasour, A. L. Traboulsee, G. R. Wayne Moore, D. K. B. Li, and A. L. MacKay, *Characterization of brain tumours with spin–spin relaxation: Pilot case study reveals unique T 2 distribution profiles of glioblastoma, oligodendroglioma and meningioma,* Journal of Neurology **264**, 2205 (2017).

[100] P. S. Tofts, *Methods for quantitative relaxation parameter mapping: Measuring T1 and T2,* , 7.

[101] M. Vargas, B. Delattre, P. Vayssiere, M. Corniola, and T. Meling, *Intraoperative MR and Synthetic Imaging,* American Journal of Neuroradiology **41**, E4 (2020).

[102] K. H. Ryu, H. J. Baek, J. I. Moon, B. H. Choi, S. E. Park, J. Y. Ha, K. N. Jeon, K. Bae, D. S. Choi, S. B. Cho, Y. Lee, and Y. J. Heo, *Initial clinical experience of synthetic MRI as a routine neuroimaging protocol in daily practice: A single-center study,* Journal of Neuroradiology **47**, 151 (2020).

[103] T. Vanderhasselt, M. Naeyaert, N. Watté, G.-J. Allemeersch, S. Raeymaeckers, J. Dudink, J. de Mey, and H. Raeymaekers, *Synthetic MRI of Preterm Infants at Term-Equivalent Age: Evaluation of Diagnostic Image Quality and Automated Brain Volume Segmentation,* American Journal of Neuroradiology **41**, 882 (2020).

[104] K. M. Kang, S. H. Choi, M. Hwang, R.-E. Yoo, T. J. Yun, J.-h. Kim, and C.-H. Sohn, *Application of Synthetic MRI for Direct Measurement of Magnetic Resonance Relaxation Time and Tumor Volume at Multiple Time Points after Contrast Administration: Preliminary Results in Patients with Brain Metastasis,* Korean Journal of Radiology **19**, 783 (2018).

[105] I. Blystad, I. Håkansson, A. Tisell, J. Ernerudh, Ö. Smedby, P. Lundberg, and E.-M. Larsson, *Quantitative MRI for Analysis of Active Multiple Sclerosis Lesions without Gadolinium-Based Contrast Agent,* American Journal of Neuroradiology **37**, 94 (2016).

[106] P. Wesseling and D. Capper, *WHO 2016 Classification of gliomas,* Neuropathology and Applied Neurobiology **44**, 139 (2018).

[107] P. Kickingereder, F. Isensee, I. Tursunova, J. Petersen, U. Neuberger, D. Bonekamp, G. Brugnara, M. Schell, T. Kessler, M. Foltyn, I. Harting, F. Sahm, M. Prager, M. Nowosielski, A. Wick, M. Nolden, A. Radbruch, J. Debus, H.-P. Schlemmer, S. Heiland, M. Platten, A. von Deimling, M. J. van den Bent, T. Gorlia, W. Wick, M. Bendszus, and K. H. Maier-Hein, *Automated quantitative tumour response assessment of MRI in neuro-oncology with artificial neural networks: A multicentre, retrospective study,* The Lancet Oncology **20**, 728 (2019).

[108] F. Isensee, P. F. Jäger, S. A. A. Kohl, J. Petersen, and K. H. Maier-Hein, *Automated Design of Deep Learning Methods for Biomedical Image Segmentation,* arXiv:1904.08128 [cs] (2020), comment: * Fabian Isensee and Paul F. J\"ager share the first authorship, arXiv:1904.08128 [cs] .

[109] M. Jenkinson and S. Smith, *A global optimisation method for robust affine registration of brain images,* Medical Image Analysis **5**, 143 (2001).

[110] M. Jenkinson, P. Bannister, M. Brady, and S. Smith, *Improved Optimization for the Robust and Accurate Linear Registration and Motion Correction of Brain Images,* NeuroImage **17**, 825 (2002).

[111] D. L. Streiner and J. Cairney, *What's under the ROC? an Introduction to Receiver Operating Characteristics Curves,* The Canadian Journal of Psychiatry **52**, 121 (2007).

[112] W. J. Youden, *Index for rating diagnostic tests,* , 5.

[113] A. Airola, T. Pahikkala, W. Waegeman, B. De Baets, and T. Salakoski, *An experimental comparison of cross-validation techniques for estimating the area under the ROC curve,* Computational Statistics & Data Analysis **55**, 1828 (2011).

[114] Z.-g. Min, C. Niu, N. Rana, H.-m. Ji, and M. Zhang, *Differentiation of pure vasogenic edema and tumor-infiltrated edema in patients with peritumoral edema by analyzing the relationship of axial and radial diffusivities on 3.0T MRI,* Clinical Neurology and Neurosurgery **115**, 1366 (2013).

[115] S. Safari, A. Baratloo, M. Elfil, and A. Negida, *Evidence Based Emergency Medicine; Part 5 Receiver Operating Curve and Area under the Curve,* Emergency (Tehran, Iran) **4**, 111 (2016).

[116] L. Nunez-Gonzalez, G. Kotek, P. A. Gómez, G. Buonincontri, M. Vogel, G. P. Krestin, D. H. Poot, and J. A. Hernandez-Tamames, *Accuracy and repeatability of QRAPMASTER and MRF-vFA,* Magnetic Resonance Imaging **83**, 196 (2021).

[117] Y. Chen, Y. Jiang, S. Pahwa, D. Ma, L. Lu, M. D. Twieg, K. L. Wright, N. Seiberlich, M. A. Griswold, and V. Gulani, *MR Fingerprinting for Rapid Quantitative Abdominal Imaging,* Radiology **279**, 278 (2016).

[118] B. Aubert-Broche, A. C. Evans, and L. Collins, *A new improved version of the realistic digital brain phantom,* NeuroImage **32**, 138 (2006).

[119] J. Hennig, *Multiecho imaging sequences with low refocusing flip angles,* Journal of Magnetic Resonance (1969) **78**, 397 (1988).

[120] B. B. Mehta, D. Ma, E. Y. Pierre, Y. Jiang, S. Coppo, and M. A. Griswold, *Image reconstruction algorithm for motion insensitive MR Fingerprinting (MRF): MORF: Mehta et al.* Magnetic Resonance in Medicine **80**, 2485 (2018).

[121] Z. Yu, T. Zhao, J. Assländer, R. Lattanzi, D. K. Sodickson, and M. A. Cloos, *Exploring the sensitivity of magnetic resonance fingerprinting to motion,* Magnetic Resonance Imaging **54**, 241 (2018).

[122] G. Cruz, O. Jaubert, T. Schneider, R. M. Botnar, and C. Prieto, *Rigid motion-corrected magnetic resonance fingerprinting,* Magnetic Resonance in Medicine **81**, 947 (2019).

[123] J. W. Kurzawski, M. Cencini, L. Peretti, P. A. Gómez, R. F. Schulte, G. Donatelli, M. Cosottini, P. Cecchi, M. Costagli, A. Retico, M. Tosetti, and G. Buonincontri, *Retrospective rigid motion correction of three-dimensional magnetic resonance fingerprinting of the human brain,* Magnetic Resonance in Medicine **n/a**, 10.1002/mrm.28301.

[124] Y. Zhang, M. Brady, and S. Smith, *Segmentation of brain MR images through a hidden Markov random field model and the expectation-maximization algorithm,* IEEE Transactions on Medical Imaging **20**, 45 (Jan./2001).

[125] V. Fonov, A. Evans, R. McKinstry, C. Almli, and D. Collins, *Unbiased nonlinear average age-appropriate brain templates from birth to adulthood,* NeuroImage **47**, S102 (2009).

[126] V. Fonov, A. C. Evans, K. Botteron, C. R. Almli, R. C. McKinstry, and D. L. Collins, *Unbiased average age-appropriate atlases for pediatric studies,* NeuroImage **54**, 313 (2011).

[127] G. J. Stanisz, E. E. Odrobina, J. Pun, M. Escaravage, S. J. Graham, M. J. Bronskill, and R. M. Henkelman, *T1, T2 relaxation and magnetization transfer in tissue at 3T,* Magnetic Resonance in Medicine **54**, 507 (2005).

[128] M. Bouhrara and R. G. Spencer, *Rapid simultaneous high-resolution mapping of myelin water fraction and relaxation times in human brain using BMC-mcDESPOT,* NeuroImage **147**, 800 (2017).

[129] K. P. Whittall, A. L. Mackay, D. A. Graeb, R. A. Nugent, D. K. B. Li, and D. W. Paty, *In vivo measurement ofT2 distributions and water contents in normal human brain,* Magnetic Resonance in Medicine **37**, 34 (1997).

[130] D. L. Tudorascu, H. T. Karim, J. M. Maronge, L. Alhilali, S. Fakhran, H. J. Aizenstein, J. Muschelli, and C. M. Crainiceanu, *Reproducibility and Bias in Healthy Brain Segmentation: Comparison of Two Popular Neuroimaging Platforms,* Frontiers in Neuroscience **10** (2016), 10.3389/fnins.2016.00503.

[131] F. Klauschen, A. Goldman, V. Barra, A. Meyer-Lindenberg, and A. Lundervold, *Evaluation of automated brain MR image segmentation and volumetry methods,* Human Brain Mapping **30**, 1310 (2009).

[132] K. O. Johnson, R. K. Robison, and J. G. Pipe, *Rigid Body Motion Compensation for Spiral Projection Imaging,* IEEE Transactions on Medical Imaging **30**, 655 (2011).

[133] D. Heesterbeek, F. Vos, M. van Gijzen, and M. Nagtegaal, *Sequence Optimisation for Multi-Component Analysis in Magnetic Resonance Fingerprinting,* in *ISMRM*, Vol. 29 (Online, 2021) p. 1561.

[134] J. Fan and R. Li, *Variable Selection via Nonconcave Penalized Likelihood and its Oracle Properties,* Journal of the American Statistical Association **96**, 1348 (2001).

[135] M. E. Poorman, M. N. Martin, D. Ma, D. F. McGivney, V. Gulani, M. A. Griswold, and K. E. Keenan, *Magnetic resonance fingerprinting Part 1: Potential uses, current challenges, and recommendations,* Journal of Magnetic Resonance Imaging , jmri.26836 (2019).

[136] H. C. Torrey, *Transient Nutations in Nuclear Magnetic Resonance,* Physical Review **76**, 1059 (1949).

[137] H.-R. Noh, *Analytical solutions and expressions of the propagator for Bloch equations,* International Journal of Modern Physics B **34**, 2050158 (2020).

[138] H. Y. Carr, *Steady-State Free Precession in Nuclear Magnetic Resonance,* NUCLEAR MAGNETIC RESONANCE , 16.

[139] P. M. Glover and R. J. Hil, *Apparatus for and method of determining values of relaxation parameters,* (2001).

[140] J. Assländer, D. S. Novikov, R. Lattanzi, D. K. Sodickson, and M. A. Cloos, *Hybrid-State Free Precession in Nuclear Magnetic Resonance,* arXiv:1807.03424 [physics] (2018), arXiv:1807.03424 [physics] .

[141] M. Lustig, D. Donoho, J. Santos, and J. Pauly, *Compressed Sensing MRI,* IEEE Signal Processing Magazine **25**, 72 (2008).

[142] G. Körzdörfer, Y. Jiang, P. Speier, J. Pang, D. Ma, J. Pfeuffer, B. Hensel, V. Gulani, M. Griswold, and M. Nittka, *Magnetic resonance field fingerprinting,* Magnetic Resonance in Medicine **81**, 2347 (2019).

[143] A. Sbrizzi, O. van der Heide, M. Cloos, A. van der Toorn, H. Hoogduin, P. R. Luijten, and C. A. van den Berg, *Fast quantitative MRI as a nonlinear tomography problem,* Magnetic Resonance Imaging **46**, 56 (2018).

[144] D. L. Abrahamson, *Pursuing Analogies between Differential Equations and Difference Equations,* The American Mathematical Monthly **96**, 827 (1989).

[145] S. Elaydi, *An Introduction to Difference Equations*, 3rd ed., Undergraduate Texts in Mathematics (Springer, New York, 2005).

[146] E. J. Putzer, *Avoiding the Jordan Canonical Form in the Discussion of Linear Systems with Constant Coefficients,* The American Mathematical Monthly **73**, 2 (1966).

[147] H. Goldstein, C. Poole, J. Safko, and S. R. Addison, Classical Mechanics, 3rd ed. American Journal of Physics **70**, 782 (2002).

[148] L. I. Sacolick, F. Wiesinger, I. Hancu, and M. W. Vogel, *B1 mapping by Bloch-Siegert shift,* Magnetic Resonance in Medicine **63**, 1315 (2010).

[149] M. G. Prammer, J. C. Haselgrove, M. Shinnar, and J. S. Leigh, *A new approach to automatic shimming,* Journal of Magnetic Resonance (1969) **77**, 40 (1988).

[150] E. Schneider and G. Glover, *Rapidin vivo proton shimming,* Magnetic Resonance in Medicine **18**, 335 (1991).

[151] D. H. J. Poot and S. Klein, *Detecting Statistically Significant Differences in Quantitative MRI Experiments, Applied to Diffusion Tensor Imaging,* IEEE Transactions on Medical Imaging **34**, 1164 (2015).

[152] Y. Shcherbakova, C. A. T. van den Berg, C. T. W. Moonen, and L. W. Bartels, *On the accuracy and precision of PLANET for multiparametric MRI using phase-cycled bSSFP imaging,* Magnetic Resonance in Medicine **81**, 1534 (2019).

[153] M. Björk, R. R. Ingle, E. Gudmundson, P. Stoica, D. G. Nishimura, and J. K. Barral, *Parameter estimation approach to banding artifact reduction in balanced steady-state free precession: Banding Artifact Reduction in bSSFP,* Magnetic Resonance in Medicine **72**, 880 (2014).

[154] M. A. Dieringer, M. Deimling, D. Santoro, J. Wuerfel, V. I. Madai, J. Sobesky, F. von Knobelsdorff-Brenkenhoff, J. Schulz-Menger, and T. Niendorf, *Rapid Parametric Mapping of the Longitudinal Relaxation Time T1 Using Two-Dimensional Variable Flip Angle Magnetic Resonance Imaging at 1.5 Tesla, 3 Tesla, and 7 Tesla,* PLoS ONE **9**, e91318 (2014).

[155] P. Ehses, N. Seiberlich, D. Ma, F. A. Breuer, P. M. Jakob, M. A. Griswold, and V. Gulani, *IR TrueFISP with a golden-ratio-based radial readout: Fast quantification of* T_1, T_2, *and proton density,* Magnetic Resonance in Medicine **69**, 71 (2013).

[156] D. W. McRobbie, R. A. Lerski, and K. Straughan, *Slice profile effects and their calibration and correction in quantitative NMR imaging,* Physics in Medicine and Biology **32**, 971 (1987).

[157] F. Santini, N. Kawel-Boehm, A. Greiser, J. Bremerich, and O. Bieri, *Simultaneous* T_1 *and* T_2 *quantification of the myocardium using cardiac balanced-SSFP inversion recovery with interleaved sampling acquisition (CABIRIA): Cardiac Relaxometry with CABIRIA,* Magnetic Resonance in Medicine **74**, 365 (2015).

[158] K. L. Miller, S. M. Smith, and P. Jezzard, *Asymmetries of the balanced SSFP profile. Part II: White matter: Asymmetries of the Balanced SSFP Profile. Part II: White Matter,* Magnetic Resonance in Medicine **63**, 396 (2010).

[159] K. L. Miller and P. Jezzard, *Modeling SSFP functional MRI contrast in the brain,* Magnetic Resonance in Medicine **60**, 661 (2008).

[160] K. L. Miller and P. Jezzard, *Balanced SSFP profile asymmetries detect small frequency shifts in white matter.* in *Water Exchange & Binding - ORAL*, Vol. 258 (Hawaii, 2009).

[161] K. L. Miller, *Asymmetries of the balanced SSFP profile. Part I: Theory and observation: Balanced SSFP Asymmetry: Theory,* Magnetic Resonance in Medicine **63**, 385 (2010).

[162] R. Dharmakumar, J. Hong, J. H. Brittain, D. B. Plewes, and G. A. Wright, *Oxygen-sensitive contrast in blood for steady-state free precession imaging,* Magnetic Resonance in Medicine **53**, 574 (2005).

[163] O. Bieri and K. Scheffler, *Effect of diffusion in inhomogeneous magnetic fields on balanced steady-state free precession,* NMR in Biomedicine **20**, 1 (2007).

[164] O. Bieri and K. Scheffler, *On the origin of apparent low tissue signals in balanced SSFP,* Magnetic Resonance in Medicine **56**, 1067 (2006).

[165] D. L. Raunig, L. M. McShane, G. Pennello, C. Gatsonis, P. L. Carson, J. T. Voyvodic, R. L. Wahl, B. F. Kurland, A. J. Schwarz, M. Gönen, G. Zahlmann, M. V. Kondratovich, K. O'Donnell, N. Petrick, P. E. Cole, B. Garra, D. C. Sullivan, and QIBA Technical Performance Working Group, *Quantitative imaging biomarkers: A review of statistical methods for technical performance assessment,* Statistical Methods in Medical Research **24**, 27 (2015).

[166] G. Buonincontri, L. Biagi, A. Retico, M. Tosetti, P. Cecchi, M. Cosottini, P. A. Gomez, R. F. Schulte, M. McLean, F. Riemer, F. Gallagher, M. J. Graves, and J. D. Kaggie, *Repeatability of 2D FISP MR Fingerprinting in the Brain at 1.5T and 3.0 T,* in *ISMRM* (2018).

[167] C. M. Pirkl, L. Nunez-Gonzalez, S. Endt, G. Buonincontri, R. F. Schulte, P. A. Gomez, M. Smits, B. H. Menze, M. I. Menzel, and J. A. Hernández-Tamames, *Accelerated 3D multiparametric MRI in glioma patients - Initial clinical experience,* in *Neuroimaging Techniques: Acquisition & Processing II* (Virtual Meeting, 2020).

[168] H. S. Thomsen, S. K. Morcos, T. Almén, M.-F. Bellin, M. Bertolotto, G. Bongartz, O. Clement, P. Leander, G. Heinz-Peer, P. Reimer, F. Stacul, A. van der Molen, and J. A. Webb, *Nephrogenic systemic fibrosis and gadolinium-based contrast media: Updated ESUR Contrast Medium Safety Committee guidelines,* European Radiology **23**, 307 (2013).

[169] M. R. Prince, H. Zhang, Z. Zou, R. B. Staron, and P. W. Brill, *Incidence of Immediate Gadolinium Contrast Media Reactions,* American Journal of Roentgenology **196**, W138 (2011).

[170] R. J. McDonald, J. S. McDonald, D. F. Kallmes, M. E. Jentoft, D. L. Murray, K. R. Thielen, E. E. Williamson, and L. J. Eckel, *Intracranial Gadolinium Deposition after Contrast-enhanced MR Imaging,* Radiology **275**, 772 (2015).

[171] T. Kanda, K. Ishii, H. Kawaguchi, K. Kitajima, and D. Takenaka, *High Signal Intensity in the Dentate Nucleus and Globus Pallidus on Unenhanced T1-weighted MR Images: Relationship with Increasing Cumulative Dose of a Gadolinium-based Contrast Material,* Radiology **270**, 834 (2014).

[172] Y. Errante, V. Cirimele, C. A. Mallio, V. Di Lazzaro, B. B. Zobel, and C. C. Quattrocchi, *Progressive Increase of T1 Signal Intensity of the Dentate Nucleus on Unenhanced Magnetic Resonance Images Is Associated With Cumulative Doses*

of Intravenously Administered Gadodiamide in Patients With Normal Renal Function, Suggesting Dechelation:, Investigative Radiology **49**, 685 (2014).

[173] N. Sushentsev, J. D. Kaggie, G. Buonincontri, R. F. Schulte, M. J. Graves, V. J. Gnanapragasam, and T. Barrett, *The effect of gadolinium-based contrast agent administration on magnetic resonance fingerprinting-based T1 relaxometry in patients with prostate cancer,* Scientific Reports **10**, 20475 (2020).

[174] M. Gonzalezballester, *Estimation of the partial volume effect in MRI,* Medical Image Analysis **6**, 389 (2002).

[175] J. Tohka, *Partial volume effect modeling for segmentation and tissue classification of brain magnetic resonance images: A review,* World Journal of Radiology **6**, 855 (2014).

[176] L. Clarke, R. Velthuizen, M. Camacho, J. Heine, M. Vaidyanathan, L. Hall, R. Thatcher, and M. Silbiger, *MRI segmentation: Methods and applications,* Magnetic Resonance Imaging **13**, 343 (1995).

[177] M. F. Glasser and D. C. Van Essen, *Mapping Human Cortical Areas In Vivo Based on Myelin Content as Revealed by T1- and T2-Weighted MRI,* Journal of Neuroscience **31**, 11597 (2011).

[178] K. Kazemi and N. Noorizadeh, *Quantitative Comparison of SPM, FSL, and Brainsuite for Brain MR Image Segmentation,* J Biomed Phys eng (2014).

[179] J. C. Haselgrove and J. R. Moore, *Correction for distortion of echo-planar images used to calculate the apparent diffusion coefficient,* Magnetic Resonance in Medicine **36**, 960 (1996).

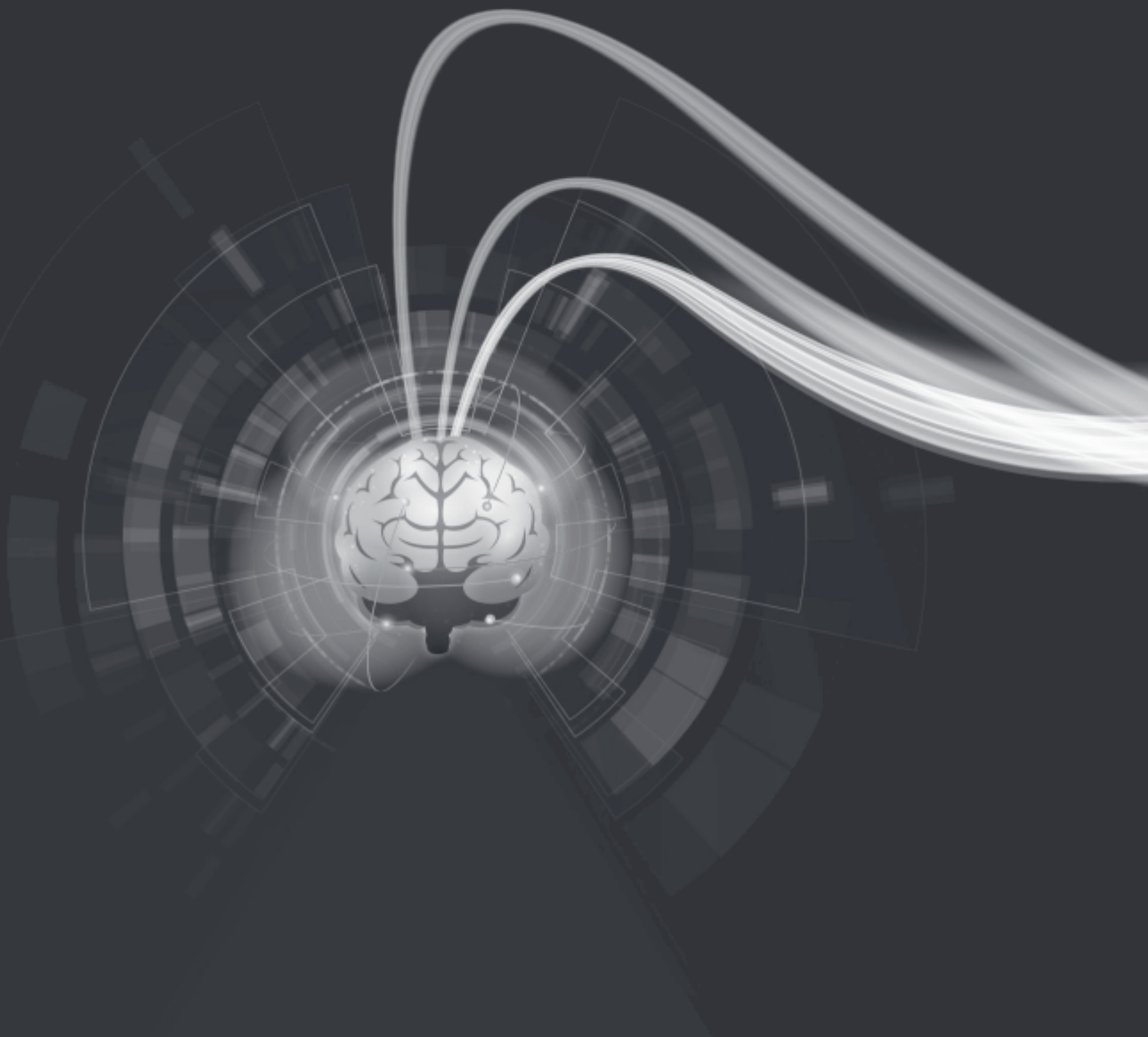

A

Appendix

A

A.1. PATENT:

BALANCED PHASE CYCLING NON STATIONARY FREE PRECESSION SEQUENCE; BANDING ARTIFACT FREE IMAGING FOR MR MULTI-PARAMETRIC ESTIMATION

A

(19) Europäisches Patentamt
European Patent Office
Office européen des brevets

(11) **EP 3 904 898 A1**

(12) **EUROPEAN PATENT APPLICATION**

(43) Date of publication:
03.11.2021 Bulletin 2021/44

(51) Int Cl.:
G01R 33/44 *(2006.01)* ***G01R 33/50*** *(2006.01)*

(21) Application number: **20172381.4**

(22) Date of filing: **30.04.2020**

(84) Designated Contracting States:
AL AT BE BG CH CY CZ DE DK EE ES FI FR GB GR HR HU IE IS IT LI LT LU LV MC MK MT NL NO PL PT RO RS SE SI SK SM TR
Designated Extension States:
BA ME
Designated Validation States:
KH MA MD TN

(71) Applicant: **Erasmus University Rotterdam Medical Center**
3015 GE Rotterdam (NL)

(72) Inventors:
- **HERNÁNDEZ TAMAMES, Juan Antonio**
  3015 GE Rotterdam (NL)
- **KOTEK, Gyula**
  3015 GE Rotterdam (NL)
- **NUÑEZ GONZÁLEZ, Laura**
  3015 GE Rotterdam (NL)
- **VOGEL, Mika**
  3015 GE Rotterdam (NL)
- **POOT, Dirk**
  3015 GE Rotterdam (NL)

(74) Representative: **V.O.**
P.O. Box 87930
2508 DH Den Haag (NL)

(54) **BALANCED PHASE CYCLING NON STATIONARY FREE PRECESSION SEQUENCE; BANDING ARTIFACT FREE IMAGING FOR MR MULTI-PARAMETRIC ESTIMATION**

(57) An MR excitation sequence comprises a repeated block (A) of excitation pulses. Each block (A) comprises a set of interleaved RF pulses with alternating small and large flip angle (α,γ) applied along different axes (x,y) to form a balanced sequence such as $\alpha_x,\gamma_y,\alpha_y,\gamma_x$. The sequence is simultaneously sensitive to various parameters such as PD, T1, T2, B1 and B0 keeping a high coherence and avoiding the formation of banding artifacts.

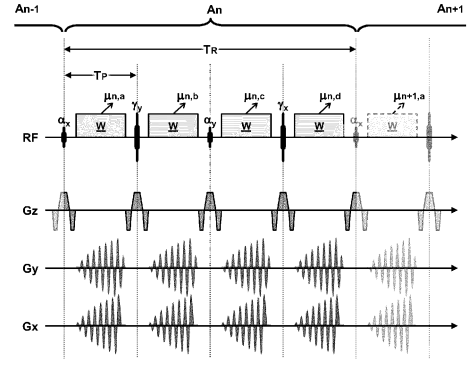

FIG 10

EP 3 904 898 A1

EP 3 904 898 A1

Description

TECHNICAL FIELD AND BACKGROUND

[0001] The present disclosure relates to an advantageous new sequence of pulses for acquiring MR data.

[0002] Magnetic resonance imaging (MRI) is used extensively in medicine and biology. It provides meaningful images of different organs and pathologies based on the magnetic properties of select nuclei present in tissues. However, MRI in current practice evolved mainly as a qualitative tool, based on "weighted" contrasts instead of exploiting absolute quantitative information. There are good reasons for this: accuracy and precision in absolute quantification require long scan times and, moreover, are challenging because of the high sensitivity to MR system imperfections such as magnetic field (known as B_0) inhomogeneity and/or radiofrequency pulse (known as B_1^+) inaccuracies. These factors make quantitative reproducibility across different experimental conditions and MR systems difficult.

[0003] In order to overcome these difficulties, Magnetic Resonance Fingerprinting (MRF) has recently emerged as a new paradigm for quantitative MR imaging [Ma D, Gulani V, Seiberlich N, Liu K, Sunshine JL, Duerk JL, et al. Magnetic resonance fingerprinting. Nature. 2013;495(7440):187.]. MRF is the first approach using the magnetization transient response to simultaneously obtain quantitative parametric maps of the intrinsic tissue properties such as T_1 (longitudinal relaxation time) T_2 (transverse relaxation time) and proton density (PD). This method suggests that the variation of the sequence parameters is essential in generating a unique signal evolution for each tissue. It consists of a pseudorandom acquisition based on the same mathematical principles as compressed sensing [Lustig M, Donoho DL, Santos JM, Pauly JM. Compressed sensing MRI. IEEE signal processing magazine. 2008;25(2):72] that, previously, was successfully applied to reconstruct fast MR imaging acquisitions. This approach, however, is not based on an analytical description of the signal evolution. In order to obtain quantitative maps, it requires an *a priori* dictionary of signals combined with a matching process to find the signal closest to the one acquired. A similar but faster alternative, Quantitative Transient Imaging (QTI), was recently published [Gómez PA, Molina-Romero M, Buonincontri G, Menzel MI, Menze BH. Designing contrasts for rapid, simultaneous parameter quantification and flow visualization with quantitative transient-state imaging. Scientific reports. 2019;9(1):8468] using a fixed time of repetition (TR) and a linearly increasing variable flip angle (vFA).

[0004] Dictionary matching is a powerful method in quantitative MR but has four important drawbacks. First, dictionaries are bound to the acquisition design and settings. Due to the lack of an analytical expression, optimization is only possible in a circular trial-and-error approach. Second, the resolution of the dictionary depends on the particular range of values of the parameters to be detected. Hence, creating a dictionary that provides uniform accuracy for any range of the parameter values is challenging. Third, to additionally include MR system imperfections in the dictionary construction could make the dictionary impractically large and thus its management cumbersome. And fourth, the dictionary is usually restricted to *a priori* ranges of standard values from healthy subjects that may not include unexpected values associated with pathologies of interest. Taken together, these shortcomings foster the need for an analytical description of the signal evolution.

[0005] The inventors previously disclosed an innovative method for magnetic resonance imaging in the international patent publication WO 2020/0046120. To avoid unnecessary repetition of the theoretical groundwork and possible implementations, the entire contents of said WO publication are incorporated herein by reference.

[0006] There is a need for further improvement in magnetic resonance imaging, e.g. to provides a sequence that is simultaneously sensitive to various parameters such as PD, T1, T2, B1 and B0 keeping a high coherence and avoiding the formation of banding artifacts.

SUMMARY

[0007] We present and evaluate a relevant and novel insight into quantitative magnetic resonance imaging. It is based on an algebraic description of the magnetization during the transient response. We exploit the correspondence between the signal evolution as a result of a repetitive sequence of radiofrequency excitation pulses, the continuous Bloch equations and a system of dissipative coupled harmonic oscillators. This approach simultaneously provides, in a single measurement, all quantitative parameters of interest as well as the system imperfections. It surpasses previous attempts like Magnetic Resonance Fingerprinting and Quantitative Transient Imaging in exploiting the magnetic resonance transient response. Moreover, our approach does not require any dictionary to estimate the parameters - instead obtaining all the maps at once in a single measurement. Finally, we demonstrate the applicability and advantages of the new concept on a clinical MRI scanner.

[0008] Here we introduce a new method that we name *Comprehensive MR Imaging*. It builds on a formalism proposed by Skinner in 2018 [Skinner TE. Comprehensive solutions to the Bloch equations and dynamical models for open two-level systems. Physical Review A. 2018;97(1):013815] that naturally continued Torrey's seminal work published almost

A

70 years earlier in 1949 [Torrey HC. Transient Nutations in Nuclear Magnetic Resonance. Physical Review. 1949;76(8):1059-68]. Until now, the most simple and manageable way of describing the transient response had been to use the recurrent matrix formulation established by Jaynes [Jaynes ET. Matrix treatment of nuclear induction. Phys Rev. 1955;98(4):1099-105] and Bloom Bloom AL. Nuclear induction in inhomogeneous fields. Physical Review. 1955;98(4):1105] in 1955. Nevertheless, as stated by Jaynes himself and even Lauterbur in Lian & Lauterbur [Liang Z-P, Lauterbur PC. Principles of magnetic resonance imaging: a signal processing perspective: SPIE Optical Engineering Press; 2000] more recently, this formulation is "tedious and not very intuitive". The only attempt to use a closed-form to measure T_1 and T_2 from the transient response had been proposed in the early days of MR by aforementioned Torrey - "The Road not Taken" -, but only for a single RF pulse. More than 50 years later, in 2003, Scheffler [Scheffler K. On the transient phase of balanced SSFP sequences. Magn Reson Med. 2003;49(4):781-3] suggested but did not fully develop the possibility of estimating T1 and T2 from the transient response. However, despite Torrey's early works and more recent related proposals, this road was not taken by the MR Imaging community. Therefore, we herein extend Torrey's solution for parameter estimation to an entire sequence of pulses. We describe the magnetization and the detected signal by the dynamic evolution of a dissipative system of three coupled harmonic oscillators [see aforementioned Skinner 2018]. We present a comprehensive analytical closed-form equation describing the signal evolution, including every parameter involved in the transient magnetization response. The resulting signal obtained, which we call the *Signature,* resembles the free induction decay (FID) - but stretched along the multiple RF pulses allowing for simultaneous measurements of PD, T_1, T_2, B_0 and B_1^+.

[0009] We demonstrate that the resulting signal evolutions are distinct for different species and provide the basis for accurate, intrinsic parameter estimation without changing the acquisition parameters. Furthermore, we argue that an explicit analytical description of the signal evolution is desirable in optimizing the acquisition sequence. Thanks to the analytical description, simple curve fitting can be applied for parameter quantification avoiding pattern-recognition-type estimations.

[0010] In order to fully exploit the possibilities of our method, we further propose a new acquisition sequence that enhances the performance of the model by preserving the spin coherence despite any intravoxel B_0 inhomogeneities, while remaining sensitive to overall B_0. The images obtained with this sequence show an excellent contrast between tissues and good accuracy and precision in both a standardized phantom and *in-vivo,* demonstrating the good performance of the proposed model.

[0011] In describing the signal evolution during the acquisition we do not rely on the concept of echo formation. As such, from a conceptual point of view, our approach is a completely new non-heuristic alternative to spin-echo, gradient echo or steady state quantitative imaging.

[0012] In order to provide a deeper understanding of quantitative MR imaging outputs, an analytical closed-form expression describing the magnetization is needed. In the present disclosure we present a new method that we named *Comprehensive MR Imaging* based on a dissipative 3D coupled harmonic oscillator (DCHO) model. This model provides a deeper understanding of MR relaxometry as well as better predictions for pulse sequence design.

[0013] Our approach represents "the road not taken" in the field of MR in that the closed-form analytical description presented in the present disclosure, as well as the associated pulse sequence, were thus far not exploited. This new approach is obviously different than previously proposed steady state techniques but also constitutes an alternative concept to both the spin-echo as well as the gradient echo concepts. In describing the signal evolution, we do not rely on the concept of echo formation. This is also a new interpretation and complete non-heuristic characterization of the transient response, different from MRF and QTI, based on DCHO.

[0014] Moreover, unlike MRF and QTI, our approach does not require any dictionary to estimate the parameters or vary the acquisition setting. The signal evolution is perfectly described by the closed-form expression and it can be directly fitted with the DCHO model obtaining all the maps in a single measurement.

[0015] These features set the current development apart from other simultaneous, multi-parametric techniques as they require either additional scans for estimating B_1^+ and B_0, or depend on more *a priori* information in the dictionary. Moreover, these additional acquisitions for B_1^+ and B_0 estimation are important sources of variability in terms of motion artifacts, different slice profiles, physiological noise and longer scan times. However, with the method here proposed, the B_0 inhomogeneity is estimated and hence does not confound the assessment of the other parameters. Our model also takes into account B_1^+ variation, reducing fidelity requirements of the applied RF pulses. Also, it intrinsically minimizes the effect of unavoidable system imperfections. The simultaneous estimation of B_0 and B_1^+ promises to make the parametric maps insensitive to system degradation rendering the estimation more robust and repeatable - even between disparate scanners and/or sessions.

[0016] Thus, as this new approach gives an all-inclusive set of tissue properties (T_1, T_2 and PD) without confounding by B_1^+ and B_0, that are also estimated in one measurement, our method constitutes *Comprehensive MR.*

[0017] The signal obtained with the DCHO, termed here *MR Signature,* resembles a stretched FID because of the close analogy to the free induction decay from Torrey's solution of the Bloch equations. The *MR Signature* has a frequency that is mainly determined by external controllable parameters (excitation flip angle and β) while the decay of the amplitude is mainly determined by the relaxation processes. As the signal is unique for each tissue, it may be considered to be the *signature* of the tissue (figure 4).

[0018] The DHCO model also explains the crucial role of the phase, β, accumulated in a propagator block. In some SSFP sequences, β is purposely manipulated with phase-cycling, or multiple bSSFP sequences are played out with excitation phase variations in order to avoid banding artifacts. In SPGR sequences β is manipulated as well, so as to spoil off-resonance spins. With DCHO, we see that the signal evolution is largely insensitive to β, thus avoiding banding artifacts and eigenvalues warping that could hinder the estimation of parametric maps. Still, sensitivity to T_1, T_2, PD, and β is maintained (figure 3).

[0019] *Comprehensive MR* can provide unique *MR Signatures* of healthy or pathological conditions and this will be explored in further studies. In all the tissues that we have examined thus, the *MR Signature* can be characterized after 50 pulses with a TR less than 10ms. A limitation of the current implementation is that full k-space sampling is needed, requiring multiple repeats of the acquisition. Furthermore, obtaining multiparametric maps, in a single measurement of less than 500ms per slice, is feasible when combining parallel imaging and compressed sensing techniques.

[0020] As shown in our *in-vitro* results, the accuracy for T_2 values is high and only T_1 shows a systematic linear bias that could be explained by the well-known magnetization transfer effect.

[0021] The experimental proof of concept was performed with 2D acquisitions. However, the concept allows direct extension to 3D acquisitions. Such extension facilitates high-spatial resolution with isotropic voxels. Parallel imaging and (deep learning based) compressed sensing acceleration factors can also be incorporated.

[0022] Illustrative of "the road not taken", our work demonstrates the applicability of the DCHO model in combination with a novel MR acquisition technique (MP-b-nSSFP) to generate a distinct signal (*MR Signature*) capable of characterizing any tissue for quantitative MR (*Comprehensive MR Imaging*). This new technique is less affected by common system imperfections allowing for the development of new (less-demanding) MR scanners. Finally, based on the robustness of the simultaneous estimation of experimental conditions and parametric maps, our method paves the way towards standardization of MR technology.

[0023] In a preferred embodiment a balanced sequence of repetitive blocks is applied until getting the stationary state. One repetitive block comprises four pulses interlacing small flip angles (alpha) and large flip angle pulses and alternating the phase as follows: α_x-γ_y-α_y-γ_x, being remarkable the phase scheme (x-y-y-x). Between every pair of adjacent RF pulses the signal is e.g. sampled with balanced spiral-out k-space trajectory. After the first "α_x" pulse the signal is proportional to PD. After any "γ_x" or "γ_y" pulse, the signal is refocused before the next "α_x" or "α_y" maximizing the transversal signal after any "α" pulse. The phase accumulates a constant precession angle, due to field inhomogeneities, local susceptibility gradients or chemical shift after any "alpha". This feature makes the sequence sensitive to B0 field inhomogeneities. In summary, the transversal magnetization is sensitive to all the relevant parameters T1, T2, PD, B1, B0. The particular phase cycling being used combines small flip angles and large flip angles keeping the intra-voxel magnetization as a single species away from the axis x and y of the rotating frame of reference avoiding typical banding artifact. The parameter estimation and the interpretation of the transient signal is compatible with different mathematical methods: either a vectoral equation derived from our previous patent application WO 2020/0046120, or Bloch equations or a dictionary as in MR Fingerprinting or Quantitative Transient Imaging.

[0024] The simultaneous estimation of MR parameters or maps have been recently achieved with different approaches: MR Fingerprinting, MAGIC, QTI or MR Signature. MR Fingerprinting and QTI can be implemented with balanced or spoiled unbalanced SSFP sequences. They are sensitive to PD, T1 and T2 but they are not sensitive to B1 or B0, despite being a balanced sequence. They require either specific B1 corrections and to increase the dictionary with signal evolutions affected by different off-resonance effects. MAGIC is sensitive to PD, T1, T2 and insensitive to B0 because it uses a spin-echo sequence and it requires an additional B1 correction. The present disclosure provides a sequence simultaneously sensitive to PD, T1, T2, B1 and B0 keeping a high coherence any avoiding the formation of banding artifacts. Regarding other simultaneous quantitative MR methods such as MR Fingerprinting, QTI or MAGIC, the sequence is sensitive to all the relevant parameters. Regarding MRF, it does not require to incorporate B0 information in the dictionaries as the B0 map can be estimated and the dictionary itself is not necessary. Regarding other balanced SSFP sequences, it intrinsically avoids the formation of banding artifacts.

A

BRIEF DESCRIPTION OF DRAWINGS

[0025] These and other features, aspects, and advantages of the apparatus, systems and methods of the present disclosure will become better understood from the following description, appended claims, and accompanying drawing wherein:

FIG 1A illustrates an example block;

FIG 1B illustrates an example sequence of repeated blocks;

FIGs 2A-2F illustrate evolution of a magnetization vector in three dimensions and in respective projections;

FIGs 3A-3E illustrate mapping of eigenvalues for various excitation schemes;

FIG 4 illustrates an image derived with the present methods and underlying measurement and fitted traces of the magnetization;

FIGs 5A and 5B illustrates estimates of T1 and T2 for various samples as function of their reference value;

FIGs 6A-6F illustrate various images generated with the present methods including a new type of image contrast $\rho^2\eta$;

FIG 7A illustrates various parameters such as magnetic fields and flip angles;

FIG 7B illustrates a preferred sequence of repeated blocks;

FIG 7C illustrates a magnetization as function of block number;

FIGs 8A and 8B illustrate representative graphs which can be used to verify an optimal combination of small and larger flip angles;

FIG 9 illustrates a repeated block in an MR sequence with Cartesian readout;

FIG 10 illustrates a repeated block in an MR sequence with spiral readout.

DESCRIPTION OF EMBODIMENTS

[0026] Terminology used for describing particular embodiments is not intended to be limiting of the invention. As used herein, the singular forms "a", "an" and "the" are intended to include the plural forms as well, unless the context clearly indicates otherwise. The term "and/or" includes any and all combinations of one or more of the associated listed items. It will be understood that the terms "comprises" and/or "comprising" specify the presence of stated features but do not preclude the presence or addition of one or more other features. It will be further understood that when a particular step of a method is referred to as subsequent to another step, it can directly follow said other step or one or more intermediate steps may be carried out before carrying out the particular step, unless specified otherwise.

[0027] Applications of NMR, such Magnetic Resonance Imaging (MRI), typically relies on a constant, homogeneous magnetic field "B0" to polarize spins in a target volume of an object to be imaged. The direction of B0 can be used define the longitudinal axis, denoted as the "z-axis"; and the transverse directions along the "x-axis" and "y-axis" (perpendicular the longitudinal axis and each other). The B0 field can create a magnetization "μ" of the spins which in equilibrium is directed along the z-axis. The magnetization can be excited (out of equilibrium) and detected at the resonance frequency of the spins in the magnetic field, referred to as the Larmor frequency. The Larmor frequency varies with magnetic field strength, and is normally in the radio frequency (RF) range.

[0028] A radio frequency (RF) energy field "B1" can be applied perpendicular to the longitudinal axis (B0) to perturb the magnetization in some manner. The flip angle "α" (or "γ") refers to the angle to which the net magnetization is rotated or tipped relative to the main magnetic field direction via the application of an RF excitation pulse at the Larmor frequency F_L. It is also referred to as the tip angle, nutation angle or angle of nutation. The radio frequency power (which is proportional to the square of the amplitude) of the pulse is proportional to "α" through which the spins are tilted under its influence.

[0029] The angle of the magnetization in the transverse plane is also referred to as the phase. It will be understood that the "RF pulse" is merely a magnetic field (B1) of short duration rotating at the Larmor frequency in the transverse

A

plane (xy). Depending on its phase, the RF pulse may be considered to be "directed" along the x-axis or γ-axis (or anywhere else in between). In a sequence or block, RF pulses can be applied along different axes by shifting the relative phase between the RF pulses. For example, a first RF pulse is applied along the x-axis followed by a second RF pulse applied along the γ-axis by phase shifting the excitation ninety degrees between the pulses.

[0030] A spatially varying magnetic field, i.e. gradient, can used to manipulate the resonance frequency across an object for selectively exciting and/or detecting spins in a specific region of the object. MRI scanners typically incorporate gradient coils to vary a magnitude the magnetic field B0 with gradients "Gx", "Gy", and "Gz" along the x-, y-, and z-directions, respectively. The strength of the respective gradients can typically be controlled by a magnetic gradient pulse sequence which can be rapidly manipulated (or "switched").

[0031] The invention is described more fully hereinafter with reference to the accompanying drawings. In the drawings, the absolute and relative sizes of systems, components, layers, and regions may be exaggerated for clarity. Embodiments may be described with reference to schematic and/or cross-section illustrations of possibly idealized embodiments and intermediate structures of the invention. In the description and drawings, like numbers refer to like elements throughout. Relative terms as well as derivatives thereof should be construed to refer to the orientation as then described or as shown in the drawing under discussion. These relative terms are for convenience of description and do not require that the system be constructed or operated in a particular orientation unless stated otherwise.

Theoretical framework - From Linear Algebra to Dissipative Coupled Harmonic Oscillators

[0032] We start with a detailed theoretical description which may help in understanding various application for improvement in the field of MR. However it will be understood that practical applications are not bound by details of this theory or the specific examples provided for explaining the various aspects. Instead, this is merely provided to convey a good understanding of the principles, while the scope of applications may include various combinations and/or extensions of these aspects.

[0033] Without being bound by theory, we provide an algebraic description of the signal evolution during the entire MR sequence. Our goal is to establish a theoretical background for quantitative sequences that utilizes a single transient response and can yield quantitative maps for all relevant parameters, intrinsic (T_1, T_2, PD) and experimental (B_0 & B_1^+), at once.

Linear operators - the propagator

[0034] An MRI sequence typically consist of a train of acquisition blocks, here called *propagators,* sequenced in a repetitive manner. Each block typically consists of radiofrequency excitations, magnetic field gradients and waiting times (periods absent of RF excitations or magnetic field gradients). The excitations, gradients and free precession can be represented by rotations of the magnetization that can be described, e.g., as linear operators.

[0035] FIG 1A illustrates an example "propagator": a single block of events. μ is the input-output magnetization, in dark gray the RF excitations and in light gray the gradients. FIG 1B illustrates a train of blocks in an MR pulse sequence. We will use identical blocks or operators $A = A_1 = A_2 = ... = A_n$.

[0036] The cumulative effect of the events within an entire block can be represented by a single operator resulting from the linear product of rotations and relaxations. We focus on a special case when the propagator, ***A,*** is identical along the train. Typically, the evolution of the magnetization can be modelled by the recursive application of the Bloch equation. However, as introduced by Skinner, the evolution of the magnetization can also be modelled as a second order differential equation of motion for dissipative coupled harmonic oscillators. This is shown in equations *A1*, *A2* and A3 (see *Appendix* section for mathematical details).

[0037] This connection provides three relevant consequences: first, the magnetization and, therefore the signal, follows a damped oscillatory pattern; second, the signal obtained resembles a stretched FID sensitive to all the intrinsic and experimental parameters (T_1, T_2, PD, B_0 & B_1^+); third, the DCHO model provides an alternative formulation with different intrinsic parameters, the eigenvalues, that allows for an alternative analysis of the pulse sequence (see Appendix for mathematical details).

Dissipative Coupled Harmonic Oscillator Model

[0038] This DHCO model provides a comprehensive interpretation of the signal in terms of intrinsic and experimental parameters. The damped oscillation is determined by the propagator, **A,** and this propagator can be fully and directly described by its eigenvalues.

A

[0039] The eigenvalues with the initial state provide an exact and compact solution in a closed-form:

$$\boldsymbol{\mu}_n = \rho^n \cdot \sin(n\varphi) \cdot \boldsymbol{v}_1 + \rho^n \cdot \cos(n\varphi) \cdot \boldsymbol{v}_2 + \eta^n \cdot \boldsymbol{v}_3 \qquad (1)$$

where μ_n is the 3D magnetization vector after the subtraction of the steady state. $\rho e^{i\varphi}$, $\rho e^{-i\varphi}$ and η are the eigenvalues of the propagator ***A,*** with real *p* and η. φ is mostly real (it is purely imaginary only in the special overdamped, on-resonance case). v_1, v_2, v_3 are the normal modes of the 3D harmonic oscillator.

[0040] FIGs 2A-2C illustrate evolution of the magnetization where the repeated block consists of an excitation with flip angle α=30°, β=14° (accumulated phase as a result of off-resonance during T_R, T_R=10 ms), relaxation times are T_1 = 878 ms, T_2= 47.5 ms. The vectors v_1 and v_2 span the plane of oscillation. In this case, the magnetization vector always points to a point of this plane. Only the orientation of the plane is fixed throughout the evolution; it shifts parallel to v_3.

[0041] FIGs 2D-2F are similar to FIGs 2A-2C but on-resonance (β=0°). The plane spanned b. v_1 and v_2 is the x-z plane throughout the entire evolution. The points represent the magnetization difference vector and its evolution along the sequence as according to Eqn.A1. The continuous line is the corresponding continuous case of Eqn.A2. It is not the fully continuous trajectory of the magnetization. However, the magnetization at the discrete time points sit on the continuous curve.

[0042] FIGs 2A and 2D illustrate evolution of the magnetization in three dimensions; FIGs 2B and 2E illustrate the x-y projection (transversal plane); FIGs 2C and 2F illustrate x and y component (signals measured in quadrature).

Design of a pulse sequence based on the analysis of the eigenvalues of the propagator

[0043] This section demonstrates how to properly design a propagator for a pulse sequence based on a simple analysis of its eigenvalues, in order to produce a signal evolution for simultaneous estimation of parametric maps: T_1, T_2, proton density (PD), B_0 and B_1^+. The consequence of this appropriate design is to produce an optimal signal evolution enhancing the effects of the desired parameters and suppressing undesired confounders (like B_0 inhomogeneities or B_1^+ imperfections).

[0044] Theoretically, any propagator with at least one RF excitation pulse could suffice for T_1, T_2 and PD mapping. In practice, however, a careful choice of the propagator is desired in order to provide sensitivity for a large range of parameters and also to maintain robustness of parameter estimation despite uncontrolled variations in experimental parameters.

[0045] FIGs 3A-3E show the mapping of a T_2-β parameter space to the eigenvalue complex plane. FIG 3A shows T_2-β species: parameter space; FIGs 3B-E are the eigenvalue maps where three eigenvalues belong to each parameter species: the complex eigenvalues ($\rho e^{i\varphi}$, $\rho e^{-i\varphi}$), and the real eigenvalue (η). In more detail, we take a two-dimensional plane T_2-β (with fixed T_1 and excitation flip angle) (FIG 3A) and look at the resulting eigenvalue space in the complex plane (FIGs 3B,3C,3D,3E for different sequences or propagators), where each T_2-β species are represented by three eigenvalues. For all of them T_1=878 ms, T_R=12 ms.

[0046] In order to illustrate the propagator design process we consider a two-dimensional plane T_2-β (where β is the accumulated phase during a TR due to off-resonance) (FIG 3A), with fixed T_1 and excitation flip angle. FIGs 3B-3E show the resulting eigenvalue space in the complex plane for different sequences or propagators. According to the 3D DCHO model, each T_2-β species is represented by three eigenvalues. As will be appreciated, the eigenvalue space can provide immediate insight into the signal evolution: the radial distance from the origin determines the decay rate, and the angular position determines the oscillation frequency of the stretched FID to be detected.

[0047] We next evaluated different pulse sequences based on different propagators. We simulated propagators based on one single pulse with flip angle "α" , with fixed arbitrary value of 30°, and played out along "x" (α_x). We then modified either the phase (playing out the pulse along "y" instead of along "x", "α_y") or the flip angle "γ" (165°). To illustrate how to perform the eigenvalues-based analysis, we used four different repetitive propagators to design the pulse sequence: "α_x", "α_x - α_y", "α_x - y_x - α_y - γ_y" and "α_x - γ_y - α_y - γ_x". The last two are almost equivalent so, from now on, we refer only the last one: "α_x - γ_y - α_y - γ_x".

[0048] The "α_x" and the "α_x - α_y" propagators show radial dependence on T_2 and angular dependence on β in the eigenvalue space. In the proximity of β = 0 the eigenvalue space is warped and thus would hinder differentiating between different T_2-β species. The "α_x - α_y" propagator shows similar patterns for low excitation flip angles and also, the eigenvalue space is wrapped around for species between β = 0 - π/4 and β = π/4 - π/2. For higher values of α, the positions of β = 0 species are swapped to the negative real half-plane and the warping disappears. The "α_x - γ_y - α_y - γ_x" propagator shows the same features as the "α_x - α_y" propagator for larger flip angles.

A

[0049] Besides the undesired warping, there is yet another problem arising in the near-resonance for "α_x" and "α_x - α_y", in particular with lower α. The trajectory becomes two-dimensional and the third normal mode vector v_3 vanishes (this can be observed in Figures 2.d and 2.e). In equation 1, the third term becomes zero and consequently, the signal (Figure 2.f.) carries no information about the real eigenvalue η.

[0050] The criteria in selecting the propagator are the following: first, the eigenvalue space preferably should carry information on T_1, T_2 and β and second, the resulting eigenvalue space preferably should not have warping so as to avoid incorrect estimations for different tissues.

[0051] The "α_x - α_y" propagator may be optimal from a conceptual perspective: it avoids warping and provides radial-angular distribution. However, it is technically challenging, especially in a 2D scan for higher flip angles, where a sharp slice profile is desired.

[0052] Therefore it is beneficial to choose a propagator where the β dependence of the eigenvalue space is limited but not absent. This allows voxels to be described as single species, even if some intra-voxel dispersion in β exists, while at the same time allowing determination of B_0. Additionally, these limited β values can also be interpreted as minimum dephasing. This is an important advantage that eliminates typical banding artifacts in bSSFP sequences.

[0053] We experimentally verified these theoretical predictions and found that the propagator "α_x - γ_y - α_y - y_x" showed the best performance due to the minimal β dispersion. This propagator then is the building block of the new sequence that we named "Multi-Phase balanced, non-Steady State Free Precession" (MP-b-nSSFP).

Demonstration of the DCHO signal evolution on a clinical scanner

[0054] The "in-vivo" study in healthy subjects was approved by the institutional review board (protocol 2014-096) and a written informed consent was obtained from the volunteer. For the validation we used a 1.5 T clinical scanner - the GE Optima MR450w (General Electric Medical Systems, Waukesha, WI) with a 16 channel head and neck coil. We could demonstrate that the proposed theoretical framework describes the experimental signal evolution with great accuracy. The acquisition was carried out by 100 times repeated 2D spiral readouts with a TR of 10 ms. For complete data collection, this experiment was repeated in 64 different spiral rotations.

[0055] FIG 4 shows measured data and theoretical model fit for the "α_x" propagator. The theoretical DCHO model (see equation 1) closely matches the data points. The 2D signal plot clearly shows that the selected voxel is not on-resonance (compare to FIGs 2B and 2C). Despite the presence of external field (B_0) inhomogeneities, the single species DCHO model describes the signal evolution remarkably well. It is also important to note that, due to the minimum dephasing, banding artifacts are lacking - as predicted by the analysis described above (FIG 3).

[0056] In FIG 4, the signal is shown as it evolves along the echo train in two voxels (depicted on the anatomical image) with the "α_x - γ_y - α_y - γ_x" propagator. The anatomical image is shown on top. The bottom left subfigures shows the respective voxel, where the spins are on-resonance. The bottom-right subfigure (other voxel) shows a spiral in the complex signal plane. This clearly shows the regularity of the evolution. The orthogonal real and imaginary components are depicted. The frequency of the oscillations is constant, the decay of the amplitudes is exponential. The steady state is not zero. The fitted curves show the fitted harmonic oscillator model.

Validation in a standardized phantom - Accuracy and Precision

[0057] FIGs 5A and 5B shows the correlation between the nominal and the DCHO derived parameters. We tested the DCHO model in a standard phantom set (ISMRM/NIST MR System Phantom). Voxels from the same phantom tube are depicted with the same grayscale. The parameters were derived from data acquired with the" α_x - γ_y - α_y - γ_x"propagator. The mean T_2 is underestimated by 10% ($\pm$ 4%). The accuracy of the T_1 maps is lower as the mean T_1 values are underestimated by 34% ($\pm$ 8%). The overall bias shows a linear dependence on the T_1 values. Apart from the bias, the precision of the T_1 maps is in the range of 10ms. This shows that both parameters are estimated independently with high voxel-wise precision.

In-vivo parametric maps

[0058] FIG 6 shows the results from the in-vivo scan. The parametric maps derived with the DCHO model are shown. Top row shows PD (proton density, a.u.), T_1 (ms); middle row shows T_2 (ms), B_0 (deviation in static magnetic field; rad/ms); Bottom row shows B_1 (excitation RF field scaling factor), and $\rho^2\eta = det(\boldsymbol{A}) = \varepsilon_2^2\varepsilon_1$ (HO: Harmonic Oscillator), estimated from the phase alternating split propagator (α_x - γ_y - α_y - γ_x).

[0059] The acquisition scheme was the same applied to the standardized phantom. Besides the usual parametric maps (PD, T_1, T_2) an additional map can be derived that we named the harmonic oscillator (HO) map. The HO map is

A

the determinant map of the propagator which is essentially the total dissipation during the entire propagator block. The HO map can be considered a quantitative map derived from a combination of T1 and T2, but free of system imperfections as the B_0 and B_1^+. They are all part of the analytical model and estimated simultaneously as well.

[0060] All these maps were obtained simultaneously in one measurement using the model and the "MP-b-nSSFP" sequence described in the present disclosure. To our knowledge, this the first time that multi-parametric maps have been obtained non-heuristically from a transient MR signal response without necessity of a dictionary. The quality and consistency of these maps demonstrate the "in-vivo" applicability of this technique.

[0061] It will be appreciated that various aspects as described herein can be embodied in practical applications for improving methods and systems related to (nuclear) magnetic resonance imaging such as an MRI device. Some aspects may also be embodied e.g. as a (non-transitory) computer readable medium with software instructions which when executed by an MRI device cause imaging as described herein. While many applications and advantages may already be apparent from the above discussion, we will highlight some of the more preferred aspects in the following. Of course it will be understood that any of these aspects can also be combined with any further teaching having the benefit of the present disclosure.

[0062] FIGs 7A-7C illustrate a method for measuring (nuclear) magnetic resonance, MR, properties of spin systems in a target volume V.

[0063] In one embodiment, a main magnetic field B0 is applied to the target volume V along a longitudinal axis Z. In another or further embodiment, an excitation sequence An is applied applying to the target volume V. In a preferred embodiment, as described herein, the sequence comprises a repeated sub-sequence or block A of excitation pulses. In some embodiments, a set of response signals μ_n is measured e.g. as a function of block number n. The response signals can be indicative of respective magnetization μ of the spin systems from the target volume V, e.g. in a respective one or more measurement windows W for each block A which typically follow one or more of the excitation pulses (in that block). In some embodiments, the MR properties of the target volume V are determined based on the set of response signals.

[0064] In a preferred embodiment, as illustrated e.g. in FIG 7B, each block A comprises a set of at least four radio frequency, RF, pulses. Most preferably, the set includes at least two small angle RF pulses and at least two large angle RF pulse. A first small angle RF pulse α_x is configured to apply a small flip angle α of less than ninety degrees along a first transverse axis X which is transverse to the longitudinal axis Z. A first large angle RF pulse γ_y is configured to apply a large flip angle y of more than ninety degrees along a second transverse axis Y which is transverse to the longitudinal axis Z and transverse to the first transverse axis X. A second small angle RF pulse α_y is configured to apply the same small flip angle α as the first small angle pulse αx but along the second transverse axis Y. A second large angle RF pulse γ_x configured to apply the same large flip angle γ as the first large angle pulse γy but along the first transverse axis X.

[0065] As described herein, the inventors find that this combination of pulses which alternatingly flip and refocus the magnetization along different axes can provide a magnetization vector which develops from block to block along an essentially three dimensional trajectory. In essence, the switching of axes forces off-resonance which means the resulting trajectory of the magnetization is not restricted e.g. to the XZ (or YZ) plane. As a consequence, this trajectory can carry additional information of the underlying system, such as deviation in static magnetic field (B0), which information would be lost on-resonance. At the same time, while such off-resonance excitation is normally undesirable since it deteriorates the signal, in this case the signal is continually refocused in each block (and within the block) by the specific symmetries of pulses.

[0066] In one embodiment, e.g. as shown in FIG 7A, the excitation sequence comprises RF pulses with an oscillating magnetic field B1 along at least one transverse axis X,Y, orthogonal to the longitudinal axis Z. The excitation or acquisition sequence typically also comprises a set of magnetic field gradients (not shown here), e.g. used for localizing the excitation to a specific volume and/or for generating a gradient echo. In another or further embodiment, one or more receiver coils are arranged for converting a transverse component of the magnetization (along one or more of the traverses axes X,Y) into an electric signal which is measured. This can be the same or different RF coil used for delivering excitation pulses.

[0067] It will be understood that the application of RF pulses along different axes (X,Y) is equivalent to applying the RF pulses with a specific relative phase ($\Delta\Phi$) compared to a phase Φ_F of the frame of the induced magnetization vector μ rotating around the longitudinal axis Z with the Larmor frequency (F_L). So when a second RF pulse is applied in different direction with respect to a first RF pulse this is equivalent to applying the second RF pulse with a different (carrier) phase relative to the phase Φ_F of the rotating frame, compared to the phase of the first pulse (relative to the to the phase Φ_F of the rotating frame). It will also be understood that the oscillating B1 field of the RF pulses can be applied along any one or more axes in the rotating frame orthogonal to the B0 field which is along the longitudinal axis Z, shifting the phase Φ_F accordingly.

[0068] In some embodiments, the phase of the initial pulse is not important, only the relative phase of subsequent pulses. In other or further embodiments, small deviation in the (relative) phase may be tolerated. So as described herein,

where a specific axis (X,Y) is indicated it will be understood that the relative phase (e.g. ninety degrees for orthogonal axes) may have a small deviation, e.g. less than ten degrees, preferably less than five degrees, most preferably less than one degree, or as small as possible.

[0069] The first large angle RF pulse γ_y is preferably applied in an orthogonal direction (+y), i.e. ninety degrees out of phase, with respect to the first small angle RF pulse α_x; or, alternatively, in the opposite (also orthogonal) direction (-y), i.e. two hundred seventy degrees out phase. The second small angle RF pulse α_y is preferably applied in the same direction (+y), i.e. with the same phase, as the first large angle RF pulse γ_y; or, alternatively, in the opposite direction (-y), i.e. hundred eighty degrees out phase. The second large angle RF pulse γ_x is preferably applied in the same direction (+x), i.e. with the same phase, as the first small angle RF pulse α_x; or, alternatively, in the opposite direction (-x), i.e. hundred eighty degrees out phase.

[0070] FIG 7C illustrates an example graph of the progression or development of the magnetization pn, as function of the sequence or block number "n". the magnetization μn measured as function of block number n. In principle various MR properties can be derived based on such measurements. For example, the measured magnetization as function of block number can be fitted to a (continuous) function "F" whose shape depends on parameters which can be characteristic of a specific tissue.

[0071] In one embodiment, the resulting magnetization μ is measured as a discrete sequence of response signals. For example, a respective response signal is acquired during a respective one or more acquisition windows W of a respective block A. In one embodiment, the sequence of (transient) response signals represents sequential evolution of the magnetization state μ resulting from a combination of manipulating of spin systems in the target volume by the blocks as well as intrinsic properties (such as PD, T1,T2) of the spin systems to be imaged. For example, the response signals are measured in the respective acquisition windows per block during a transient phase before a steady state response signal to the consecutive series of blocks develops.

[0072] In one embodiment, the discrete sequence of response signals is fitted to a fit function F that is based on an analytically modeled evolution of the magnetization state. For example, a shape of the fit function is determined by a set of fit parameters related to intrinsic properties PD,T1,T2 of the spin systems to be imaged and/or experimental settings. In some embodiments, the fit function F is a closed form expression that is continuously dependent on a variable n which at integer values equals a sequence number of the respective block "An" and corresponding response signal.

[0073] In one embodiment, the magnetization is modeled as a three dimensional magnetization vector, wherein an effect of a block on the magnetization is modeled using matrices as operators on the magnetization vector. For example, consecutive application of blocks is modelled as repeated multiplication by an operator matrix, wherein the repeated matrix multiplication is calculated using eigenvalues of the operator matrix. For example, the modelled fit function is based on a projection of the magnetization vector in a measurement direction of the measured responses. In some embodiments, a shape of the fit function is determined according to the analytically modelled evolution based at least on the experimental settings such as the repetition time TR, the specific choice of flip angles α and γ, the waiting time or phase evolution β' as well as intrinsic parameters r,λ_3,φ,δ to be fitted. Accordingly the intrinsic parameters can be related to the intrinsic properties PD,T1,T2 of the spin systems to be imaged. Of course also other models can be used.

[0074] In some embodiments, an image of the target volume V is determined based on at least one of the set of fit parameters which match the fit function to the discrete sequence of response signals. In a preferred embodiment, the fit function has both dissipative and oscillatory terms. For example, the fit function is of the form

$$F_n = a \cdot e^{-|ln\, r|\cdot n} \cos(\varphi n + \delta) + b \cdot e^{-|ln\, \lambda_3|\cdot n} + c\ ,$$

where F_n is the value of the function to be fitted for the respective measurement of block number n; and a, b, c, φ, δ, r, λ_3 are fit parameters. In principle, an image of the target volume V can be constructed based directly on fitted values of one or more fit parameters in the fit function F. Alternatively, the fitted values can be converted to the more familiar properties such as T1,T2.

[0075] FIGs 8A and 8B illustrates representative graphs which can be used to verify an optimal combination of small and larger flip angles α,γ in a sequence (αx,γy,αy,γx) applied to typical tissue with the indicated values for T1 and T2, in different combination, T1=800ms, T2=50ms (top); T1=800,T2=200 (middle); T1=1100 ms, T2=200ms (bottom). The grayscale indicates the suitability of the respective combination. Specifically, the brightness of respective areas in the graph indicates a magnitude of the square root of a diagonal element of the Cramer Rao Lower bound matrix (CRLBs), which gives a good prediction for the standard deviation of the respective parameters in actual experiments. Hence the figures show the CRLBs divided by the nominal value for T1 and T2 to predict the respective coefficient of variation (CoV) that can be expected in actual experiments upon a global scaling factor that linearly relates to the noise level in the experiment. The graphs in FIG 8A are without magnetic field inhomogeneity (B=0 rad/ms); whereas in FIG 8B there is inhomogeneity (B=0.30 rad/ms). It may be noted that the corresponding graphs of FIGS 8A and 8B are very similar, illustrating that the inhomogeneity has only small effect on the determination of T1 and T2.

A

[0076] The terms "large" and "small" flip angles pulses are used herein to distinguish the different type of pulses based on their relative flip angle being relatively large or small, e.g. more or less than ninety degrees. In some embodiments, the small flip angles α_x,α_y are between ten and eighty degrees, preferably between fifteen and sixty degrees, most preferably between twenty and forty degrees, e.g. thirty degrees (plane angle). In other or further embodiments, the large flip angles γ_x,γ_y are between hundred twenty and hundred eighty degrees, preferably at least one hundred forty degrees, one hundred fifty degrees, or one hundred sixty degrees, and most preferably equal or less than one hundred seventyfive degrees, e.g. one hundred sixty degrees.

[0077] It will be noted that while these ranges, especially in combination, can provide particularly optimal behavior of the system for the measurements as described herein, in principle also other combinations of flip angles can be used to provide at least some of the benefits. For example, the graphs show that also a combination of only large flip angles can provide relatively low CoV. However, also other factors may be taken into consideration, e.g. maximum energy deposition in the tissue. This is one reason why the combination of small and large flip angles is most preferred.

[0078] Most preferably, in each block A, the set of RF pulses are applied in a sequence $\alpha,\gamma,\alpha,\gamma$ interleaving the small angle RF pulses α_x,α_y with the large angle RF pulses γ_x,γ_y. Advantageously, using this sequence, after any large flip angle γx, γy pulse, the signal can be refocused before the next small flip angle αx, αy providing the desired transversal signal after any "alpha" pulse. At the same time, the phase accumulates a constant precession angle, due to field inhomogeneities, local susceptibility gradients or chemical shift after any "alpha" - thus improving sensitivity to B0 field inhomogeneities.

[0079] In one embodiment, the RF pulses are applied in a sequences with the first small angle pulse α_x followed by the first large angle pulse γ_y followed by the second small angle pulse α_y followed by the second large angle pulse γ_x; or a cyclic variant thereof. For example, each block may comprise a sequences selected from: {αx,γx,αy,γy}; {αx,γy,αy,γx}; {αy,γy,αx,γx}; {αy,γx,αx,γy}.

[0080] In some embodiments, , in each block A, the set of RF pulses are applied in a sequence $\alpha,...,\gamma$ starting with one of the small angle RF pulses α_x,α_y and ending with one of the large angle RF pulse γ_x,γ_y, wherein at least one measurement window W follows directly after a large angle RF pulse γ_x,γ_y Advantageously, beginning with a small flip angle and ending with a large flip angle, may refocus the magnetization after each block. On the other hand, since the blocks are repeated, and in principle, the measurement window W can be between any two pulses, the block can also start with a large flip angle γ pulse and end with a small flip angle α pulse. Additionally, or alternatively, a measurement window can also be disposed directly following one of the small angle RF pulses α_x,α_y. This signal may in principle carry similar information.

[0081] In the sequence, the blocks are preferably repeated before the (transverse) signal has completely decayed. So the repetition time TR (from one block "An" to the next block "An"$_{+1}$) is ideally on the order of, or smaller than the transverse (spin-spin) relaxation time T2 of the spin systems to be measured. In a preferred embodiment, the blocks are repeated with a repetition time T_R of less than two or three times T2. For example, the blocks are repeated with a (block) repetition time T_R of less than hundred milliseconds, preferably less than sixty milliseconds, most preferably less than twenty milliseconds, e.g. between one and fifteen milliseconds. In principle, the shorter the repetition time, the faster the acquisition but this also has to be weighed against other factors such as system and tissue limitations.

[0082] Preferably, a variation or progressive development of the (transverse) magnetization μ is measured from block to block before a steady state response to the repeated blocks develops. So, the measurement time of all blocks in a sequence combined is preferably on the order of the longitudinal (spin-lattice) relaxation time T1 of the spin systems to be measured. In a preferred embodiment, the sequence of all blocks combined is extended over a period of at least a tenth of T1, e.g. up to T1, or longer. For example, the excitation sequence for determining a respective MR property comprises at least ten repeated blocks A1...A10, preferably at least twenty repeated blocks A1...A20, most preferably at least forty repeated blocks A1...A50, or more, e.g. between fifty and hundred repeated blocks. For example, as shown in FIG 4, the most information / signal is retrieved in the first fifty blocks.

[0083] In one embodiment, the RF pulses are applied with a pulse-to-pulse time Tp between subsequent RF pulses in each block A, wherein the pulse-to-pulse time Tp is less than fifty milliseconds, preferably between one and fifteen milliseconds, or less. For example, the limits may be determined by the measurement apparatus and/or maximum energy that can be safely deposited by the RF pulses.

[0084] Preferably, the set of RF pulses in each of the repeated blocks A is identical. While this provides the easiest and most predictable sequence, also variation, e.g. in the sequence of small and large angle pulses, within each block can be envisaged.

[0085] FIG 9 illustrates an example with a repeated block "An" in an MR sequence with Cartesian readout;
In some embodiments, in addition to the RF pulses, each block comprise a set of magnetic field gradients or gradient pulses G. For example, the gradient pulses can be used to generate a gradient echo and/orimprove, e.g. maximize a magnitude of, the measured signal in the measurement window W, also referred to as the echo time. Alternatively or additionally, the gradient pulses can be used for localizing the target volume V in an object.

[0086] In a preferred implementation, the present pulse sequence is used in magnetic resonance imaging (MRI). For

example, one or more of the determined MR properties are used for generating a two or three dimensional image of an object comprising the target volume V. Also other types of MR measurements can be envisaged for obtaining various quantitative parametric maps of an object or volume.

[0087] In one embodiment, each block A comprises a set of magnetic field gradient pulses G for selecting sub regions to be imaged in the target volume V. In one embodiment, e.g. as shown, a slice select gradient Gss is applied during each RF pulse for selectively exciting the target volume in an object slice. In another or further embodiment, a phase encoding gradient Gpe is applied before (or during) each measurement window W for encoding a first spatial dimension of the target volume in the object slice. In another or further embodiment, a frequency encoding gradient Gfe is applied during each measurement window W for encoding a second spatial dimension of the target volume in the object slice.

[0088] The inventors find that the present sequences perform optimally when the gradient pulses G for each block are applied according to a balanced sequence. Preferably, the gradients are balanced at least from block-to-block. So for each applied gradient in a block "An" opposite gradient is applied to restore the phases before the next block. In some embodiments, e.g. as shown, the gradients are also balanced between subsequent pulses within each block. So for each applied gradient during and after a first pulse in a block "An" opposite gradient is applied to restore the phases before the next pulse in the same block.

[0089] FIGs 9 and 10 illustrates that in principle the signal can be readout between each pulse to yield a respective indication of how the magnetization develops from block to block. These multiple readouts per block may provide additional information. In other or further embodiments (as shown in previous FIGs 1-7), the signal is only readout once per block, e.g. after the four subsequent pulses. For example, the phase encoding gradient Gpe and a frequency encoding gradient Gfe need only be applied once per block, optionally with the four pulses closer together. Also many other readout schemes can be envisaged in combination with the present sequence of RF pulses. In principle, each block can also have more than four pulses, e.g. six or eight pulses which alternate between small and large flip angles.

[0090] FIG 10 illustrates a repeated block "An" in an MR sequence with spiral readout. In a preferred embodiment, between every pair of adjacent RF pulses, the signal is sampled with balanced spiral-out k-space trajectory. Of course also other readout schemes can be used.

[0091] It will be understood that aspects of the present disclosure can be embodied as an MR device configured to perform operational acts as described herein. For example, an MRI device can be programmed to apply the present disclosed pulse sequence to a tissue and construct an image based on the response signals. In some embodiments, the MRI device comprises a lookup table for distinguishing different tissue types in the image based on one or more distinct fit values of intrinsic parameters depending on tissue type, as fitted to a measured sequence of response for a predetermined set of experimental settings. Aspects of the present disclosure can also be embodied as a computer program, e.g. a non-transitory computer readable medium with software instructions which when executed by an MRI device cause imaging with a pulse sequence as described herein.

Appendix A

[0092] The operator in FIG 1, $\boldsymbol{A}_n$ updates the magnetization $(\boldsymbol{\mu}_n \overset{A_n}{\rightarrow} \boldsymbol{\mu}_{n+1})$ along the train of acquisition blocks.

[0093] We focus on a special case, where the propagator $\boldsymbol{A}$ is constant, i.e. the acquisition train is strictly repetitive. This constraint leads to a simple recursive formula:

$$\boldsymbol{\mu}_{n+1} = \boldsymbol{A} \cdot \boldsymbol{\mu}_n \text{ , with the solution: } \boldsymbol{\mu}_n = \boldsymbol{A}^n \cdot \boldsymbol{\mu}_0 \qquad \text{(A1a - A1b)}$$

where $\boldsymbol{\mu}$ is the difference in magnetization from the steady-state and $\boldsymbol{\mu}_0$ is the initial state. It is important to realize at this point that even if $\boldsymbol{A}$ is constant, the set of events in the blocks along the train are not necessarily identical, however their cumulative effect is.

[0094] The recursive equation (Eqn. A1.b) is equivalent to a discrete-in-time equation of motion for the magnetization vector. Mathematically, this equation of motion is a very simple one: it is a linear, first order, homogenous and autonomous difference equation. The continuous analogue is the following vector differential equation:

A

$$\dot{\boldsymbol{y}}(t) = \boldsymbol{A} \cdot \boldsymbol{y}(t), \text{ with the solution: } \boldsymbol{y}(t) = e^{A \cdot t/T_R} \cdot \boldsymbol{y}(0) \ , \qquad \text{(A2a - A2b)}$$

where T_R is the duration of the block ***A***.

[0095] Further time derivative of equation A2a leads to the familiar second order differential equation of motion of a system of dissipative coupled harmonic oscillators.

$$\ddot{\boldsymbol{y}}(t) = \boldsymbol{A}^2 \cdot \boldsymbol{y}(t) \qquad \text{(A3)}$$

[0096] The propagator can be expressed as a 3x3 real-valued matrix. Its determinant, $\det(\boldsymbol{A}) = \varepsilon_2^2 \, \varepsilon_1 \neq 0,$ where $\varepsilon_{1,2} = \exp(-T_R/T_{1,2})$; represents the total dissipation during the repetition time T_R. ***A*** can be diagonalized and has three non-zero eigenvalues. This diagonalization is desirable as it allows derivation of an expression of $\boldsymbol{A}^n$, which is used in equation 1.b. The diagonalization can be achieved by expansion with the eigenvectors [Hargreaves]. With the matrix ***P*** formed from the eigenvectors of ***A***, Λ as a diagonal matrix with the eigenvalues of ***A***, $\boldsymbol{\mu}_n$ can be expressed as:

$$\boldsymbol{\mu}_n = \boldsymbol{P}\, \boldsymbol{\Lambda}^n \boldsymbol{P}^{-1} \cdot \boldsymbol{\mu}_0 \qquad \text{(A4)}$$

[0097] This is a linear combination of the n_{th} power of the eigenvalues. Unfortunately, the eigenvectors are complex-valued in most cases, therefore the expression in eqn.4. is not immediately useful for a closed-form expression in eqn. A1.b.

[0098] It is more useful to express the solution with the normal modes instead of the eigenmodes. As a consequence of the Cayley-Hamilton theorem, any function of a 3x3 matrix ***A*** can be expressed as a function of ***A*** and $\boldsymbol{A}^2$. This expansion leads to the following exact equation:

$$\boldsymbol{A}^n = \rho^n \cdot \sin(n\varphi) \cdot \boldsymbol{M}_1 + \rho^n \cdot \cos(n\varphi) \cdot \boldsymbol{M}_2 + \eta^n \cdot \boldsymbol{M}_3 \ , \qquad \text{(A5)}$$

where the eigenvalues of ***A*** are $\varrho e^{i\varphi}$, $\varrho e^{-i\varphi}$ and η.

[0099] The real-valued, normal modes are $\nu_1 = \boldsymbol{M}_1 \cdot \boldsymbol{\mu}_0$, $\nu_2 = \boldsymbol{M}_2 \cdot \boldsymbol{\mu}_0$ and $\nu_3 = \boldsymbol{M}_3 \cdot \boldsymbol{\mu}_0$ where $\boldsymbol{\mu}_0$ is the initial state.

$$\boldsymbol{M}_1 = \frac{\boldsymbol{A}}{\rho \cdot \sin\varphi} - \frac{\boldsymbol{I} \cdot \cos\varphi}{\sin\varphi} + \left(-\frac{\eta}{\rho} + \cos\varphi\right) \cdot \boldsymbol{M}_3$$

$$\boldsymbol{M}_2 = \boldsymbol{I} - \boldsymbol{M}_3$$

$$\boldsymbol{M}_3 = \frac{(\boldsymbol{A}^2 + \varrho^2 \boldsymbol{I} - 2\varrho \cdot \cos\varphi \cdot \boldsymbol{A})}{\rho^2 + \eta^2 - 2\varrho \cdot \eta \cdot \cos\varphi} \qquad \text{(A6)}$$

[0100] The application of A5 over the initial magnetization state generates the expression shown in equation 1.

[0101] Equation A5 describes two modes exhibiting decaying oscillations with the same frequency and with a constant relative phase. The third mode exhibits an exponential decay. The temporal evolution is neatly separated into oscillatory and exponential decay coefficients determined by the eigenvalues of A. The advantage of this normal mode expansion over the eigenvector expansion is that the resulting expression is real and the modes are easy to interpret and visualize. The expression A5 is in effect providing a new set of coordinates. Choosing the normal modes as a coordinate system, the magnetization is described as three uncoupled oscillators. The oscillation is in a plane where the trajectory of magnetization is along a circle with exponentially decreasing radius.

[0102] In general, the normal mode vectors are not orthogonal. They do not necessarily form a complete set either in 3D. As illustrated in FIG 2 in case of on-resonance $|\nu_3| = 0$. Nevertheless, they always span the subspace that contains

A

the trajectory of the magnetization. In case of the off-resonance to on-resonance transition, the dimensionality of the trajectory collapses: 3D → 2D. This poses a serious problem in quantification. The signal evolution does not contain information about η in the on-resonance case (see equation A5). In practical MR, the problem of off-resonance cannot be fully controlled. An important task in the design of the propagator is to avoid such a dimensionality reduction at any possible frequency offset. In other words, the propagator preferably should guarantee that the trajectory of the magnetization evolution remains a 3D object for any frequency offset.

[0103] For the purpose of clarity and a concise description, features are described herein as part of the same or separate embodiments, however, it will be appreciated that the scope of the invention may include embodiments having combinations of all or some of the features described. Although we focus here on the concept, its proof and feasibility on actual clinical scanners, it is straightforward to translate these results to other fields in magnetic resonance such as multi-parametric proton NMR spectroscopy, dynamic contrast enhanced MRI, dynamic susceptibility contrast MRI, MR Thermometry and to extend the model with diffusion weighting and magnetization transfer.

[0104] In interpreting the appended claims, it will understood that the word "comprising" does not exclude the presence of other elements or acts than those listed in a given claim; the word "a" or "an" preceding an element does not exclude the presence of a plurality of such elements; any reference signs in the claims do not limit their scope; several "means" may be represented by the same or different item(s) or implemented structure or function; any of the disclosed devices or portions thereof may be combined together or separated into further portions unless specifically stated otherwise. Where one claim refers to another claim, this may indicate synergetic advantage achieved by the combination of their respective features. But the mere fact that certain measures are recited in mutually different claims does not indicate that a combination of these measures cannot also be used to advantage. The present embodiments may thus include all working combinations of the claims wherein each claim can in principle refer to any preceding claim unless clearly excluded by context.

Claims

1. A method for measuring magnetic resonance, MR, properties of spin systems in a target volume (V), the method comprising

   applying a main magnetic field (B0) to the target volume (V) along a longitudinal axis (Z);
   applying an excitation sequence (An) comprising a repeated block (A) of excitation pulses to the target volume (V);
   measuring a set of response signals (μ_n) indicative of respective magnetization (μ) of the spin systems from the target volume (V) in a respective one or more measurement windows (W) for each block (A) following one or more of the excitation pulses; and
   determining the MR properties of the target volume (V) based on the set of response signals;
   wherein each block (A) comprises a set of radio frequency, RF, pulses including at least

      a first small angle RF pulse (α_x) configured to apply a small flip angle (α) of less than ninety degrees along a first transverse axis (X) which is transverse to the longitudinal axis (Z);
      a first large angle RF pulse (γ_y) configured to apply a large flip angle (γ) of more than ninety degrees along a second transverse axis (Y) which is transverse to the longitudinal axis (Z) and transverse to the first transverse axis (X);
      a second small angle RF pulse (α_y) configured to apply the same small flip angle (α) as the first small angle pulse (α_x) but along the second transverse axis (Y);
      a second large angle RF pulse (γ_x) configured to apply the same large flip angle (γ) as the first large angle pulse (γ_y) but along the first transverse axis (X).

2. The method according to claim 1, wherein the small flip angles (α_x,α_y) are between fifteen and sixty degrees.

3. The method according to any of the preceding claims, wherein the large flip angles (γ_x,γ_y) are between one hundred forty and one hundred seventyfive degrees.

4. The method according to any of the preceding claims, wherein, in each block (A), the set of RF pulses are applied in a sequence (α,γ,α,γ) interleaving the small angle RF pulses (α_x,α_y) with the large angle RF pulses (γ_x,γ_y).

5. The method according to any of the preceding claims, wherein the RF pulses are applied in a sequences with the first small angle pulse (α_x) followed by the first large angle pulse (γ_y) followed by the second small angle pulse (α_y) followed by the second large angle pulse (γ_x).

A

6. The method according to any of the preceding claims, wherein, in each block (A), the set of RF pulses are applied in a sequence (α,...,γ) starting with one of the small angle RF pulses (α_x,α_y) and ending with one of the large angle RF pulse (γ_x,γ_y), wherein at least one measurement window (W) follows directly after a large angle RF pulse (γ_x,γ_y)

7. The method according to any of the preceding claims, wherein the blocks (A) are repeated with a repetition time (T_R) of less than hundred milliseconds.

8. The method according to any of the preceding claims, wherein the excitation sequence for determining a respective MR property comprises at least twenty repeated blocks.

9. The method according to any of the preceding claims, wherein the RF pulses are applied with a pulse-to-pulse time (Tp) between subsequent RF pulses in each block (A), wherein the pulse-to-pulse time (Tp) is between one and fifteen milliseconds.

10. The method according to any of the preceding claims, wherein each block comprise a set of magnetic field gradients or gradient pulses (G) used to produce a maximum magnitude of the signal in the measurement window (W) and/or for localizing the target volume (V) in an object.

11. The method according to any of the preceding claims, wherein one or more of the determined MR properties are used for generating a two dimensional image of an object comprising the target volume (V).

12. The method according to any of the preceding claims, wherein the gradient pulses (G) for each block are applied according to a balanced sequence.

13. The method according to any of the preceding claims, wherein between every pair of adjacent RF pulses the signal is sampled with balanced spiral-out k-space trajectory.

14. An MRI device configured to execute the method according to any of the preceding claims for imaging an object.

15. A non-transitory computer readable medium with software instructions which when executed causes an RF coil in an MR device to generate a sequence of repeated blocks,
wherein each block (A) comprises a set of radio frequency, RF, pulses including at least

a first small angle RF pulse (α_x) configured to apply a small flip angle (α) of less than ninety degrees along a first transverse axis (X) which is transverse to the longitudinal axis (Z);
a first large angle RF pulse (γ_y) configured to apply a large flip angle (γ) of more than ninety degrees along a second transverse axis (Y) which is transverse to the longitudinal axis (Z) and transverse to the first transverse axis (X);
a second small angle RF pulse (α_y) configured to apply the same small flip angle (α) as the first small angle pulse (α_x) but along the second transverse axis (Y);
a second large angle RF pulse (γ_x) configured to apply the same large flip angle (γ) as the first large angle pulse (γ_y) but along the first transverse axis (X).

EP 3 904 898 A1

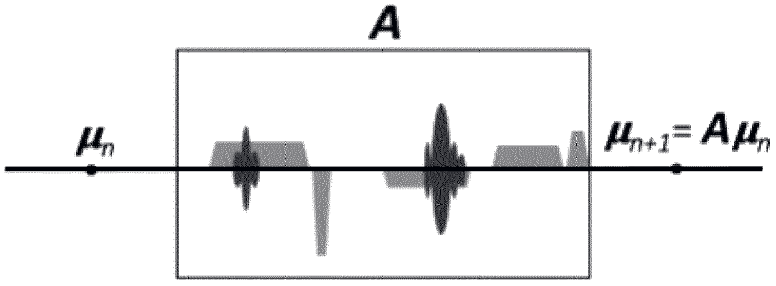

FIG 1A

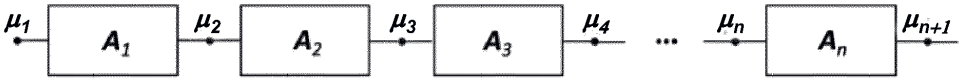

FIG 1B

EP 3 904 898 A1

A

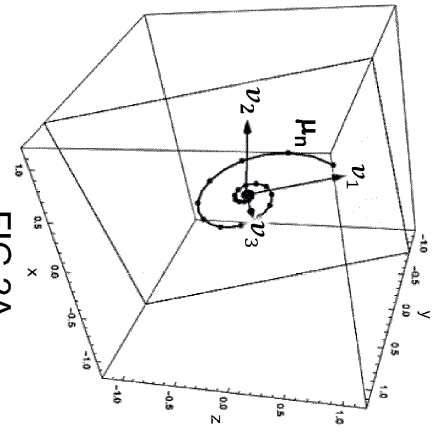

FIG 2A

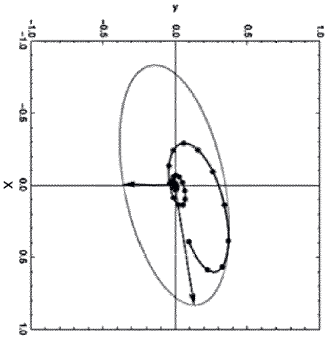

FIG 2B

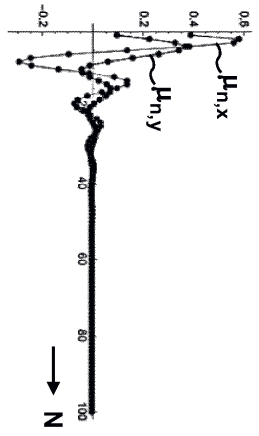

FIG 2C

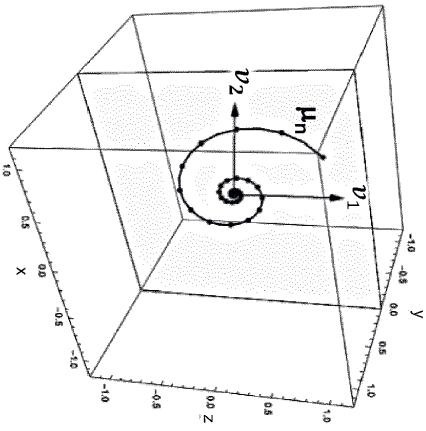

FIG 2D

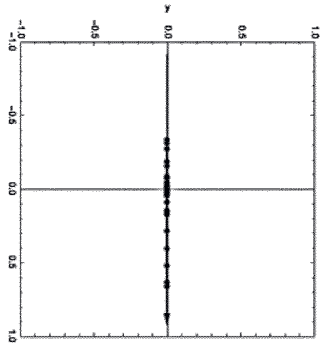

FIG 2E

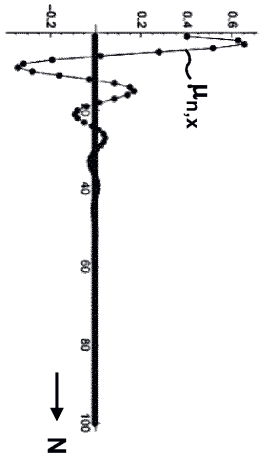

FIG 2F

EP 3 904 898 A1

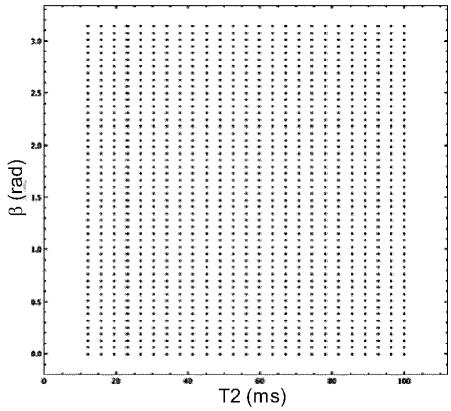

FIG 3A

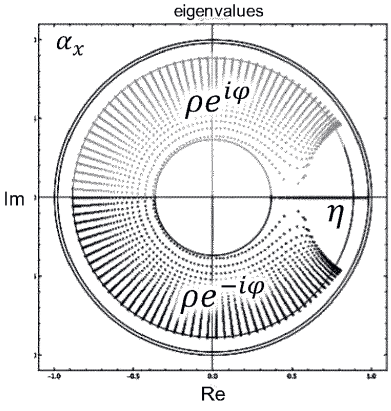

FIG 3B

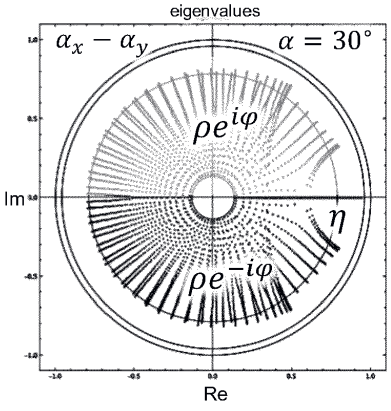

FIG 3C

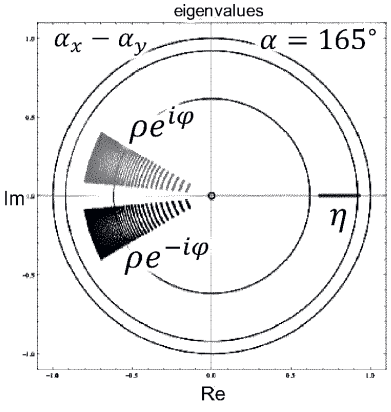

FIG 3D

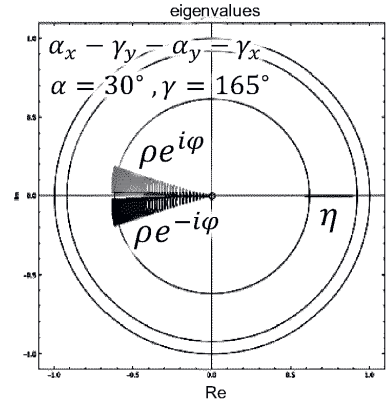

FIG 3E

EP 3 904 898 A1

A

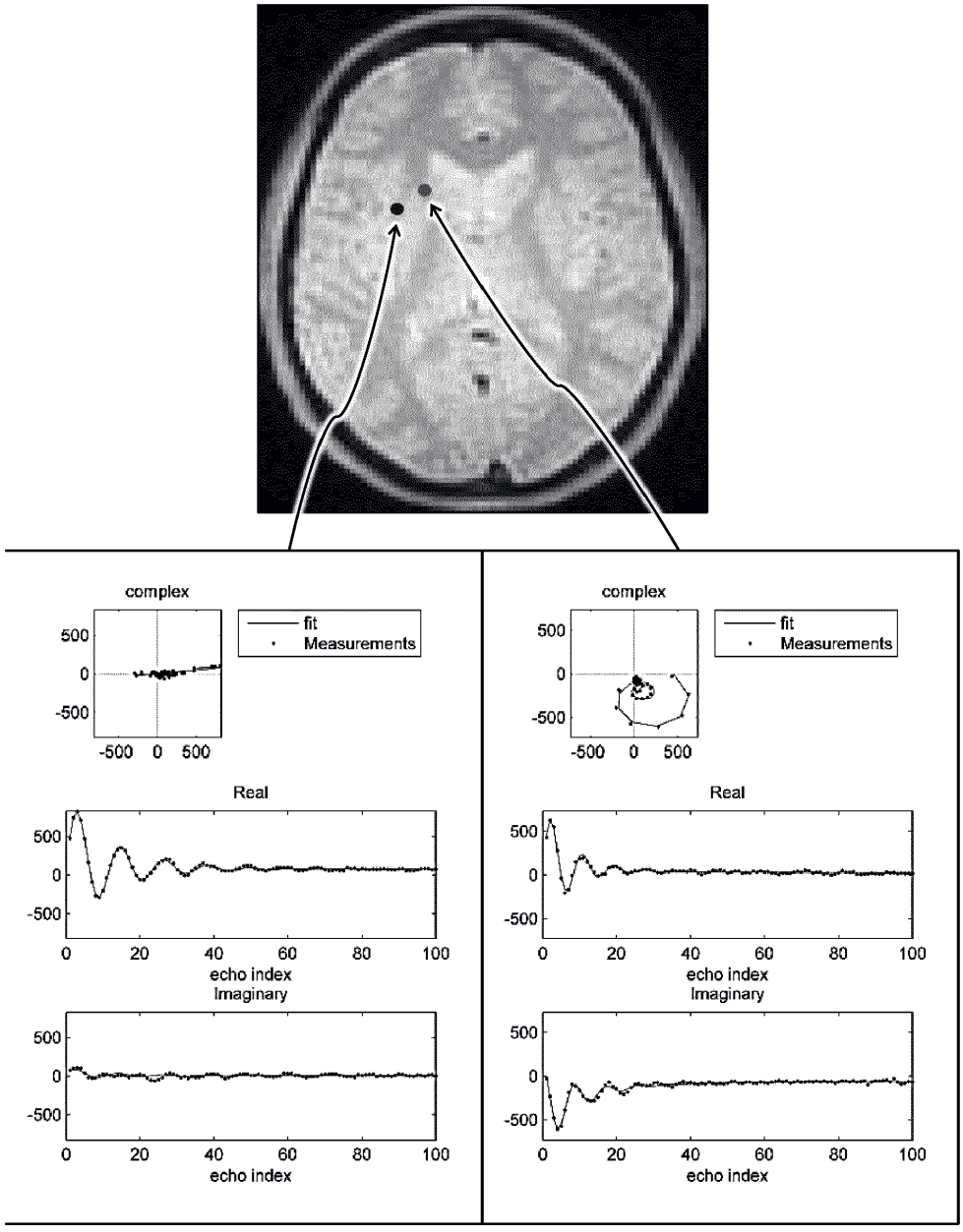

FIG 4

EP 3 904 898 A1

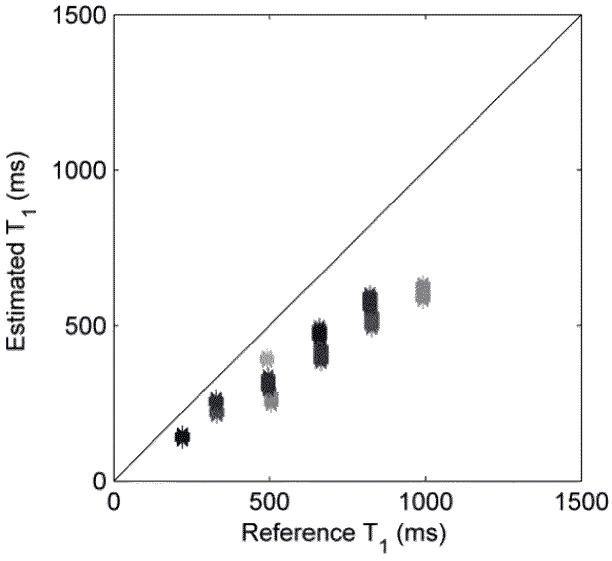

FIG 5A

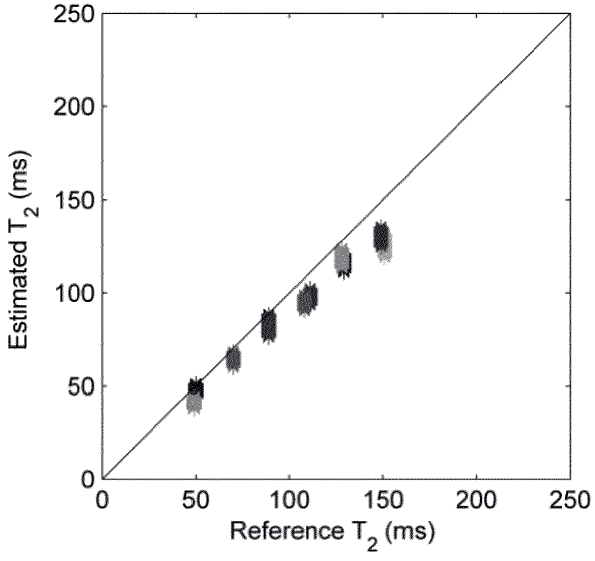

FIG 5B

EP 3 904 898 A1

A

PD

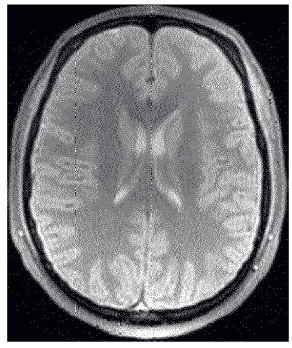

FIG 6A

T1

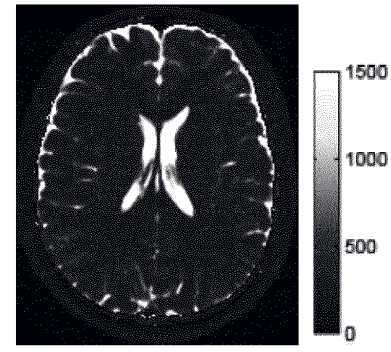

FIG 6B

T2

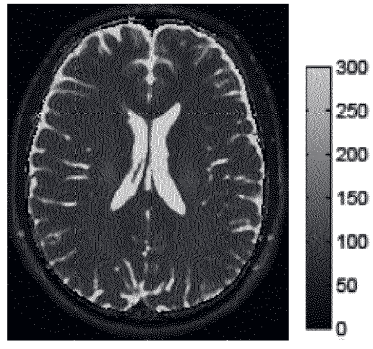

FIG 6C

B0

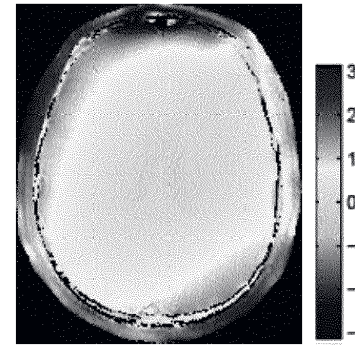

FIG 6D

B1

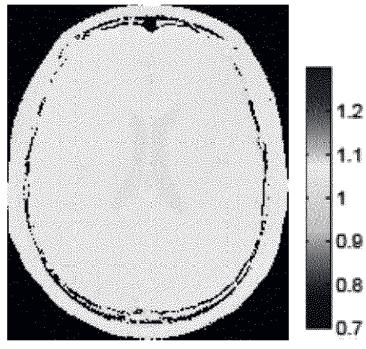

FIG 6E

$\rho^2\eta = det(\boldsymbol{A}) = \varepsilon_2^2\varepsilon_1$

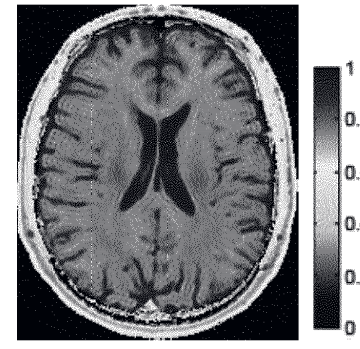

FIG 6F

EP 3 904 898 A1

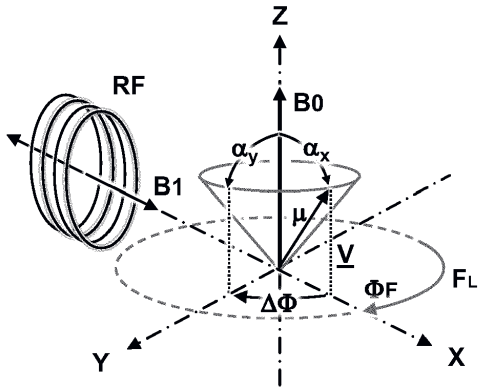

FIG 7A

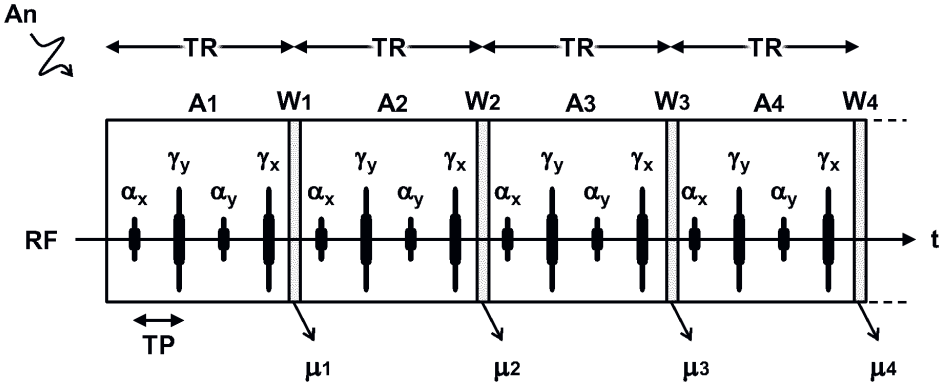

FIG 7B

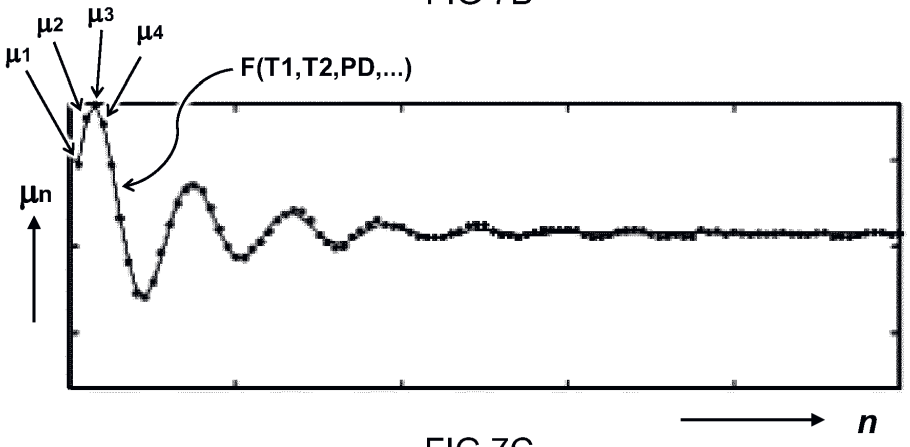

FIG 7C

EP 3 904 898 A1

A

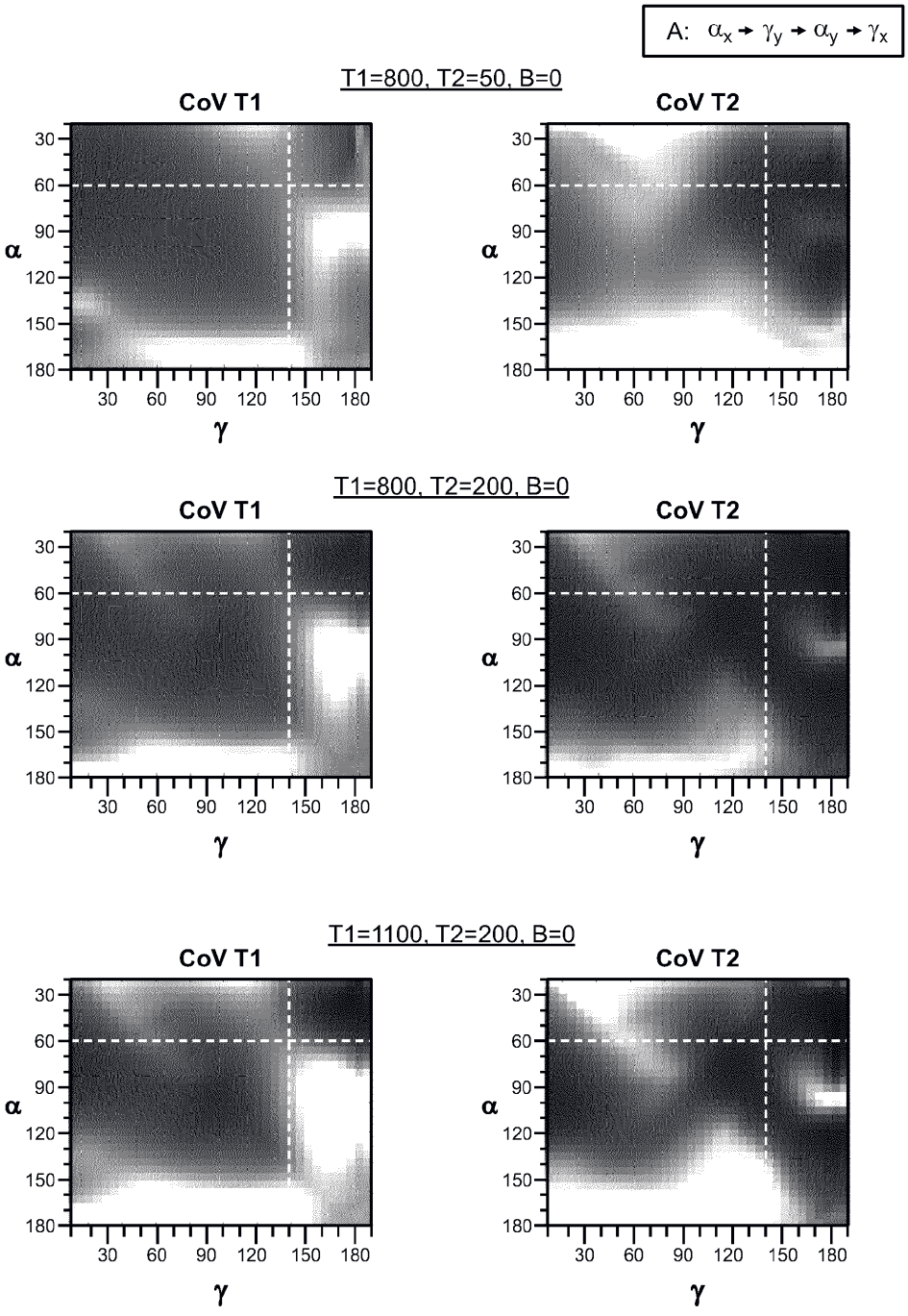

FIG 8A

EP 3 904 898 A1

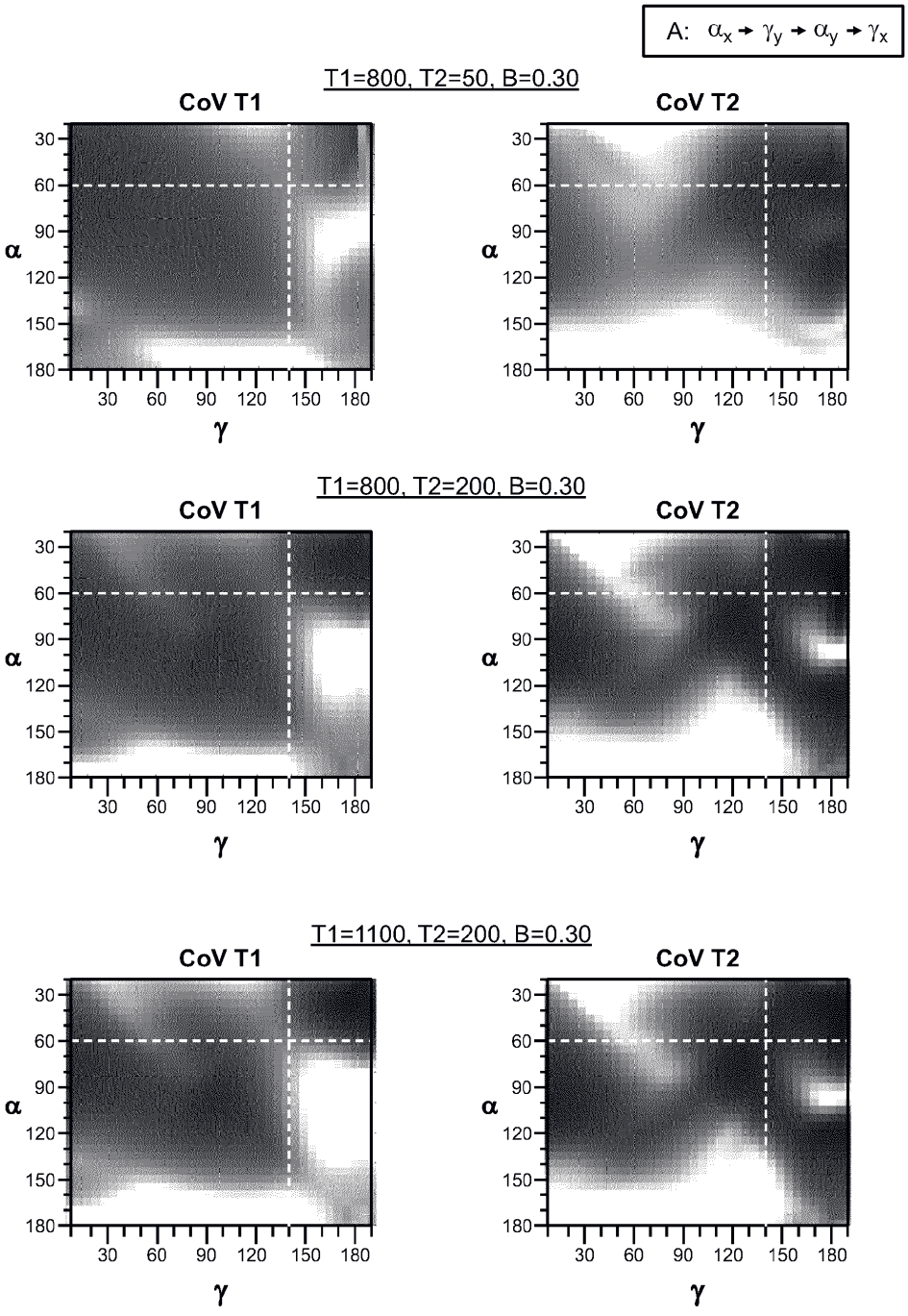

FIG 8B

EP 3 904 898 A1

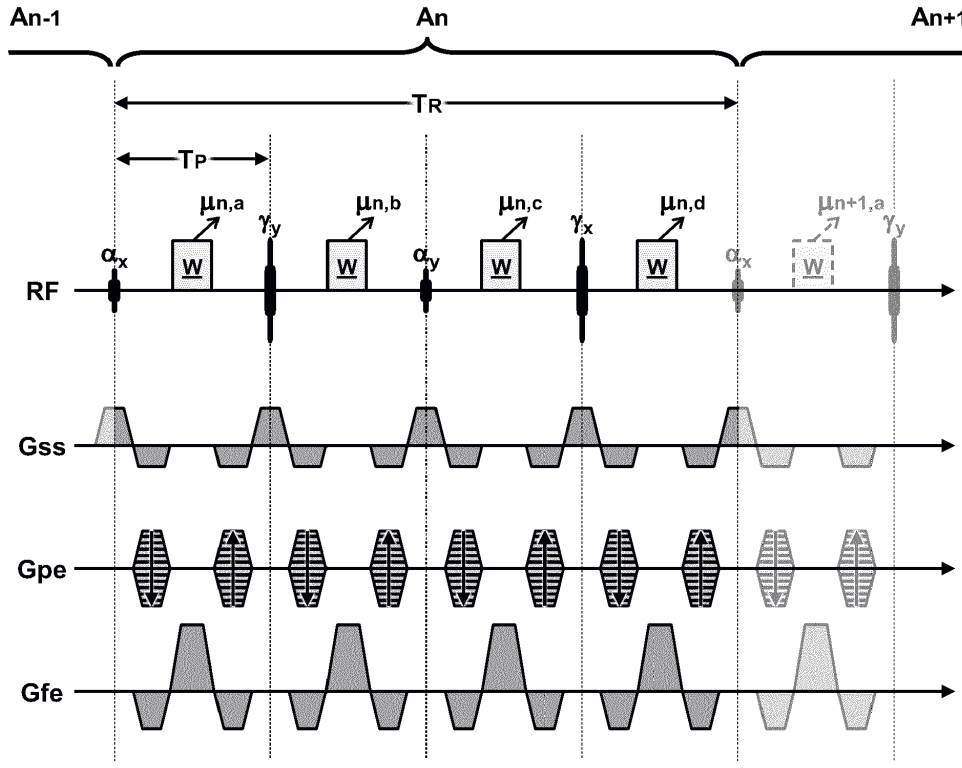

FIG 9

EP 3 904 898 A1

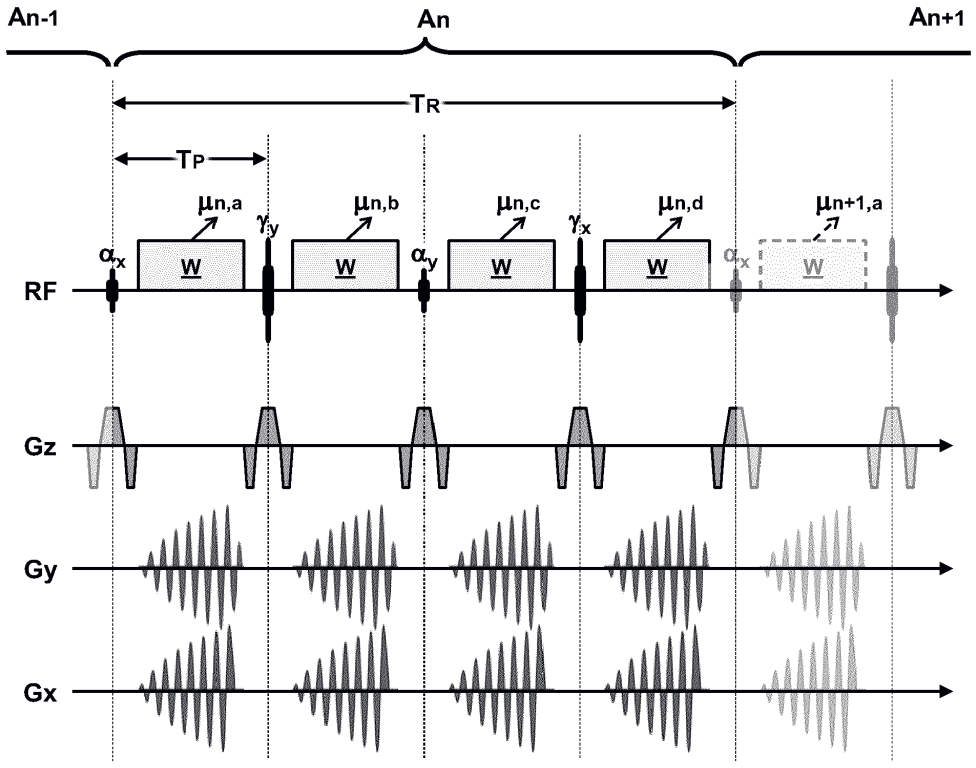

FIG 10

EP 3 904 898 A1

A

Europäisches Patentamt
European Patent Office
Office européen des brevets

EUROPEAN SEARCH REPORT

Application Number
EP 20 17 2381

DOCUMENTS CONSIDERED TO BE RELEVANT

Category	Citation of document with indication, where appropriate, of relevant passages	Relevant to claim	CLASSIFICATION OF THE APPLICATION (IPC)
A	US 6 291 996 B1 (GLOVER PAUL MARTIN [GB] ET AL) 18 September 2001 (2001-09-18) * abstract; claims 1-6,20 * * column 1, line 60 - column 4, line 66; figures 2,3,5,6a,6b,8 * * column 6, line 40 - line 59 *	1-15	INV. G01R33/44 G01R33/50
A	WANG GUAN ET AL: "Minimum acquisition methods for simultaneously imagingT1,T2, and proton density withB1correction and no spin-echoes", JOURNAL OF MAGNETIC RESONANCE, ACADEMIC PRESS, ORLANDO, FL, US, vol. 242, 1 March 2014 (2014-03-01), pages 243-255, XP028644584, ISSN: 1090-7807, DOI: 10.1016/J.JMR.2014.02.010 * figures 7-9 *	1-15	
A	US 2012/112743 A1 (GRANLUND KRISTIN L [US] ET AL) 10 May 2012 (2012-05-10) * paragraphs [0021] - [0024], [0039], [0052]; claim 12 *	1-15	TECHNICAL FIELDS SEARCHED (IPC) G01R
A,D	WO 2020/046120 A1 (UNIV ERASMUS MED CT ROTTERDAM [NL]) 5 March 2020 (2020-03-05) * the whole document *	1-15	

The present search report has been drawn up for all claims

Place of search	Date of completion of the search	Examiner
Munich	28 October 2020	Faber-Jurk, Sonja

CATEGORY OF CITED DOCUMENTS

X : particularly relevant if taken alone
Y : particularly relevant if combined with another document of the same category
A : technological background
O : non-written disclosure
P : intermediate document

T : theory or principle underlying the invention
E : earlier patent document, but published on, or after the filing date
D : document cited in the application
L : document cited for other reasons

& : member of the same patent family, corresponding document

EPO FORM 1503 03.82 (P04C01)

EP 3 904 898 A1

A

ANNEX TO THE EUROPEAN SEARCH REPORT ON EUROPEAN PATENT APPLICATION NO. EP 20 17 2381

This annex lists the patent family members relating to the patent documents cited in the above-mentioned European search report. The members are as contained in the European Patent Office EDP file on
The European Patent Office is in no way liable for these particulars which are merely given for the purpose of information.

28-10-2020

Patent document cited in search report	Publication date	Patent family member(s)	Publication date
US 6291996 B1	18-09-2001	EP 1004034 A1	31-05-2000
		JP 2001515736 A	25-09-2001
		US 6291996 B1	18-09-2001
		WO 9909428 A1	25-02-1999
US 2012112743 A1	10-05-2012	NONE	
WO 2020046120 A1	05-03-2020	EP 3617731 A1	04-03-2020
		WO 2020046120 A1	05-03-2020

EPO FORM P0459

For more details about this annex : see Official Journal of the European Patent Office, No. 12/82

REFERENCES CITED IN THE DESCRIPTION

This list of references cited by the applicant is for the reader's convenience only. It does not form part of the European patent document. Even though great care has been taken in compiling the references, errors or omissions cannot be excluded and the EPO disclaims all liability in this regard.

Patent documents cited in the description

- WO 20200046120 A **[0005] [0023]**

Non-patent literature cited in the description

- **MA D ; GULANI V ; SEIBERLICH N ; LIU K ; SUNSHINE JL ; DUERK JL et al.** Magnetic resonance fingerprinting. *Nature,* 2013, vol. 495 (7440), 187 **[0003]**
- **LUSTIG M ; DONOHO DL ; SANTOS JM ; PAULY JM.** Compressed sensing MRI. *IEEE signal processing magazine,* 2008, vol. 25 (2), 72 **[0003]**
- **GÓMEZ PA ; MOLINA-ROMERO M ; BUONINCONTRI G ; MENZEL MI ; MENZE BH.** Designing contrasts for rapid, simultaneous parameter quantification and flow visualization with quantitative transient-state imaging. *Scientific reports,* 2019, vol. 9 (1), 8468 **[0003]**
- **SKINNER TE.** Comprehensive solutions to the Bloch equations and dynamical models for open two-level systems. *Physical Review A,* 2018, vol. 97 (1), 013815 **[0008]**
- **TORREY HC.** Transient Nutations in Nuclear Magnetic Resonance. *Physical Review,* 1949, vol. 76 (8), 1059-68 **[0008]**
- **JAYNES ET.** Matrix treatment of nuclear induction. *Phys Rev.,* 1955, vol. 98 (4), 1099-105 **[0008]**
- **BLOOM BLOOM AL.** Nuclear induction in inhomogeneous fields. *Physical Review,* 1955, vol. 98 (4), 1105 **[0008]**
- **LIANG Z-P ; LAUTERBUR PC.** Principles of magnetic resonance imaging: a signal processing perspective. SPIE Optical Engineering Press, 2000 **[0008]**
- **SCHEFFLER K.** On the transient phase of balanced SSFP sequences. *Magn Reson Med.,* 2003, vol. 49 (4), 781-3 **[0008]**

A.2. PORTFOLIO

Name Ph.D. student	Laura Núñez González
Erasmus MC Department	Radiology & Nuclear Medicine
Promotor	Prof. Dr. J.A. Hernández Tamames
Co-Promotors	Dr. D.H.J. Poot and Dr. G. Kotek

Training activity	**Year**	**ECTs**
2016 European EPIC Course	2016	3.00
EPIC Training	2017	3.00
34th Annual Scientific Meeting	2017	1.00
Simultaneous multi-slice/multiband imaging	2018	1.00
Research Integrity	2018	0.00
ISMRM Annual Meeting	2018	2.00
MR Image processing	2018	1.00
BROK course	2018	1.50
EMC - CE08 Repeated Measurements	2019	1.70
English Biomedical Writing and Communication	2019	3.00
ESMRMB 2019 meeting	2019	1.00
Oral presentation ESMRMB 2019	2019	1.00
11th ISMRM Benelux Chapter meeting	2019	1.00
ISMRM Annual Meeting	2019	2.00
Advanced MR Physics I	2020	5.00
Talks and Poster Sessions	2016-2021	4.00
MR Physics group seminars	2016-2021	3.50
Supervision of trainee	2021	0.50
Paper review	2021	0.30
Total ECTs	**2016-2021**	**35.50**

A

A.3. PUBLICATIONS

JOURNAL PUBLICATIONS

Pirkl CM, **Nunez-Gonzalez L**, Kofler F, Endt S, Grundl L, Golbabaee M, et al. *Accelerated 3D whole-brain T1, T2, and proton density mapping: feasibility for clinical glioma MR imaging.* Neuroradiology 2021. https://doi.org/10.1007/s00234-021-02703-0.

Kotek G, **Nunez-Gonzalez L**, Vogel MW, Krestin GP, Poot DHJ, Hernandez-Tamames JA. *From signal-based to comprehensive magnetic resonance imaging.* Sci Rep 2021;11:17216. https://doi.org/10.1038/s41598-021-96791-w.

Nunez-Gonzalez L, Kotek G, Gómez PA, Buonincontri G, Vogel M, Krestin GP, et al. *Accuracy and repeatability of QRAPMASTER and MRF-vFA.* Magnetic Resonance Imaging 2021;83:196207. https://doi.org/10.1016/j.mri.2021.09.004.

Nunez-Gonzalez L.*, Nagtegaal M.*, Poot D.H.J., Bresser J., van Osch M.J.P., Hernandez-Tamames J.A., Vos F.M. *Accuracy and repeatability of joint sparsity multi-component estimation in MR Fingerprinting.* Submitted. These authors contributed equally.

Nunez-Gonzalez L., van Garderen K.A., Smits M., Jaspers J., Méndez Romero A., Poot D.H.J., and Hernandez-Tamames J.A. *MAGiC pre-contrast in gliomas: Are quantitative MRI parameters different in tumors with or without contrast-enhancement?* Submitted.

PATENTS

Juan A. H-T, Gyula K, **Laura N.G.**, Dirk H.J. P, Mika V. *Balanced Phase Cycling non Stationary Free Precession Sequence; Banding Artifact Free Imaging For MR Multi-Parametric Estimation.* 3904898, 2021.

ABSTRACTS

L. Núñez González, D. Papp, G. Kotek, J. A. Hernández-Tamames. *Flow sensitization in an inhomogeneous excitation field MR Fingerprinting approach.* In: Magnetic Resonance Materials in Physics, biology and Medicine. ESMRMB 2017. #558

L. Núñez González, G. Kotek, R. Schulte, P. Gómez, M. Vogel, G. Buonincontri, J. A. Hernández-Tamames. *Accuracy and Repeatability study of MAGiC and MR Fingerprinting.* In: Body Language. ISMRM Benelux, 2019. #P-066

Carolin M Pirkl, **Laura Nuñez-Gonzalez**, Pedro A Gómez, Sebastian Endt, Rolf F Schulte, Guido Buonincontri, Marion Smits, Bjoern H Menze, Marion I Menzel, and

Juan A Hernandez-Tamames. *Accelerated 3D multiparametric MRI in glioma patients - Initial clinical experience.* ISMRM 2020. #0559 Summa Cum Laude Award.

ORAL PRESENTATIONS

L. Núñez González, G. Kotek, R. Schulte, P. Gómez, M. Vogel, G. Buonincontri, J. A. Hernández-Tamames. *Accuracy and Repeatability study of MAGiC and MR Fingerprinting.* In: Quantitative MRI. ESMRMB, 2019. #S21.05

A.4. ABOUT THE AUTHOR

Laura Núñez González was born on April 18th, 1990 in Leganés (Madrid), Spain. She studied a double degree and master in Telecommunication engineering and Computer Science in Fuenlabrada (Madrid), Rey Juan Carlos University, from 2008 to 2015. In her final project supervised by Susana Borromeo López, "Processing and analysis of olfactory evoked potentials", she applied several filters to the electroencephalogram signal to distinguish and extract olfactory evoked potentials. This initial experience of a joint medicine-technological project motivated her towards the research with medical applications.

After finishing her studies, she started to work at the "Biometrics and Medical Image Analysis Laboratory" (LAIMBIO) at Rey Juan Carlos University. In this laboratory, she learned the principles of medical imaging, especially MRI. One year later, she moved in 2016 to Rotterdam to start her Ph.D. at Erasmus Medical Center in the MR-Physics group and focused her research in MR quantitative relaxometry.

In this thesis, she studied and evaluated different multi-parametric quantitative MR techniques in phantom, healthy volunteers, and gliomas patients. Furthermore, she deepened her knowledge in MR-Physics and applied it to the development of a new quantitative MR sequence, MP-b-nSSFP, which is patented under the number WO 2021/221501.

A